High Speed Applications for Electromagnetic Propulsion Technology

Hany Mahmoud

A thesis submitted for the degree of

Doctor of Philosophy

Department of Electronic and Electrical Engineering

May 2018

ABSTRACT

In the last decades a magnetic lead screw device has been proposed for many applications, such as wave energy conversion, artificial heart, automotive and aerospace actuation. The device is able to convert rotational motion to linear motion and vice-versa by the action of magnetic poles mounted on the magnetic screw and magnetic nut. Compared to a mechanical screw, the magnetic screw device has no physical contact between its part ensuring long life time, high durability, no lubricants required, and low maintenance requirements. Simply, a magnetic lead screw consists of a translator that can move in a linear direction and a rotor which rotates around the linear motion axis.

In this thesis, different types of the magnetic lead screw systems are considered, and the effects of the key design parameters, such as magnet thickness, air-gap length, pole-pitch, number of pole-pairs, dimension etc. on the force/torque transmission are investigated. Investigations on different types of the magnetic lead screw showed that, the magnet-to-magnet type MLS can achieve the highest shear stress value, while the magnet-to-conductor type MLS has the lowest shear stress. Furthermore, although the magnet-to-reluctance type exhibited a lower force transmission capability than the magnet-to-magnet, the simplicity of the screw design and the reduced use of PM material, which is confined to the nut, makes this topology a good candidate for many applications. Moreover, research into the realisation of helical magnetisation distribution employing a novel impulse magnetisation process is undertaken, in order to reduce the complexity and cost of manufacture. This avoids the complex and/or time consuming methods, which may require the assembly of a large number of small magnets to approximate helical magnetisation distribution.

A prototype reluctance type magnetic screw system is realised, it consists of a double start mechanical screw and a permanent magnet nut equipped with impulse magnetised cylindrical permanent magnets, using purpose designed double-sided impulse magnetising fixture. Furthermore, a test-rig to measure the transmitted force is developed and used to compare the predicted and measured results.

A case study, investigating the feasibility of magnetic screw system as a launching platform for UAVs is undertaken. It has been shown that reluctance type magnetic screw would provide the most cost effective solution for such applications.

ACKNOWLEDGEMENTS

First and foremost, I would like to thank God for his grace, mercy, and provision during one of the toughest times of my life. I would like to express the deepest appreciation to my supervisor Professor Kais Atallah for his continuous support and valuable advices.

I would like to thank the technical staff in my department for their support in my experimental work specially Mr. Richard Garraway and Mr. Clive Thompson.

My special thanks to my colleagues and friends in my department for their assistance and countless hours of discussion. Special thanks to Essam Khalaf, Glynn Cooke, Dave Hewitt, Harry Harrison, Abdulla Shanshal, Mohammed Khatab, and, Tamer Kamel for their constructive discussions that helped my understanding and shaping my experience in research.

An endless appreciation for my parents and family for their continuous encouragement during the hard times of research. Last but not least, I am genuinely grateful to my wife for her endless support throughout my life.

TABLE OF CONTENTS

Page

LIST OF FIGURES

Page

LIST OF TABLES

Page

LIST OF SYMBOLS

Alphabetic symbols

A	Cross-sectional area of the conductor (m^2)
a	Acceleration (m/s^2)
A_f	Frontal area facing the air flow in m^2
B	Magnitude of magnetic flux density (T)
C	Capacitance of the capacitor bank (F)
C_d	Non-dimensional drag coefficient
C_p	Specific heat capacity of copper (385 J/kgK)
d	Maximum deflection of the screw beam (m)
E	Young’s modulus of elasticity of the beam’s material (Pa)
F	Thrust force of a magnetic lead screw (N)
F_c	Concentrated point load at the centre of the beam screw (N)
F_d	Aerodynamic drag force (N)
F_m	Transmitted magnetic force (N)
F_{nut}	Transmitted force on the nut (N)
F_s	Stiction force (N)
F_t	Total required force (N)
f	Frequency (Hz)
G	Gear ratio
I	Current in a conductor (A)
I_m	Area moment of inertia of the beam (m^2)
J_{load}	Equivalent inertia of the load ($kg.m^2$)
J_{motor}	Inertia of the motor ($kg.m^2$)
J_{nut}	Equivalent inertia of the nut ($kg.m^2$)
J_{screw}	Inertia of the screw ($kg.m^2$)
J_{total}	Total inertia referred to the shaft of the motor ($kg.m^2$)
k_a	Anomalous loss coefficient

k_e	Eddy current loss coefficient
k_h	Hysteresis loss coefficient
L	Inductance of the fixture (H)
L_b	Length of the beam (m)
m	Mass of the copper winding (kg)
m_{nut}	Mass of the nut (kg)
$m_{platform}$	Mass of the platform (kg)
m_t	Combined mass of the nut, the UAV and the platform (kg)
m_{UAV}	Mass of the UAV (kg)
M(x)	Moment at distance x along the screw length (kgm)
P	Power loss (W)
P_a	Anomalous loss (W)
P_e	Classical eddy current loss (W)
P_{Fe}	Iron loss (W)
P_h	Hysteresis loss (W)
R	Resistance of the fixture (Ω)
ΔR	Change in resistance (Ω)
R_0	Initial resistance of the fixture (Ω)
s	Travelled distance before take-off (m)
T	Torque (N.m)
T_{motor}	Torque produced by the motor (N.m)
T_{screw}	Transmitted torque on the screw (N.m)
ΔT	Temperature change in copper windings (°C)
V	Linear velocity (m/s)
V_i	Initial voltage on the capacitor (Volt)
V_{nut}	Linear speed of the nut (m/s)
V_o	Initial velocity (m/s)
V_{slip}	Linear slip speed (m/s)
w	weight of the beam (N)

Greek symbols

α	Temperature coefficient of copper ($3.9\times10^{-3}/^{0}$C)
η	Magnetic efficiency
ℓ	Length of the coil (m)
λ	Single lead of a magnetic lead screw (m)
ρ	Resistivity of copper (1.7×10^{-8} Ω/m at 20 ºC)
ρ_a	Air density (kg/m^3)
ϱ	Density of copper (8960 kg/m^3)
τ_p	Magnetic pole-pitch (m)
ω	Angular velocity (rad/s)
ω_{screw}	Rotational speed of the screw (rad/s)
ω_{slip}	Rotational slip speed (rad/s)

1 Introduction

1.1 Motivation

In the last decades, the idea of using the electromagnetic field as a source of propulsion force has appeared in many areas. According to the application, electromagnetic propulsion has been used in two main areas:

a) Military applications.
b) Civilian applications.

The aim of using the electromagnetic field as a source of propulsion force is the ability of providing a large pulsed force to meet the requirements of the particular application.

1.1.1 Military applications

Electromagnetic propulsion is the "acceleration of an object by electromagnetic forces along a guideway to initiate subsequent flight" [1]. Electromagnetic launch systems used in military applications have been widely utilised in the last decades. It is one of the most promising technologies for meeting short and long-term propulsion requirements. Electromagnetic launch technology has been proposed for applications in advanced launching systems, space launch, and propulsion. One of the interesting potential applications for using the electromagnetic field is the launch of aircraft from the deck of an aircraft carrier [2]. This system of propulsion can be called as “Railgun”. At the most basic level, a railgun based on a launcher and a power supply system. It converts enormous amounts of electrical energy to mechanical energy in very short time. Furthermore, it can be driven by several different power supply configurations according to the desired application. The generated force responsible for pushing the payload forward is called “Lorentz force” [3]. The most significant advantages of using electromagnetic propulsion in military applications for launching heavy aircraft and UAVs, over conventional launching systems, are efficiency and the possibility of improved velocity control [4, 5].

The launching system can be achieved by linear machines, which can be permanent magnet synchronous machines [5-7] or Linear induction machines [8, 9]. These consist of two main parts a stator and a mover. Fig. 1.1 shows quantification of velocity for railgun, mechanical, and magnetic lead screws. A railgun can achieve a launching velocity up to 85 m/s in case of launching an aircraft (i.e. F-18) [10]. However, a railgun can achieve a velocity up to 3000 m/s in case of firing projectiles [11]. On the other hand, a coilgun system can achieve a velocity up to 2500 m/s in firing applications only [12]. A magnetic and mechanical screws exhibit lower velocities depending on critical speed, stiffness, dimensions of screw (i.e. diameter and length) and the external motor providing the rotation speed for specified transmitted linear speed [13]. The mechanical and magnetic screws can achieve speed up to 10 m/s depending on the bearing used in the application [14].

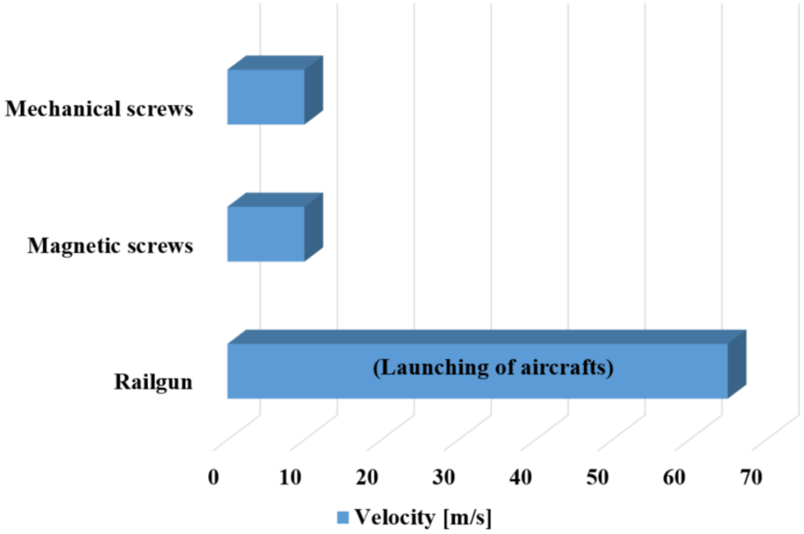

Fig. 1.1: Velocity rates for railgun, mechanical, and magnetic screws.

1.1.2 Civilian applications

Not only that electromagnetic propulsion technology can be used in military applications, but also it has many civilian applications. Linear machines can be used in applications such as, ride launchers, and maglev trains, for example. With maglev, a vehicle is levitated a short distance away from a guideway [15-17]. Other potential civilian applications for the electromagnetic propulsion technology are propelling space payloads such as satellites, and UAVs [18, 19].

1.1.3 Research problem

The previous types of linear motors are the conventional types of motors that are used in electromagnetic propulsion technology. The contribution in the research area is to use a new technique by utilising rotary to linear motion conversion device that can provide the same functionality of linear motors but with potentially less cost and complexity, while providing higher force, efficiency, and reliability. The idea came from using what is called “Trans-rotary magnetic gear” or “Magnetic lead screw” to convert rotation into translation motion. This translation motion is used to launch a civilian UAV which is employed in agriculture surveillance purpose, geometrical photography, altitude photography for mapping, and other civilian purposes. In brief, a magnetic lead screw assembly will be utilised as the platform for launching the UAV. The magnetic lead screw can be divided into two main sections, rotor, and translator as shown in Fig. 1.2. The study for the types of the magnetic lead screw is discussed in detail concerning the maximum shear stress that can be obtained, maximum thrust force required to launch the UAV and the maximum thrust force gained from the proposed models. In addition, helical magnetisation distribution has so-far been achieved employing discrete magnets arranged in a helical shape. Therefore, in order to facilitate the manufacture of magnetic lead screw assemblies, it is proposed to imprint helical magnetisation distributions on cylindrical permanent magnets using impulse magnetisation techniques. Moreover, losses and efficiency for different types of magnetic lead screw are addressed.

The research questions might be concerning the ability of the generated linear force to propel a certain mass to a desired velocity with the new technique. Also, the ability of the magnetic screw to produce the required force for the acceleration of the payload taking into consideration the specified physical and cost constraints [20] as detailed in chapter 6. Finally, the ability of the impulse magnetisation to imprint a helical magnetisation distribution on cylindrical shape magnet.

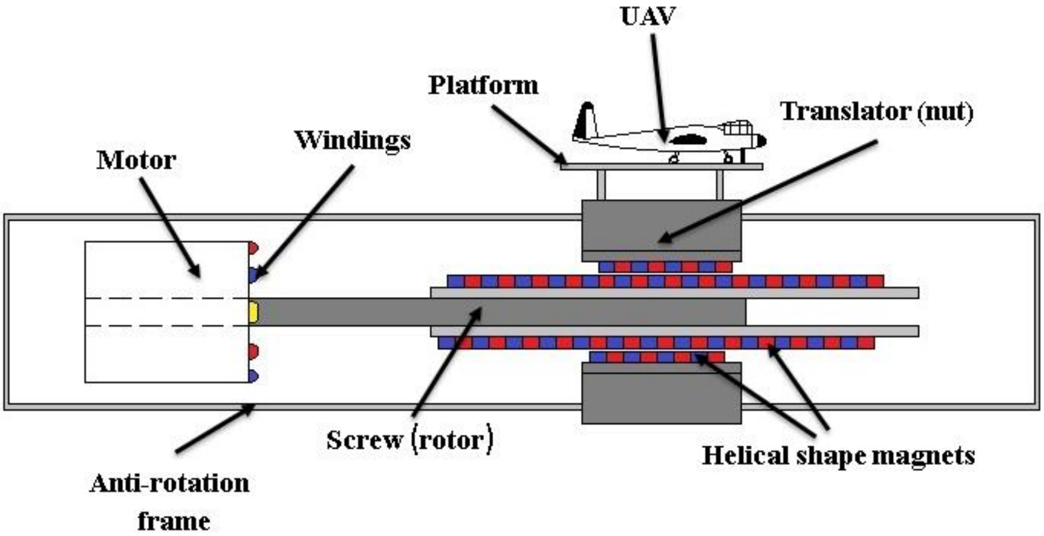

Fig. 1.2: Proposed MLS model.

1.1.4 Aim and Methodology

Before answering the research questions, it is necessary to answer why the magnetic lead screw was chosen for linear propulsion.

The answer might be useful if we know that the magnetic lead screw can convert rotational motion into linear one and vice-versa with long life duration as there is no mechanical contact between translator and rotor which is the source of wear and, therefore, less maintenance requirements. The use of permanent magnets in these types provides high force density, high reliability, and durability.

The aim of this research is to investigate the ability to use a magnetic lead screw as a launching platform for UAVs. Although UAVs are employed as the main example to be integrated with a magnetic lead screw, the outcome of the research will be relevant to other launching applications. Thus, different types of the magnetic lead screw are investigated for different parameters as magnet thickness, air-gap length, pole-pitch, number of pole pairs, diameter, and volume of the rotor and translator. The performance characteristics which have to be considered are transmitted force, torque, inertia, and efficiency. Furthermore, research is also including the methods of realising the magnetic screw system, and a novel impulse magnetisation process is investigated since it would significantly reduce the complexity of manufacture and improve the viability of the proposed solution. Also, replacing the old fashioned way for assembling small magnets in a helical way to produce a helical shape magnetic field. Moreover, the success of this magnetisation process means that the helical shape magnets can be assembled in a MLS as one part instead of using thousands of small magnets to be assembled together.

1.2 History

The idea of converting rotational motion into a linear one is not entirely new, but it was proposed many decades ago, and many patents have been filed, and many investigations have been reported. In 1925 [21], Benjamin Andrews has described a magnetic screw, as shown in Fig. 1.3, which is based on a screw with helical grooves filled with windings in which the current flows causing the magnetic coupling between the core and the casing providing reciprocal motion which was required to pump liquid back and forth. Then in 1945 [22], Harold T. Faus patented “magnetic transmission” which was the first to use permanent- magnet (PM) to get linear motion from rotation between a translator and a rotor. The translator was used to measure the level of liquid in a tank by its back and forth motion as shown in Fig. 1.4. In 1970, Gerrard and Paul [23, 24] proposed "recti-linear machine", in 1978 an electromagnetic (EM) rotary to linear coupler was proposed by Dawkins and Rhodes [25]. The aim was developing translation motion from rotating field. In 1997, Hashimoto et al. [26] proposed a magnetic screw device as shown in Fig. 1.5. The device includes a soft magnetic material screw, which is helically grooved on its outer cylindrical surface, and a nut mounted around the screw. The nut body consists of two parts, a back-iron (soft steel) cylinder which is concentric with the magnetic screw shaft and helically shaped magnets mounted on its inner surface as shown in Fig. 1.6. When the magnetic shaft is rotated, the nut can be moved in a linear motion as a result of magnetic interactions.

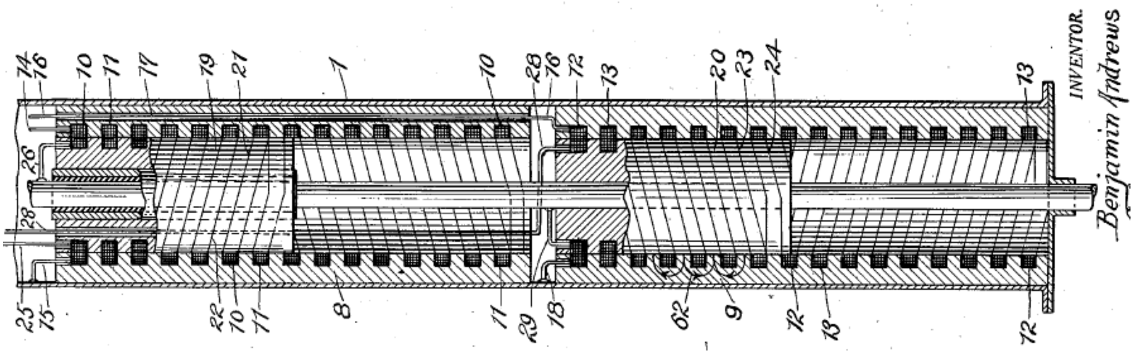

Fig. 1.3: Cross section of proposed magnetic screw in [21].

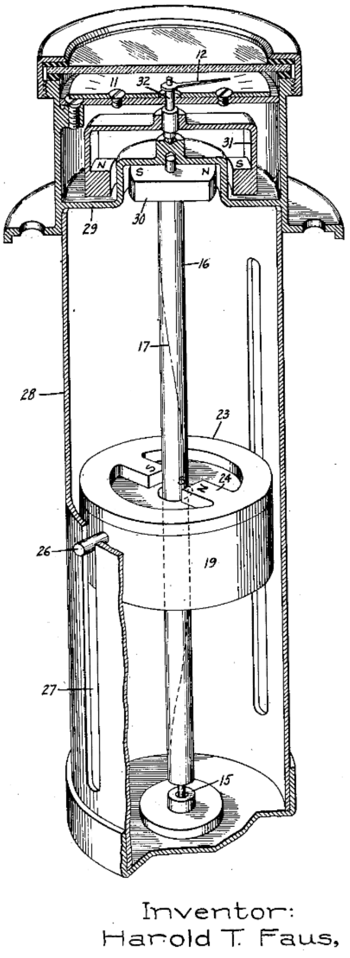

Fig. 1.4: Linear to rotary magnetic transmission for measuring liquid level in a tank [22].

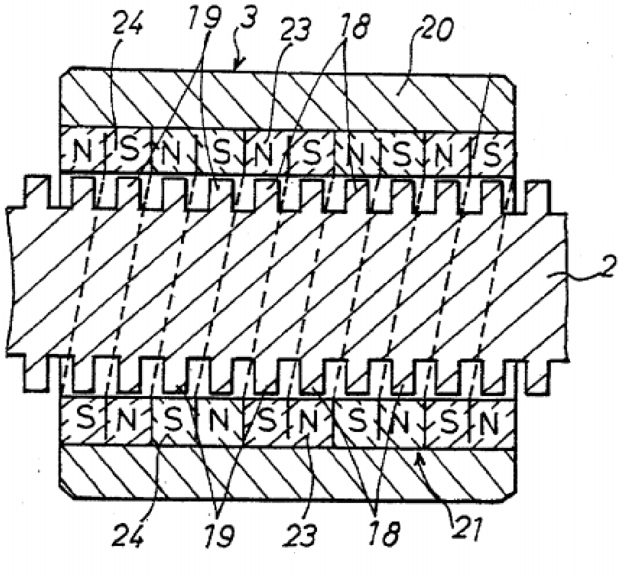

Fig. 1.5: Magnetic screw stated in [26].

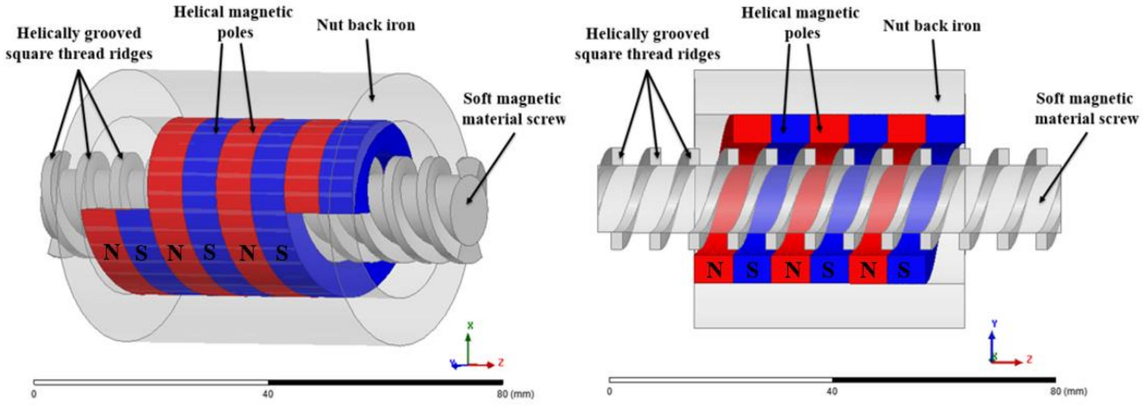

(a) (b)

Fig. 1.6: Magnetic screw device: (a) 3D view, (b) Cross-section showing square thread ridges.

1.3 Advantages of magnetic screw

A rotation motion can be converted to linear one and vice-versa by the action of magnetic poles mounted on the magnetic screw device. Compared to mechanical screw, the magnetic screw device has a lot of advantages to be mentioned that makes it more desirable than the mechanical one. In mechanical screw, friction occurs due to metal-to-metal contact between screw parts, this leads to short life as a result of wear, lubricants are needed to decrease friction and noise resulting from contact between mechanical parts. Also a magnetic lead screw has been proposed for energy wave conversion, artificial heart, automotive and aerospace actuation [27-33]. The magnetic lead screw is a high force density linear actuator proposed in [34] that can replace the present mechanical lead screw for many applications.

On the other hand, a magnetic screw device has no contact between its parts ensuring long life time, high durability, and no lubricants are required. Hence, making it suitable for systems acquiring high reliability requirements.

Cost of production is one of the most important issues while preparing a prototype to be used for mass production. Therefore, using helically shaped magnets on both nut and screw shaft will increase the cost of production due to price of the permanent magnets and the complexity of manufacturing helically shaped magnets. However, higher force density will be achieved while using magnets on both sides, accordingly, product requirements must be achieved to get the desired specifications with acceptable cost. In design of magnetic screw, rotor and translator lengths should not be the same. Fig. 1.7 shows a magnet-to-magnet screw where the active length is the section where the magnets on the nut are facing those on the screw.

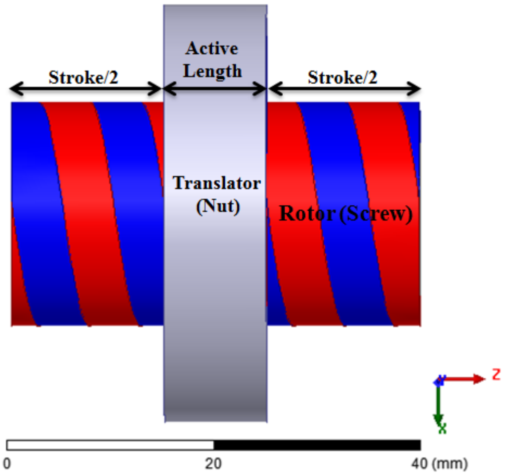

Fig. 1.7: Two-pole magnetic lead screw showing difference between stroke and active length.

1.4 Magnetic screw types

Numerous topologies for magnetic lead screw (MLS) have been proposed. Those will be briefly discussed in next pages. A magnet-to-magnet type MLS is a device which consists of two main parts:

1- A translator which can move in linear direction.
2- A rotor which rotates around the linear motion axis.

Each one of these parts could be the screw or the nut according to the application. Magnetic poles are mounted on the outer surface of the screw and on the inner surface of the nut as shown in Fig. 1.8. The magnet-to-magnet type MLS can be double start MLS or more than double start depending on the application used for the MLS.

In [30], Jinhua Ji et al. have proposed a new technique used in a magnetic lead screw by replacing the conventional alternating magnetic north-south poles by Halbach array with axially and radially magnetized magnets taking the advantage of reducing leakage flux by the presence of axially magnetized magnets (which offer magnetic path for the flux instead of passing via back-iron and return back in case of radially magnetized magnets only). The magnet-array is mounted on the surface of the back-iron of both nut and screw. By using Halbach array, each pole-pitch comprises two magnets with four magnets for every pole pair, the configuration of Halbach array enhances the air-gap magnetic field, and, hence, increased thrust force is obtained. Yet, the magnetization process for Halbach array in helical form is still tricky.

Enhancing thrust force doesn't mean that we get the highest possible thrust force of the proposed model because the thrust force is a function of the relative position between the facing magnets on nut and screw. Zero thrust force is obtained when the magnets on nut and screw are aligned with each other, thrust force begin to increase when the relative position between the facing magnets on nut and screw increases until maximum thrust force is obtained when the relative position between the facing magnets on nut and screw became equivalent to half pole-pitch, τ_p.

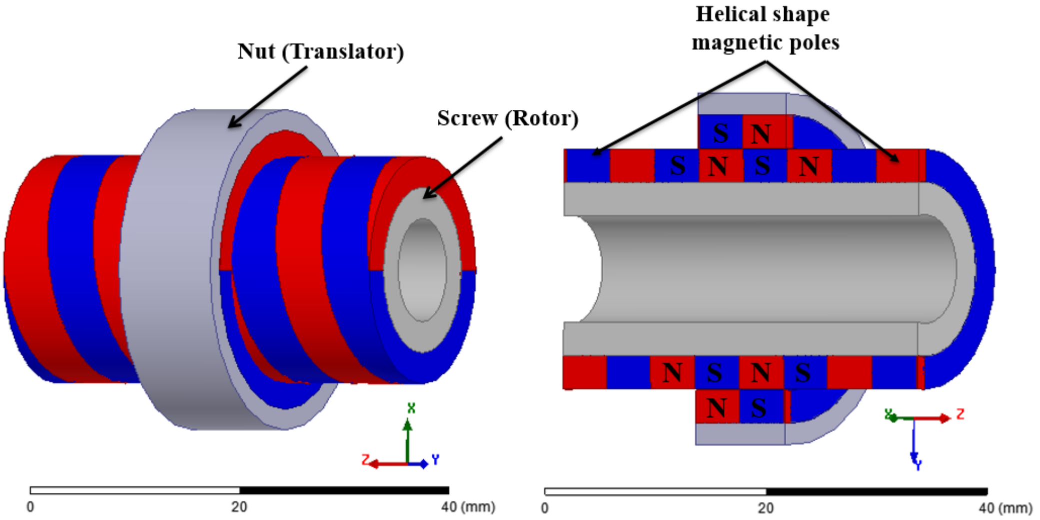

(a) (b)

Fig. 1.8: Two-pole double start magnet-to-magnet type MLS: (a) 3D view, (b) Cross section.

The previously described magnet-to-magnet magnetic screw can be named as conventional type magnetic lead screw, where, if the magnets on screw or nut are replaced by helical shaped square type threads, in that case the magnetic screw can be named as reluctance type MLS [35]. In order to obtain acceptable force density from this type, the width and height of the square type threads are optimized regarding amount of flux leakage, magnetic resistance, and flux density to achieve high thrust force. Not only square threads can be maintained as ridges and grooves for the magnetic screw but also the ridges can be trapezoidal and the grooves can be arc, trapezoid or V-shape, but square threads were chosen as they have high mechanical strength [36] as shown in Fig. 1.9.

Moreover, the air-gap between the nut and the screw is maintained to be as minimum as possible to ensure higher magnetic coupling and as a result higher force and torque transmission can be achieved.

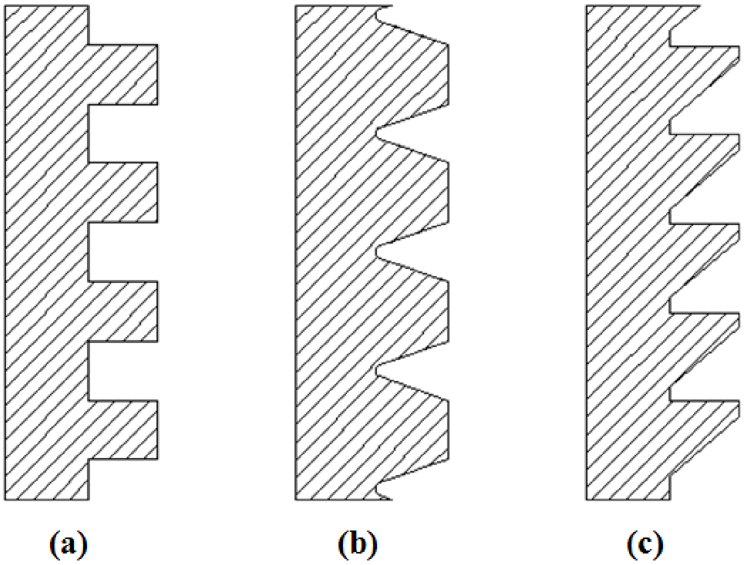

Fig. 1.9: Different thread shapes: a) Square thread, (b) V- shape thread and (c) Buttress thread form (Triangle).

In [35], to ensure the power of using MLS with magnets mounted on both translator and rotor, it was compared with reluctance and induction type MLS. For induction type MLS, the magnets on rotor are replaced by conductive sheet mounted on the outer cylindrical surface of the translator as shown in Fig. 1.10. It was shown that the force density of MLS with helical magnets mounted on both translator and rotor is much higher than reluctance and induction type MLS.

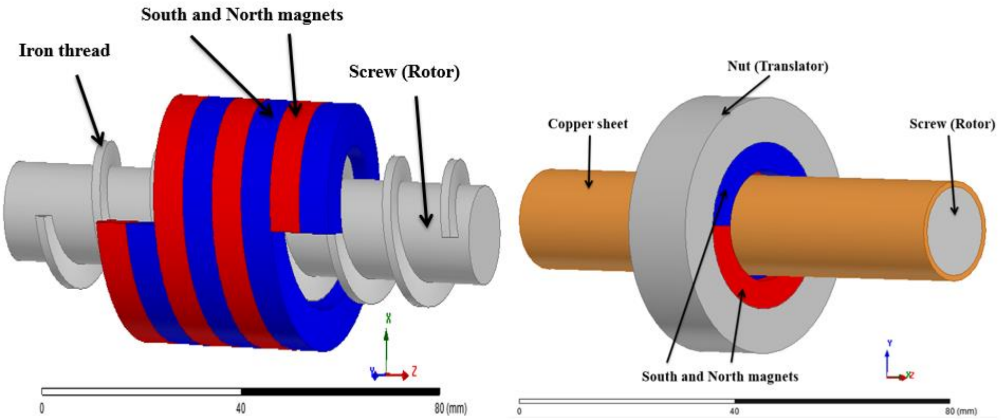

(a) (b)

Fig. 1.10: (a) Reluctance type MLS, (b) Induction type MLS.

Thrust force can be related to torque in terms of pole-pitch as for one complete rotation, 360^{o} or two pole-pitches, of the rotor, the translator is displaced for linear distance equivalent to twice magnetic pole-pitch, τ_p, or single lead, λ, if the screw or nut is "Double-start" type. Lead and pitch are intimately related to each other. Lead is equivalent to the axial distance covered by the screw for one complete rotation of the nut. Pitch is the distance measured between the crests of two successive threads in case of soft magnetic screw (reluctance type MLS) and distance between the centers of two successive magnetic poles in case of surface mounted magnets on screw (magnet-to-magnet type MLS). Double-start screw type means that two helical magnetic poles or two ridges are wound around the cylindrical shape of the screw, so that each complete rotation is equal to twice pole-pitch or single lead as shown in Fig. 1.11. As a concept, lead is equal to X times pitch, where X is equal to number of starts. For large translation motion requirements, multiple start screws are preferred to be used.

The direction of motion for translator can be also controlled by the direction of rotation of helically mounted magnets either right-handed or left-handed type. When the helix is twisted in clockwise direction, this is known as right-handed type and left-handed type is when the helix is twisted in anti-clockwise direction as shown in Fig. 1.12. The right-handed type is the mostly common used as when the screw is twisted the helix moves away from the starting point of rotation.

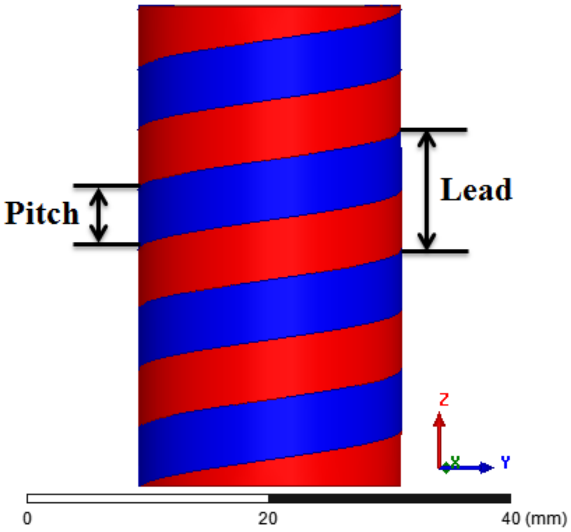

Fig. 1.11: Double start magnet-to-magnet screw.

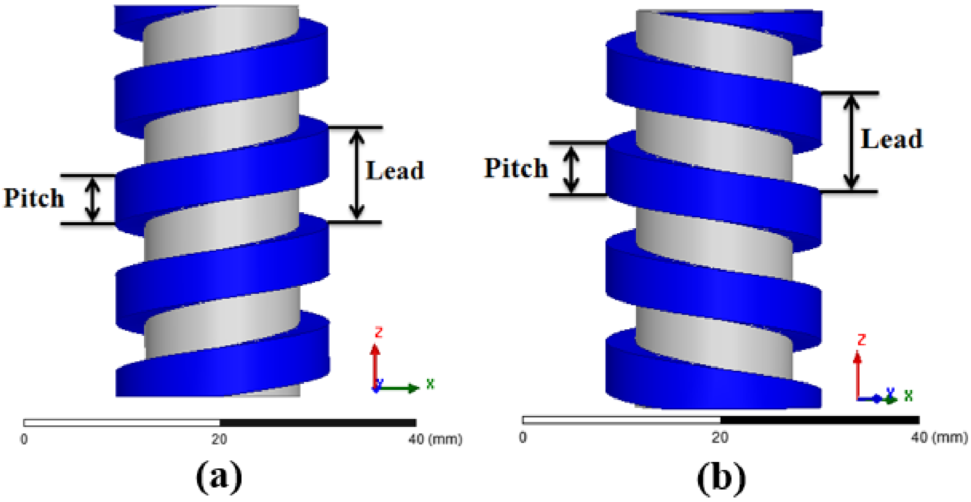

Fig. 1.12: Difference between: (a) Right handed helix, (b) Left handed helix.

During the design of magnetic lead screw a lot of design parameters that affect the thrust force must be taken in consideration, such as, thickness and axial lengths of magnets. Therefore, optimizing these parameters is significant to achieve better thrust force.

1.5 Different approaches to achieve helical magnets

Simplicity in design of a MLS is the aim for production requirements. Kaiyuan Lu et al. introduced a new simplified helical magnetic pole for magnetic lead screw [37]. This new approach is achieved as the manufacturing of helical shape magnets is the main difficult portion of magnetic lead screw technology. It was claimed that, simply by shaping or rotating half ring-shape magnetic pole, the complicated helical-shape magnetic poles can be realized. As a result, two 180° arc-shaped magnets are enough to create a complete revolution of helical-shape magnetic pole.

Two possible ways of approximation are maintained, first, in Fig. 1.13, a side view of normal half ring of radius R and width of lead λ is shown. If the shaded parts are removed in Fig. 1.13 (b), the remaining part will be a good agreement of half helix in Fig. 1.13 (c) which also is clearly shown in 3D view in Fig. 1.13 (d). Second approximation is rotating a half ring magnet as shown in Fig. 1.14 and the shaded areas are removed for achieving smooth outer surface. Although, good approximation of helix is achieved, a misalignment occurs at the boundary between the inner surfaces of the two half-helix.

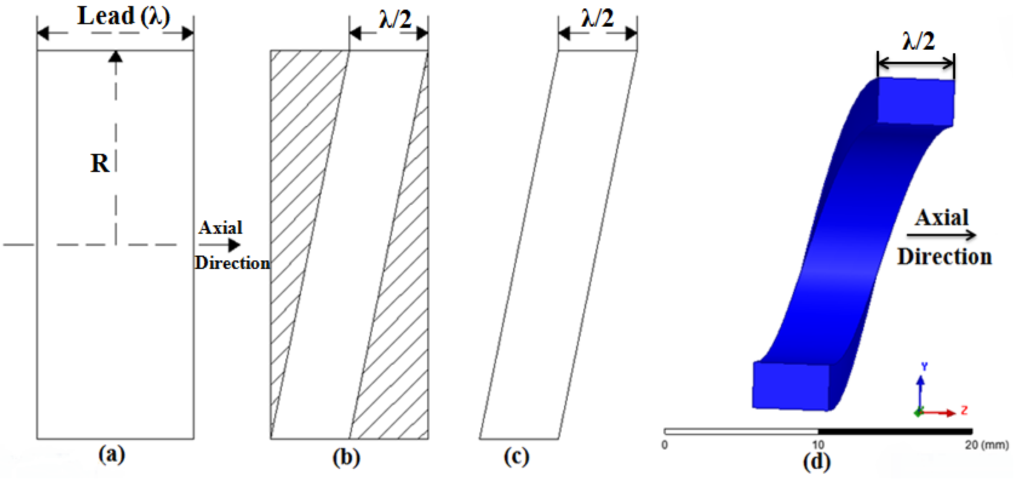

Fig. 1.13: First approach: (a) Side view of normal half ring, (b) Cutting the shaded area, (c) A helical half ring magnet and (d) 3D view of helical-shape half ring.

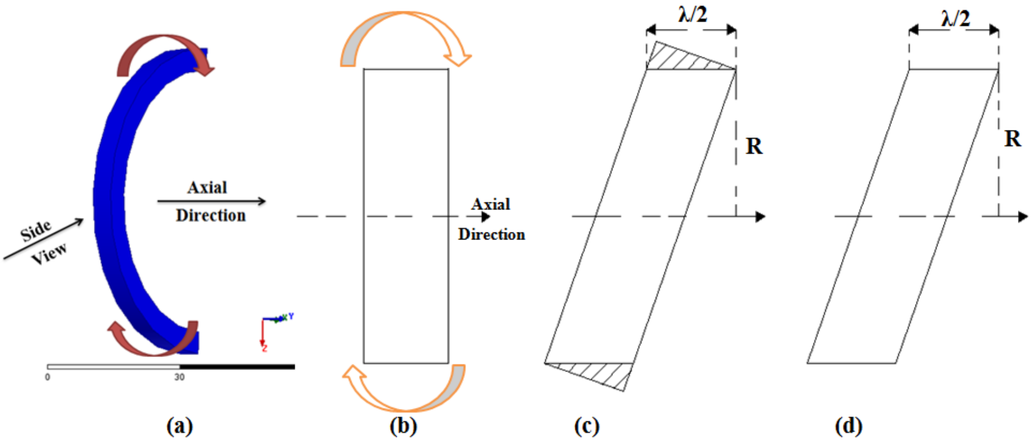

Fig. 1.14: Second approach: (a) 3D view of half ring magnet, (b) 2D side view of normal half ring, (c) Rotation about axial axis, (d) A helical half ring magnet after removal of the shaded area.

Helical-shape coils can be integrated with helical grooves in the screw shaft offering wide range of force control by controlling the injected current in the coils, however, the magnetic lead screw with ideal helically shaped magnets mounted on rotor and translator still offering higher force density than using helically shaped coils. The challenge in designing ideal helically shaped magnetic poles lies in using a large number of magnet stacked piece-by-piece together with small shift between adjacent magnets to achieve the required lead in only one revolution. As mentioned in [29], 4000 pieces of round magnets were used for rotor length of only 400 mm. The arrangements of magnets are similar to skewed rotor magnets in conventional PM machine that is used as a way of cogging torque reduction. On the other hand in [38], a 15^{o} arc-shaped magnets were enough to attain fine approximation of helical shape magnetized magnets, which means only 24 pieces are used to create one complete revolution, 360^{o}, of a helix, however, it is also not easy to realize this step for mass production.

After these ways of approximation proposed by Kaiyuan Lu et al., it can be seen that the previously 24 magnet pieces used to create 360^{o} helical magnet pole can now be reduced to only two magnet arc-shape segments.

1.6 Force density of a MLS

High force density linear electromagnetic actuators, utilising the setup of MLS, are compared to other actuators in terms of force density [34]. For example, hydraulic actuators can provide high force densities up-to 35 MPa, however, they suffer from maintenance requirements, cost, and low reliability due to oil leakage and fluid weight. On the other hand, pneumatic actuators shows lower force density than hydraulic actuators with pressure varying from 550 kPa to 700 kPa. Also, electromechanical actuators can provide high force densities by converting rotary motion to linear one. However, it suffers from friction that requires continuous maintenance to avoid deformation of mechanical transmission and thus high cost requirements. For the aforementioned reasons, electromagnetic actuation may offer a lot of advantages, such as, nearly no friction occurs, no maintenance and thus high efficiency and reliability demands are achieved. As mentioned in [34], a force density of more than 10 MN/m^3 can be realized in magnetic screw systems for air-gaps of less than 1mm.

1.7 New approach for helical grooved screws

If the helical-shape magnetic poles are mounted only on the inner surface of the nut and the screw is only made of soft magnetic material with helical grooves on its cylindrical material then it is preferred to have smooth and round outer shape of screw with longer and cleaner operational life time, that's what was done in [39] by Masahiro Mita et al. where a mixture of ferrite and carbide alloy is used to fill the grooves between soft magnetic threads in the magnetic screw as shown in Fig. 1.15. The alloy has "Dual-State" magnetic property where it is originally soft magnetic material and when it is exposed to heat, it became non-magnetic material offering similar magnetic flux path in the soft magnetic threads in-between the alloy and smooth outer shape of screw rod. However, lower thrust force is achieved than the magnet-to-magnet MLS.

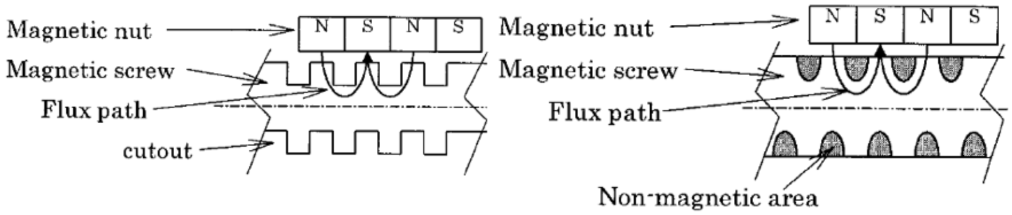

(a) **(b)**

Fig. 1.15: (a) Reluctance type MLS, (b) Dual-state magnetic screw [39].

1.8 Gear ratio of a MLS

As previously reported, the MLS is able to convert rotary motion to linear translation providing gearing effect through the synchronous motion of the nut and the screw, hence it is considered from the family of magnetic gear. The ratio, G, between the angular velocity, ω (rad/s), and the linear velocity, V (m/s), of translator is given by:

$$G = {}^{\omega}/_{V} = {}^{2\pi}/_{\lambda} \tag{1.1}$$

An example of 4-pole MLS with 60 mm lead, the translator moves linearly at 0.5 m/s while the rotor is rotating at nearly 500 rpm. The relation between the torque (T) and thrust force (F) is:

$$T = \frac{\tau_p}{\pi} F = \frac{\lambda}{2\pi} F \tag{1.2}$$

Also, gear ratio can be defined in terms of force, F, and torque, T, as

$$\frac{F}{T} = \frac{2\pi}{\lambda} = \frac{\omega}{V} = G \tag{1.3}$$

1.9 Applications of MLS

In [40], a device able to convert rotor torque to linear force is to be used in artificial heart application. The device is similar to magnetic lead screw with magnets mounted on both outer surface of rotor and inner surface of translator. The translator is connected to a mechanism that prevents it to rotate with the rotation of the rotor but support a linear motion instead as a result of magnetic coupling between rotor and translator.

In [41], Kaiyuan Lu et al. have proposed new MLS called "current exited lead screw" or "Electromagnetic lead screw (EMLS)". In this design, instead of having helical shape magnets on the translator, it was replaced by iron threads and a coil is wounded around the iron threads in a helical shape fed by DC current to provide the same helical shape magnetic field gained form the magnet-to-magnet MLS and also saving the PM material as shown in Fig. 1.16. The ability to design helical shape magnets mounted over the translator is such a noticeable problem that makes EMLS is much more simple to design and more easy to be manufactured. Two coils were wound around the iron threads in helical shape, they are connected in series to form one coil providing the helical shape magnetic field. In terms of magnetic field strength, the magnetic field produced from magnet-to-magnet MLS will be higher than that of EMLS. Therefore, pull-out force of magnet-to-magnet MLS is much greater than that of EMLS. However, in EMLS we can get simple and robust structure than magnet-to-magnet MLS. It is worth to mentioning that, the value of pull-out force gained from EMLS can be controlled by controlling the injected current in the coil wound around the iron threads.

During the invention of the magnetic lead screw along the previous decades, the main difficulty in fabrication is the production of helically shaped magnets mounted around the screw shaft of MLS. By achieving this ideal helical shape magnets, an ideal sin wave shape magnetic field can be maintained. To simplify this approach a new design of MLS was implemented by discretizing axially magnetized field magnets and placing them between discretised ferromagnetic iron pieces [42]. A set of two poles and ferromagnetic iron piece placed between them to form what is called a cell. This cell is longitudinally shifted by certain displacement with its neighbour until forming one complete turn (360^{o}). The shape of ideal helix magnetic field depends on the number of discrete PMs used. The highest numbers of discretised PMs used, the smoother sine wave magnetic field can be achieved. As we get higher number of segments, difficulty in assembly will be faced during manufacturing. So, the discretised PMs are surrounded with ideal helical ferromagnetic iron ring to support and extract the ideal helix magnetic field from the segmented cells as shown in Fig. 1.17.

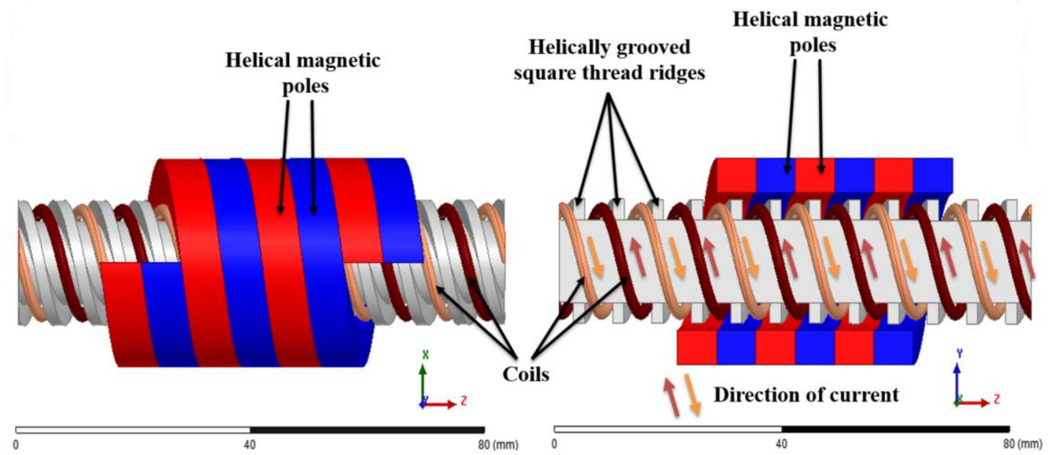

Fig. 1.16: Coils wounded around the helical shape square threads: (a) 3D view, (b) Cross-section.

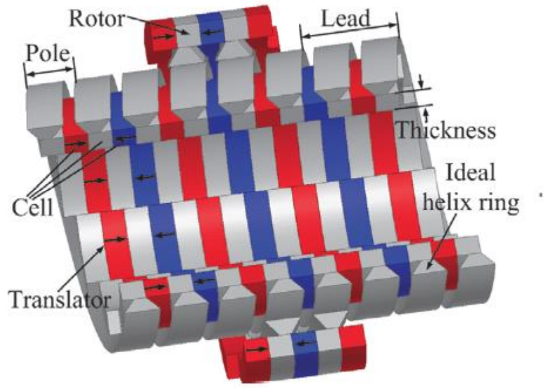

Fig. 1.17: Configuration of magnetic screw in [42].

Furthermore, MLS was designed to be used as dampers with high efficiency and reliability than hydraulic or pneumatic damper systems in vehicles. The start was by using Linear Permanent Magnet Machines (LPMM) as an absorber or damper for the vehicles by using the MLS as a part of damping system [43-45], the advantages for using such idea as an absorber were great as it supports long life usage due to contact less between mechanical parts and the vehicle is separated from sudden hits along the road path. The main disadvantage that made researchers start to find another solution instead of using LPMM as a shock absorber is the low efficiency of the system resulting from high copper loss due to high currents and, hence, high power loss [46]. Also, using LPMM in vehicles damping systems require liquid cooling [47], this will make the system more complicated and maintenance requirements will increase. In [48], Nick Ilsoe et al. used a MLS as an alternative to LPMMs for their good results [49]. The MLS can achieve higher shear stress than other LPMMs as a result of magnets which are mounted on both translator and rotor sides [50, 51]. That’s why it is preferred to use MLS for its benefits and fewer disadvantage compared to LPMM.

1.10 Outline of this thesis

This thesis will be divided into separate chapters as follows:

Chapter 2 – Types of MLS are presented. Investigation on pull-out force and shear stress is carried out on each type of MLS. Effect of magnet dimensions, e.g.: thickness and pole-pitch, on pull-out force and shear stress is discussed. A 2D and 3D simulation model for each type of MLS is concluded to validate the results. Based on the results, the recommended types of MLS are selected.

Chapter 3 – The magnets mounted on the MLS are magnetized using capacitor-discharge magnetizer. Different fixture coil configurations are presented. The design parameters for the magnetizing fixture are investigated. MATLAB/SIMULINK model is included to estimate the maximum current and the change in coil resistance and temperature during magnetization process. A transient 2D MAXWELL model is employed for each fixture configuration to validate results from SIMULINK. Comparison between single and double sided fixtures are carried out regarding peak current pulse gained from magnetizer, magnetic field density on the surface of the magnet, temperature rise, and resistance change during magnetization process.

Chapter 4 – Losses and efficiency of MLS are calculated at different velocities. Using 3D JMAG simulation package, joule losses for magnet-to-magnet and reluctance type MLS are investigated. Effect of using glue on eddy current loss is studied using separate 3D JMAG model for magnet-to-magnet and reluctance MLS. Average total loss of magnet-to-magnet MLS at different velocities is compared with the average total loss of reluctance type MLS.

Chapter 5 – A detailed description of the manufacturing procedures for the selected magnetising fixture is included. The selected fixture is utilised in a novel impulse magnetisation technique for magnetising a cylindrical shaped magnet to generate a helically shaped magnetic field. A test rig is developed for the measurement of the force produced by the magnet-to-reluctance type MLS and results are compared with predictions and discussed. Moreover, two methods are carried out for measurement of the maximum transmitted force in order to eliminate stiction.

Chapter 6 – A case study is performed to investigate the feasibility of MLS in UAV launching applications. This study is based on the analysis of the performance of the MLS in previous chapters. Effects of screw dimensions on transmitted force, launch distance, and required torque are addressed.

Chapter 7 – Summary of the work in the thesis is presented, and main conclusions are highlighted. Proposals for future work are also provided.

1.11 Key contributions of the thesis

The contributions in this thesis can be summarised as follows:

- Realisation of helical magnetisation distribution employing a novel impulse magnetisation process.
- Investigation of the feasibility of magnetic screw system as a launching platform for UAVs.
- Comparison of performance of magnet-to-magnet, magnet-to-reluctance, and magnet-to-conductor magnetic screws for long stroke applications.

2 Investigation of different types of MLS

It is imperative to investigate the effect of the main design parameters of MLS, such as lead, magnet thickness, and air-gap length of the screw/nut system on the transmitted force/torque, shear stress, and inertia/mass etc. Comprehensive simulation studies are carried out on the three types of MLS: magnet-to-magnet, magnet-to-reluctance, and magnet-to-conductor. The performances of the three types of MLS are compared for similar output requirements.

2.1 Magnet-to-magnet type MLS

A schematic of a magnet-to-magnet type MLS is shown in Fig. 2.1, where the helically magnetised magnets are mounted on the nut and screw. The effect of different magnet dimensions, pole-pitch, lead, and air-gap length are investigated and discussed. A magnet-to-magnet type MLS is modelled and its parameters are given in Table 2.1. Fig. 2.2 shows the developed 2D and 3D finite element models, whilst Fig. 2.3 shows the variation of the transmitted force with the linear displacement of the screw for a fixed nut. It can be seen that there is very good agreement between 2D and 3D simulations, and both methods of realising helical magnetisation lead to similar force transmission values. As a consequence, 2D simulations can be employed for the investigation of the effects of the main design parameters.

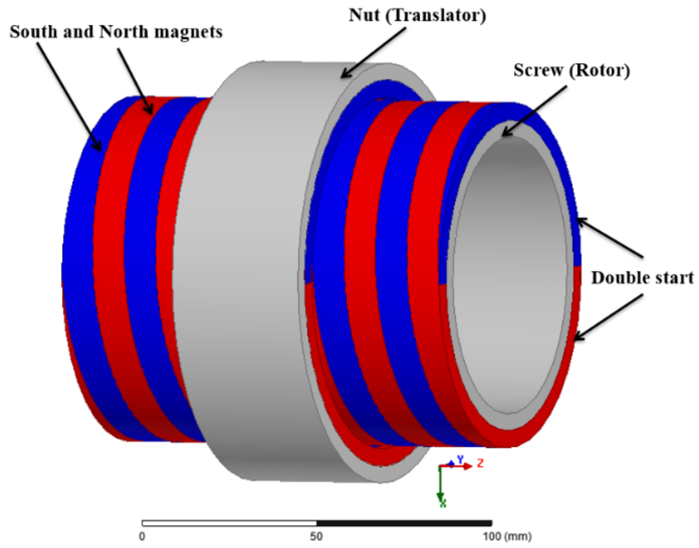

Fig. 2.1: Two-pole double start magnet-to-magnet type MLS,

Table 2.1: Parameters for magnet-to-magnet type MLS

Inner radius of screw	0 mm (i.e. solid core)
Screw back-iron thickness	8 mm
Air-gap	1 mm
Magnet thickness	1 mm
Pole-pitch	7 mm
Nut back-iron thickness	8 mm

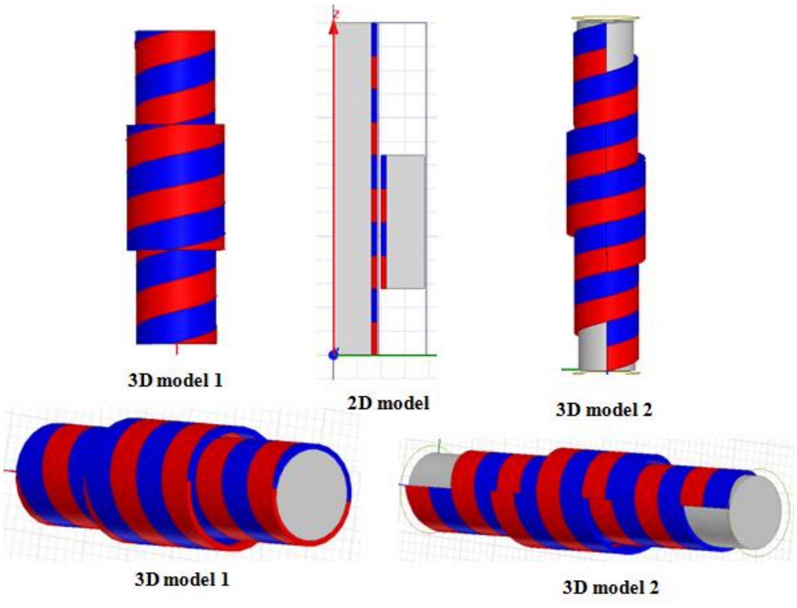

Fig. 2.2: 2D and 3D magnet-to-magnet MLS with different screw realisation methods.

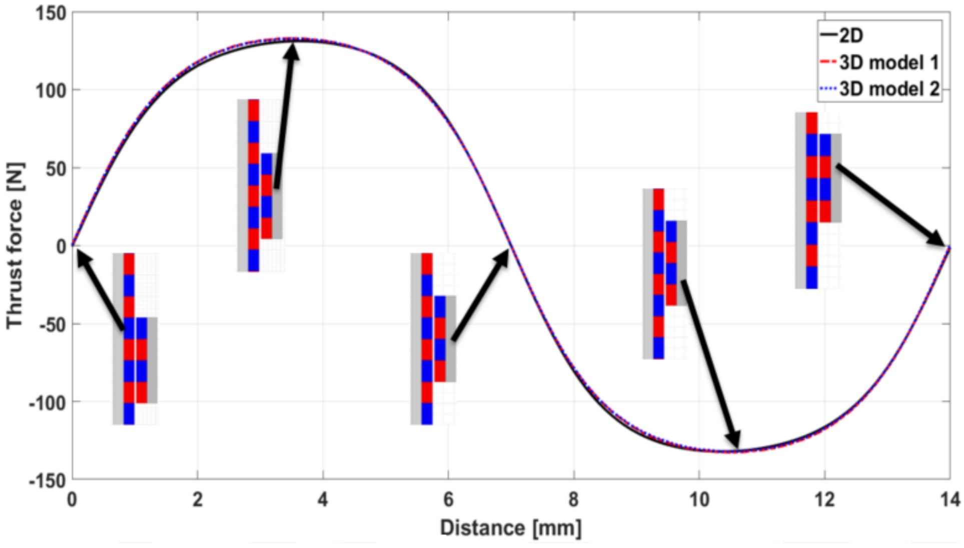

Fig. 2.3: 2D and 3D results for magnet-to-magnet type MLS (i.e. 7mm pole-pitch).

Agreement between 2D and 3D models has demonstrated for this combination of parameters in Table 2.1, this agreement is likely to hold for parameters that do not deviate too far from those used in comparison.

2.1.1 Effect of magnet thickness

Thickness has a significant effect on the magnetic field produced by a magnet and, hence, affecting the force transmitted by a MLS. So, the effect of varying the magnet thickness on the pull-out force is investigated for the magnet-to-magnet MLS. The investigation is undertaken for a fixed air-gap diameter. This provides fair comparison for the produced shear stress at different magnet thicknesses. For a 1 mm air-gap, and for a nut equipped with a single lead, Fig. 2.4 and 2.5 show the variations of the transmitted force and air-gap shear stress with the lead at different magnet thicknesses. It can be seen that, for a given magnet thickness lead lengths exist for which the pull-out force and the air-gap shear stress are maximum. Furthermore, as expected increasing the PM thickness can enhance the thrust force, but also affects the value of the lead for which the transmitted force is maximum. Fig. 2.6 shows the variation of maximum shear stress with magnet thickness, it can be seen that the rate of increase in maximum shear stress with magnet thickness decreases with increasing magnet thickness. Accordingly, an optimum magnet thickness should be selected as a compromise between force transmission and cost.

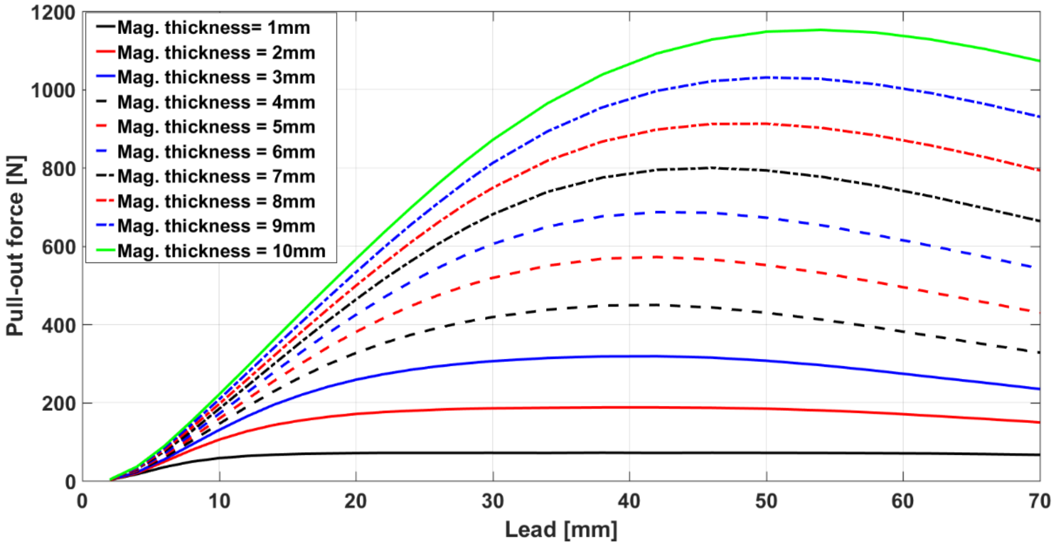

Fig. 2.4: Variation of Pull-out force with lead for different magnet thickness at 1 mm air-gap.

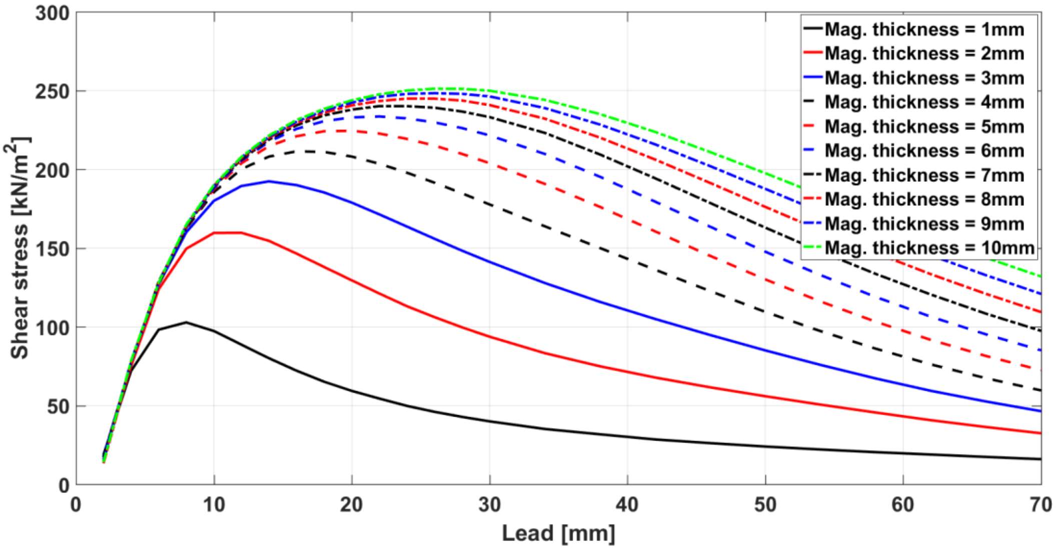

Fig. 2.5: Variation of shear stress with lead for different magnet thickness at 1 mm air-gap.

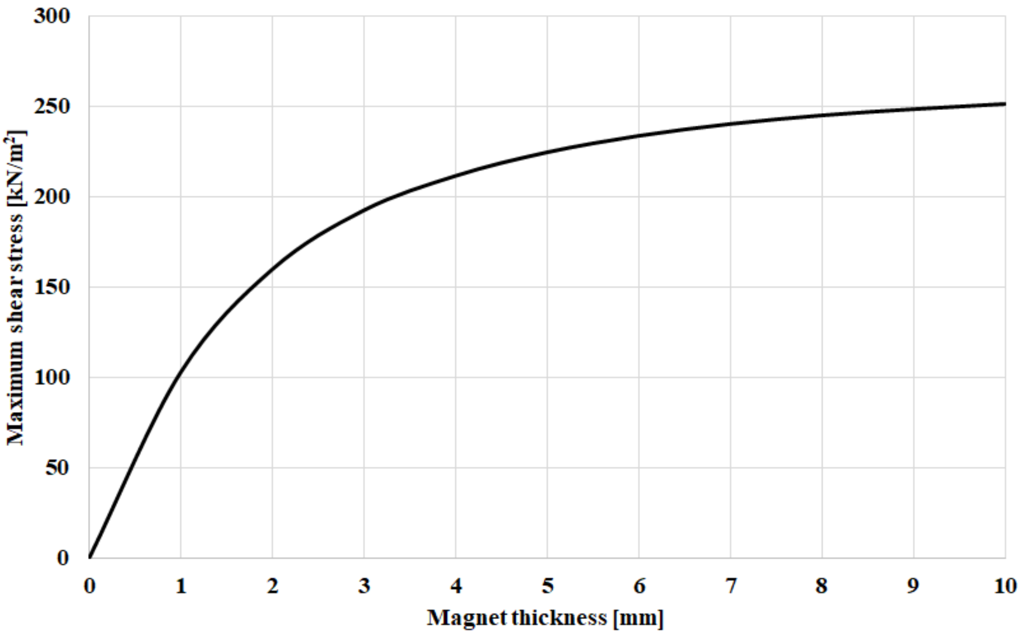

Fig. 2.6: Variation of maximum shear stress with magnet thicknesses for magnet-to-magnet MLS.

2.1.2 Effect of air-gap length

Results in section 0 are for a constant air-gap length of 1 mm. In this section, the effect of changing the air-gap on shear stress is investigated. For a constant lead of 14 mm the variation of shear stress with air-gap length at different magnet thicknesses is shown in Fig. 2.7. It can be seen that the air-gap length has a significant effect on the shear stress and for a given magnet thickness shear stress decreases with increasing the air-gap. It can also be seen that for a given air-gap length increasing the magnet thickness beyond a certain value results in negligible increase in shear stress. However, as it is always the case, the selection of the air-gap length is compromise between the magnetic performance, cost, and practical realisation.

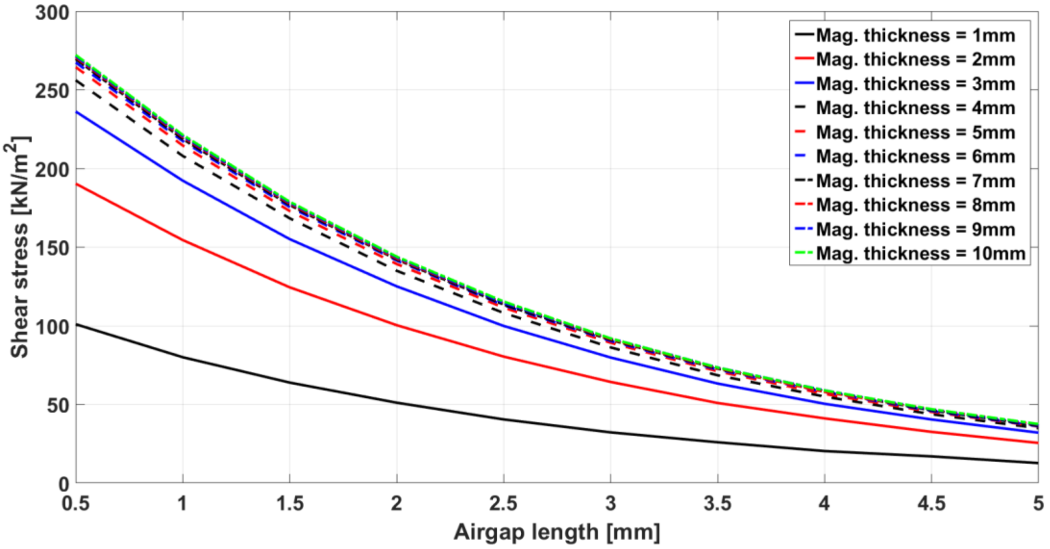

Fig. 2.7: Variation of shear stress with air-gap length at different magnet thicknesses.

2.2 Magnet-to-reluctance type MLS

For a magnet-to-reluctance type MLS, magnetic poles on the screw (rotor) are replaced by iron threads as shown in Fig. 2.8. Replacing the magnets on the screw, results in lower thrust force, however, production and material costs are also reduced. Effects of changing the dimensions of iron threads, pole-pitch, air-gap, and magnet thicknesses on the shear stress are investigated to achieve an improved understanding of the general characteristics of magnet-to-reluctance type MLS and the effects of the key design parameters.

Similarly to the magnet-to-magnet MLS, and in order to justify the selection of 2D modelling for the simulations studies, initial 2D and 3D simulations are undertaken on a magnet-to-reluctance MLS. The parameters of the MLS are given in Table 2.2. Fig. 2.9 shows the variation of the transmitted force with the position of the nut for a fixed screw. It can be seen that good agreement between 2D and 3D models exists for both. Two 2D cases are considered. The first represents an infinitely long nut, where a periodic boundary condition is applied, and the second represents a 2-pole nut. Therefore, it would be acceptable to employ 2D modelling for the investigation of the effects of the main design parameters.

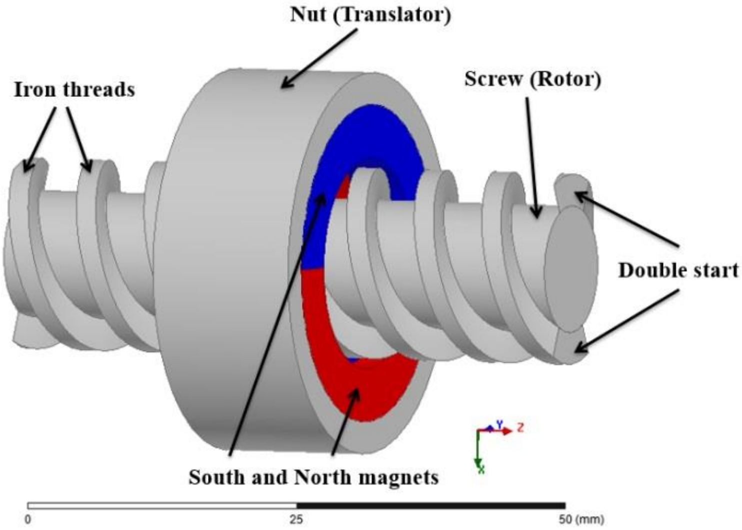

Fig. 2.8: Two-pole double start magnet-to-reluctance type MLS.

Table 2.2: Parameters for magnet-to-reluctance type MLS

Initial radius of screw	0 mm
Screw back-iron radius	6 mm
Iron thread depth	3 mm
Iron thread width	2 mm
Air-gap	1 mm
Magnet width	5 mm
Pole-pitch	7 mm
Nut back-iron thickness	8 mm

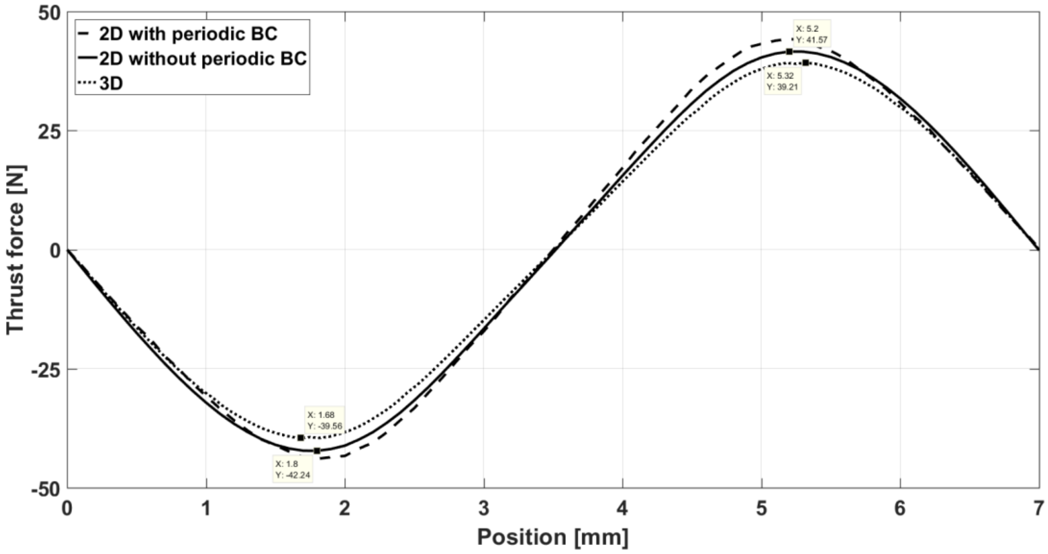

Fig. 2.9: Variation of transmitted force with position of the nut for a fixed screw.

2.2.1 Effect of iron thread dimensions

The effect of changing the dimensions of iron thread on shear stress is investigated. For comparison purposes, 7 mm pole-pitch is selected for magnet-to-reluctance MLS. In the analysis, the magnet thickness and the air-gap diameter are fixed. Two main parameters characterise the screw, the width of the iron thread as percentage of pole-pitch, and the depth of the thread. For a magnet thickness of 3 mm and an air-gap length of 1 mm, Fig. 2.10 shows the variation of shear stress with iron thread width for different iron thread depth.

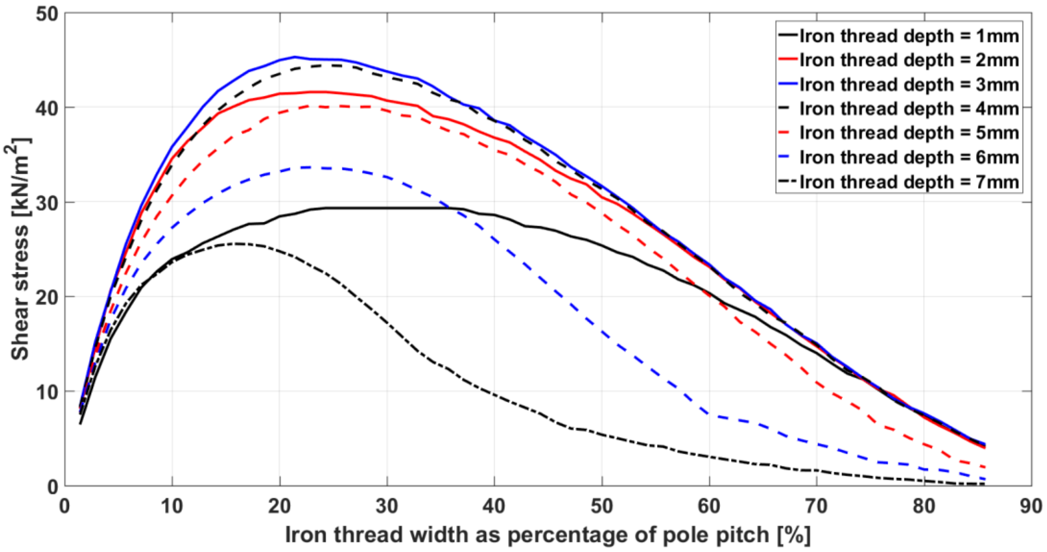

Fig. 2.10: Variation of shear stress with iron thread width at magnet thickness of 3 mm.

It can be seen that iron thread width exists for which the shear stress is maximum, and an iron thread width between 20% and 30% of pole-pitch should be selected. It can also be seen that the iron thread depth of 3 mm results in the highest shear stress. Saturation of the core is as a result of it being too thin with increased the iron thread depth.

2.2.2 Effect of magnet thickness

The effect of magnet thickness on the shear stress is investigated. In this section, the magnet thickness is varied between 3 mm and 10 mm with the iron thread width from 1% and 85% of pole–pitch for different iron thread depth. As for a magnet-to-magnet type MLS, the model is simulated at fixed air-gap diameter. For a 6 mm magnet thickness, and a 1 mm air-gap, Fig. 2.11 shows the variation of shear stress with iron thread width for different iron thread depth.

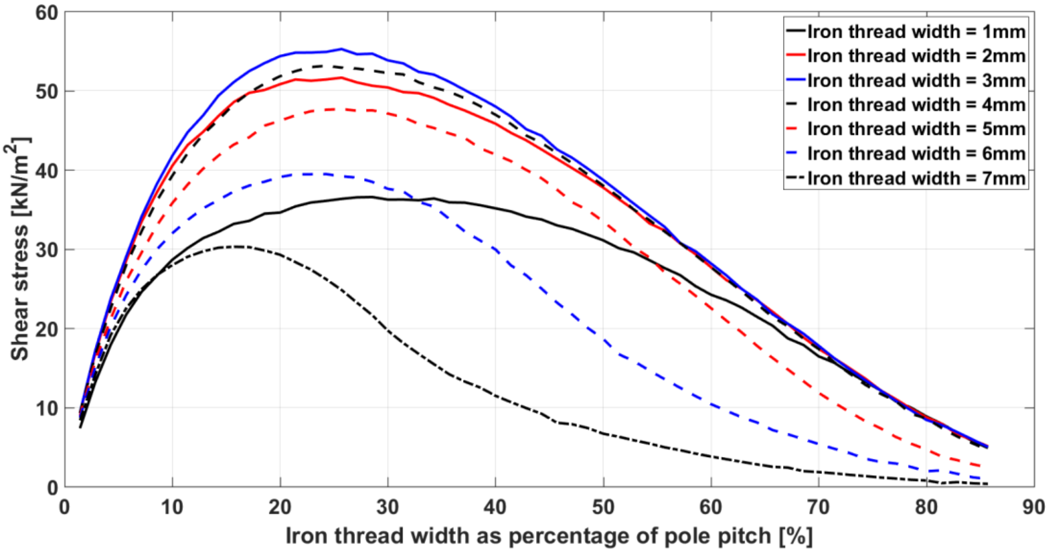

Fig. 2.11: Variation of shear stress with iron thread width at magnet thickness of 6 mm.

It can also be seen that an iron thread width exists for which the shear stress is maximum. Therefore, an iron thread width between 20 % and 30 % of pole-pitch should be selected. Moreover, iron thread depth of 3 mm results in the highest shear stress.

Although the magnet thickness was varied from 3 mm to 10 mm, the same behaviour for reluctance type MLS is exhibited. Further investigations are carried out as shown in Figs. 12, 13, 14, 15, 16, 17. The investigation shows the variation of shear stress with magnet thickness for different iron thread depth. For each figure the highest values of shear stress can be obtained as the width of iron thread is between 20 % and 30 % of the length of the pole-pitch. It can be seen that the rate of increase in shear stress with magnet thickness decreases with increased magnet thickness. This investigation shows that the highest shear stress can be obtained from iron thread depth of 3 mm with iron thread width of ~25 % of the length of the pole-pitch.

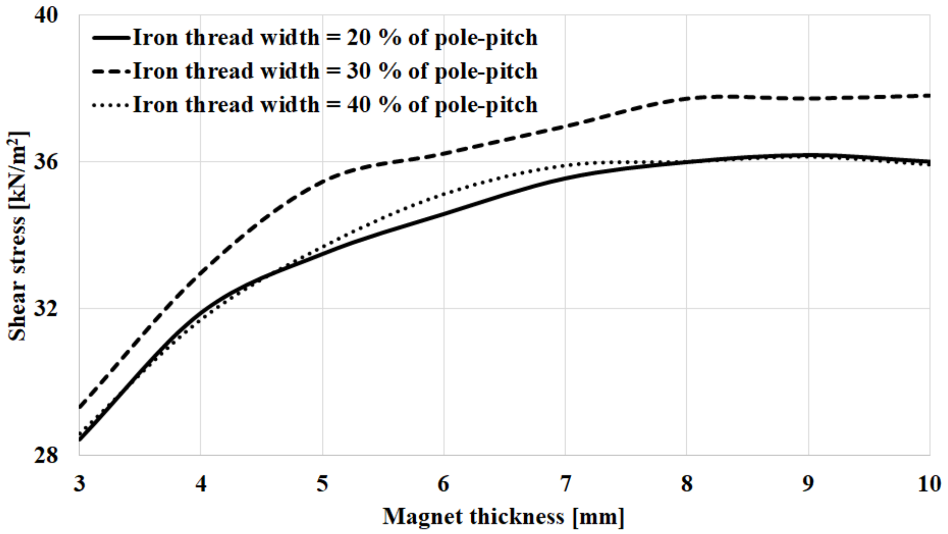

Fig. 2.12: Variation of shear stress with magnet thickness for different iron thread width at iron thread depth of 1 mm.

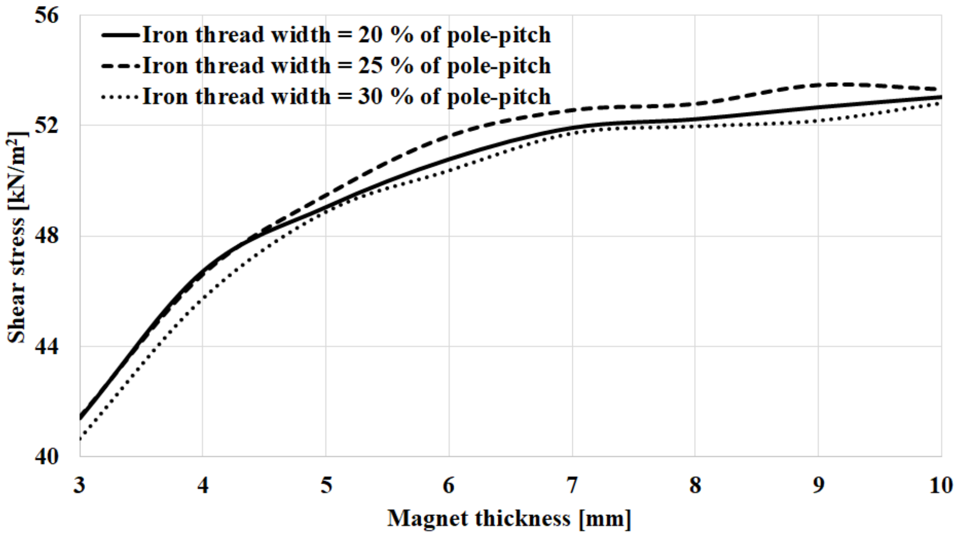

Fig. 2.13: Variation of shear stress with magnet thickness for different iron thread width at iron thread depth of 2 mm.

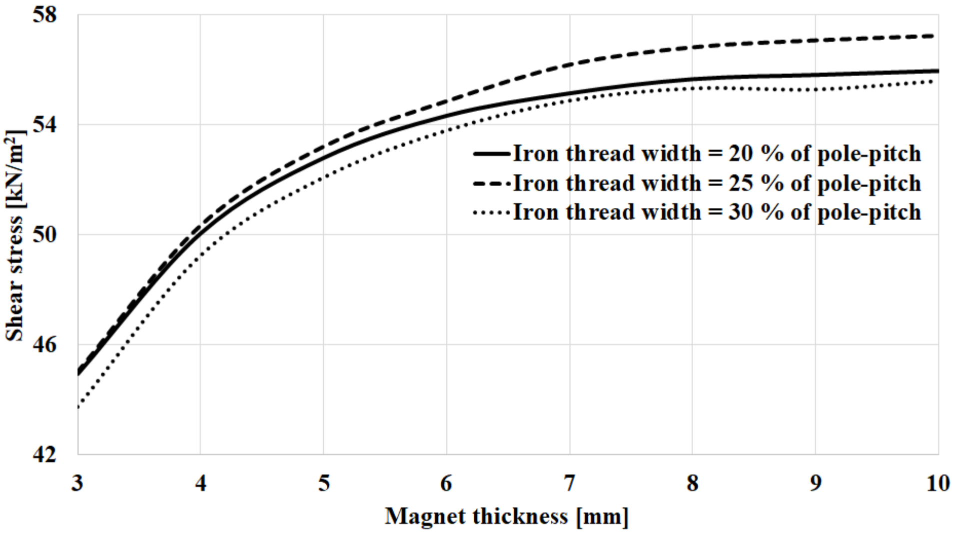

Fig. 2.14: Variation of shear stress with magnet thickness for different iron thread width at iron thread depth of 3 mm.

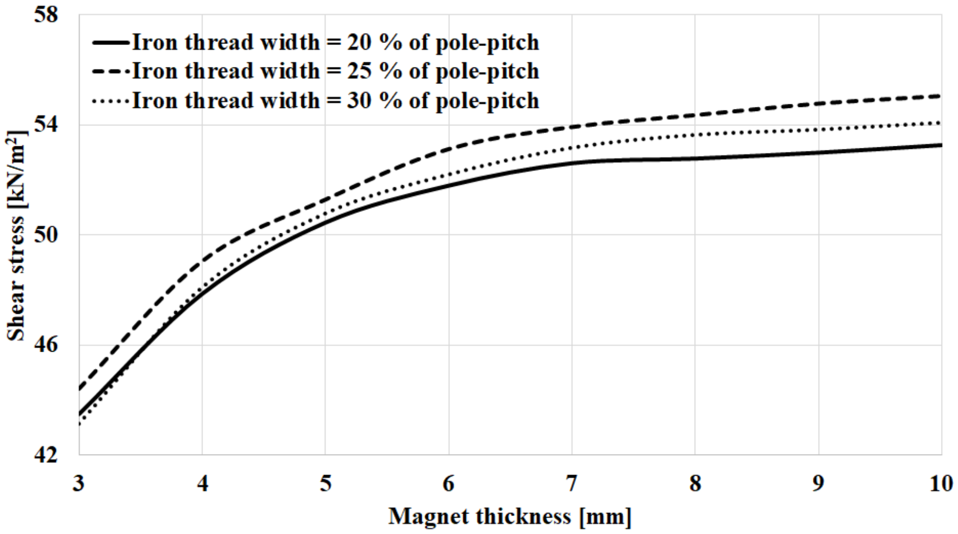

Fig. 2.15: Variation of shear stress with magnet thickness for different iron thread width at iron thread depth of 4 mm.

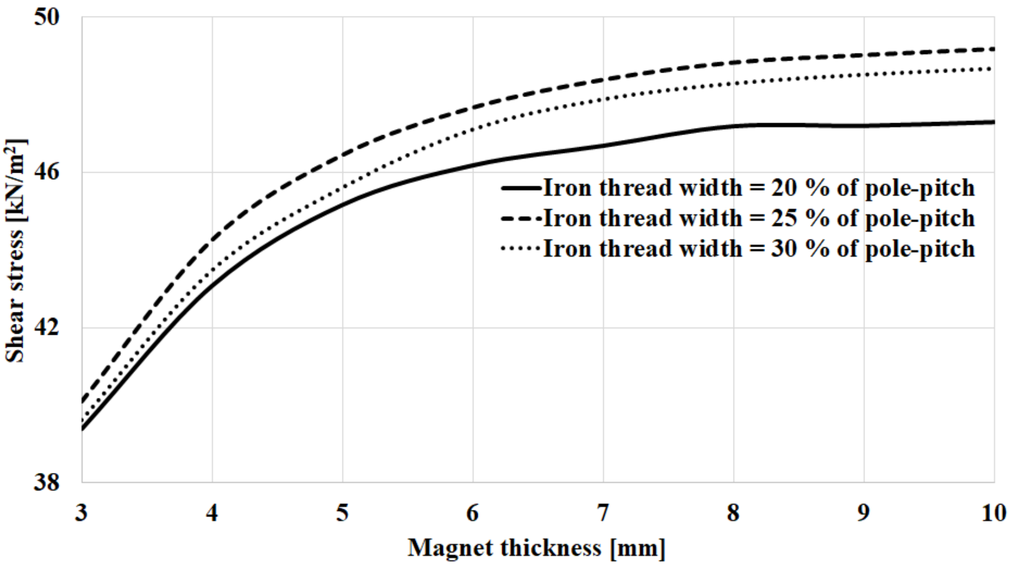

Fig. 2.16: Variation of shear stress with magnet thickness for different iron thread width at iron thread depth of 5 mm.

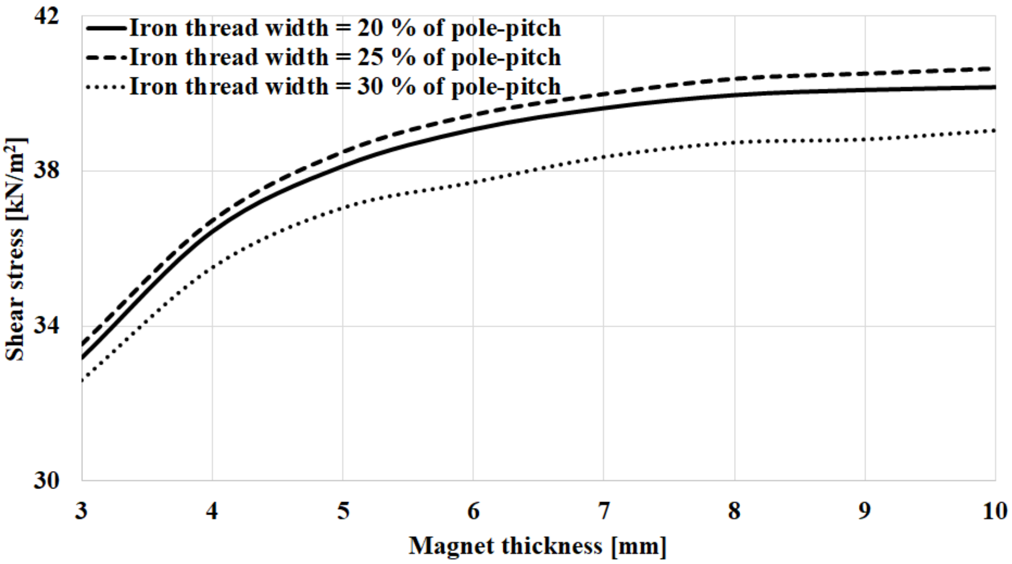

Fig. 2.17: Variation of shear stress with magnet thickness for different iron thread width at iron thread depth of 6 mm.

Fig. 2.18 shows the variation of the iron thread width at which the maximum shear stress occurs with the magnet thickness at different iron thread depth. It can be seen that the highest shear stress occurred when the iron thread width is between 20 % and 30 % of the length of the pole-pitch even for different iron thread depth.

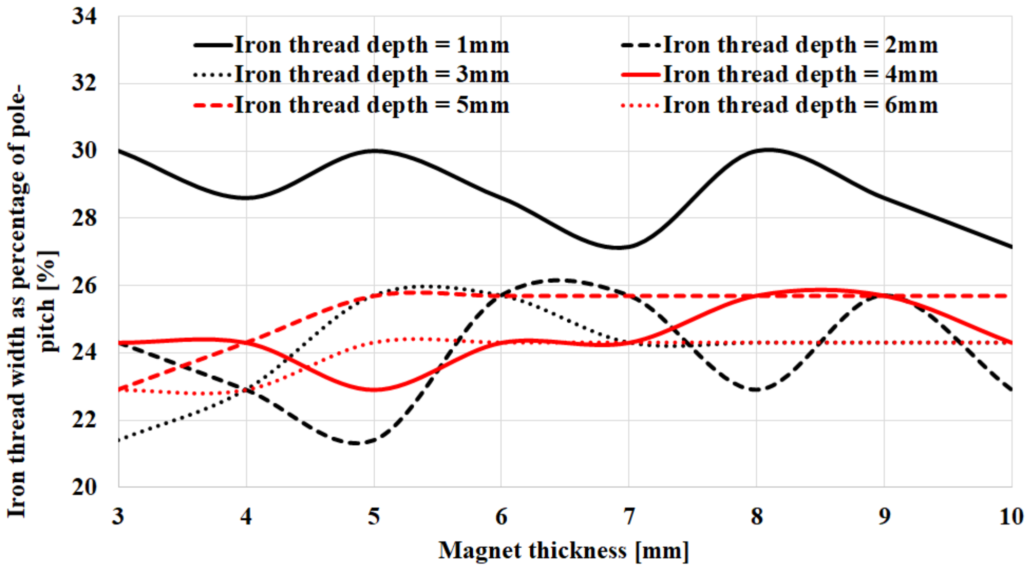

Fig. 2.18: Variation of the iron thread width at which the maximum shear stress occurs with the magnet thickness at different iron thread depth.

Therefore, two main parameters are selected for optimum performance of reluctance type MLS. Firstly, the iron thread width is between 20% and 30% of pole-pitch length. Secondly, the iron thread depth of 3 mm is selected. The maximum shear stress achieved for different magnet thicknesses for iron thread depth of 3 mm with 1 mm and 0.5 mm air-gaps is shown in Fig. 2.19.

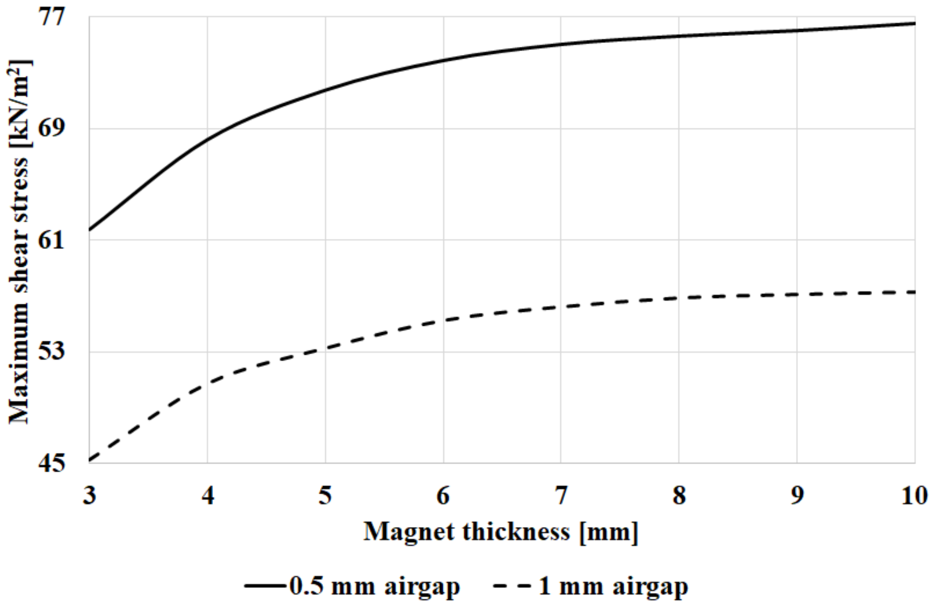

Fig. 2.19: Variation of maximum shear stress with magnet thickness for different air-gap lengths at 7 mm pole-pitch and 3 mm iron thread depth.

The figure indicates that there is a magnet thickness beyond which increase in shear stress is not significant.

As the air-gap decreased to 0.5 mm, the maximum shear stress is increased with the increase of magnet thickness. Moreover, the rate of increase in the maximum shear stress is decreasing with the increasing of magnet thickness. Also, the reduction of air-gap length by 0.5 mm provides 33.7 % increase in the maximum shear stress compared to 1 mm air-gap length.

2.2.3 Effect of pole-pitch

In this section, the effect of pole-pitch on the shear stress is investigated. Previously in sections 2.2.1 and 2.2.2, the pole-pitch was fixed at 7 mm. To investigate the effect of changing the pole-pitch on the shear stress, simulations are carried out for different pole-pitches higher and lower than the 7 mm pole-pitch, namely 5 mm and 10 mm pole-pitches.

2.2.3.1 Pole-pitch = 5 mm

Fig. 2.20 shows the variation of shear stress with iron thread width for different iron thread depth. It can be seen that, the highest shear stress is also for iron thread depth of 3mm, and iron thread width as a percentage of pole-pitch ranging from 20% and 30 %. Fig. 2.21 shows the variation of maximum shear stress with magnet thickness. A 59.56 % increase in the value of the maximum shear stress can be achieved when the air-gap is decreased from 1 mm to 0.5 mm. Furthermore, as expected, the maximum shear stress also increases with the magnet thickness.

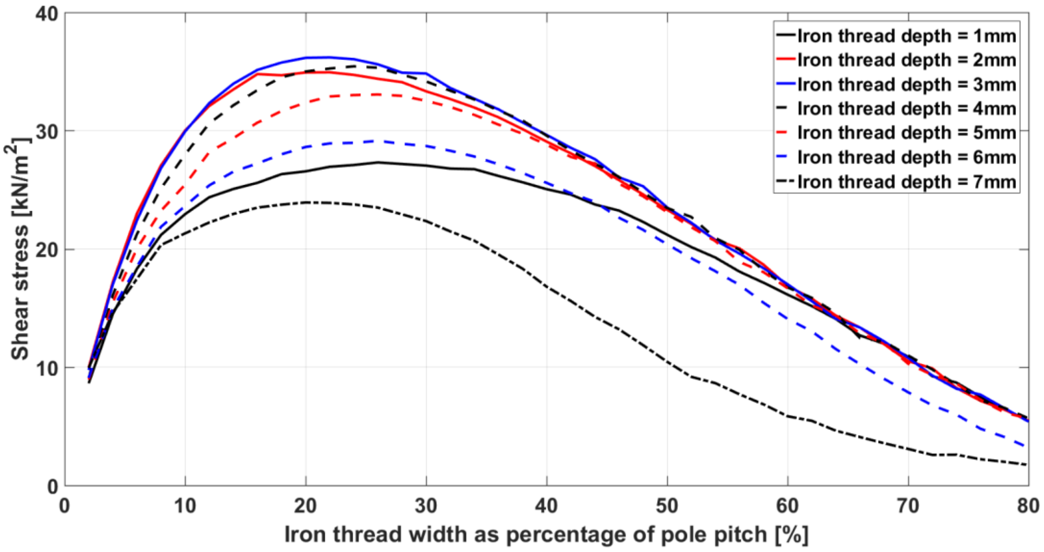

Fig. 2.20: Variation of shear stress with iron thread width as percentage of pole-pitch for different iron thread depth at magnet thickness of 3 mm.

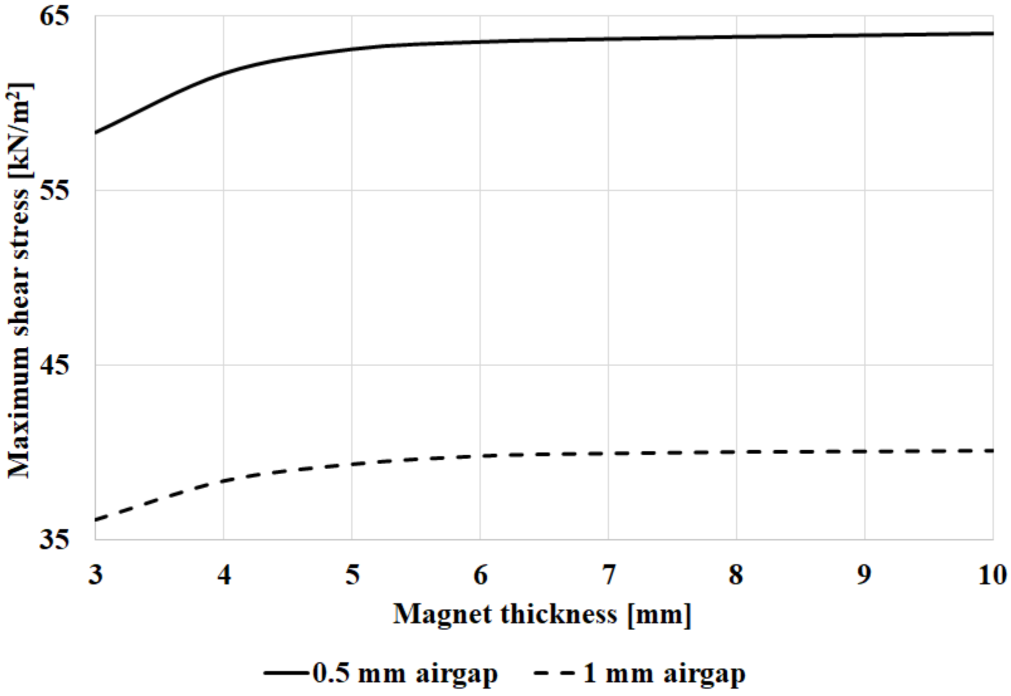

Fig. 2.21: Variation of maximum shear stress with magnet thicknesses for different air-gap lengths at 5 mm pole-pitch and 3 mm iron thread depth.

2.2.3.2 Pole-pitch = 10 mm

Fig. 2.22 shows the variation of maximum shear stress with magnet thickness. Again, for a pole-pitch of 10 mm, the maximum shear stress is also obtained for iron thread depth of 3 mm. It can also be seen that a 19 % increase in maximum shear stress is achieved when the air-gap length is reduced from 1 mm to 0.5 mm.

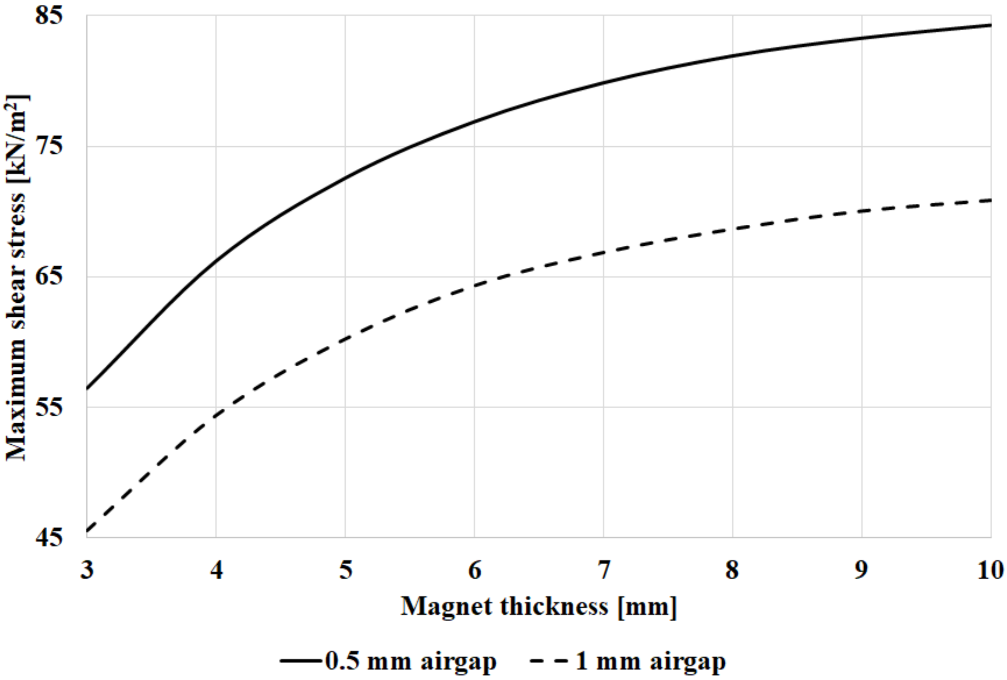

Fig. 2.22: Variation of maximum shear stress with magnet thicknesses for different air-gap lengths at 10 mm pole-pitch and 3 mm iron thread depth.

Fig. 2.23 shows the variation of the maximum shear stress with the magnet thickness for different pole-pitches and air-gap lengths. In summary, it can be deduced that as magnet thickness increases the values of maximum shear stress begin to saturate and as air-gap length decreases, a higher shear stress can be achieved.

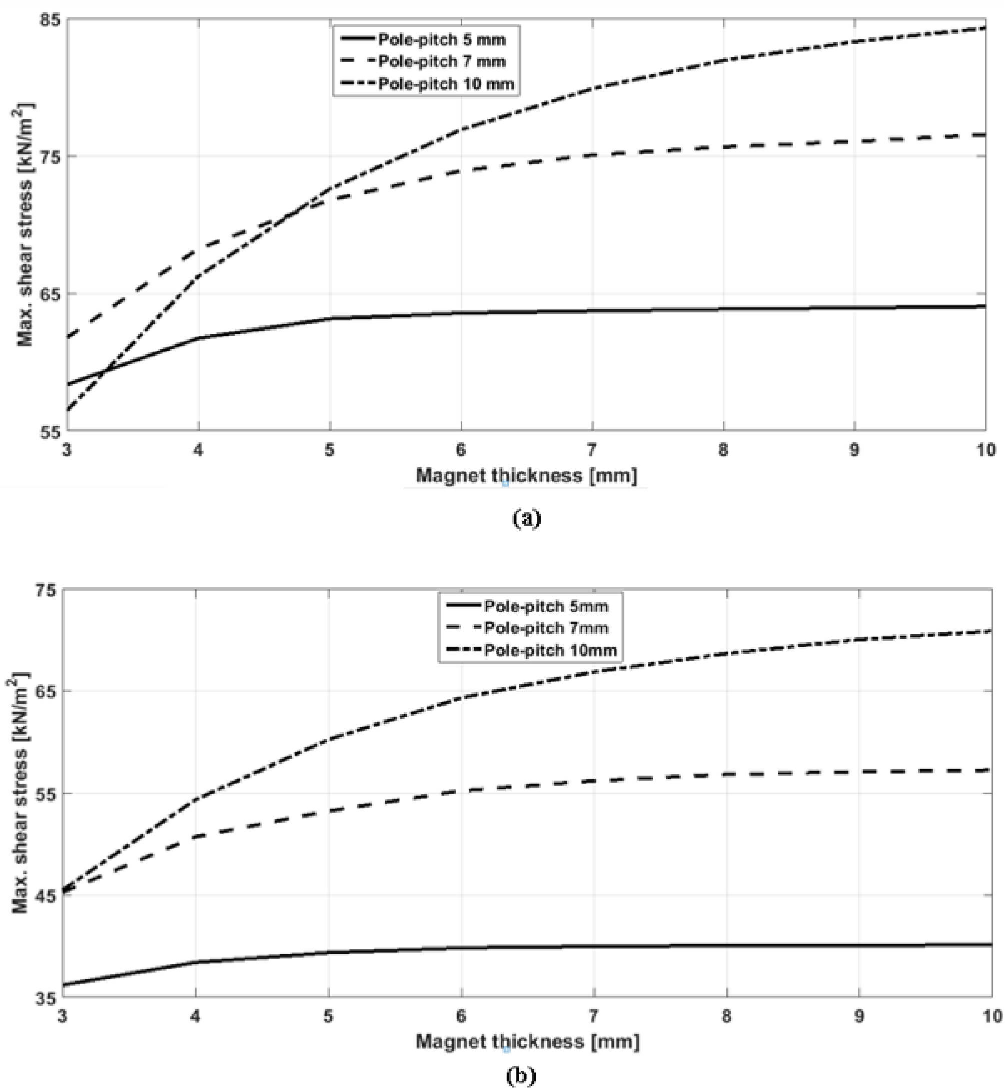

Fig. 2.23: Maximum shear stress at different pole-pitches for magnet-to-reluctance type MLS at (a) 0.5 mm air-gap, (b) 1 mm air-gap.

2.2.4 Summary and conclusion

In spite of higher thrust force gained from magnet-to-magnet MLS, reluctance type MLS may be preferred in cost sensitive applications. From the previous results, it can be summarised that there are optimum dimensions for the iron thread. The lower air-gap length the higher shear stress gained, however, mechanical and manufacturing factors must be taken into consideration for selection of the air-gap length. As pole-pitch increases the maximum shear stress increases, albeit the rate of increase of shear stress with pole-pitch is smaller when the air-gap decreases.

2.3 Magnet-to-conductor type MLS

For the magnet-to-conductor MLS, a copper sheet is mounted on the screw, as shown in Fig. 2.24. The motion of the translator or the rotation of the screw generates a variation in the magnetic field on the copper sheet resulting in generation of eddy currents. The effect of changing the lead, magnet thickness, air-gap and the slip velocity on the shear stress is presented.

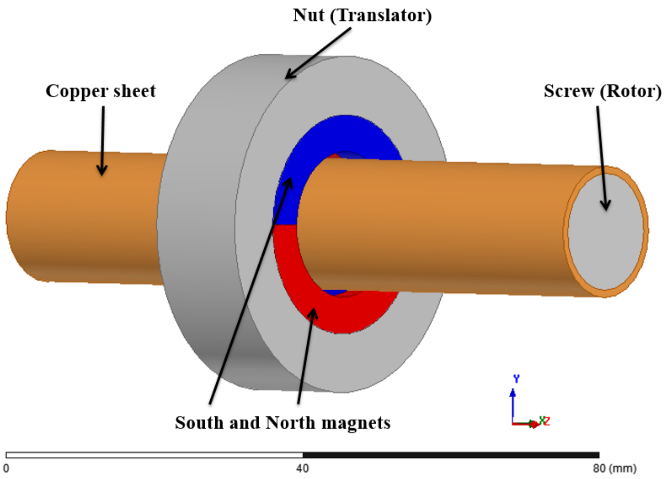

Fig. 2.24: Two-pole magnet-to-conductor type MLS.

When the screw is rotating,

$$\omega_{screw} = \left(V_{nut} \times \frac{2\pi}{\lambda}\right) \pm \omega_{slip}$$

$$\omega_{slip} = V_{slip} \times \frac{2\pi}{\lambda}$$

where +ve when the screw is driving the nut, and –ve when the nut is driving the screw. ω_{screw} is the rotational speed of the screw, and V_{nut} is the linear speed of the nut. ω_{slip} and V_{slip} are the corresponding rotational and linear slip speeds, respectively. For this type of MLS, a pole-pitch of 7 mm and air-gap length of 1mm are initially adopted. Similarly, to the previous types of MLS, and in order to justify the selection of 2D modelling for the simulations studies, 2D and 3D finite element analysis are initially employed on a magnet-to-conductor MLS. Fig. 2.25 shows a comparison between 2D and 3D simulations for pole-pitch of 7 mm at different copper sheet thicknesses. It can be seen that there is a significant difference between 2D and 3D analysis. More results for different pole-pitches are shown in Fig. 2.26 and Fig. 2.27. It can be seen that again significant discrepancies exist between 2D and 3D analysis. In 2D the induced eddy currents flow in shorter circular paths, which represents a linear magnetic eddy current coupling. In 3D, however, follow longer spiral paths characterised by larger impedances, which limits the magnitudes of the induced eddy current. Fig. 2.28 shows the helical shape eddy current which results in reduced shear stress compared to the circular eddy current in 2D configuration.

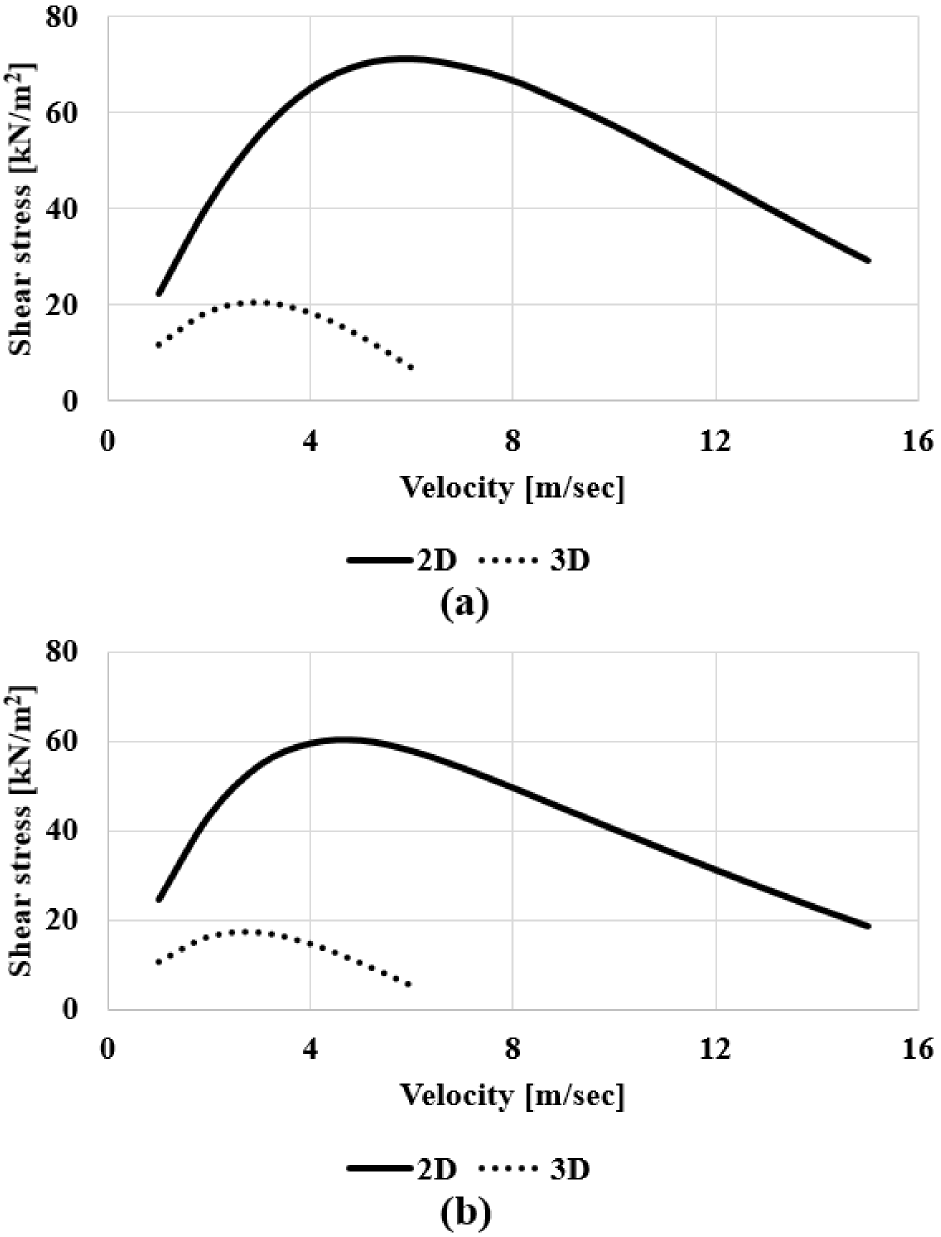

Fig. 2.25: 2D and 3D simulation results for magnet-to-conductor type MLS at pole – pitch of 7 mm for copper sheet thickness of (a) 1mm and (b) 2 mm.

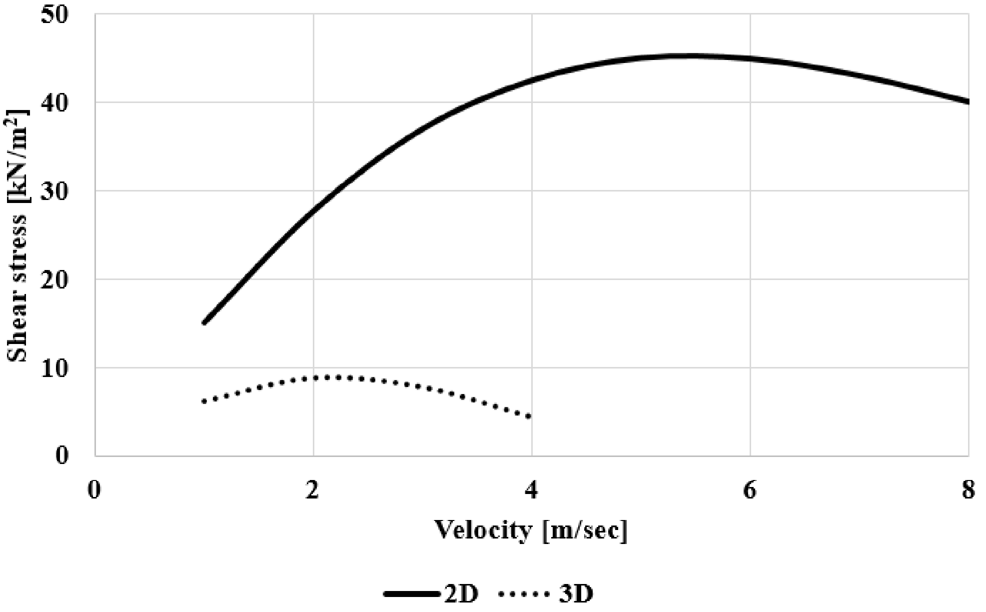

Fig. 2.26: 2D and 3D simulation results for magnet-to-conductor type MLS at pole – pitch of 5 mm and copper sheet thickness of 1 mm.

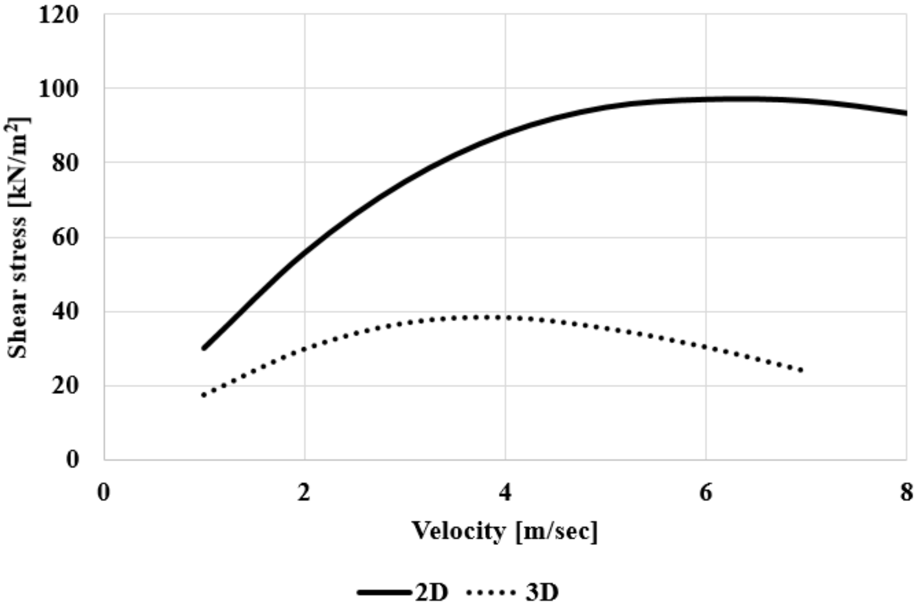

Fig. 2.27: 2D and 3D simulation results for magnet-to-conductor type MLS at pole – pitch of 10 mm and copper sheet thickness of 1 mm.

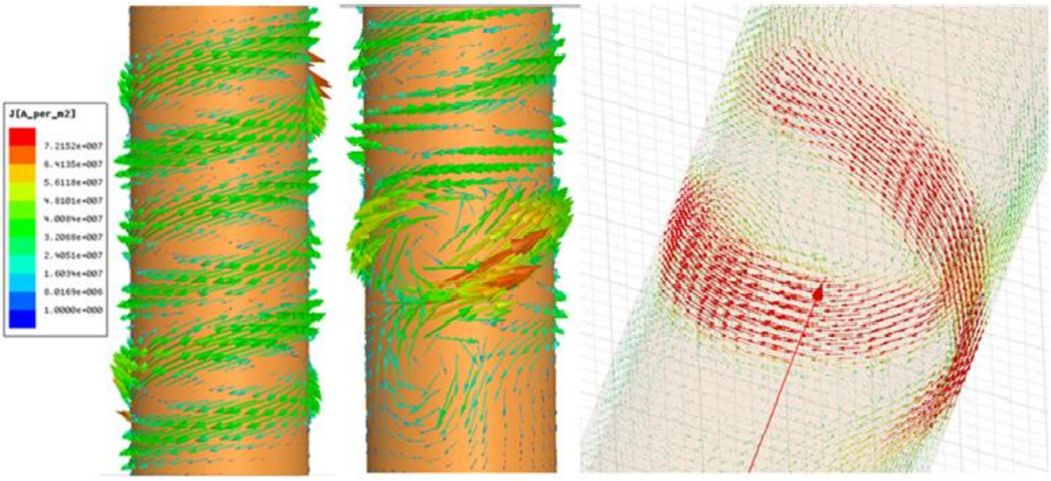

Fig. 2.28: 3D eddy current for magnet-to-conductor type MLS.

2.4 Summary and conclusion

Following an in-depth investigation of the effect of the main design parameters on the force transmission of the magnet-to-magnet, magnet-to-reluctance and magnet-to-conductor type MLS; the magnet-to-magnet type MLS can achieve the highest shear stress value, while the magnet-to-conductor type MLS has the lowest shear stress. For both magnet-to-magnet and magnet-to-reluctance, 2D analysis is sufficiently accurate, however, for the magnet-to-conductor there is a significant difference between the 2D and 3D analysis, with the latter exhibiting significantly lower transmitted forces. Furthermore, although the magnet-to-reluctance type exhibited a lower force transmission capability than the magnet-to-magnet, the simplicity of the screw design and the reduced use of PM material, which is confined to the nut, makes this topology a good candidate for many applications. In Table 2.3, the highest shear stress results for different types of MLS are stated.

Table 2.3: Summery results for different types of MLS.

Type of MLS	**Maximum shear stress [kN/m^2]**
Magnet-to-magnet	300 [i.e. 0.5mm air-gap]
	250 [i.e. 1mm air-gap]
Magnet-to-reluctance	84 [i.e. 0.5mm air-gap]
	71 [i.e. 1mm air-gap]
Magnet-to-conductor	39 [i.e. 1mm air-gap]

3 Impulse magnetisation of helical shaped magnet

3.1 Introduction

A material that can produce magnetic field without an external excitation is called a magnet [52]. The magnetic behaviour of materials differ from one to another according to the structure and distribution of the atoms and electrons spinning on their orbits. For example, in each atom there is a tiny magnetic moment resulting from the orbital spinning motion of the electrons, however, without the application of an external magnetic field, these moments would be randomly oriented, making the resultant magnetic moment negligible. Magnetic materials can be grouped depending on their reaction to externally applied fields. If the externally applied field tends to align the magnetic moments of the atoms in a way to increase the resultant magnetic field, then the material is called paramagnetic, and if the alignment of the magnetic moments decreases the net magnetic field, then the material is called diamagnetic. Other materials offer strong magnetic moments which can either oppose or support the applied magnetic field as superparamagnetic, ferromagnetic, and antiferromagnetic materials [53].

In other words, magnetisation process can be defined as the process at which the magnetic moment of each atom is aligned along the direction of the externally applied field. Some materials can be magnetised in any direction and these are called isotropic materials, while others exhibit anisotropic properties with a preferred direction of magnetisation [53-56], as well as higher level of energy products.

The magnetisation process applied to a magnetic material cannot produce a fully magnetised permanent magnet (PM) unless saturation is achieved. It is hard to fully magnetise (saturate) a magnet over the entire volume due to current limitations and restrictions on a magnetising fixture [57]. The net magnetic moments of the virgin magnet is zero, however, for each domain containing some atoms, random orientation of magnetic moments can be observed. In an anisotropic material, e.g., a rare-earth magnet, saturation can be achieved if the applied magnetic field is aligned with the easy axis direction of the material [58]. However, it is hard to fully magnetise a rare-earth magnet as it demands high field strength [59].

Methods of magnetisation can be varied according to the procedure of magnetising a PM. A PM magnetisation can be carried out using special magnetising fixture, where, the magnet is magnetised as a single unit without being assembled with other objects [60]. On the other hand, a sub-assembly magnetisation can also be achieved by magnetising the magnets while assembled on the motor using a specially designed fixture [61]. Alternatively, the whole motor can be assembled with virgin magnets, and the windings of the motor are used for magnetising the magnets, known as post-assembly (in-situ) magnetisation [59, 62, 63]. Fixing magnetised magnets on the machine is a process which may require special attention as it might attract magnetic dust as well as generate significant forces. As a result, post-assembly magnetisation can eliminate some hazardous effects during magnetisation process [64-66]. However, due to design restrictions, spaces between the magnet and magnetising windings can decrease the percentage of magnet volume saturation, and the magnet cannot be fully saturated [56, 59, 64]. Also, high coercivity magnets require high current values to be magnetised which may be difficult using the stator windings as they may not be able to withstand the high pulsed current used for magnetising the magnet [67].

For the previously mentioned methods of magnetisation, each can be done by different equipment depending on how much fields needed to saturate the magnet. For example, DC magnetizers cannot provide saturated magnetisation for a rare-earth magnet because of low applied field strength. They can be used to magnetise ferrites and alnicos as the limited produced field strength can do the job. However, the large pulse provided can cause excessive heat and energy dissipation [58].

Another way to magnetise ferrites and alnicos, for a low level of coercivity, is using a PM which provides a field having the same value required for saturation and this is known as PM magnetizer. Also, a half-cycle magnetizer is utilised in case of higher field requirements and controllable magnetisation process. The output current can achieve high values if a transformer is integrated into the system. The drawback of this scheme is the energy loss generated as a fixed input frequency is used which gives repeated constant pulse width. Also, the design of the device is obsolete [68]. Although higher currents can be gained from half cycle magnetizer, a capacitor discharge magnetizer is a better solution for magnetising PMs that require high field strength to reach saturation [69-75]. In 1944, Dr Weston invented the first capacitive discharge magnetizer [68]. Simply a capacitor discharge magnetizer is based mainly on a capacitor bank that stores a certain amount of energy. This energy is transformed from a rectifier that acts as an interface between the AC power supply and the capacitor bank. The stored energy is then discharged in a specific magnetising fixture represented by series R-L circuit via a switch. A diode is connected between the terminals of the R-L circuit to prevent reverse charging of the capacitors as shown in Fig. 3.1. The high discharged current pulse provides a sufficient field strength capable of magnetising the magnet to saturation. The width of current pulse can be controlled by controlling the values of capacitance and inductance of the system [70, 76-78]. Saturation of magnet can be achieved when a high magnetic field, regarding 3-4 times of the coercive force or magnetic field strength of 2-4 T, is provided [79-81].

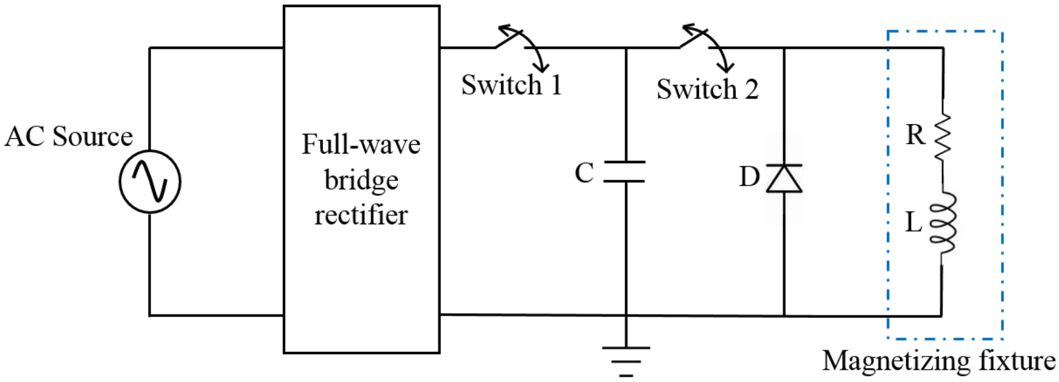

Fig. 3.1: Capacitor discharge magnetizer system.

Mechanical constraints on the design of impulse magnetisation fixture must be taken into consideration as a result of high mechanical stresses that face the fixture because of the high current pulse generated from the magnetizer [55, 58]. The windings face high-stress forces during magnetisation. These forces must be resolved otherwise failure of the fixture will occur. Sometimes aluminium tube, inserted between the magnet and fixture windings, can be used to provide support for the magnetising fixture against high currents and forces [82]. A non-magnetic, non-conductive sleeve can also be inserted between the coil and the magnet [68, 83]. Also, strong dielectric insulation is recommended between the iron core and the conductors. This will increase the dielectric strength and, thus, longer lifetime for fixture can be achieved. The high flux density generated from the large current leads to a noticeable rise in fixture's temperature [77, 82]. It is highly recommended to keep an eye on temperature rise during the discharging phase of magnetisation process. This leads to a significant change in the resistance which also affects the current impulse [59]. If this issue is not correctly estimated it could result in failure of the fixture and hence uncompleted magnetisation process [74, 78, 84]. At high temperature the non-fully magnetised magnet may face high risk in changing of its properties than a fully saturated one leading to a noticeable change in its properties [59]. The increase in temperature can be mitigated by cooling or increasing the time between pulses if multi-pulses are used [58].

To achieve successful magnetisation, some steps must be taken into consideration concerning the value of current required to saturate the magnet for a given voltage and capacitance, number of turns and position of windings. Also, the cycle time for the magnetizer if multi-shoot magnetisation is carried out, cooling process due to temperature rise during the discharging phase and finally a complete simulation of magnetisation procedure should be considered in order to avoid any problems may lead to failure of the process [59, 64]. In other words, the previous steps can be rewritten as:

a) How much current needed to saturate a percentage volume of the magnet?

b) What is the value of peak current that can be obtained from circuit parameters including capacitor bank and conductor dimensions considering temperature rise during discharge?

c) Comparing the peak current gained in (b) to the current in (a) required for magnet saturation.

In order to increase the volume of the saturated magnet, it may be better to use a mild steel core in a magnetising fixture, especially when relatively lower current is applied [59]. However, if a mild steel core is utilised in a magnetising fixture, the significantly induced eddy currents tend to oppose the magnetising field resulting in a non-fully magnetised magnet, and the behaviour of inductance begins to be non-linear as a result of mild steel saturation [64]. Thus, an air-cored magnetising fixture is usefully preferred when a high value of current is applied to decrease the effect of high induced eddy currents [74, 83]. The induced eddy current is a source of the non-uniform magnetic field which affects and reduces saturation of the whole magnet volume [55, 72]. Another reason for non-uniform magnetisation pattern of the magnet is the error occurred during positioning of the winding inside the magnetising fixture [85]. A non-fully magnetised magnet produces lower magnetic flux than a fully magnetised one. To fully magnetise hard magnetic material, a specific value of magnetic field strength has to be applied on the material. This value is not usually provided by the manufacturer [82]. During magnetisation process, the time required to align the magnetic domains in a magnet during impulse magnetisation is in order of 10^{-8} to 10^{-9} seconds [68]. Current pulse should be as short as possible to reduce the thermal effect on the fixture [59]. However, the current pulse preferred to be broad enough to decrease the influence of eddy currents which oppose the field that magnetise the magnet [58, 73].

Magnetising fixtures can have different configurations. One of these configurations is called single sided fixture, where the coil is wound to face either the inner or the outer side of the magnet. Other is called double-sided fixture, in which the coil is facing both the inner and the outer side of the magnet. Double-sided fixtures are usually preferred than single sided fixtures for magnetising PMs as they provide higher field strength, more saturation, more alignment of magnetic dipoles during magnetisation and gives higher symmetrical magnetisation pattern along the axial length of the magnet than single sided fixtures [55, 83].

In this chapter, a new magnetisation process is investigated. The magnetisation process will introduce a helically shaped magnetisation distribution. The windings are wound around the fixture in a helical configuration to generate a helically shaped magnetic field during magnetisation process. Different winding groups are introduced including single, double and four conductor configurations as shown in Fig. 3.2.

Comparison between single sided and double sided fixtures is undertaken in terms of temperature rise, resistance change, and magnetic flux density distribution in the magnet. In the analysis, the specifications of the impulse magnetiser available at the University of Sheffield are considered, with maximum voltage of 3kV, and a maximum current of 30kA corresponding to a total energy 30kJ. Circuit coupled 2D transient finite element using MAXWELL 2D is employed for the simulations, and results are compared with purpose developed time-domain simulation model using MATLAB/SIMULINK. Due to mild steel saturation, the values of the inductance will vary with current in a non-linear fashion. So, these values are calculated and imported in a look-up table in MATLAB/SIMULINK. Change in temperature during simulation, which affects the value of the resistance of the fixture and the final temperature, is also taken into consideration, by assuming an adiabatic process, where at each time step the copper losses are calculated, the temperature rise is estimated and the value of the resistance is updated accordingly. In the transient finite element simulations, the change in temperature and resistance during magnetisation process are not taken into account, which leads to a difference in current between MATLAB/SIMULINK and finite element analysis.

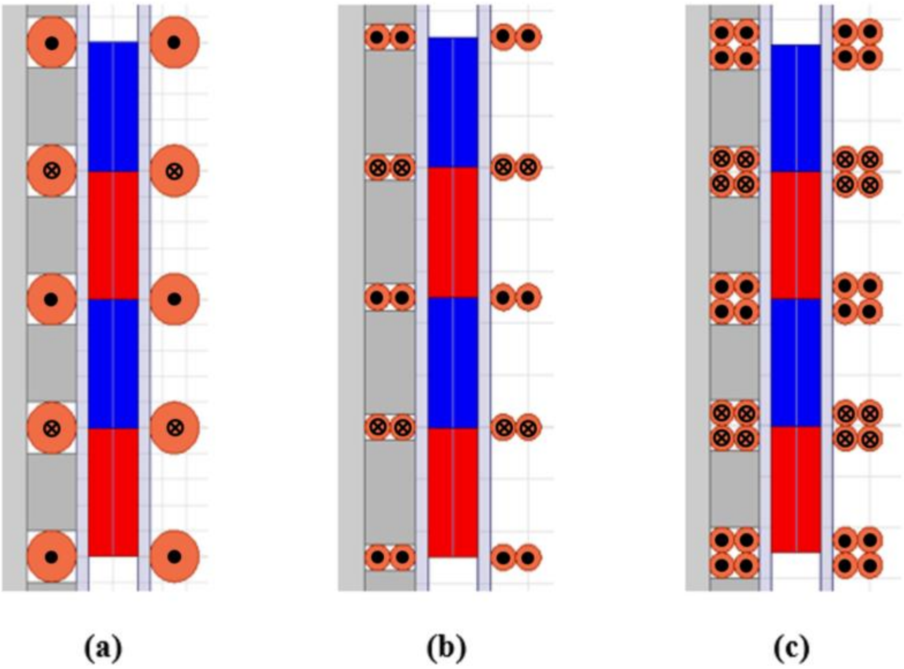
(a) (b) (c)

Fig. 3.2: Different winding groups (a) Single, (b) Dual, and, (c) Quad conductors.

3.2 Dynamic behaviour of magnetisation process

As shown in Fig. 3.1, after charging the capacitor C, switch 1 is opened and switch 2 is ready to be triggered to start the process of magnetisation. When switch 2 is closed the initial voltage on the capacitor is $V_{i,}$ and the circuit can be assumed a series RLC circuit as shown in Fig. 3.3. Initially, the current is zero and the initial voltage value at time t=0 is known. By applying Kirchhoff's law, the differential equation of series RLC circuit is as follows.

$$L\frac{di(t)}{dt} + IR + \frac{1}{C}\int i(t)dt = 0 \tag{3.1}$$

$$L\frac{d^2i(t)}{dt^2} + R\frac{di}{dt} + \frac{i(t)}{C} = 0 \tag{3.2}$$

$$\frac{d^2i(t)}{dt^2} + \frac{R}{L}\frac{di}{dt} + \frac{i(t)}{LC} = 0 \tag{3.3}$$

At

$$\mathrm{t} = 0,\ i(0) = 0 \tag{3.4}$$

Then

$$\frac{di(0)}{dt} = \frac{V_i}{L} \tag{3.5}$$

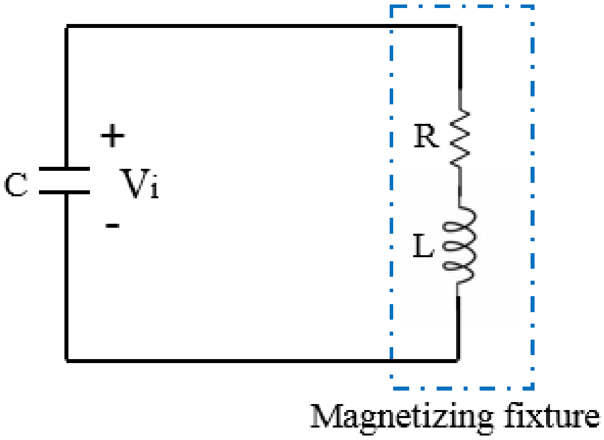

Fig. 3.3: Equivalent circuit during discharge phase.

where, L is the inductance of the fixture, R is the resistance of the fixture, C is the capacitance of the capacitor bank and V_i is the initial voltage of the capacitor. The inductance is calculated initially by applying a constant voltage source across its terminals. At this moment, values for current, through the inductor, with time can be extracted in a table, then, di/dt can be easily calculated.

The initial resistance value of the fixture can be calculated from:

$$R_0 = \frac{\rho\ell}{A} \tag{3.6}$$

where, ρ is the resistivity of copper (1.7×10^{-8} Ω/m at 20 °C), ℓ is the length of the coil and A is cross-sectional area of the conductor.

At this step, the initial value of the resistance is known. Thus, resistance change due to rise in temperature generated from the high pulsed current can be found as:

$$\Delta R = R_0 \alpha \Delta T \qquad (3.7)$$

where, ΔR is the change in resistance, α is the temperature coefficient of copper ($3.9\times10^{-3}/^{0}$C) and ΔT is temperature change in copper windings.

Due to high pulsed current, the temperature of the fixture can be elevated. It is highly recommended to estimate the temperature rise in the fixture and keep it in acceptable ranges to ensure safety and success of magnetisation process. The temperature change in copper windings ΔT can be calculated in (3.8) where it is a function of power loss and mass of the winding given in (3.9) and (3.10).

$$\Delta T(t) = \int_0^t \frac{P}{mC_p} dt \qquad (3.8)$$

$$P = I^2 \times R \qquad (3.9)$$

$$m = \varrho \times \ell \times A \qquad (3.10)$$

where, P is the power loss, m is the mass of the copper winding. C_p is the specific heat capacity of copper (385 J/kgK^0) and ϱ is the density of copper (8960 kg/m^3).

The second order differential equation (3.3) is solved using MATLAB/SIMULINK. The initial values for resistance, and temperature are known. The capacitance value and initial voltage are indicated in series RLC branch. The resistance of the fixture is modelled as controlled voltage source, which changes with current and temperature. The output current is the input for power loss calculation block which is multiplied by ($1/mC_p$) as gain. The output is then integrated to calculate the temperature change ΔT. Once ΔT is calculated, the output is taken as input for the variable winding resistance R block. R(ΔT) and the value of current are multiplied giving the voltage drop across the new calculated resistance of the fixture as shown in Fig. 3.4.

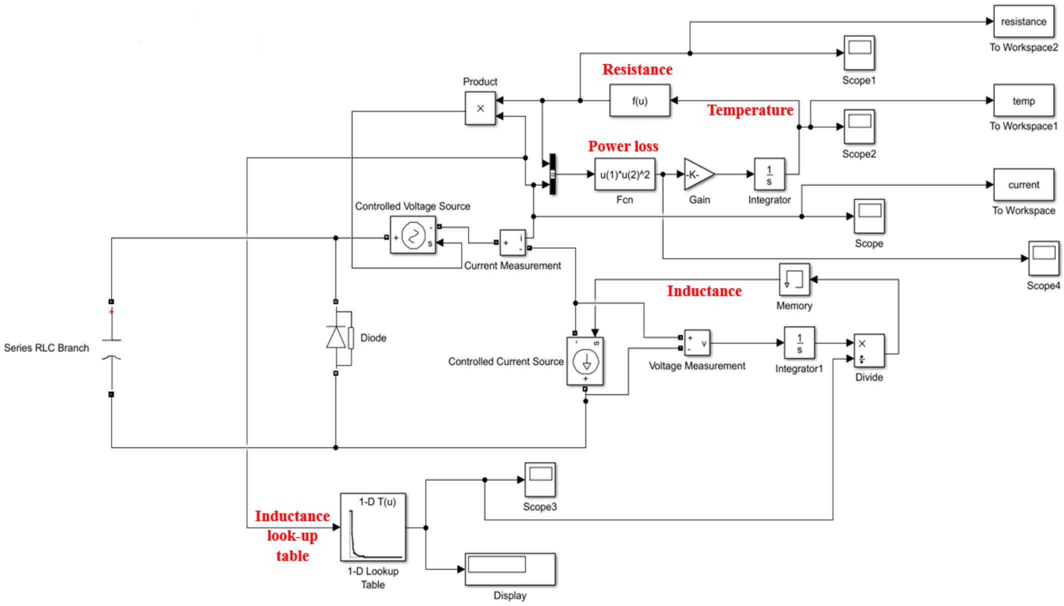

Fig. 3.4: Block diagram of discharging phase for magnetizer.

At the same time, the current passing through the inductance, which is modelled as controlled current source, has an equivalent inductance value recalled from a look-up table determined from finite element analysis. The voltage drop across the inductance is integrated and divided by the corresponding inductance value from the look-up table to give corresponding current value.

3.3 Design parameters

In this section, full design details will be shown including dimensions and materials of the magnet, the inner core, and the outer core of magnetising fixture. The magnet is sintered anisotropic Nd-Fe-B grade N45SH with second quad B-H curve given in Fig. 3.5. Its residual flux (B_r) is 1.32 T with nominal normal coercivity (H_{cB}) of 1015 kA/m [86]. The inner diameter of the magnet is 16 mm, and the outer diameter is 19 mm with 1.5 mm thickness. During simulation, the permeability of the magnet is assumed to equal 1. Thus, it can be represented as an air-gap. The pole-pitch is chosen to be 5 mm with a lead of 10 mm. The total length of the magnet is 20 mm which is equivalent to 2 pole-pairs. The length of the fixture is chosen to be 60 mm to eliminate the effect of flux from the end winding from affecting the magnetising flux during magnetisation process. The magnetising fixture is designed with helical grooves to house the helical shape windings that are wound around the fixture as shown in Fig. 3.6. For single sided fixture, the inner core is chosen to be mild steel with non-linear B-H curve. The inner diameter of the double start screw is 10 mm, and the outer diameter is 15 mm as shown in Fig. 3.7 (a). The material of the inner core is chosen to enhance the magnetic flux gained from a given current pulse and, thus, increase the percentage of saturated volume of the magnet. The helical grooves have different dimensions from one fixture to another according to the number of conductors used. For double-sided fixture, the outer core of the magnetising fixture is chosen to be Tufnol strengthened by a glass fibre over wrap to enhance the mechanical strength of the fixture and to overcome the effects of forces exerted on the fixture during magnetisation process. The inner diameter is 25 mm, and the outer diameter is 38 mm as shown in Fig. 3.7 (b).

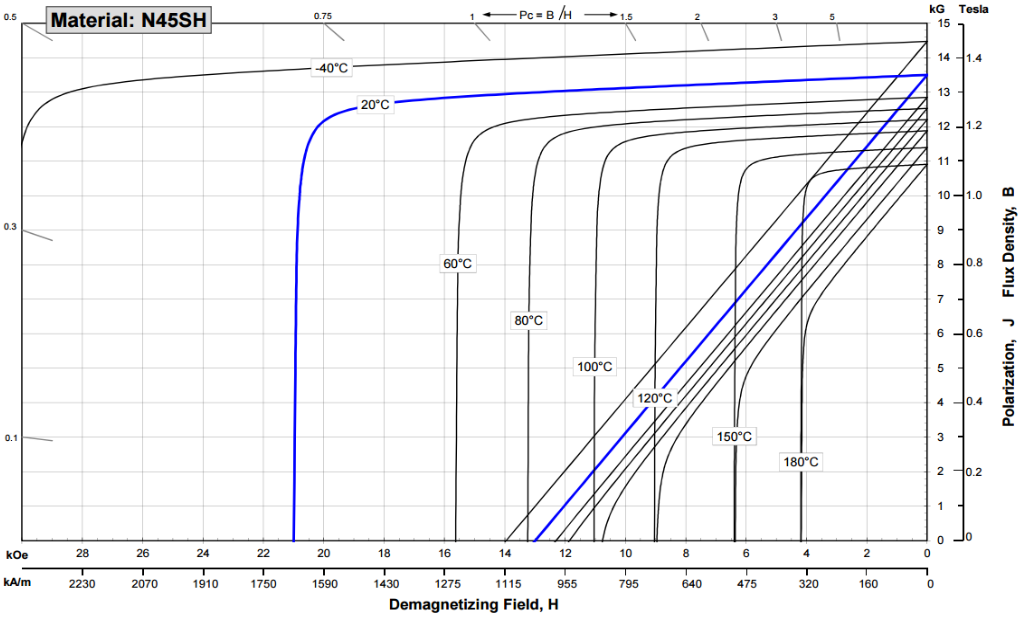

Fig. 3.5: Second quadrant B-H for N45SH magnet [86].

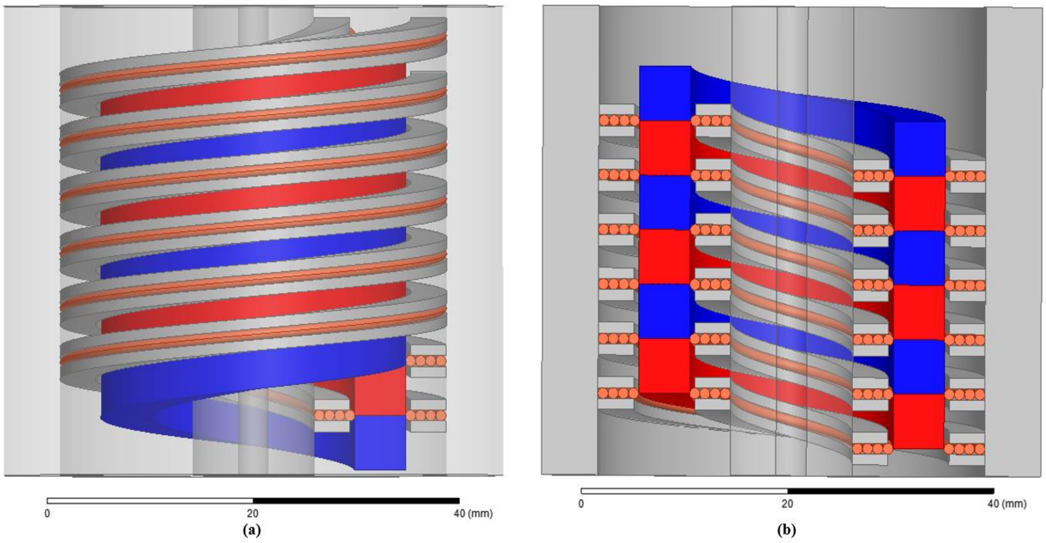

Fig. 3.6: Helical grooves with magnetising windings (a) 3D view, (b) cross section.

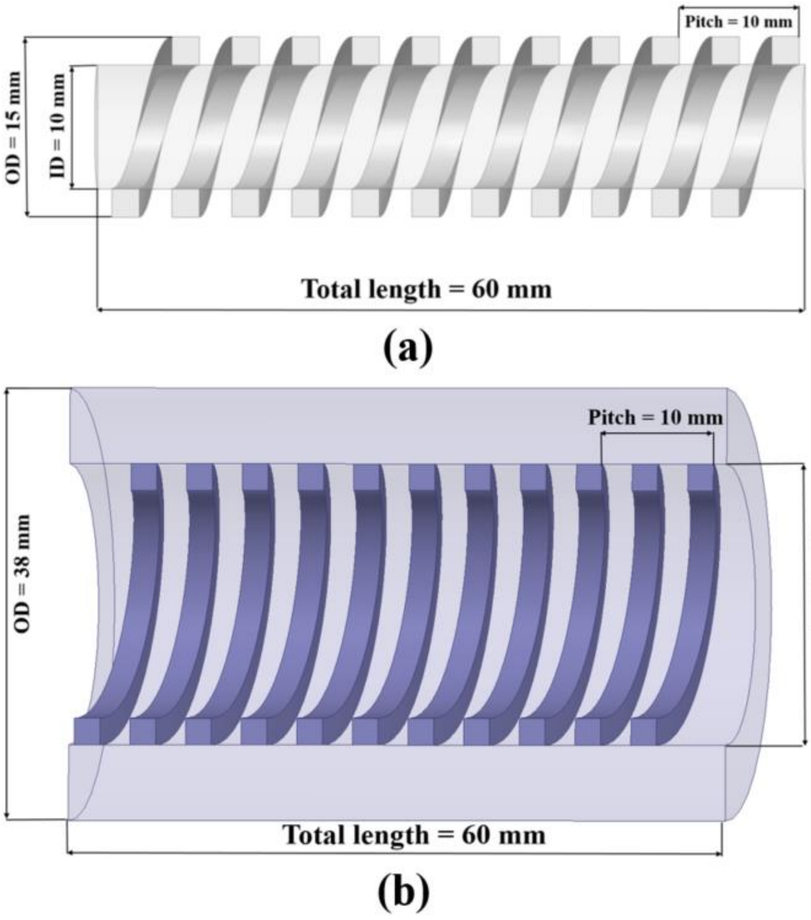

Fig. 3.7: Fixture cross section of (a) mild steel inner core, (b) Tufnol outer core.

3.4 Single sided fixture

The dynamic behaviour of magnetising fixture and parameters calculation were introduced in the previous sections. The simulation of the magnetisation process of the N45SH magnet will be carried out using MAXWELL 2D, and the value of current pulse will be compared to MATLAB/SIMULINK results. As mentioned before, the dimension of mild steel core is 10 mm and 15 mm for inner and outer diameters, respectively. Simulations studies for single sided fixture will be undertaken for single, double and four conductor configurations. Also, the effect of removing the mild steel core will be investigated. The magnet will be encapsulated with an insulating cylinder of 0.5 mm thickness on the inner and the outer surface of the magnet to increase the mechanical strength of the fixture during discharging pulse.

3.4.1 Single conductor magnetising fixture

The single conductor single sided fixture, shown in Fig. 3.8, is realised from a single conductor coil of 1 mm radius wound around double start screw with a lead of 10 mm. The helical shape winding shown in Fig. 3.8 (a,b) can provide a helical shape magnetic field. The 3D model is assumed to be cut in Fig. 3.8 (b) such that the magnets can be seen as shown in the figure. Any change in the vertical cut plan will lead to two pole-pairs of the magnets. The current is assumed to be in opposite direction in two successive turns. This direction can produce north and south magnetic poles on the magnet. The direction of current can be shown in Fig. 3.8 (c).

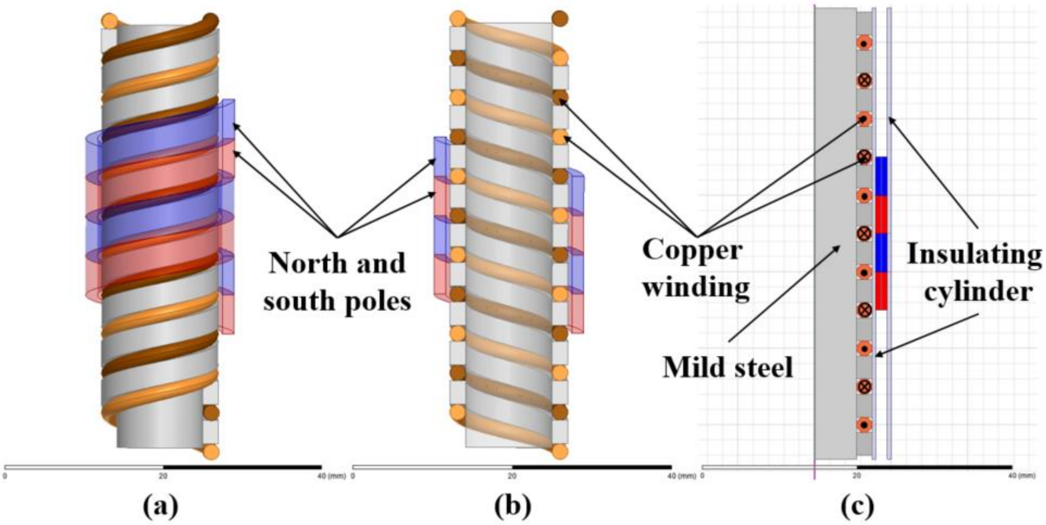

Fig. 3.8: Single sided fixture (a) 3D view, (b) Cross section, and, (c) 2D view.

The capacitance of the capacitor bank and the initial voltage is chosen according to the limitation of the real magnetizer. The voltage was initially set to 500 V applied to a capacitance of 0.5 mF. The resistance of the fixture was calculated to be 2.43 mΩ, and the variation of inductance with current pulse of 10.2 μs rise time is shown in Fig. 3.9. Circuit coupled transient finite element analysis, where eddy currents in the mild steel core are considered, is shown in Fig. 3.10.

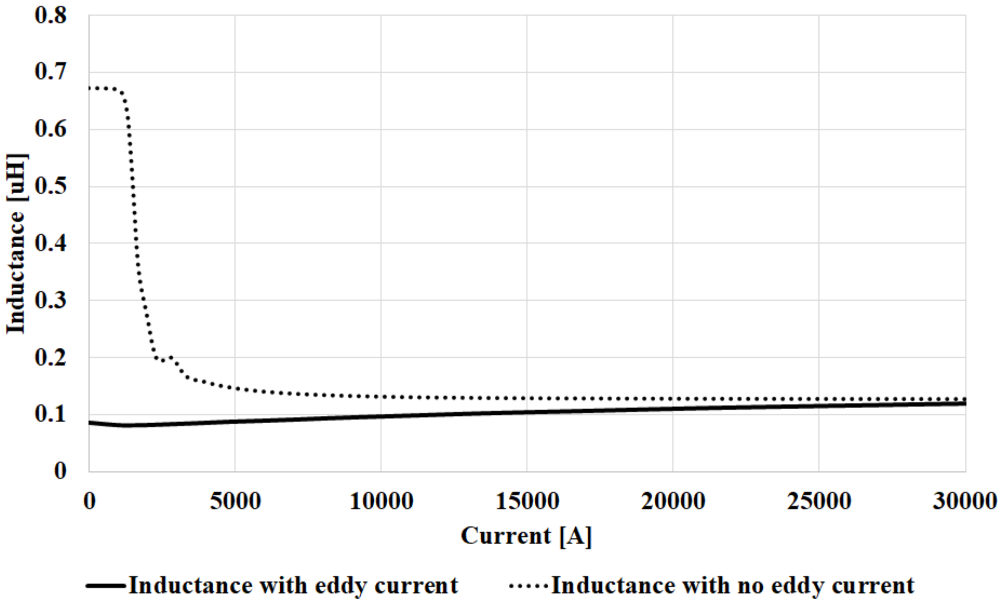

Fig. 3.9: Inductance variation with current for single conductor single sided fixture.

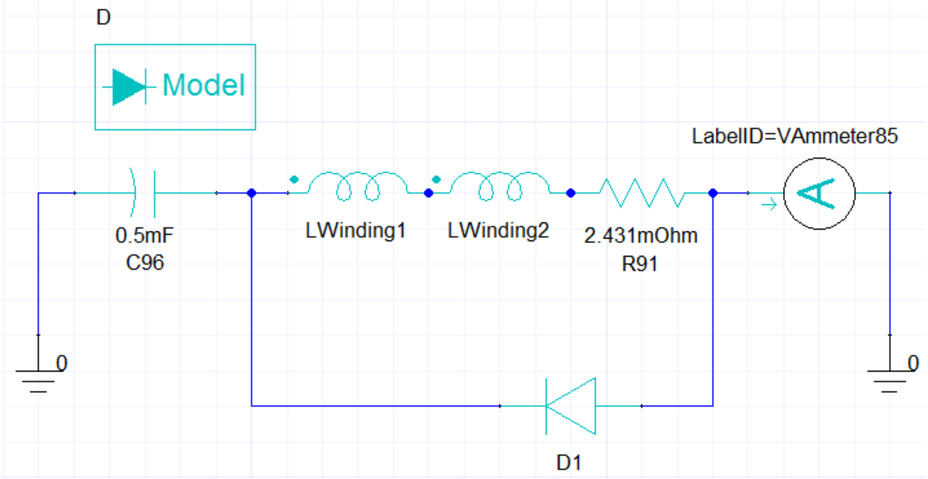

Fig. 3.10: Excitation circuit of single conductor single sided fixture (MAXWELL 2D or 3D).

During discharge phase, the effect of induced eddy current on the current pulse is shown in Fig. 3.11. The induced eddy current starts to oppose the magnetic field generated from the magnetising current. The change in resistance and temperature can be shown in Fig. 3.12 and Fig. 3.13 respectively. The temperature rise calculated by SIMULINK is 12^{o}C, and the resistance change is 0.11 mΩ. The direction of magnetisation and the distribution of magnetic field density can be shown in Fig. 3.14. At the maximum value of the current pulse, the radial component of the magnetic field is recorded on the inner, mid, and outer surface of the magnet pole-pitch. At each position on the magnet surface, the effect of induced eddy current is shown in Fig. 3.15, 16 and 17.

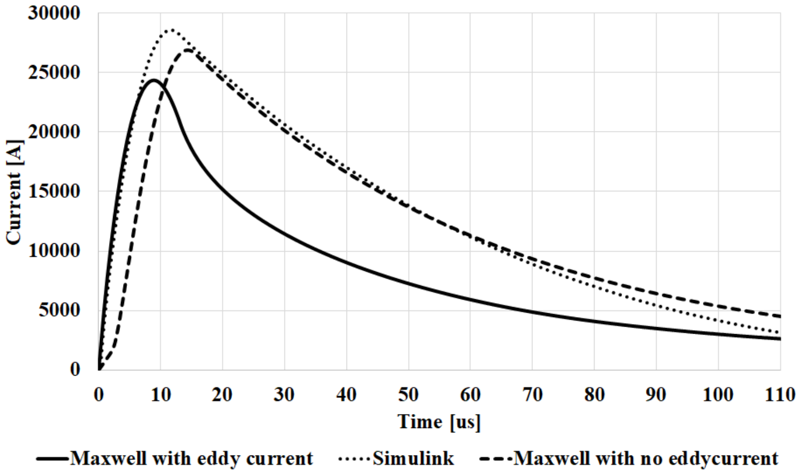

Fig. 3.11: Current pulse for single conductor single sided fixture.

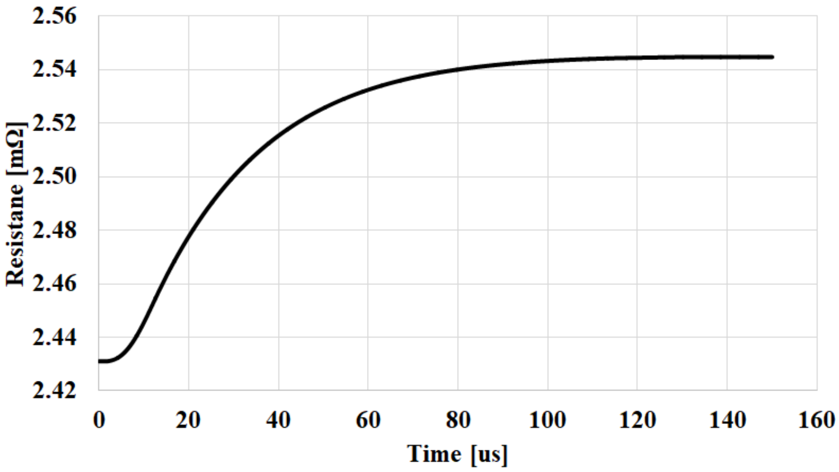

Fig. 3.12: Resistance variation during magnetisation process.

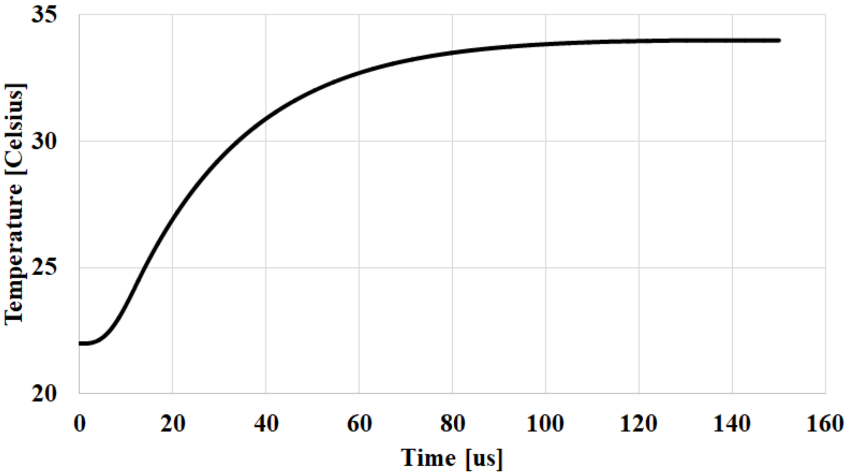

Fig. 3.13: Temperature variation during magnetisation process.

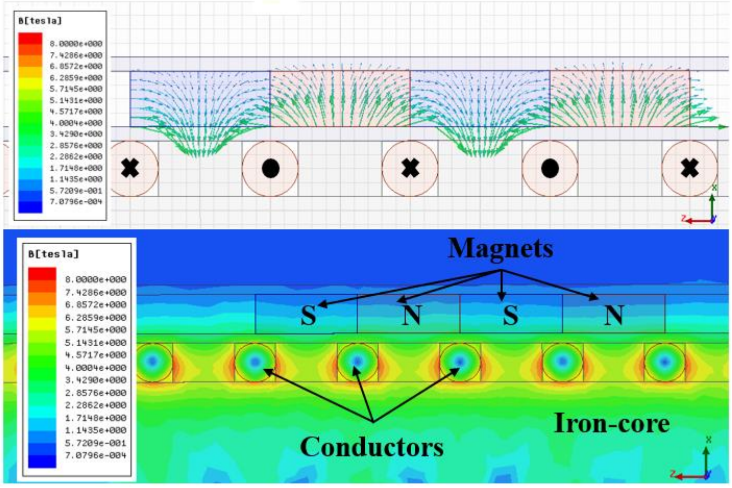

Fig. 3.14: Direction of magnetisation and field distribution for single conductor single sided fixture.

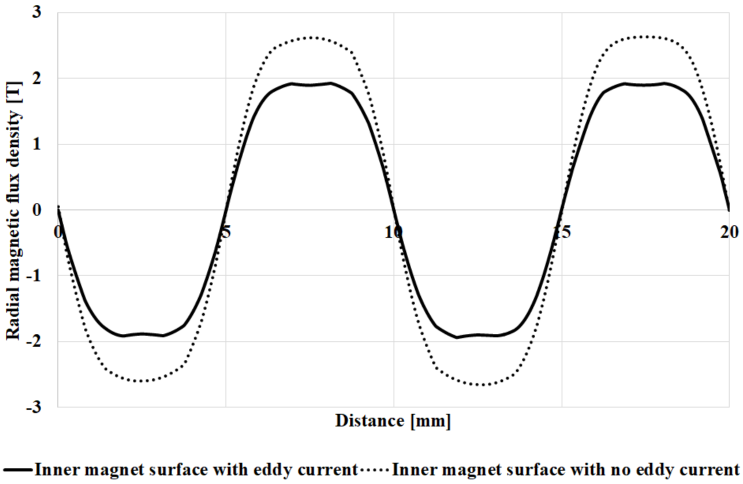

Fig. 3.15: Magnetic flux density waveform along the inner magnet surface.

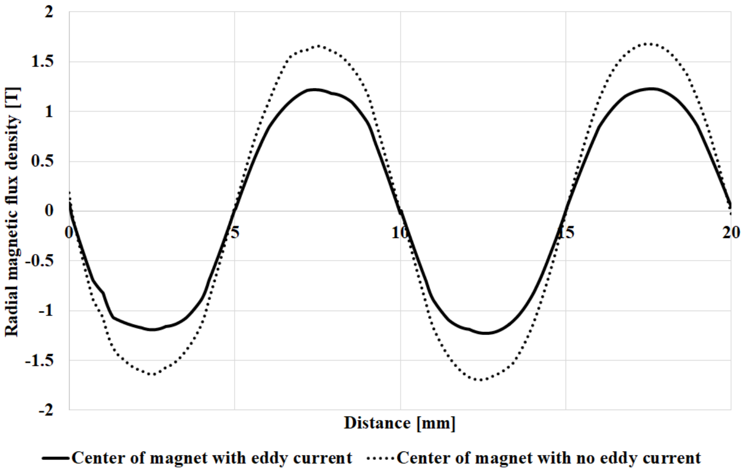

Fig. 3.16: Magnetic flux density waveform along the centre of magnet surface.

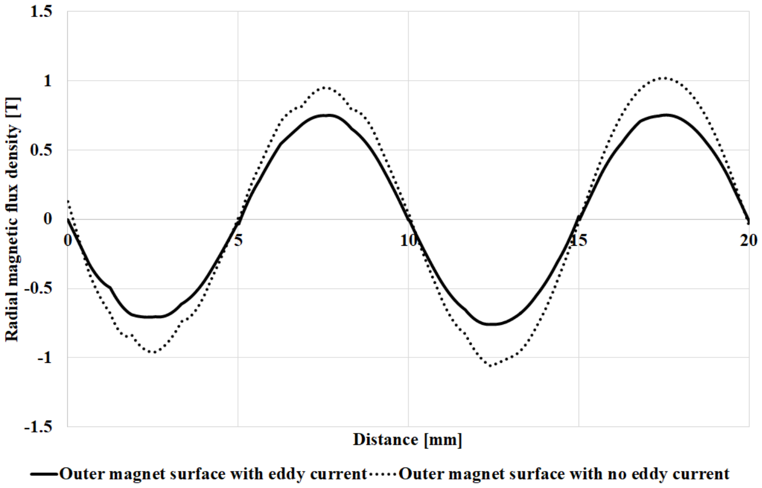

Fig. 3.17: Magnetic flux density waveform along the outer magnet surface.

3.4.2 Dual conductor magnetising fixture

In this case, the helical grooves of the fixture are housing two conductors per slot to improve the magnetic field strength at a given current as shown in Fig. 3.18. The diameter of each conductor is 1 mm. The total calculated resistance of the fixture is 19.45 mΩ. The capacitor bank of capacitance 1 mF is charged to 1200 V. The maximum output current is 29.5 kA which causes 318 ^{o}C rise in temperature as shown in Fig. 3.19. Temperature rise causes a change in fixture's resistance by 22.5 mΩ as shown in Fig. 3.20. The direction of magnetisation and the distribution of magnetic field density can be demonstrated in Fig. 3.21. At the maximum value of the current pulse, the radial component of the magnetic field is recorded on the inner, mid, and outer surface of the magnet's pole-pitch. At each position on the magnet surface, the effect of induced eddy currents is shown in Fig. 3.22, 23 and 24. Induced eddy currents tend to oppose the magnetising field resulting in reduction of the percentage volume saturation of the magnet.

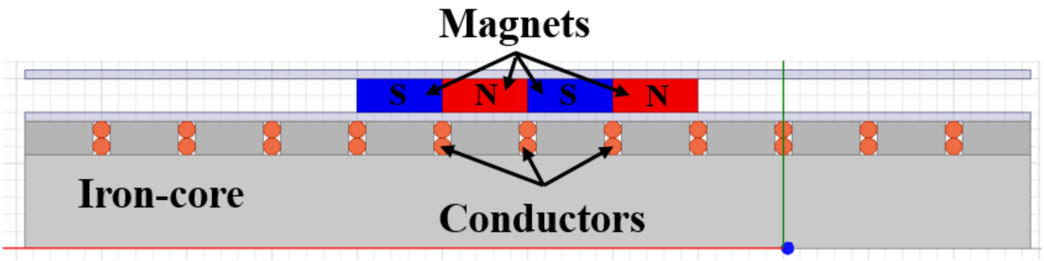

Fig. 3.18: 2D view of dual conductor single sided fixture.

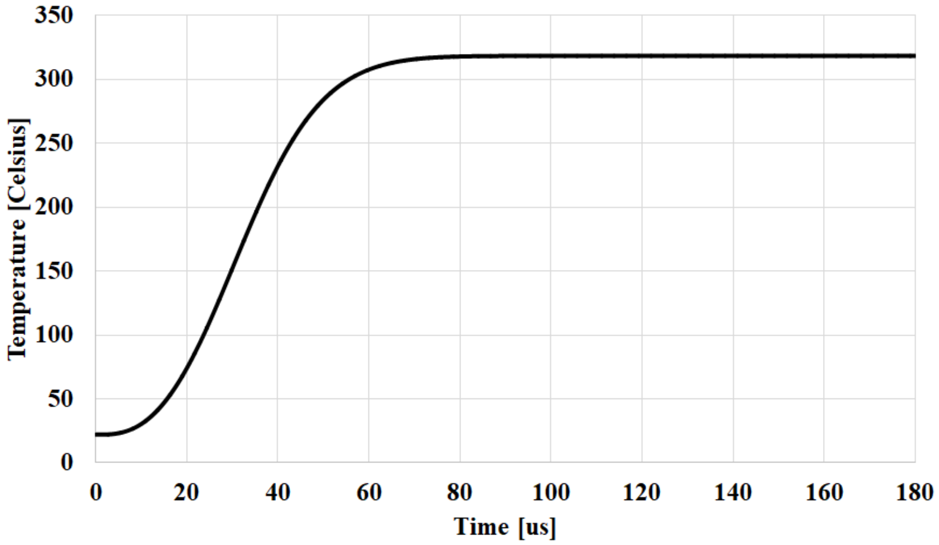

Fig. 3.19: Temperature rise in fixture during magnetisation process.

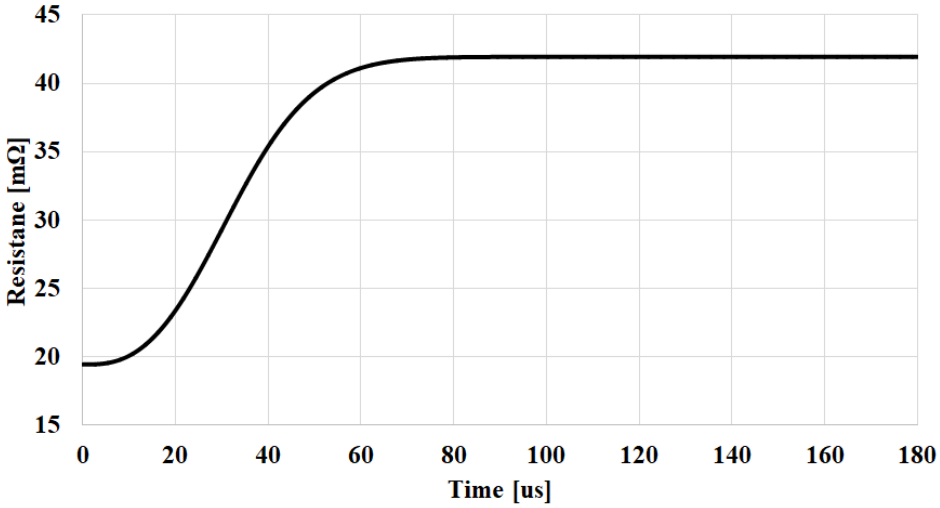

Fig. 3.20: Resistance variation in dual conductor single sided fixture.

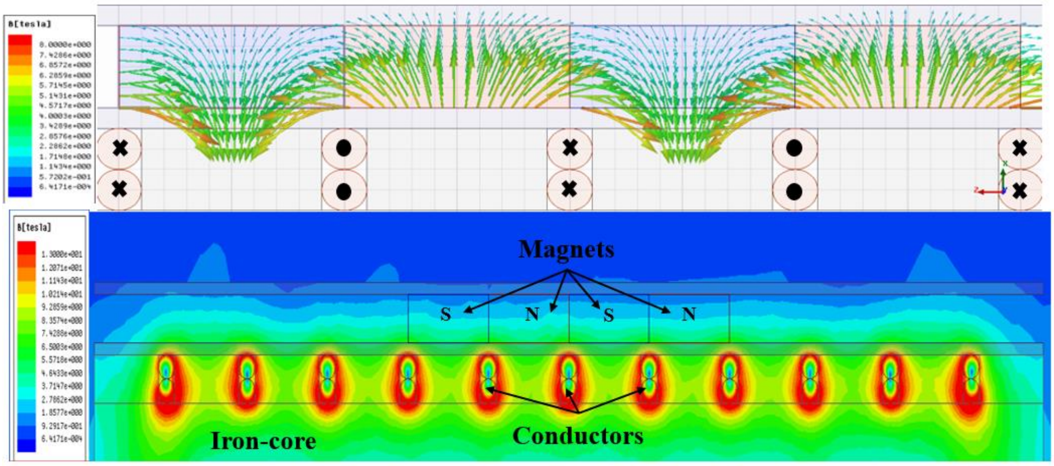

Fig. 3.21: Direction of magnetisation and field distribution for dual conductor single sided fixture.

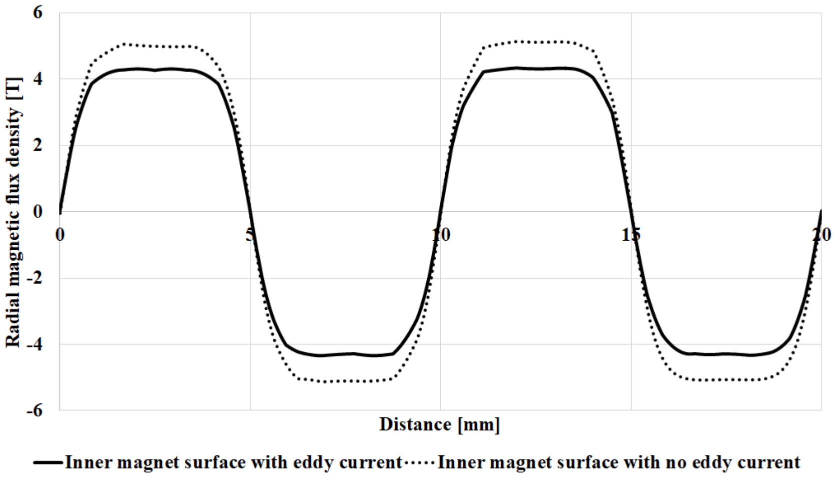

Fig. 3.22: Magnetic flux density waveform along the inner magnet surface.

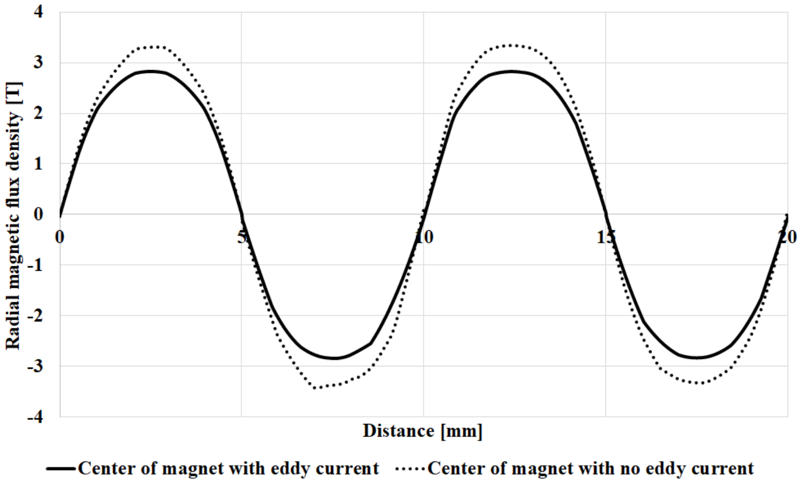

Fig. 3.23: Magnetic flux density waveform along the centre of magnet surface.

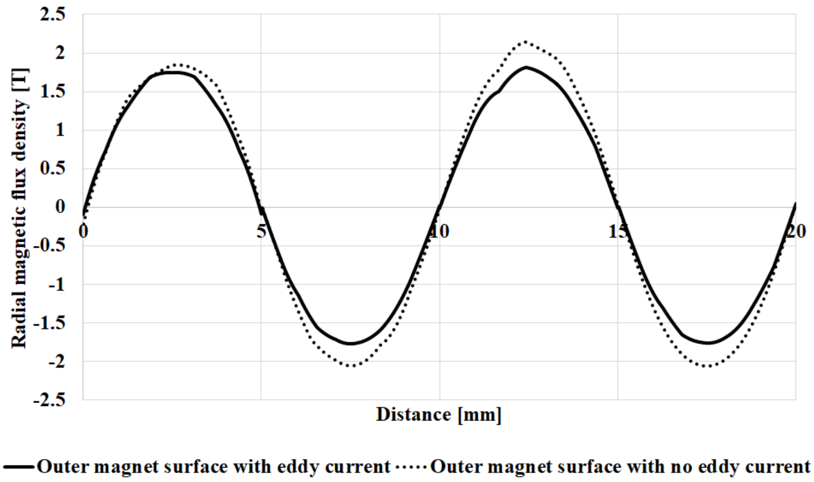

Fig. 3.24: Magnetic flux density waveform along the outer magnet surface.

3.4.3 Quad conductor magnetising fixture

In this single sided fixture, each slot of the magnetising fixture is housing four conductors. A maximum current pulse of 27.58 kA can be obtained when 1 mF capacitor bank is charged at an initial voltage of 2100 V. The initial resistance of 39 mΩ has increased by 68.8 mΩ. The high current pulse causes a temperature raise of 452.7 ^{o}C from the ambient temperature. The magnetic flux density on the inner and outer surface of the magnet is enhanced. However, the high temperature may cause system failure. The direction of magnetisation and the distribution of magnetic field density on the surface of the magnet can be shown in Fig. 3.25.

With the effect of eddy current, the maximum value of the magnetic flux density is 8.33 T at the inner surface of the magnet, 5.35 T at the mid-surface, and 3.29 T at the outer surface of the magnet as shown in Fig. 3.26, 27 and 28 respectively. As seen in figures, the eddy current effect is decreasing on the outer surface of the magnet and doesn’t have much effect as the inner magnet surface which is much closer to the mild steel core. Although the high magnetic flux density on the inner surface of the magnet which can saturate the magnet easily, the rise in temperature can be a noticeable cause for not recommending this type of fixtures for magnetisation of magnets.

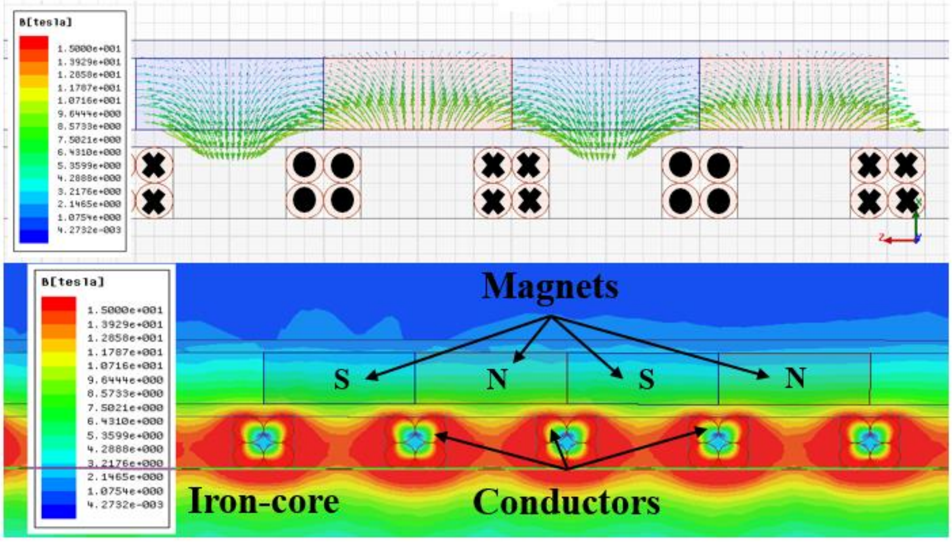

Fig. 3.25: Direction of magnetisation and field distribution for quad conductor single sided fixture.

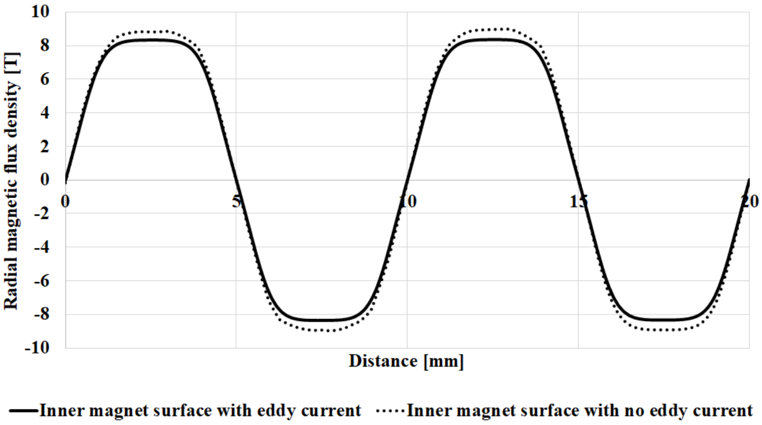

Fig. 3.26: Magnetic flux density waveform along the inner magnet surface.

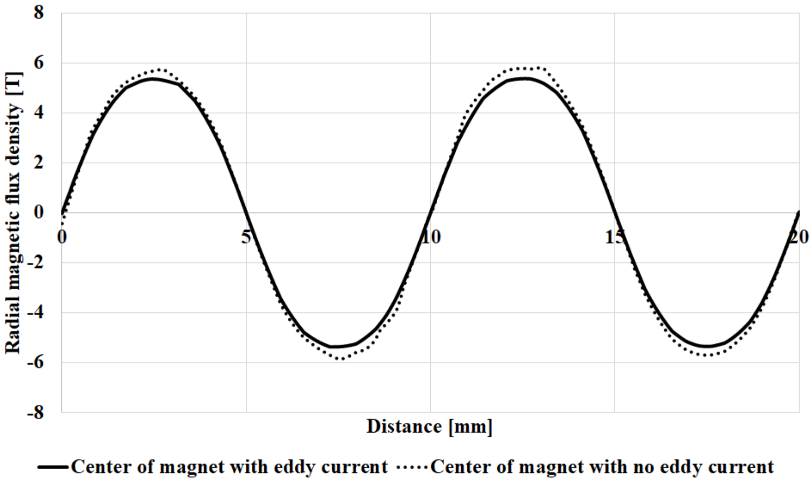

Fig. 3.27: Magnetic flux density waveform along the centre of magnet surface.

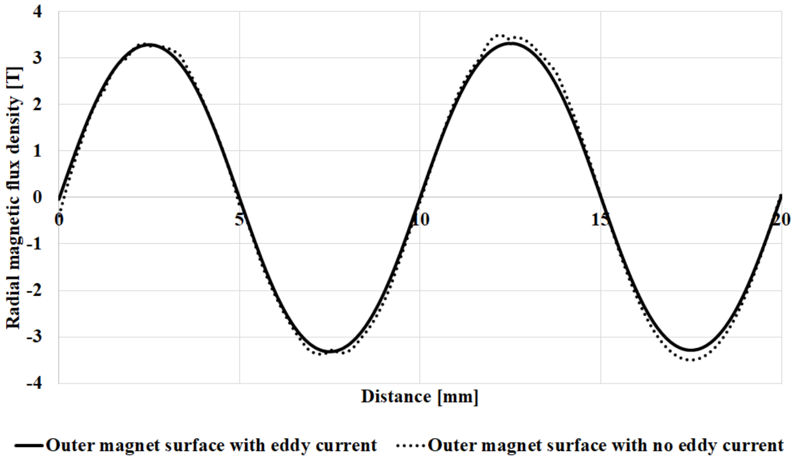

Fig. 3.28: Magnetic flux density waveform along the outer magnet surface.

For the single sided fixture, the values for magnetic flux densities on the outer surface of the magnet are not promising for different conductor configurations. That is why single sided fixture is not recommended to fully saturate the magnet. Even for high magnetic flux density on the inner magnet surface, the magnetic flux density on the outer surface of the magnet needed to be enhanced, however, high temperature may cause a failure to the system. So, for more magnet saturation, the double-sided fixture is recommended to be employed instead.

3.5 Double sided fixture

This type of fixture differs from the single sided fixture as a helical coil is wound around the outer surface on the magnet as shown in Fig. 3.29. The outer coil is housed into the grooves of a helical shape threads of Tufnol core. The magnet is inserted between two helical shape coils that concentrate the direction of magnetisation and provide better alignment of the domains with enhanced values of magnetic flux density over the volume of the magnet.

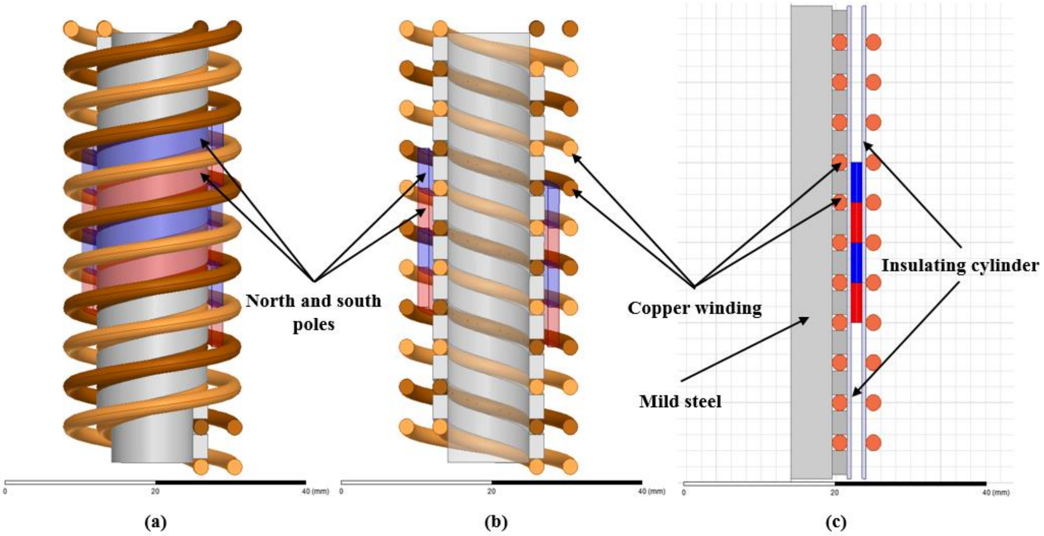

Fig. 3.29: Double sided fixture (a) 3D view, (b) Cross section, and, (c) 2D view.

3.5.1 Single conductor magnetising fixture

The double-sided fixture is supporting the generated magnetic field by wound a coil in the grooves of an outer Tufnol core with an inner diameter of 20 mm and outer diameter of 38 mm. In this case, the capacitance of the capacitor bank and the initial voltage are chosen to be 1.5 mF and 600 V respectively. These values provide a current pulse of maximum 27.7 kA which is in the limit of the real magnetizer that will be used in actual magnetisation process. The initial resistance of the fixture was calculated and found to be 6.54 mΩ, and the variation of inductance with current is recorded in the same manner as section 3.4.1. During discharge phase, the current obtained from MAXWELL and MATLAB/SIMULINK is shown in Fig. 3.30, where it shows the effect of eddy current on the magnetising pulse. The variation of temperature and resistance with the current pulse is shown in Fig. 3.31 and Fig. 3.32 respectively. The temperature raised by 20.5 ^{o}C and the resistance increased by 0.52 mΩ. To figure out the distribution of magnetic flux density, the radial component of the magnetic field is recorded on the inner, mid, and outer surface of the magnet pole-pitch at the maximum value of current pulse. The direction of magnetisation and the distribution of magnetic field density can be shown in Fig. 3.33, as shown in the figure, the distribution of the magnetic flux density over the cross-section area of the magnet is much better than single sided fixture. The maximum value of the magnetic field is 3.58 T at the inner surface of the magnet, 3.2 T at the mid-surface, and 3.26 T at the outer surface of the magnet as shown in Fig. 3.34, 35 and 36 respectively. In spite of the presence of induced eddy current, the single conductor double sided fixture can provide a magnetic flux density between 3-4 Tesla which can saturate high coercivity magnets. Compared with single sided fixture results, the double-sided fixture can provide an enhancement in the value of the magnetic flux density over the volume of the magnet.

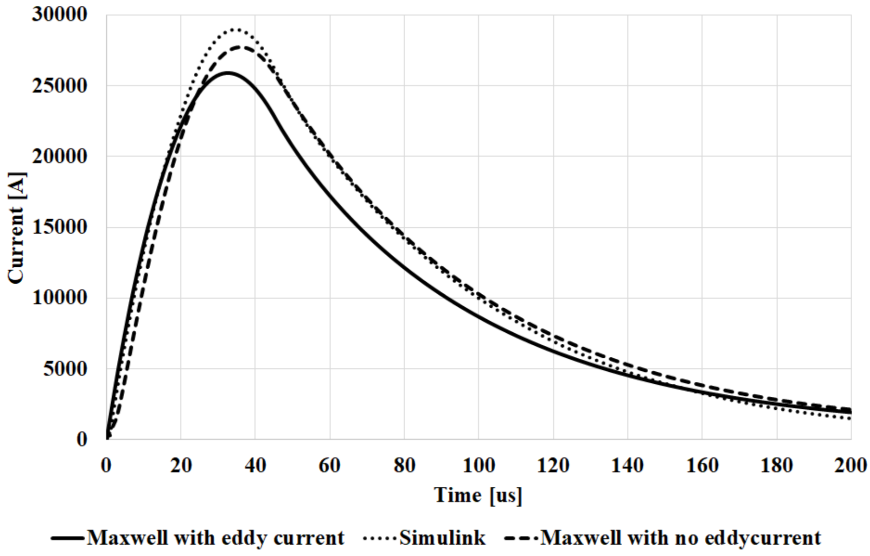

Fig. 3.30: Magnetising current pulse of single conductor double-sided fixture.

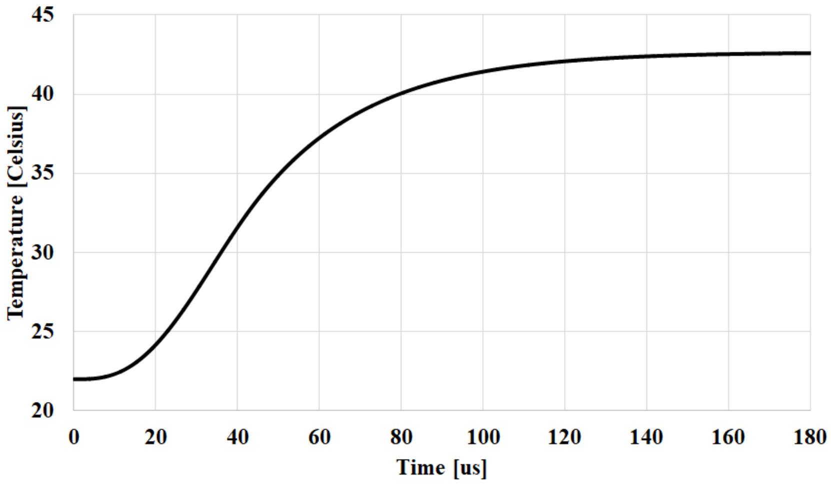

Fig. 3.31: Temperature rise in fixture during magnetisation process.

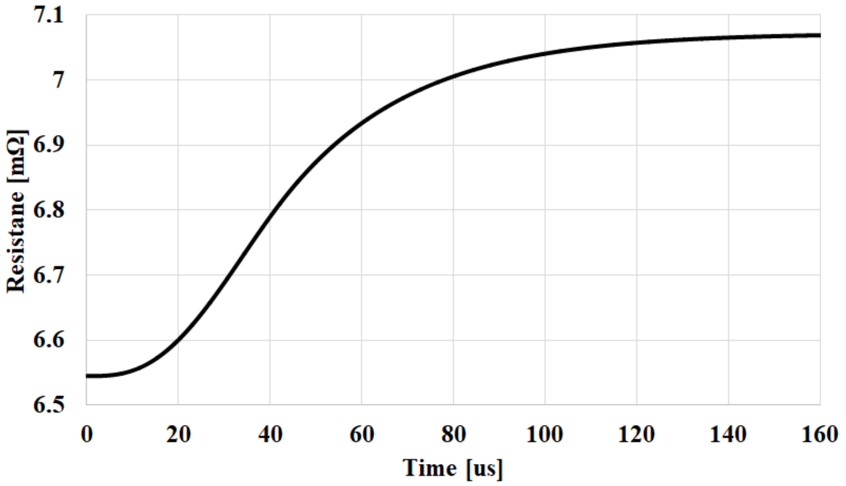

Fig. 3.32: Resistance variation in single conductor double-sided fixture.

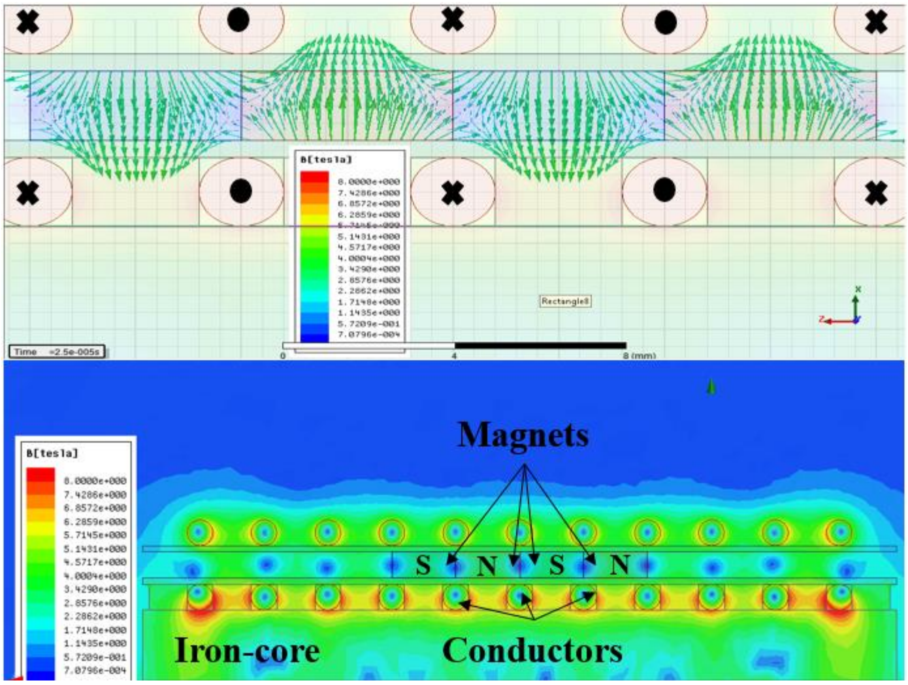

Fig. 3.33: Direction of magnetisation and field distribution for single conductor double-sided fixture.

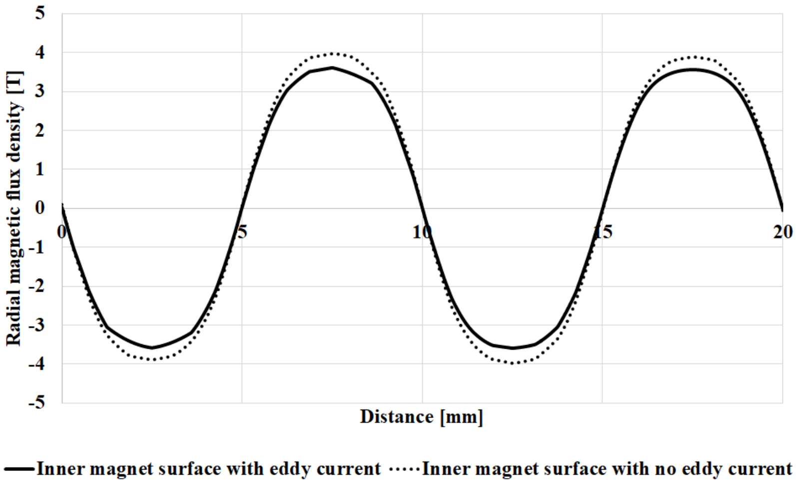

Fig. 3.34: Magnetic flux density waveform along the inner magnet surface.

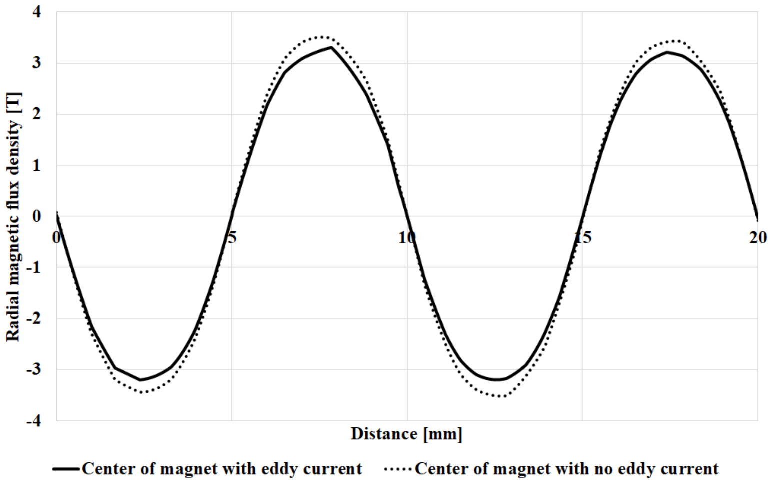

Fig. 3.35: Magnetic flux density waveform along the centre of magnet surface.

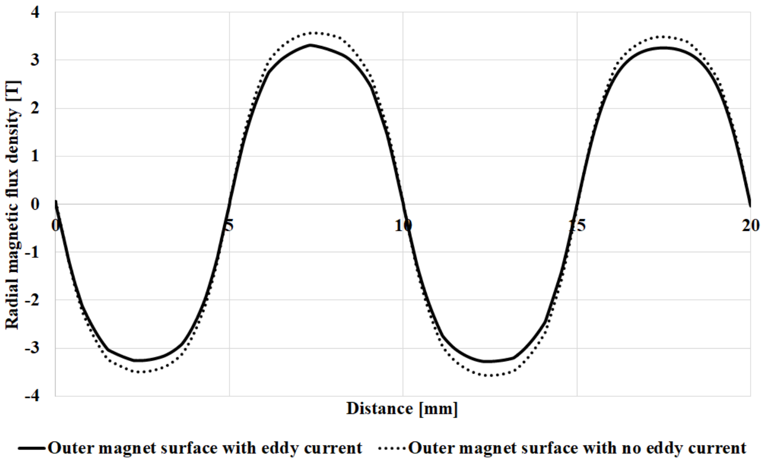

Fig. 3.36: Magnetic flux density waveform along the outer magnet surface.

3.5.2 Dual conductor magnetising fixture

The helical grooves are hosting two conductors each of diameter 1 mm as shown in Fig. 3.37. The total resistance of the fixture is 52.36 mΩ. The capacitor bank of capacitance 1 mF is charged to 1300 V. The output current pulse is capable of providing a magnetic flux density more than 3 Tesla even under the effect of induced eddy current. The output current pulse causes a temperature increase in the fixture to 150.5 ^{o}C as shown in Fig. 3.38 accompanied by a change in fixture's resistance by 26.3 mΩ as shown in Fig. 3.39. The maximum value of the magnetic field is 3.98 T at the inner surface of the magnet, 3.62 T at the mid-surface, and 3.64 T at the outer surface of the magnet as shown in Fig. 3.40, 41 and 42 respectively.

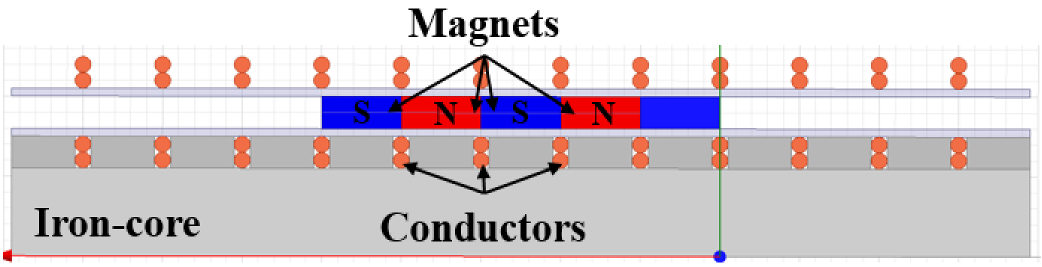

Fig. 3.37: 2D view of dual conductor double-sided fixture.

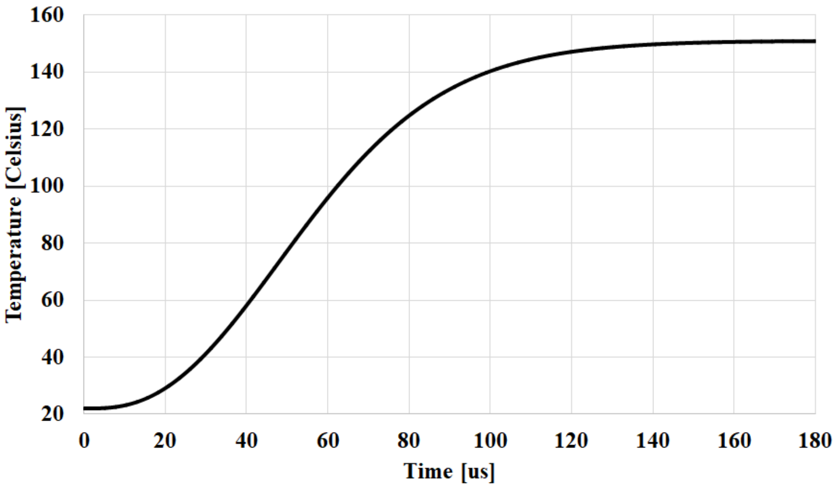

Fig. 3.38: Temperature rise in fixture during magnetisation process.

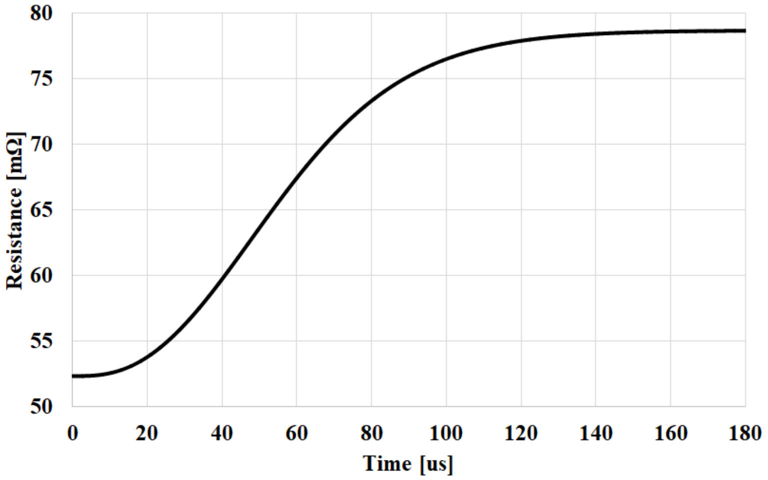

Fig. 3.39: Resistance variation in dual conductor double-sided fixture.

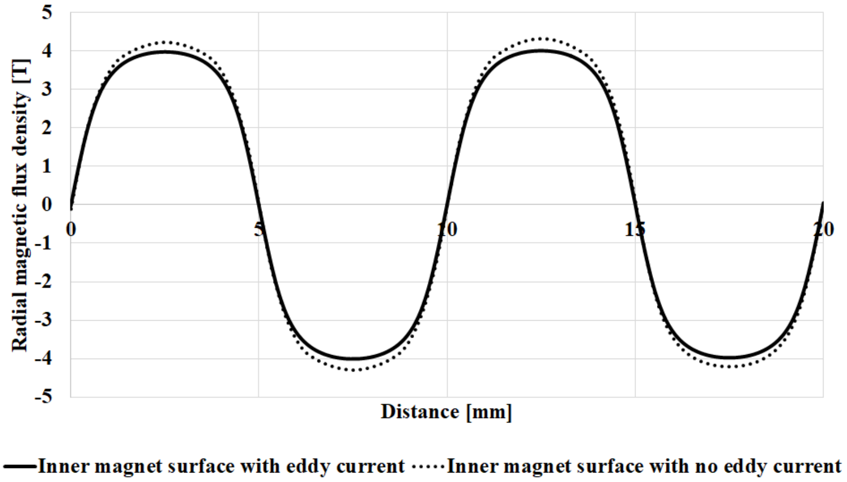

Fig. 3.40: Magnetic flux density waveform along the inner magnet surface.

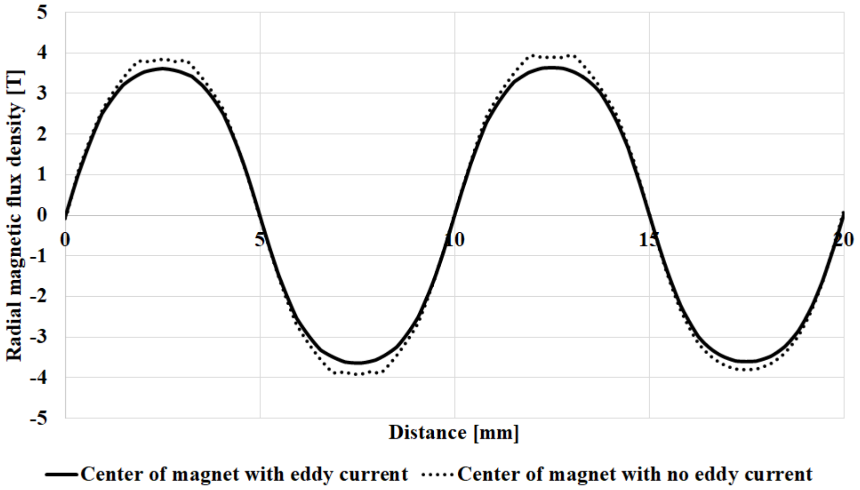

Fig. 3.41: Magnetic flux density waveform along the centre of magnet surface.

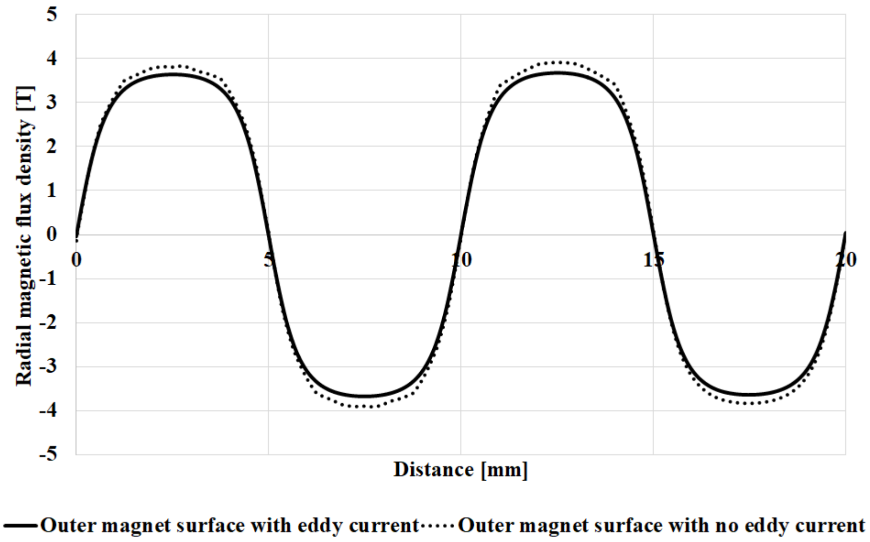

Fig. 3.42: Magnetic flux density waveform along the outer magnet surface.

3.5.3 Quad conductor magnetising fixture

With the same manner taken previously for parameters calculation, the highest magnetic flux density on the surface of the magnet is achieved from four conductors double-sided fixture even under the effect of induced eddy currents. The maximum value of the magnetic flux density is 4.25 T on the inner surface of the magnet, 3.74 T on the mid-surface, and 3.84 T on the outer surface of the magnet as shown in Fig. 3.43, 44 and 45 respectively. The direction of magnetisation and the distribution of magnetic field density can be shown in Fig. 3.46, as shown in the figure, the distribution of the magnetic flux density over the cross-section area of the magnet is much better than the previous coil configurations either in single or double sided fixtures. So, the double-sided fixture has a better effect than single sided fixture regarding the radial component of magnetic flux density especially on the outer surface of the magnet due to the presence of the outer winding. Also, about energy saving, the double-sided fixture can reach the required magnetic flux density without an unwanted excess of energy to magnetise the outer surface of the magnet as in the case of the single-sided fixture.

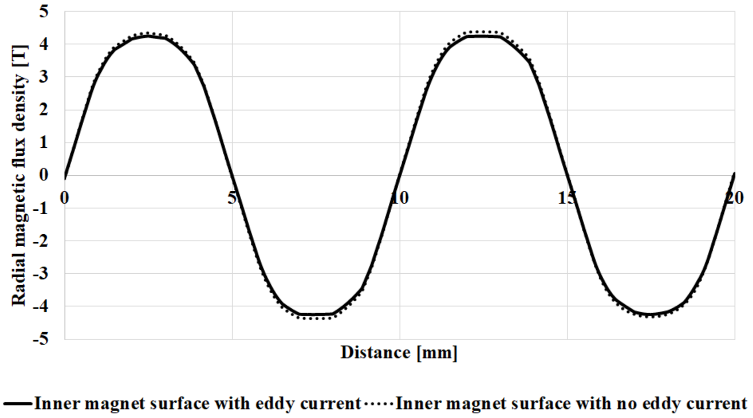

Fig. 3.43: Magnetic flux density waveform along the inner magnet surface.

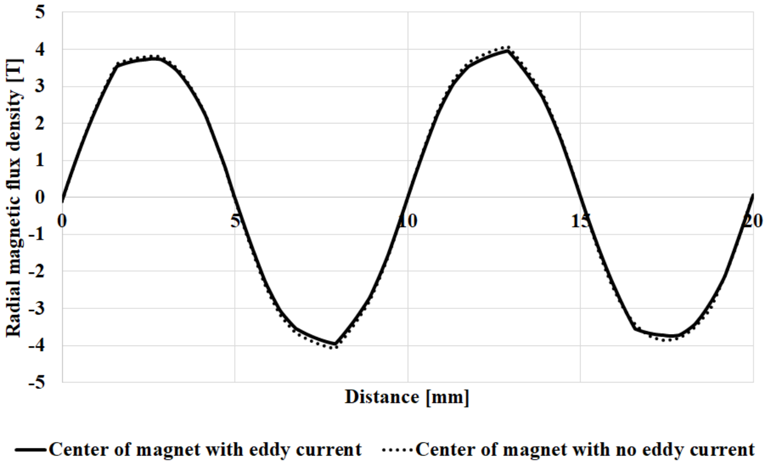

Fig. 3.44: Magnetic flux density waveform along the centre of magnet surface.

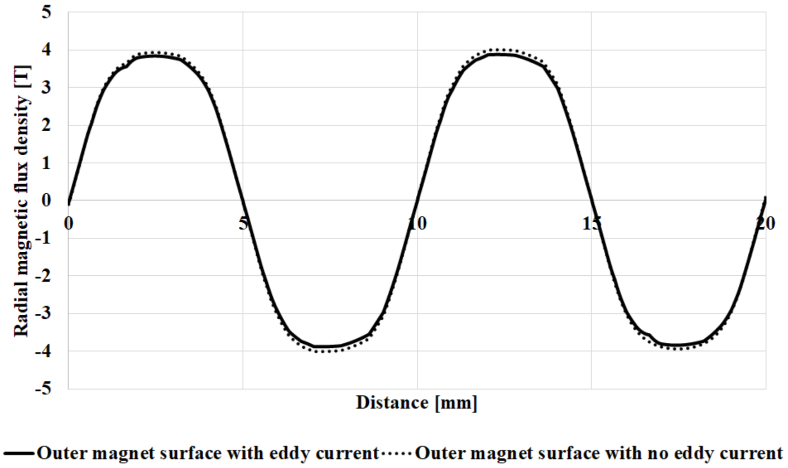

Fig. 3.45: Magnetic flux density waveform along the outer magnet surface.

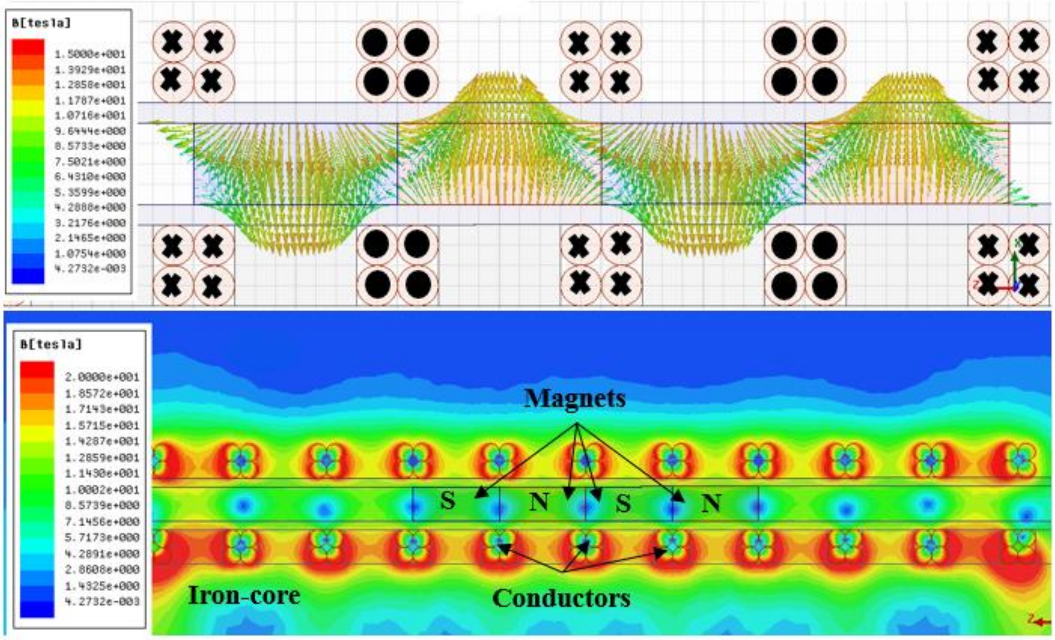

Fig. 3.46: Direction of magnetisation and field distribution for quad conductor double-sided fixture.

Regarding temperature rise, the double-sided fixture has lower temperature rise than single sided fixture where the mass of conductors is increased. More domains alignments are achieved with double-sided fixture than single sided one. For the aforementioned reasons, the double-sided fixture is preferred to be used than single sided fixture as also mentioned before in [55, 83].

3.6 Assessment of benefits of iron core

The fixtures considered up to this point have been based on an inner iron-core. In order to assess the benefits of this iron-core a further fixture is modelled in which the inner iron-core is replaced with a non-magnetic material. The inner mild steel iron-core is replaced by air during simulation as shown in Fig. 3.47. In this case, the value of inductance shows no change with the current pulse during the magnetisation process, as shown in Fig. 3.48, hence, the iron-cored fixture is the cause of inductance non-linearity. Accordingly, the differences between current pulses in SIMULINK and MAXWELL, for different coil configurations, became lower as shown in Fig. 3.49, 50 and 51 respectively. Iron-cored fixtures show higher values for the magnetic flux density at the inner surface of the magnet for single, double, and quad conductor double sided fixture as shown in Fig. 3.52, 53 and 54 respectively. Also, the magnetic flux density on the mid surface of the magnet is slightly higher in the case of iron cored fixtures as shown in Fig. 3.55, 56 and 57.

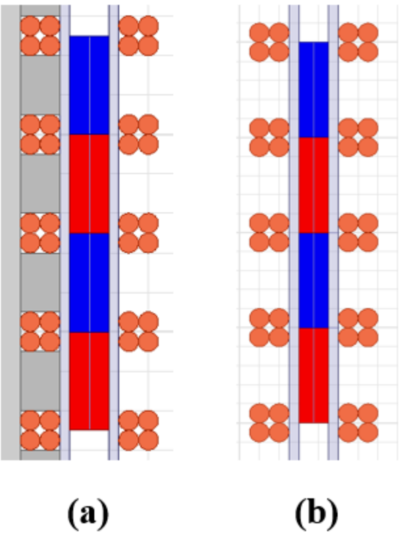

Fig. 3.47: Quad conductor double-sided fixture (a) iron-cored, (b) air-cored.

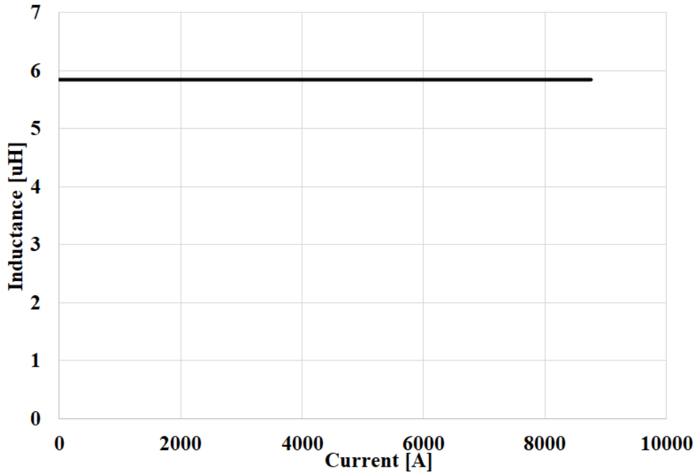

Fig. 3.48: Inductance variation with current for air-cored four conductors double-sided fixture.

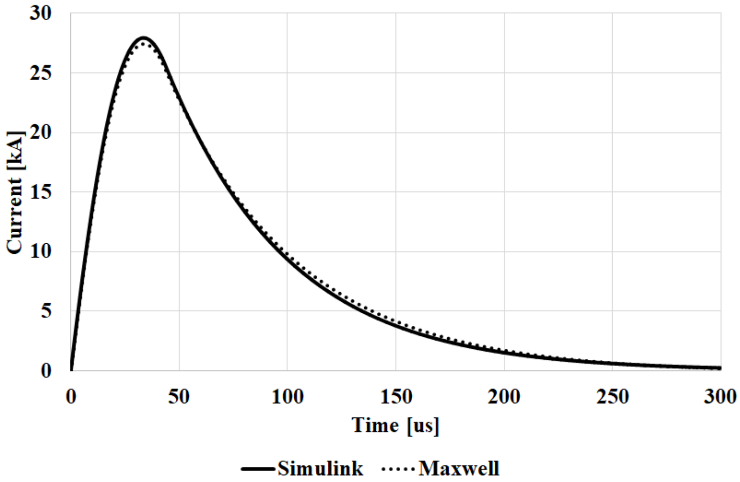

Fig. 3.49: Magnetising current pulse of single conductor air-cored double-sided fixture.

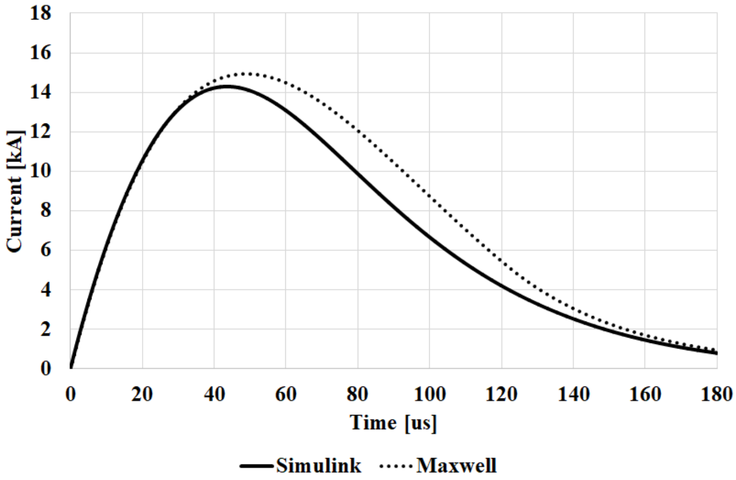

Fig. 3.50: Magnetising current pulse of dual conductor air-cored double-sided fixture.

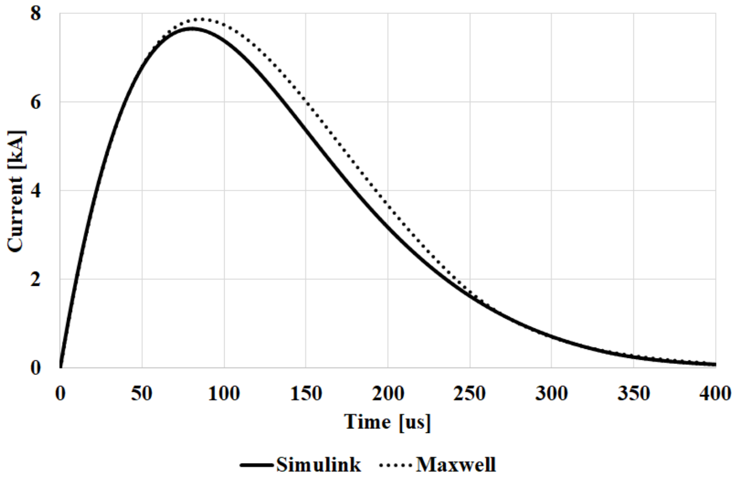

Fig. 3.51: Magnetising current pulse of quad conductor air-cored double-sided fixture.

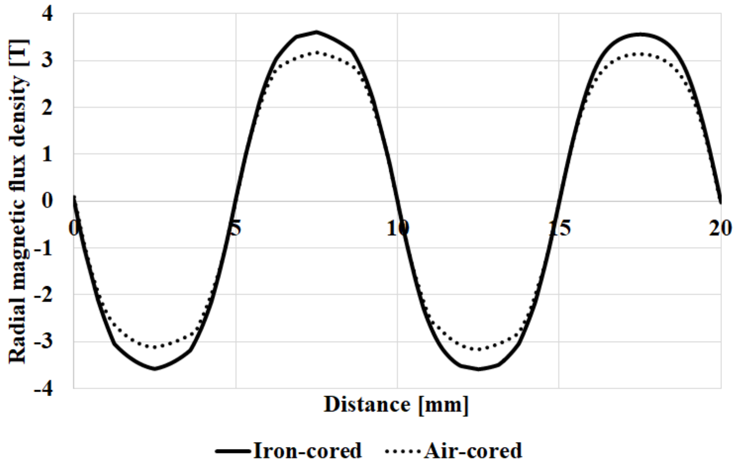

Fig. 3.52: Inner magnet surface for single conductor double-sided fixture.

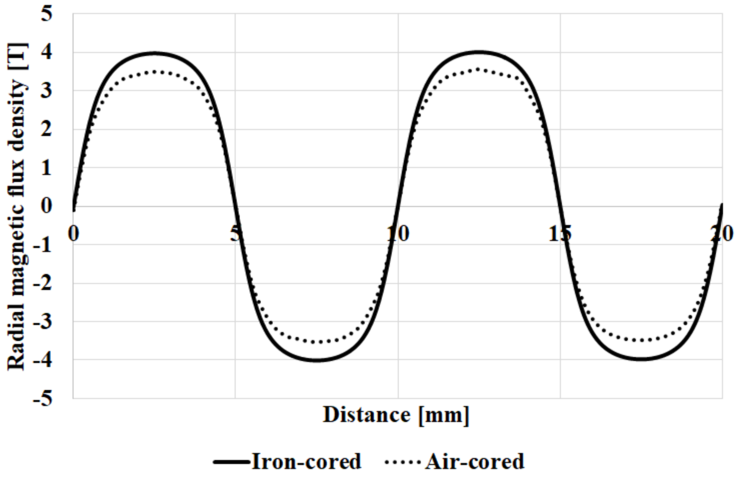

Fig. 3.53: Inner magnet surface for double conductor double-sided fixture.

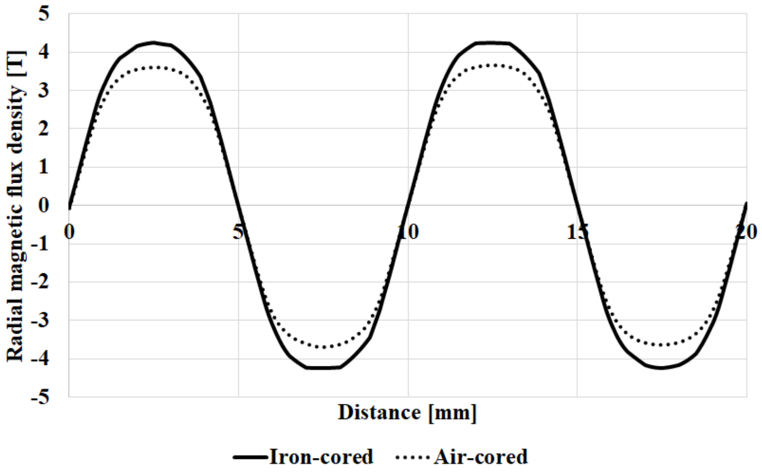

Fig. 3.54: Inner magnet surface for quad conductor double-sided fixture.

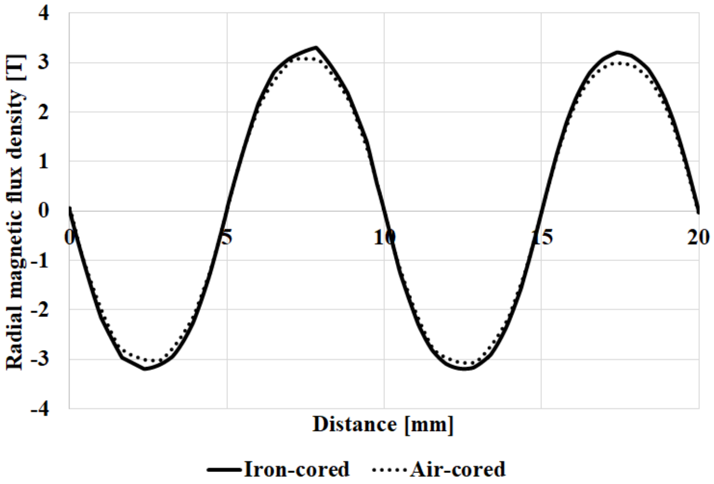

Fig. 3.55: Centre of magnet surface for single conductor double-sided fixture.

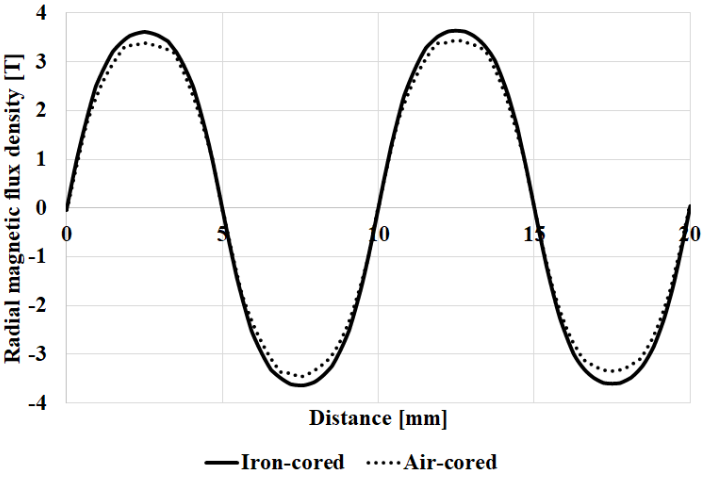

Fig. 3.56: Centre of magnet surface for double conductor double-sided fixture.

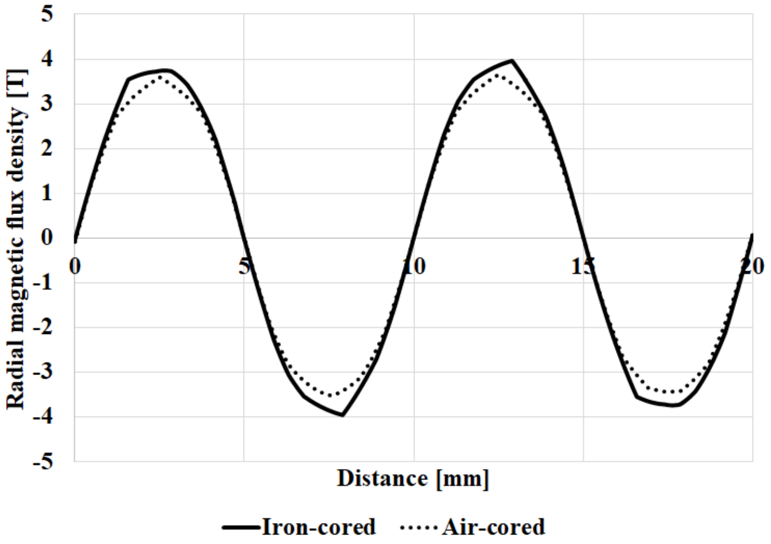

Fig. 3.57: Centre of magnet surface for quad conductor double-sided fixture.

Very small differences are detected for the magnetic flux density on the outer surface of the magnet for both iron and air cored fixtures as the outer coil is wound around non-magnetic, non-conductive outer core as shown in Fig. 3.58, 59 and 60 respectively. So, according to the values of the radial component of magnetic flux density, the iron-cored double sided fixture is recommended for enhancement of magnetisation process.

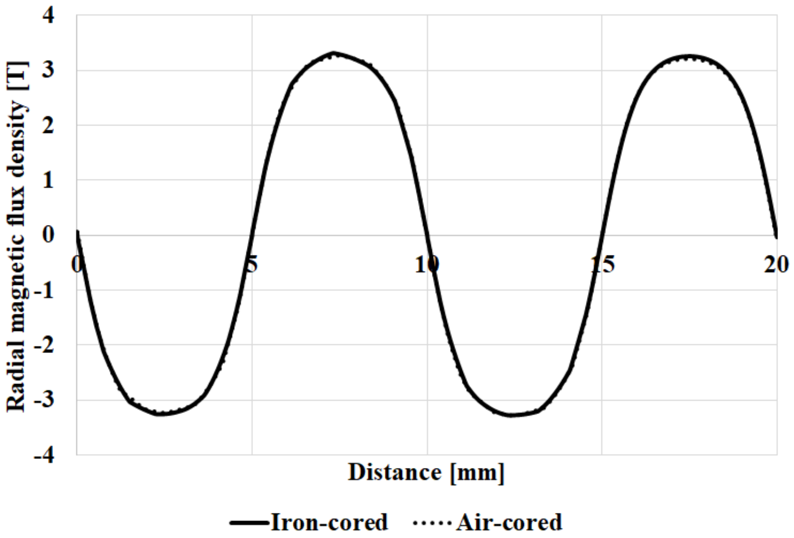

Fig. 3.58: Outer magnet surface for single conductor double-sided fixture.

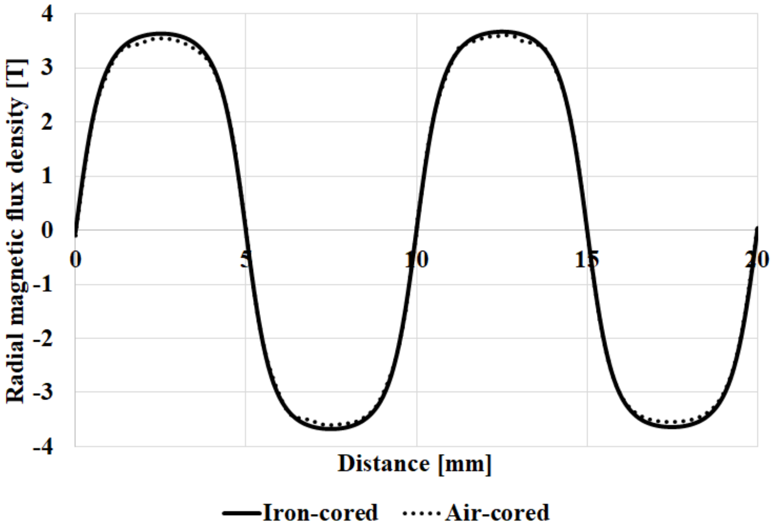

Fig. 3.59: Outer magnet surface for double conductor double-sided fixture.

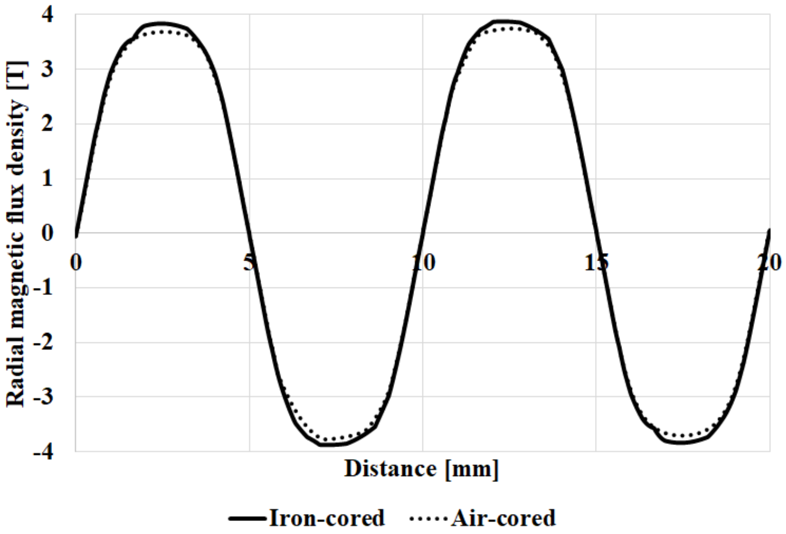

Fig. 3.60: Outer magnet surface for quad conductor double-sided fixture.

3.7 Conclusion

This chapter presented a novel method for manufacturing a multipole helical magnet array. The magnetisation process is carried out assuming usage of a capacitor discharge magnetiser. Different winding groups and different fixtures are discussed. For each winding group and each fixture, the dynamic behaviour of the magnetisation process is presented and the effect of temperature rise and resistance change is modeled so that the risk of fixture’s failure is minimal. The effect of iron-core on the generated magnetising field is also presented and the effect of the eddy current on the magnetising field is discussed. Results show that, the double sided fixture can provide better magnetising field on the outer surface of the magnet than a single sided one. In addition, the double sided fixture can save more energy wasted on magnetising a magnet using a single sided fixture.

4 Losses and Efficiency for MLS

4.1 Introduction

Losses are the issue that determines the efficiency of a system. They are dissipated in an undesired form as thermal energy which results in lower performance and increased risk of over-heating. For an electric machine, the losses can be divided into two main parts: mechanical and electromagnetic loss [87, 88]. Mechanical loss can be in the form of friction due to physical contact between parts and aerodynamic drag or windage which can be significant in high speed machines. Electromagnetic losses can be divided into two main parts: copper, and iron loss, which mainly depends on magnet and core eddy current loss for the proposed MLS. Copper loss is due to the flow of current in the conductors of the windings, and it is proportional to the square of electric current and is highly dependent on the temperature [88]. Thus, increasing the cross sectional area of the conductor will have a significant effect in reducing the copper loss but at the expense of mass/size of the device. Iron loss, in laminated structures consists of hysteresis and eddy current loss [89]. The eddy current loss consists of a classical component which assumes a homogeneous lamination material, and the excess eddy current component. A model for the prediction of the excess parameter is presented in Bertotti's model [89, 90]. So, the iron loss can be represented by the modified Steinmetz equation which is composed of hysteresis, eddy current and excess (anomalous) loss as follows [88, 90-95]:

$$P_{Fe} = P_h + P_e + P_a$$
$$P_{Fe} = k_h f B^2 + k_e f^2 B^2 + k_a f^{1.5} B^{1.5}$$

where P_{Fe} is the iron or core loss. P_h , P_e and P_a are hysteresis, classical eddy current and anomalous loss respectively. f is the frequency, B is the magnitude of magnetic flux density, k_h, k_e and k_a are the hysteresis, eddy current and anomalous loss coefficient respectively.

Hysteresis loss is generated by the domain wall motion as the domain moves under the effect of an external magnetic field. The energy required to move the magnetic domains in the magnetic material is the hysteresis loss [96]. Eddy current loss is generated due to the variation of the magnetic field applied on a conductive material which induces eddy current [88, 97]. For permanent magnet machines, eddy current loss can lead to excessive temperatures, which result in irreversible demagnetization of magnets and hence, causing a decrease in performance and efficiency of the machine [88, 92, 98-100].

In permanent magnet machines, eddy current loss can be minimized either by magnet segmentation [100-103] or stator lamination [97] or by using high resistivity magnets [87]. However, the highly conductive magnets, e.g rare-earth PM, can produce lower eddy current loss if the magnet's motion is synchronized with the stator winding magnetic field [99, 103]. Also, highly resistive magnets, e.g ferrite magnets, have lower remanence.

For the MLS in our study, the screw and the nut are made of solid mild steel, and conductive permanent magnets, thus, eddy current loss would be dominant and the prediction of these losses is necessary to predict the MLS efficiency.

In this chapter, a commercial 3D time stepping finite element package, JMAG 3D, is utilized to study the eddy current loss generated in the magnets mounted on the nut and the screw of the MLS and the mild steel these are mounted on. Transient JMAG 3D model is chosen for simulations to generate the real steady state motion of the MLS where the screw is rotating and the nut is under linear motion, or vice versa, at the same time. The steady state motion couldn't be simulated using MAXWLL 3D, either rotation or translation motion is simulated at a time. The angular velocity of the rotation is set to be equivalent to the linear motion applied on the nut that varies from 1 to 8 m/s. Time steps of the simulation were varied according to the velocity. The main concern of this study is to analyse the induced eddy currents in PMs, screw core and the back-iron of the nut. Conductivity of mild steel and PM was set by the software. The mild steel of the MLS is presented with corresponding B-H curve as shown previously in Fig. 3.5. The N45SH grade Nd-Fe-B PMs are described with their magnetic and electric characteristics [86].

4.2 Losses of MLS

In this section, losses are calculated for magnet-to-magnet and magnet-to-reluctance type MLS utilising the 3D finite element software “JMAG”. As mentioned before, losses are calculated given the conductivity of the PM and the mild steel of the screw core. Hysteresis and excess losses are neglected as the magnet and core eddy current loss would be dominant. For both types of MLS, losses are calculated at different load conditions of the nut to check the effect of variation of the load on these losses. Also, the effect of the glue between the mild steel and the magnets on the losses is investigated. Table 1 provides the dimensions of the magnet-to-magnet and magnet-to-reluctance models and the parameters of the materials used.

Table 4.1: Dimensions and parameters for magnet-to-magnet and magnet-to-reluctance type MLS models.

Common dimensions	
Inner radius of screw	0 mm (i.e. solid core)
Nut back-iron thickness	4 mm
Air-gap	1 mm
Nut magnet thickness	1.5 mm
Pole-pitch	5 mm
Nut magnet pole-pairs	4
Screw length	100 mm
Magnet-to-magnet type MLS	
Screw back-iron radius	5.5 mm
Screw magnet thickness	1.5 mm
Magnet-to-reluctance type MLS	
Screw iron thread depth	3 mm
Screw iron thread width	1 mm
Screw back-iron radius	4 mm
Material properties	
Magnet type	N45SH
Remanence	1.32 T
Coercivity	979 kA/m
Magnet density	7500 kg/m^3
Magnet resistivity	180 μΩ.cm
Mild steel density	7860 kg/m^3
Mild steel conductivity	6289308 S/m

For parameters mentioned in Table 4.1, losses are calculated in permeant magnet, screw core, and back-iron of the nut (translator). Results are recorded at the steady state condition of the MLS, after the screw has rotated one complete rotation and the nut is moved one complete lead (10 mm) as shown in Fig. 4.1 and losses are calculated at various velocities varied from 1 m/s to 8 m/s in steps of 1 m/s.

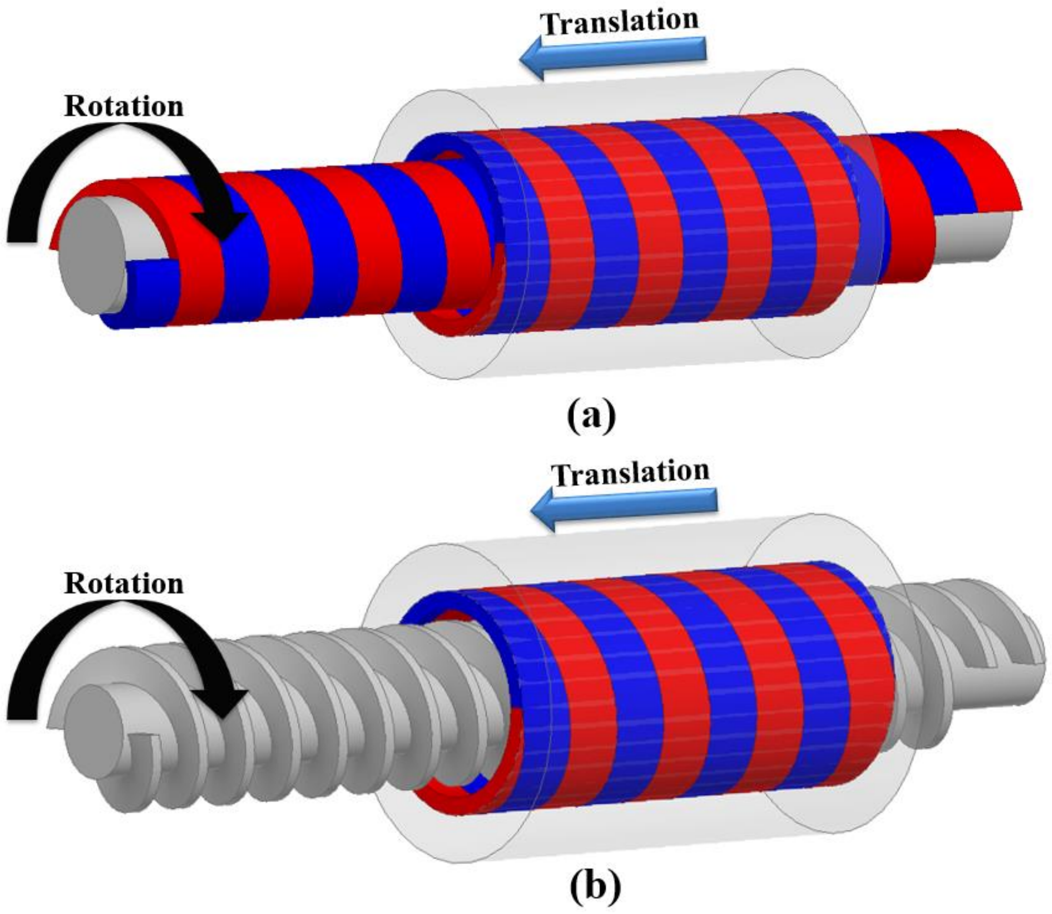

Fig. 4.1: Steady state motion for (a) magnet-to-magnet, (b) magnet-to-reluctance type MLS.

4.3 Magnet-to-magnet type MLS

Initially, for the magnet-to-magnet type MLS, the magnet is assumed to be in direct contact with the mild steel without any insulation. The average steady state loss is calculated at various velocities ranging from 1 m/s to 8 m/s for the nut, screw, magnets and also total loss. To apply the steady state condition, the linear velocity of the translator is inserted in JMAG with the equivalent rotational angular speed of the screw. For each velocity, the average steady state loss for the model is recorded. Furthermore, a 0.1 mm insulating glue line is inserted between the magnets and the mild steel. The effect of the glue line on the nut, magnets, screw, and total loss is shown in Fig. 4.2 to Fig. 4.5.

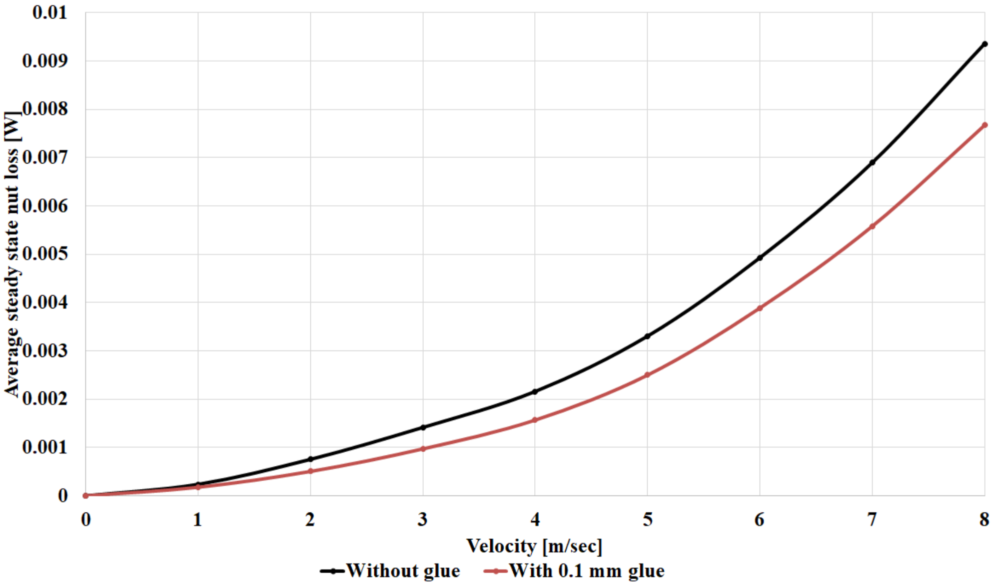

Fig. 4.2: Variation of average steady state nut loss for magnet-to-magnet type MLS with linear velocity.

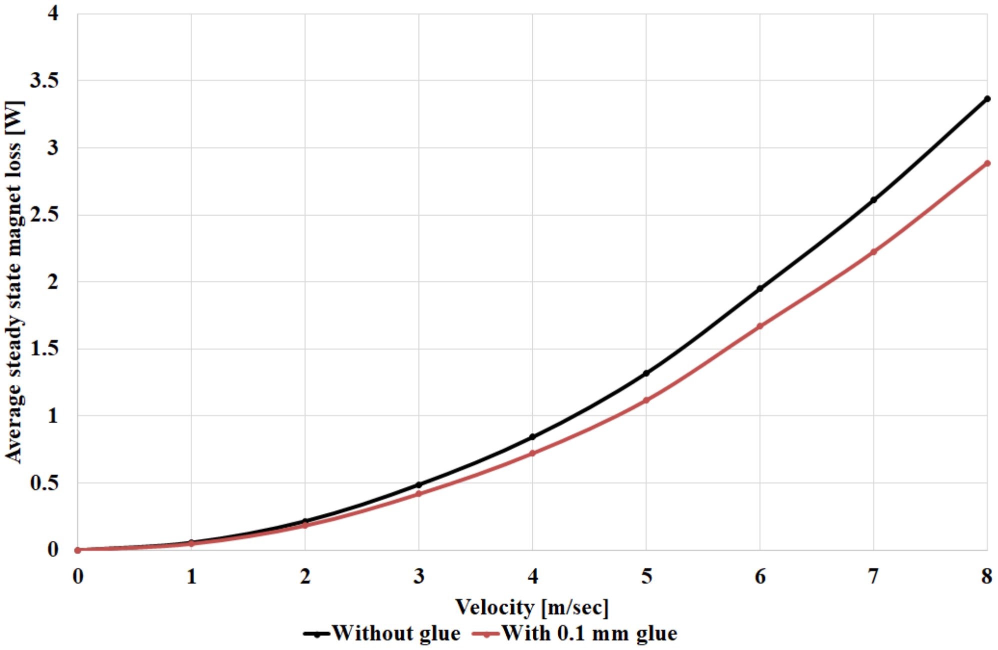

Fig. 4.3: Variation of average steady state magnet loss for magnet-to-magnet type MLS with linear velocity.

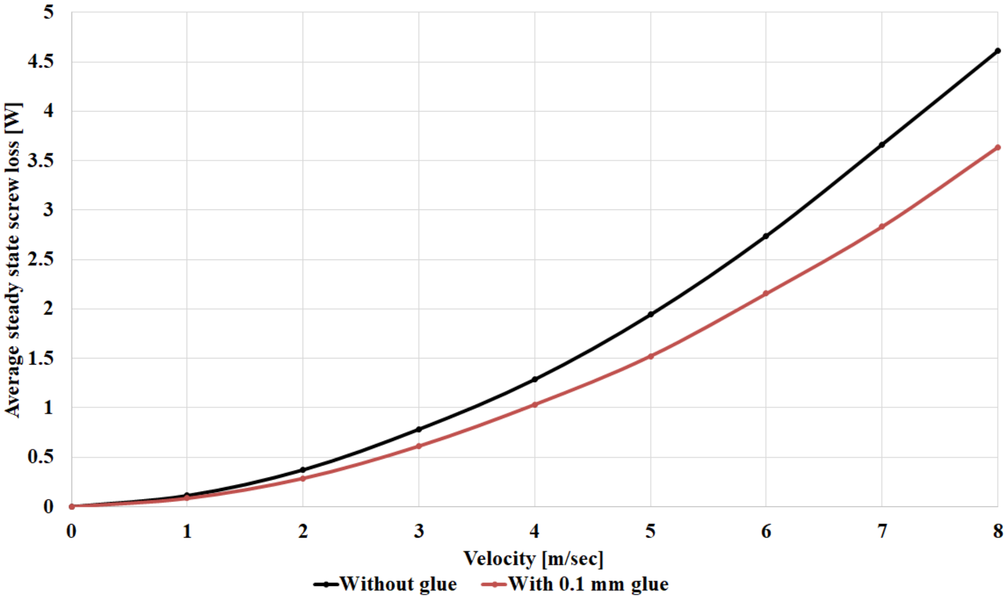

Fig. 4.4: Variation of average steady state screw loss for magnet-to-magnet type MLS with linear velocity.

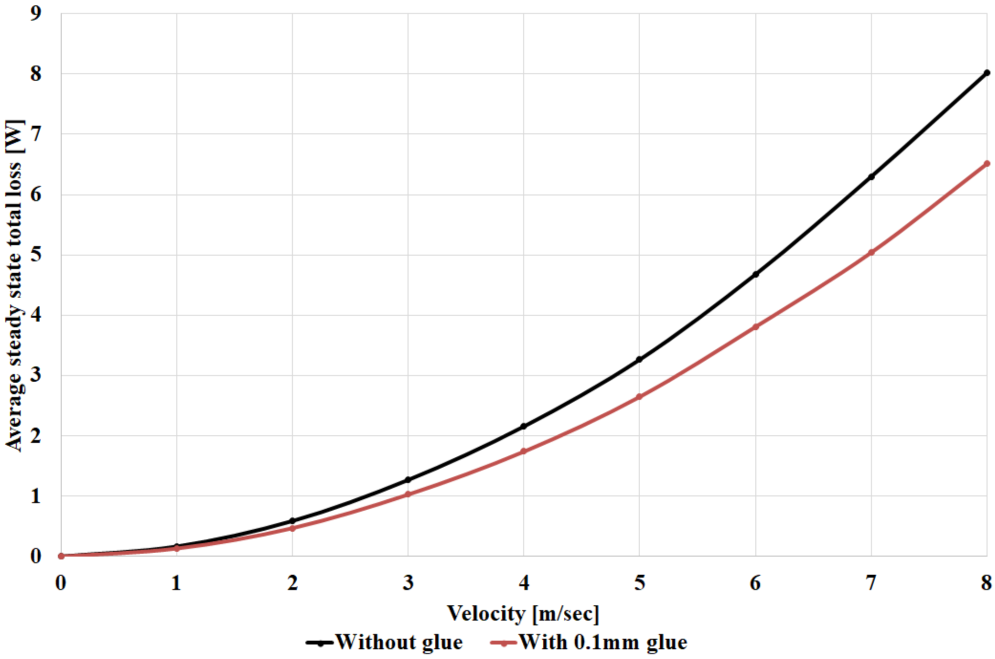

Fig. 4.5: Variation of average steady state total loss for magnet-to-magnet type MLS with linear velocity.

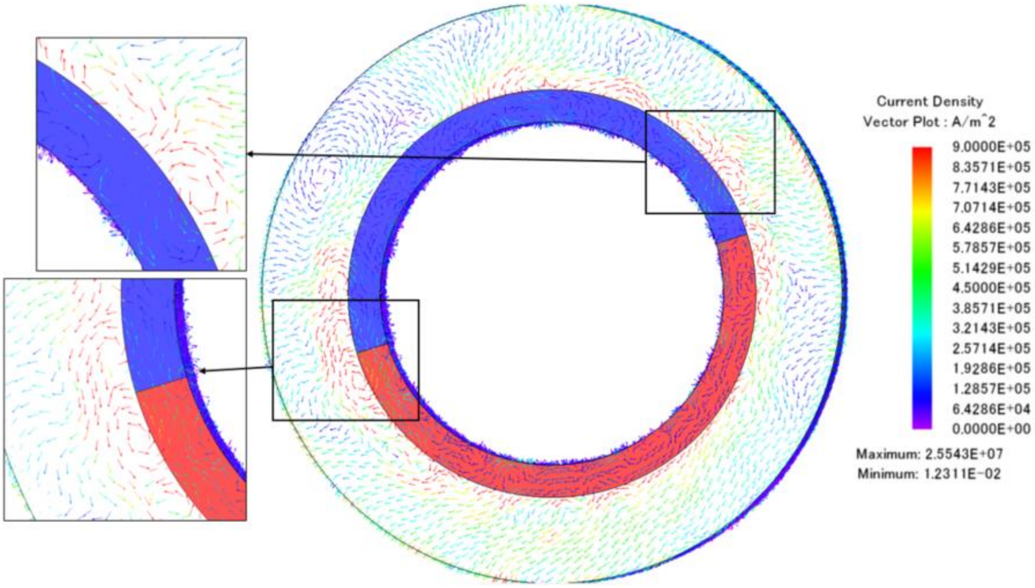

Fig. 4.6: Eddy current path between magnets and outer nut in the absence of the glue.

As shown in Fig. 4.2 to Fig. 4.5, the average steady state loss for magnet-to-magnet type MLS with 0.1 mm insulating glue thickness is lower than that without glue. The reason for the drop in the average steady state loss is due to the interruption to the eddy current path caused by the presence of the glue insulation gap between the magnets and the mild steel. Fig. 4.6 shows a smooth flow of eddy current between the magnet and the outer nut in the absence of the glue. However, the effect of the glue on the eddy current path is shown in Fig. 4.7. The 0.1 mm insulating glue thickness is simulated as an air-gap in JMAG model. This small gap affects the path of the eddy current and hence, the reduction in the average steady state total loss for the magnet-to-magnet type MLS.

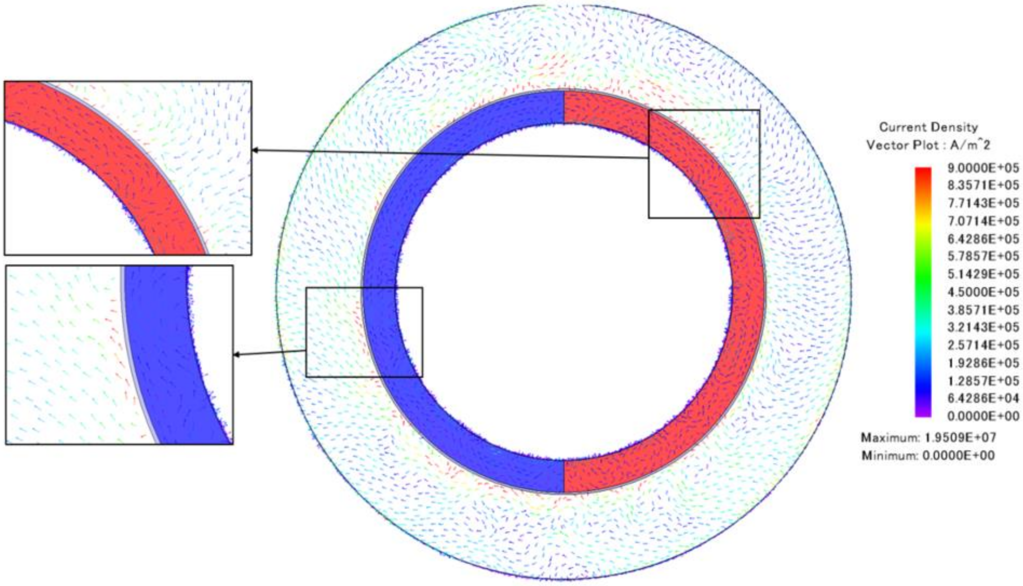

Fig. 4.7: Eddy current path between magnet and outer nut in the presence of the glue.

Also, for the inner screw, by inserting the 0.1 mm insulating glue thickness between the magnet and the mild steel, the eddy current path is affected and hence, the average steady state total loss is reduced. The flow of eddy current between the magnet and the inner screw in the absence of the glue can be shown in Fig. 4.8. On the other hand the interruption of eddy current can be seen in Fig. 4.9 as the 0.1 mm insulating glue thickness acts as an insulation gap.

]

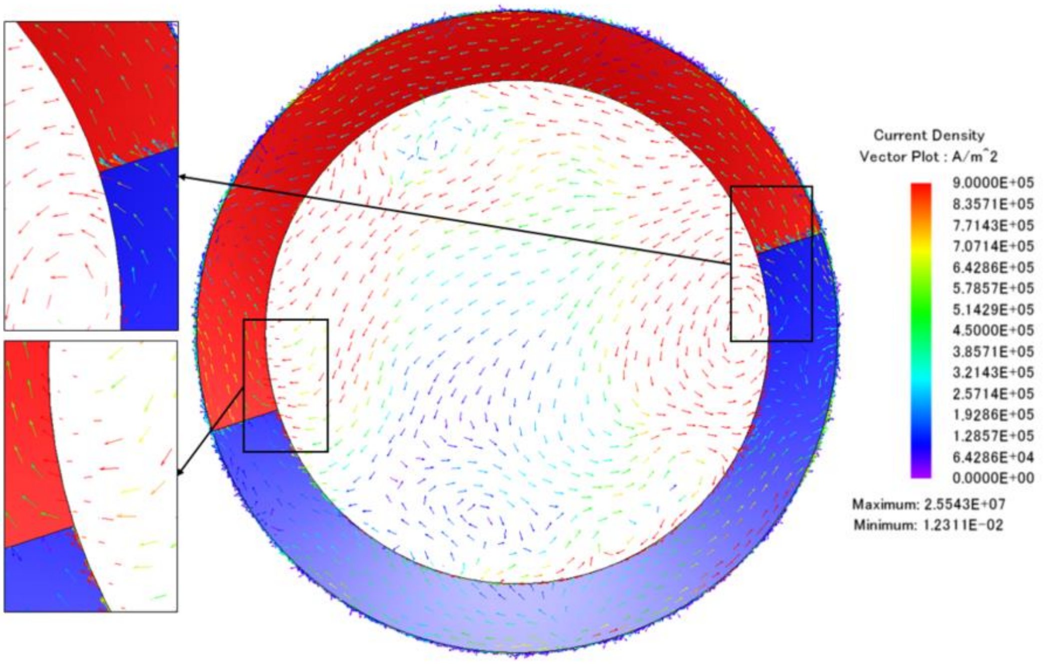

Fig. 4.8: Eddy current path between magnet and inner screw in the absence of the glue.

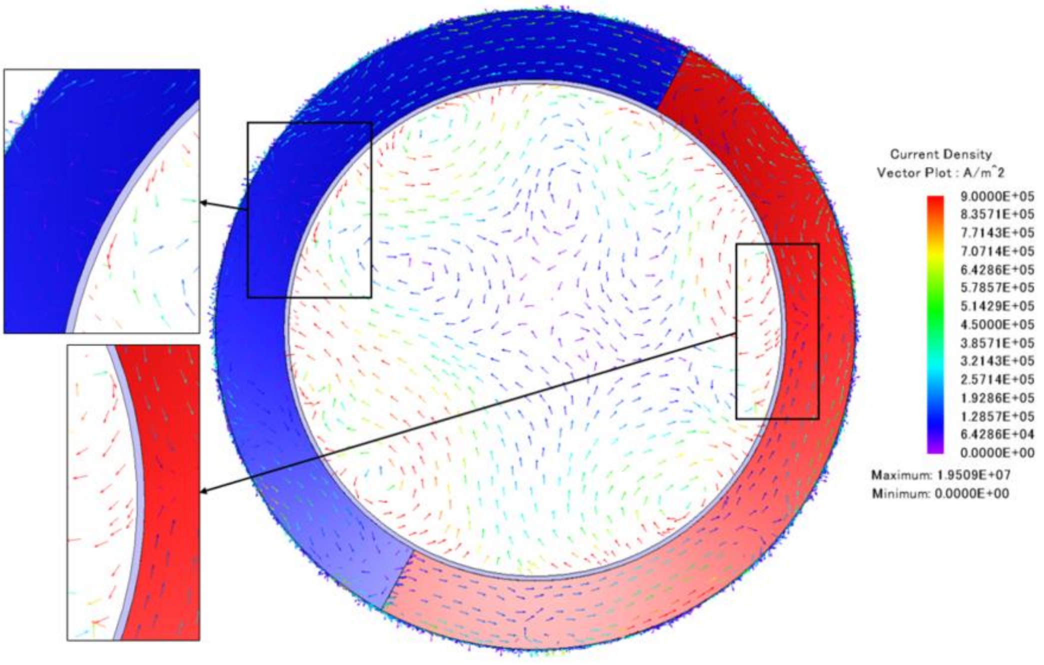

Fig. 4.9: Eddy current path between magnet and inner screw in the presence of the glue.

4.3.1 Effect of load condition

Previously, the simulations are carried out where the relative position of the screw and the nut is zero (i.e. they are in aligned position). This means that the magnet poles on the screw and the nut are totally facing each other, and no force/torque is produced. To see whether the initial position of the nut relative to the screw affects the losses, the initial position of the nut relative to the screw is moved by half pole-pitch such that the maximum force of the MLS is transmitted. Fig. 4.10 shows the thrust force of the magnet-to-magnet type MLS when the nut is moving and the screw is stationary. Fig. 4.11 shows the maximum thrust force achieved during the steady state motion where the steady state thrust force is the same thrust force at maximum position as confirmed by Fig. 4.10.

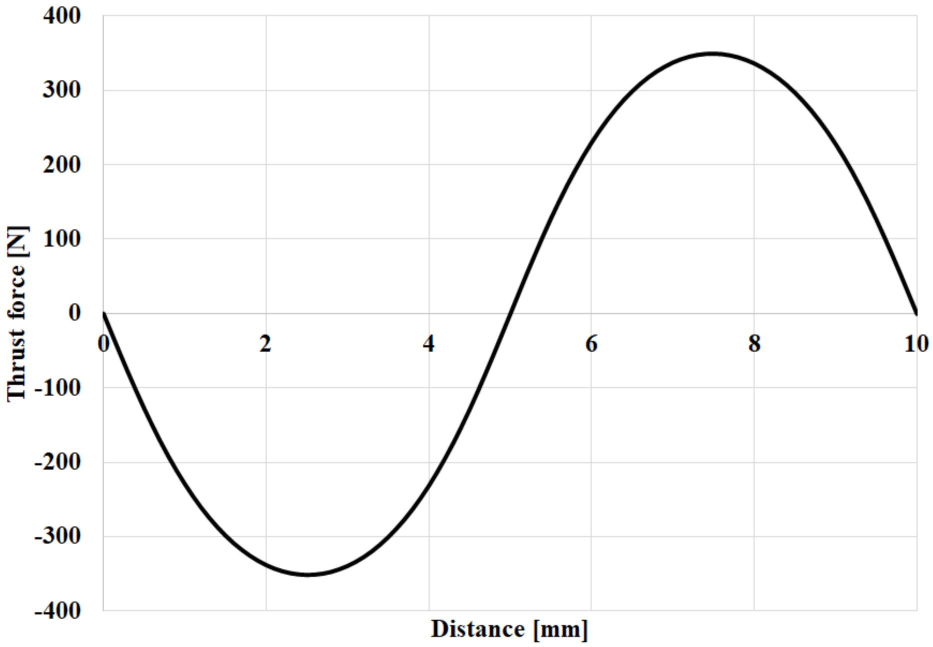

Fig. 4.10: Thrust force for magnet-to-magnet type MLS for one lead when the nut is moving and the screw is stationary.

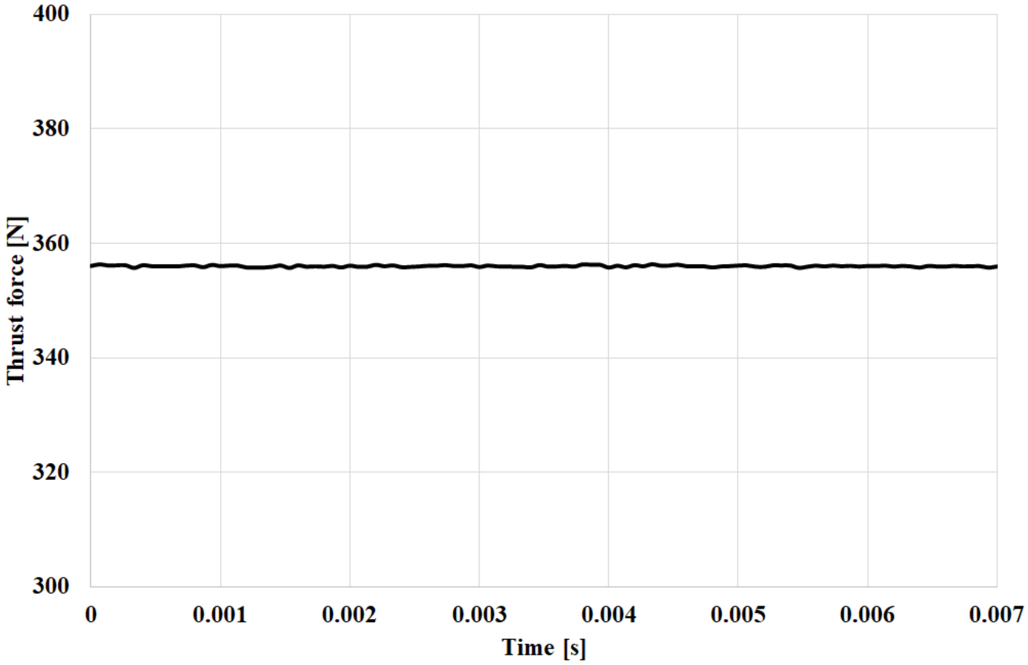

Fig. 4.11: Steady state thrust force for magnet-to-magnet type MLS when relative position between the nut and the screw is half pole-pitch.

Results confirmed that the losses of the magnet-to-magnet type MLS are load dependent and the losses are dominant in the screw and the magnets rather than the nut as shown in Fig. 4.12 to Fig. 4.15 .

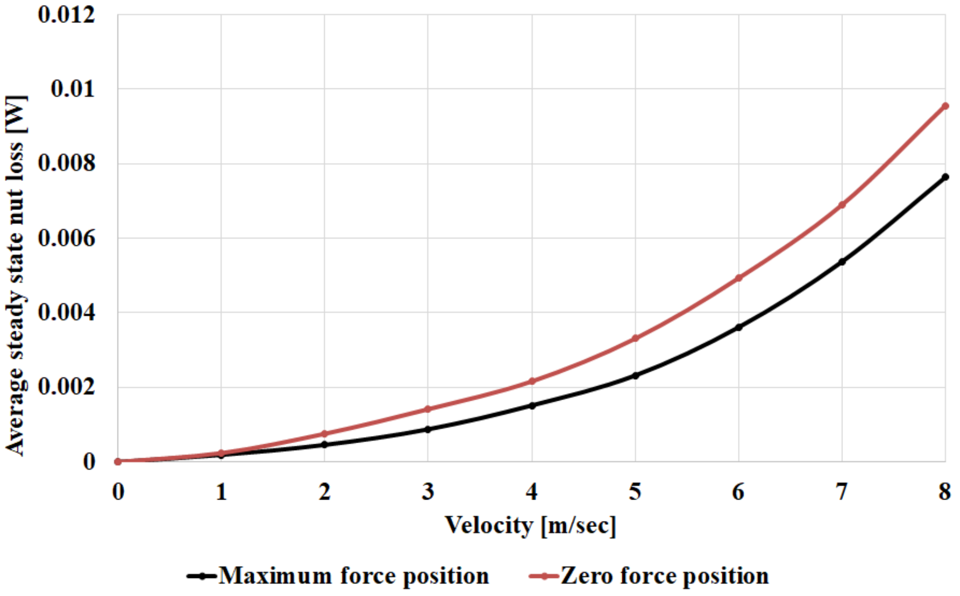

Fig. 4.12: Variation of average steady state nut loss for magnet-to-magnet type MLS with linear velocity at different load conditions.

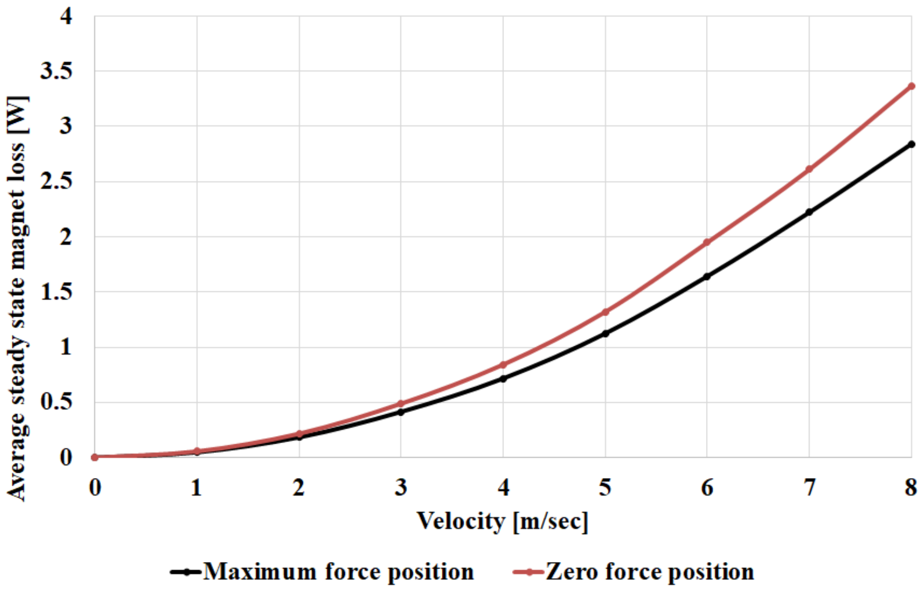

Fig. 4.13: Variation of average steady state magnet loss for magnet-to-magnet type MLS with linear velocity at different load conditions.

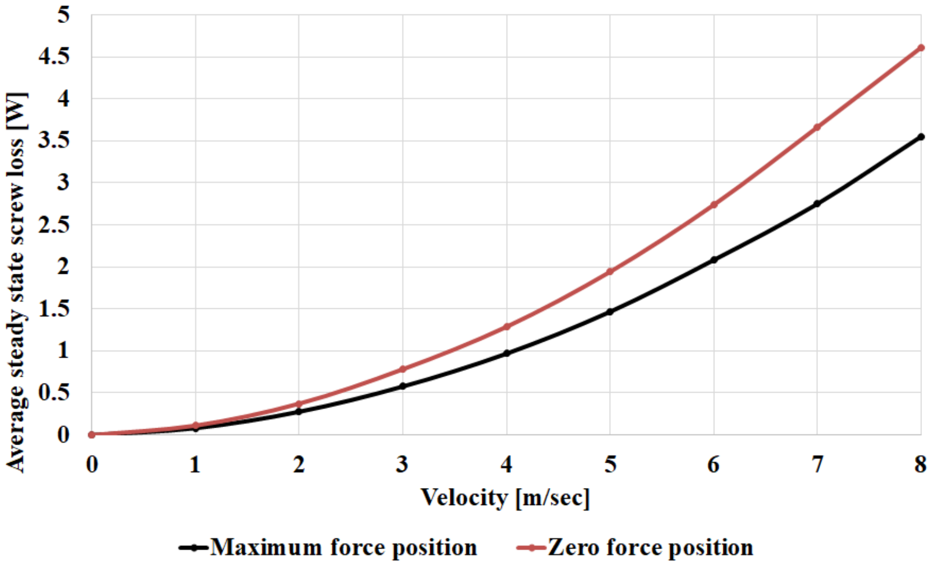

Fig. 4.14: Variation of average steady state screw loss for magnet-to-magnet type MLS with linear velocity at different load conditions.

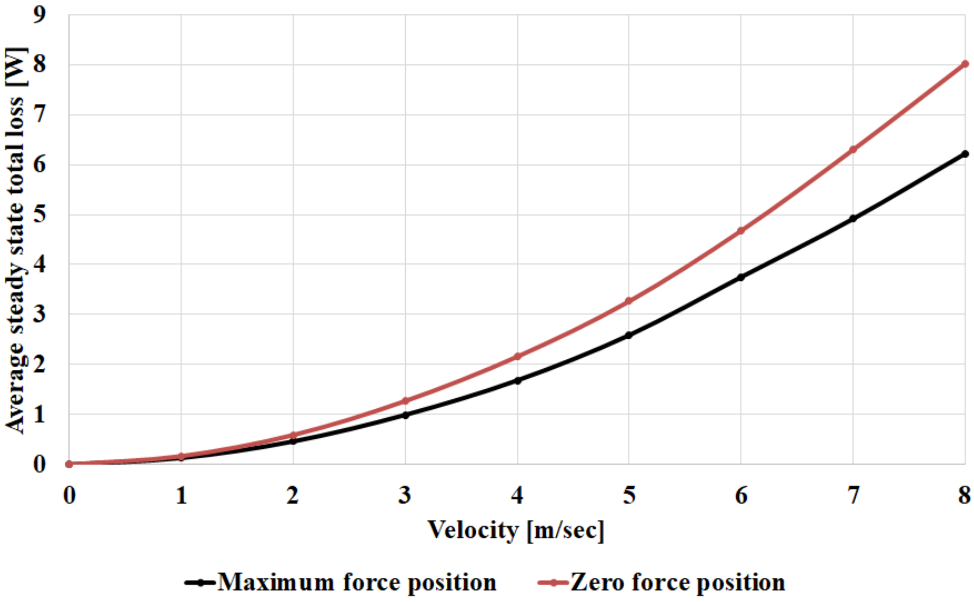

Fig. 4.15: Variation of average steady state total loss for magnet-to-magnet type MLS with linear velocity at different load conditions.

4.4 Magnet-to-reluctance type MLS

In this section, the effect of an insulating glue thickness on eddy current loss for magnet-to-reluctance type MLS is investigated. As for the magnet-to-magnet type MLS, firstly, the magnet is initially assumed to be in direct contact with the mild steel without any insulation. Similarly, the average steady state total loss is calculated at various velocities ranging from 1 m/s to 8 m/s with 1 m/s increment for each step both with and without a glue layer. The effect of glue insulation gap on the losses of the nut, the magnets, the screw, and total loss can be shown in Fig. 4.16 to Fig. 4.19. The main losses are generated in the screw as losses in the nut and the magnets are in negligibly small.

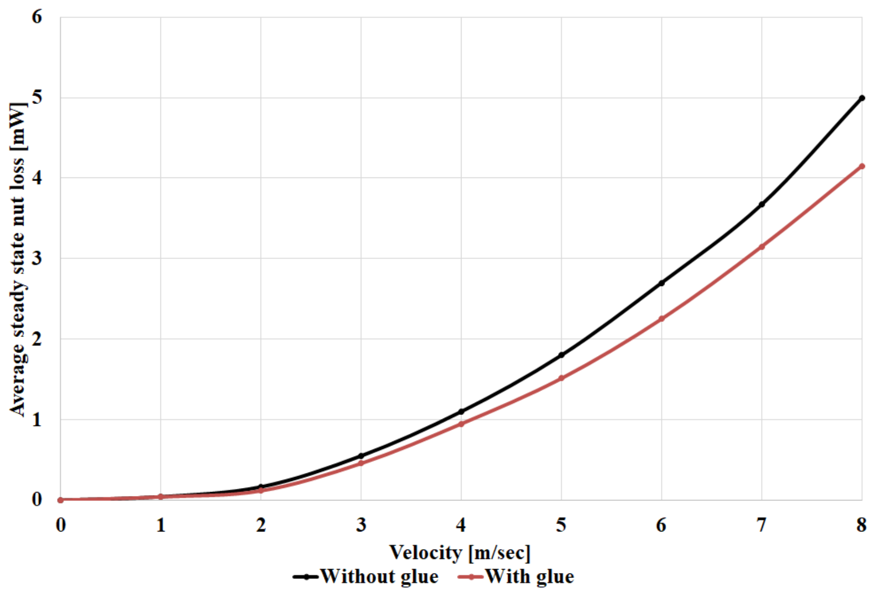

Fig. 4.16: Variation of average steady state nut loss for magnet-to-reluctance type MLS with linear velocity.

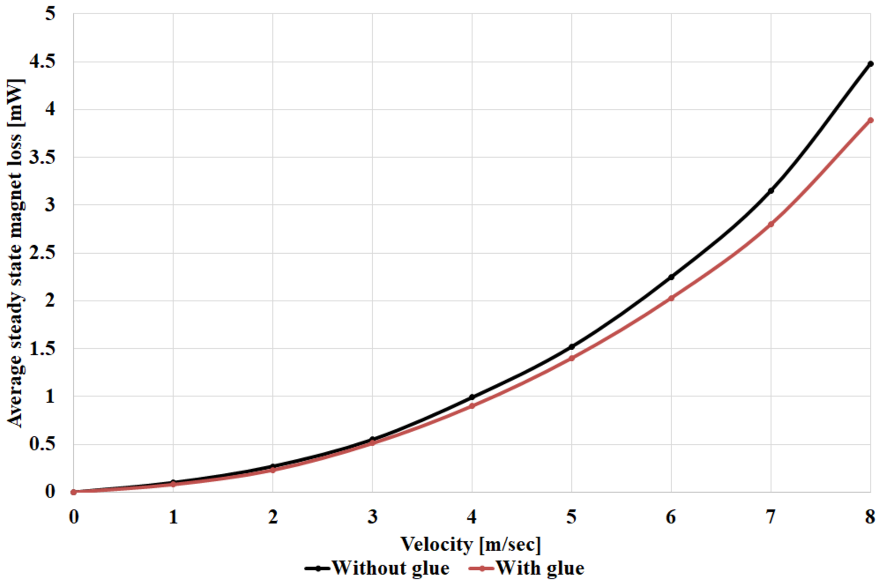

Fig. 4.17: Variation of average steady state magnet loss for magnet-to-reluctance type MLS with linear velocity.

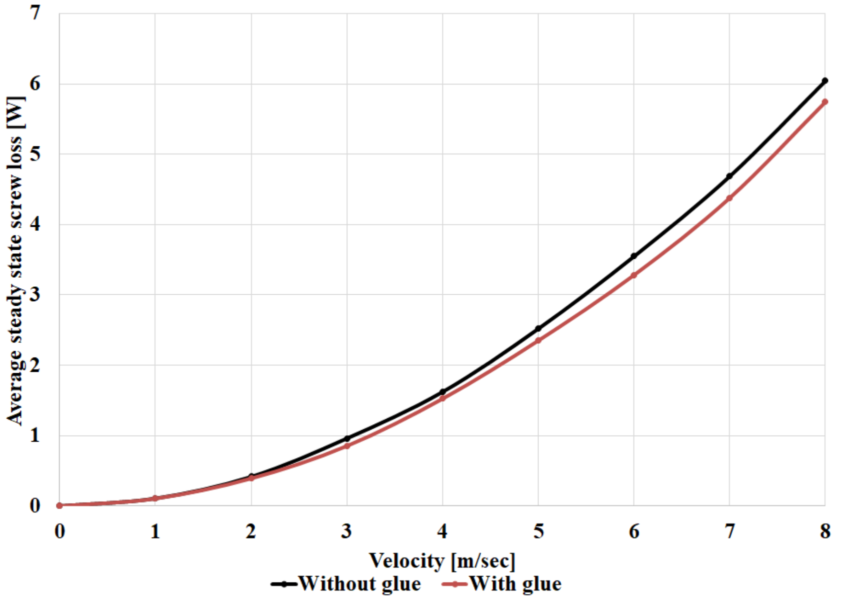

Fig. 4.18: Variation of average steady state screw loss for magnet-to-reluctance type MLS with linear velocity.

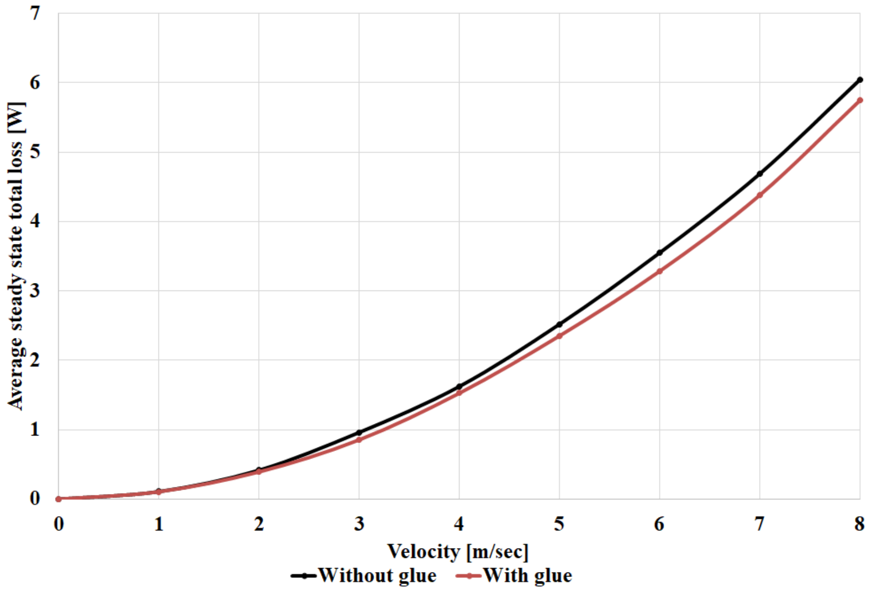

Fig. 4.19: Variation of average steady state total loss for magnet-to-reluctance type MLS with linear velocity.

4.4.1 Effect of load condition

Similarly to the magnet-to-magnet type MLS, initially, the simulations are carried out where the relative position of the screw and the nut is zero (i.e. they are in aligned position). The initial position of the nut relative to the screw is moved by quarter pole-pitch such that the maximum force of the MLS is achieved. Fig. 4.20 shows the thrust force of the magnet-to-reluctance type MLS when the nut is moving and the screw is stationary. Fig. 4.21 shows the maximum thrust force achieved during the steady state motion where the steady state thrust force is the same thrust force at maximum position as confirmed by Fig. 4.20. Results confirmed that the magnet-to-reluctance type MLS is also load dependent and the initial position of the nut relative to the screw affects the losses generated from the MLS as shown in Fig. 4.22 to Fig. 4.25.

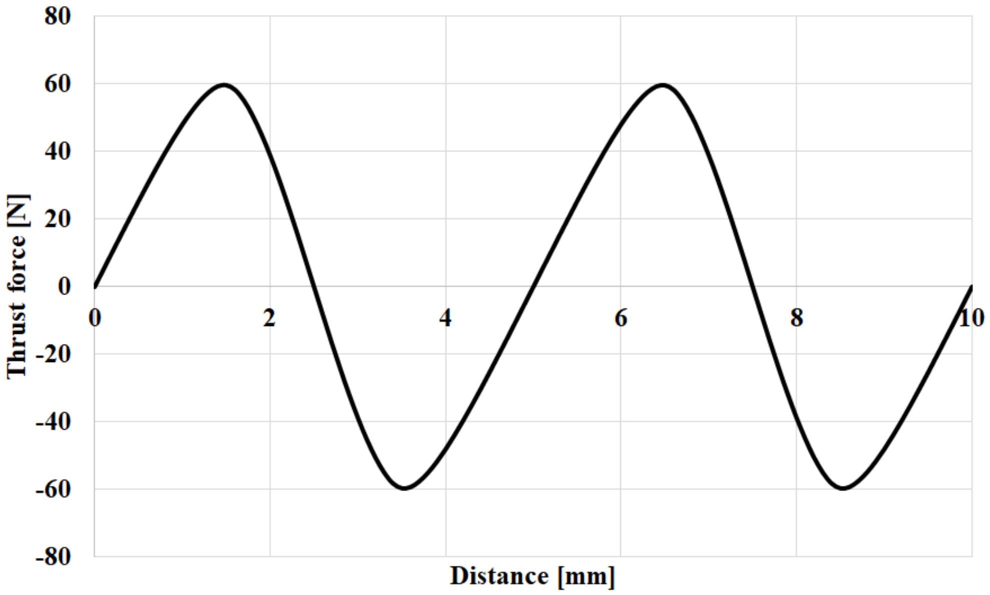

Fig. 4.20: Thrust force for magnet-to-reluctance type MLS for one lead when the nut is moving and the screw is stationary.

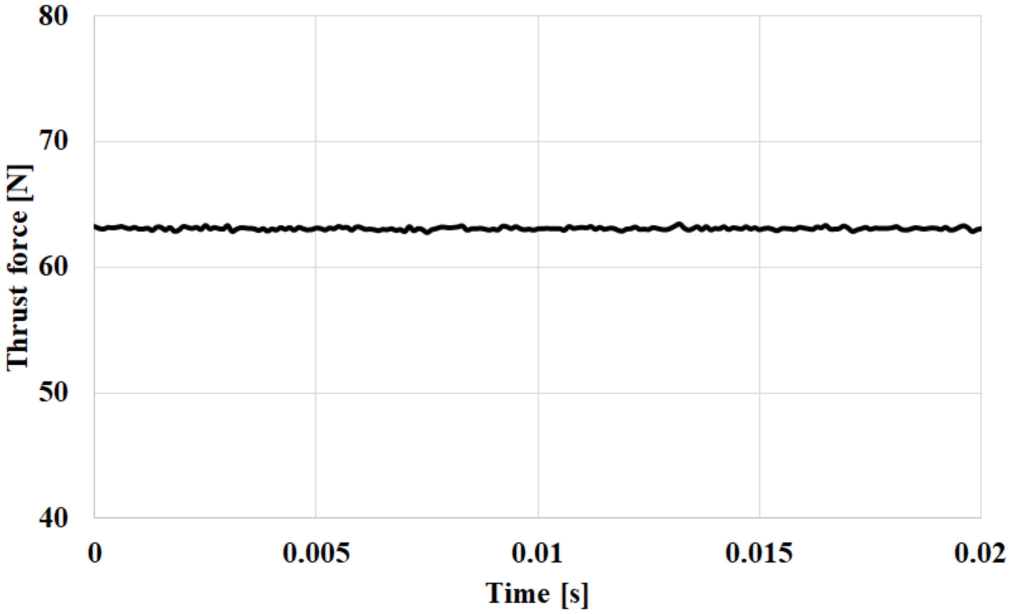

Fig. 4.21: Steady state thrust force for magnet-to-reluctance type MLS when relative position between the nut and the screw is quarter pole-pitch.

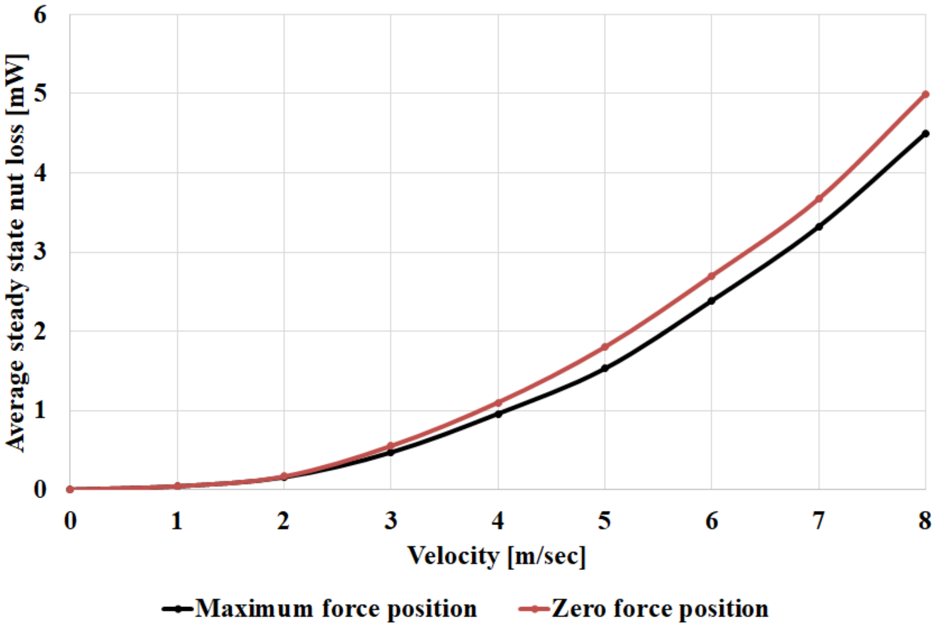

Fig. 4.22: Variation of average steady state nut loss for magnet-to-reluctance type MLS with linear velocity at different load conditions.

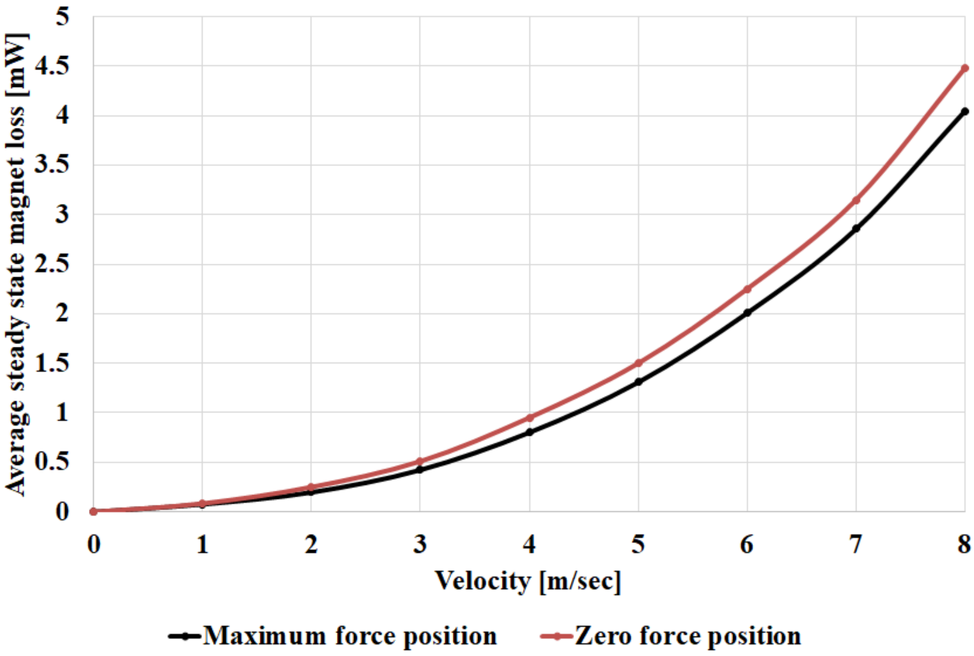

Fig. 4.23: Variation of average steady state magnet loss for magnet-to-reluctance type MLS with linear velocity at different load conditions.

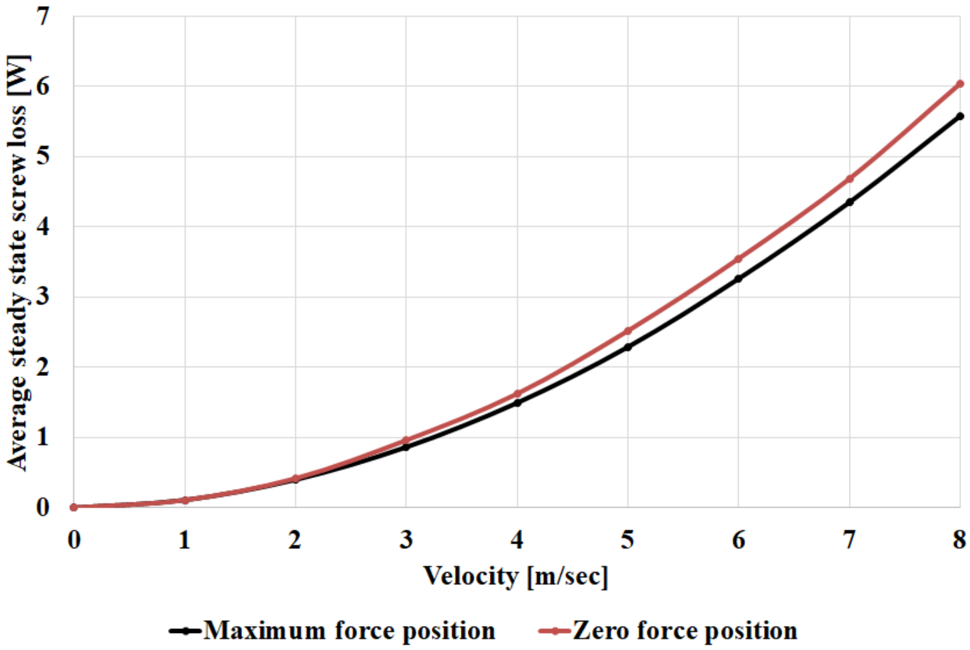

Fig. 4.24: Variation of average steady state screw loss for magnet-to-reluctance type MLS with linear velocity at different load conditions.

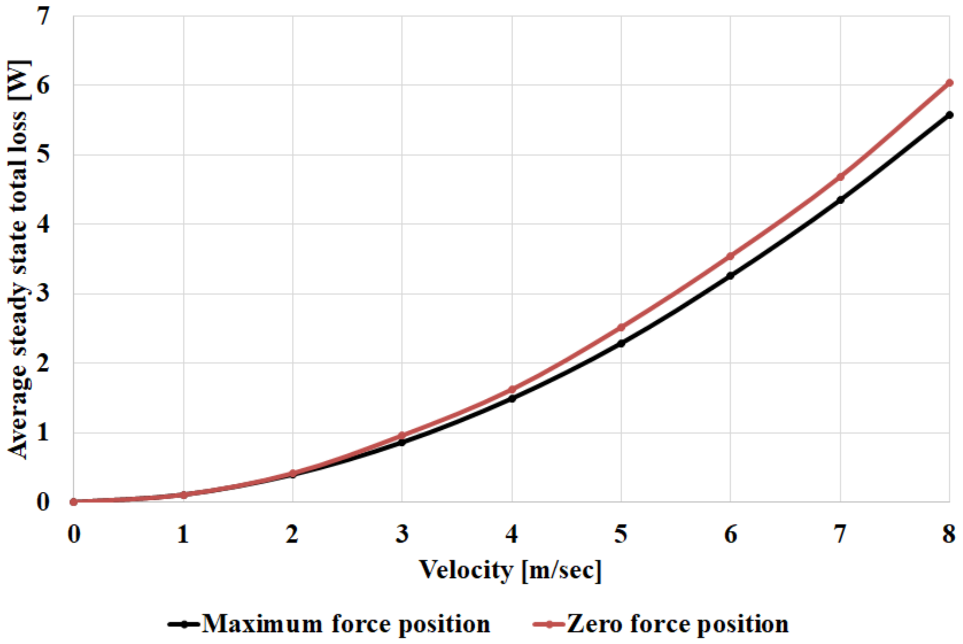

Fig. 4.25: Variation of average steady state total loss for magnet-to-reluctance type MLS with linear velocity at different load conditions.

4.5 Loss comparison

In this section, the average steady state total loss is compared between the two types of MLS, magnet-to-magnet and magnet-to-reluctance type MLS. Firstly, Fig. 4.26 compares the average steady state total loss between magnet-to-magnet and magnet-to-reluctance type MLS in case of the absence of the glue insulation gap. The losses for magnet-to-reluctance type MLS is lower than magnet-to-magnet type MLS. Secondly, Fig. 4.27 compares the average steady state total loss between magnet-to-magnet and magnet-to-reluctance type MLS when 0.1 mm glue insulation gap is injected between the magnets and mild steel. Results confirmed that the losses for magnet-to-reluctance type MLS is lower than magnet-to-magnet type MLS.

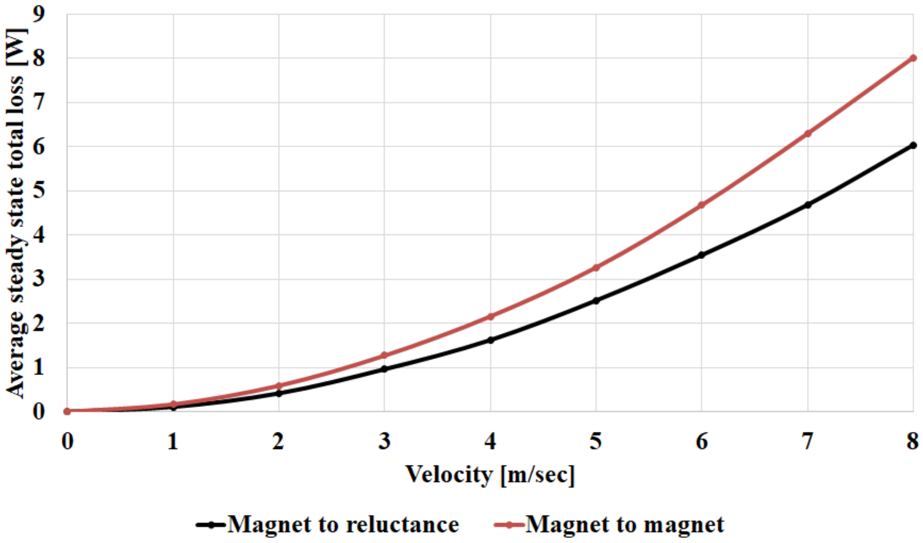

Fig. 4.26: Variation of average steady state total loss for MLS with linear velocity in the absence of glue insulation gap.

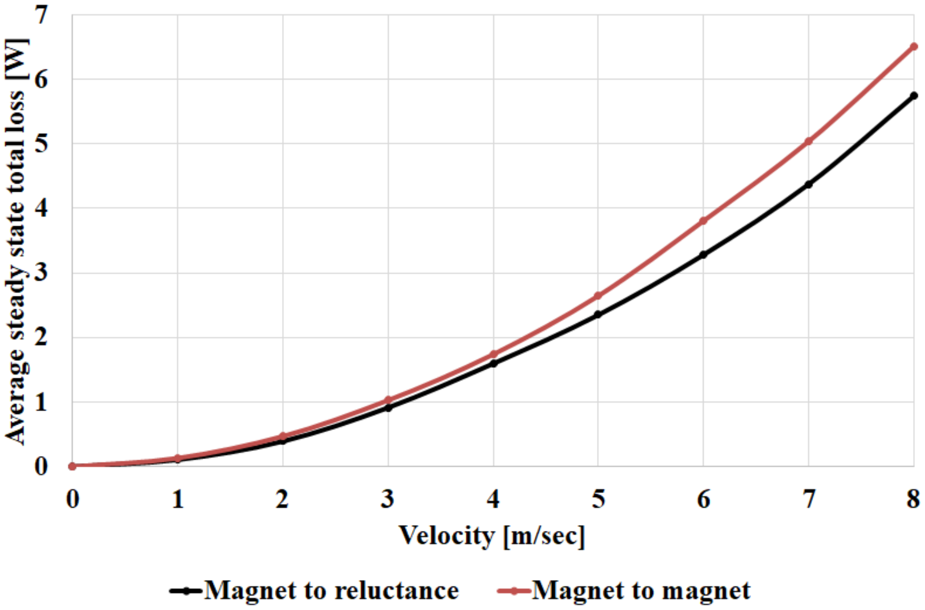

Fig. 4.27: Variation of average steady state total loss for MLS with linear velocity in the presence of glue insulation gap.

4.6 Estimated efficiency of MLS

4.6.1 Magnet-to-magnet type MLS

Efficiency is always defined as the ratio of the useful output power over the total input power of a system. In this sub-section, the efficiency of a magnet-to-magnet MLS will be calculated for a selected model of the previously simulated models. For example, at V = 8 m/s and at the maximum force position the average torque on the screw, T_{Screw} is 0.5652 Nm and the average translator force on the nut, F_{Trans} is 355.84 N as shown in Fig. 4.28 and Fig. 4.29. In this case $F_{Trans} \times \frac{\lambda}{2\pi} > T_{Screw}$ meaning that the nut is driving the screw. The output power can be calculated by multiplying the output translator force by the linear velocity and the total input power is calculated by adding the output power with the average steady state total loss. Fig. 4.30 shows an efficiency map for magnet-to-magnet MLS where the efficiency is calculated at 40%, 80% and 100% of the transmitted thrust force at different velocities.

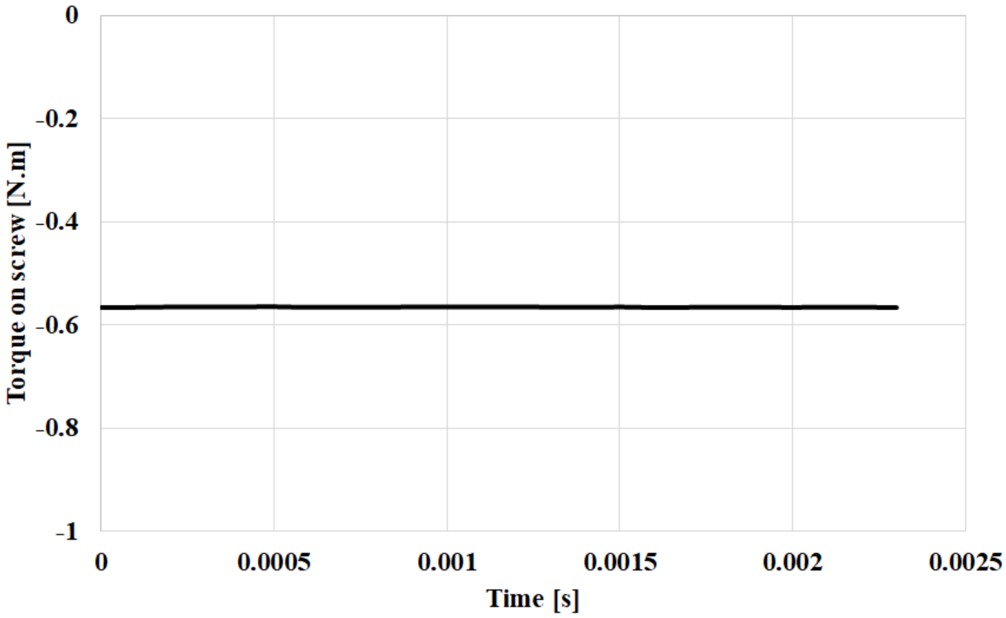

Fig. 4.28: Steady state torque for magnet-to-magnet type MLS when relative position between the nut and the screw is half pole-pitch.

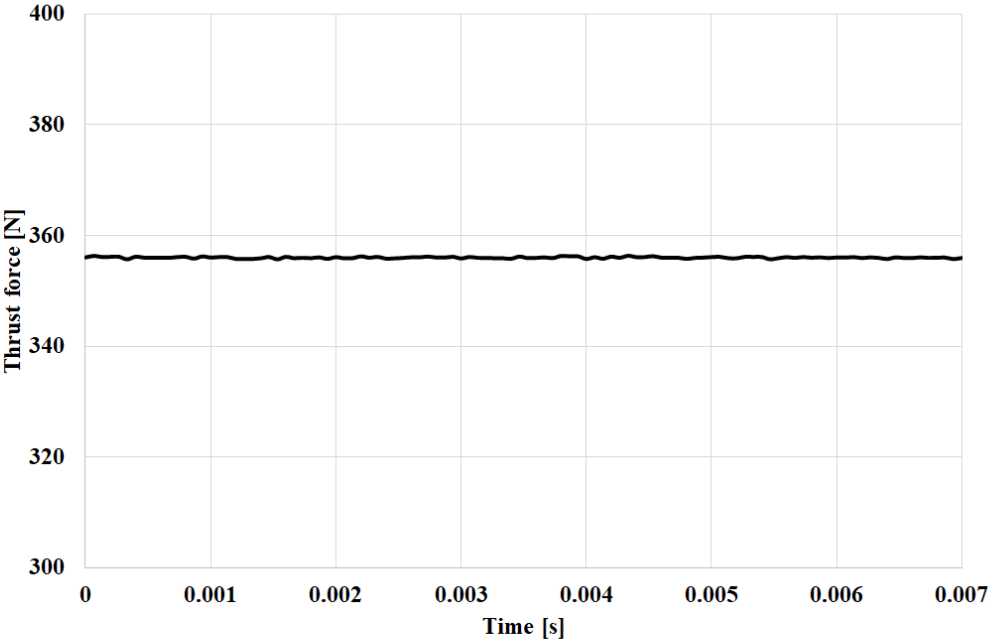

Fig. 4.29: Steady state thrust force for magnet-to-magnet type MLS when relative position between the nut and the screw is half pole-pitch.

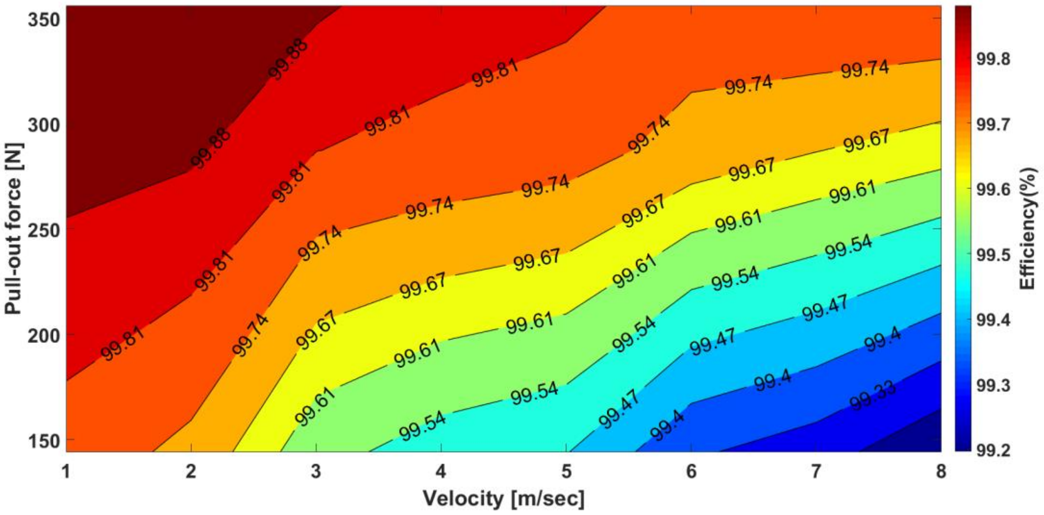

Fig. 4.30: Efficiency map for magnet-to-magnet type MLS.

It can be said that, the magnetic efficiency "η", as the ratio between the output and input power, can reach up to 99.8 % at V= 1m/s and 99.33 % at the proposed launching velocity.

4.6.2 Magnet-to-reluctance MLS

Similarly, for a magnet-to-reluctance MLS at V = 8 m/s, and at the maximum force position the average output torque is 0.1 Nm and the average translator force is 62.37 N as shown in Fig. 4.31 and Fig. 4.32. In this case $F_{Trans} \times \frac{\lambda}{2\pi} < T_{Screw}$ which means that the screw is driving the nut. Fig. 4.33 shows an efficiency map for magnet-to-reluctance MLS where the efficiency is calculated at 40 %, 80 % and 100 % of the transmitted thrust force at different velocities. The figure shows that, the magnetic efficiency "η", as the ratio between the output and input power, can reach up to 99.6 % for low velocity and drops to 97.4 % at the proposed launching velocity.

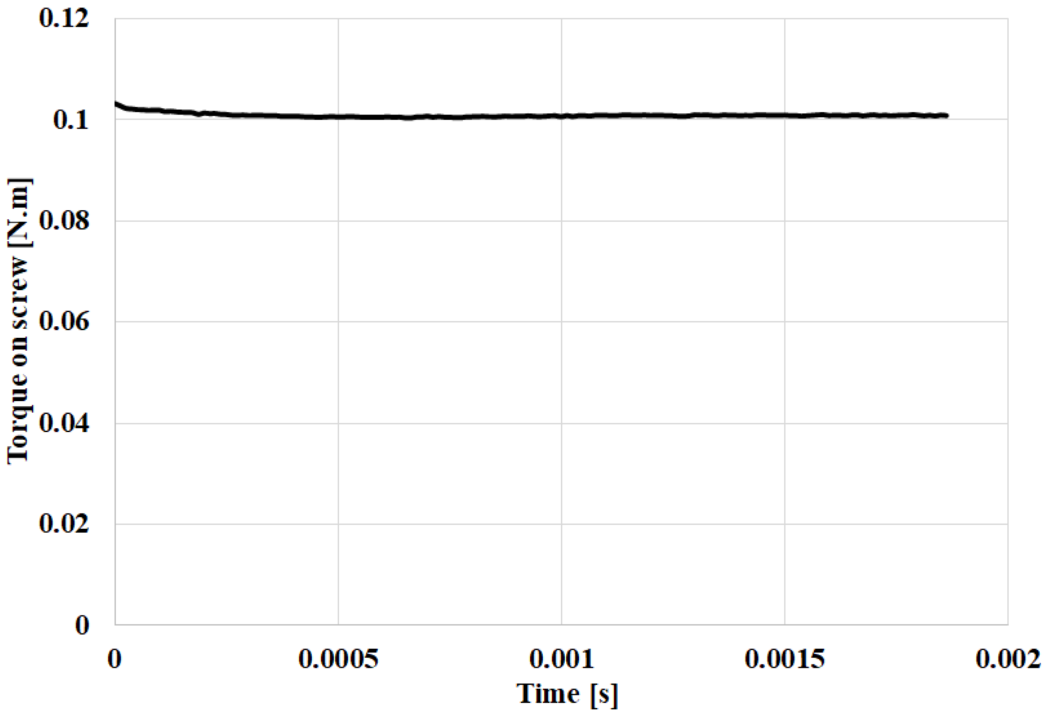

Fig. 4.31: Steady state torque for magnet-to-reluctance type MLS when relative position between the nut and the screw is quarter pole-pitch.

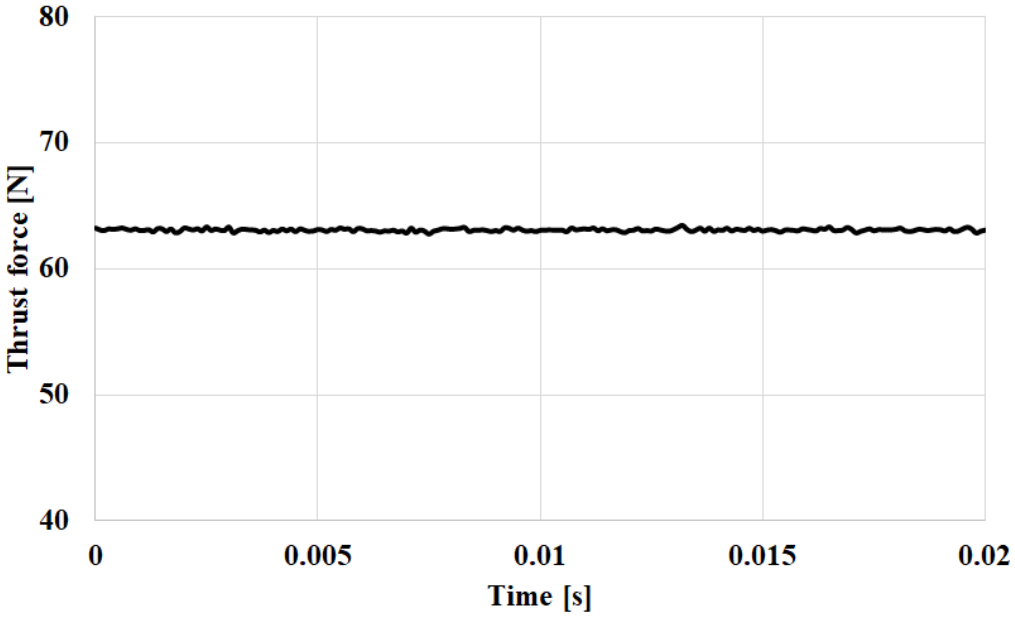

Fig. 4.32: Steady state thrust force for magnet-to-reluctance type MLS when relative position between the nut and the screw is quarter pole-pitch.

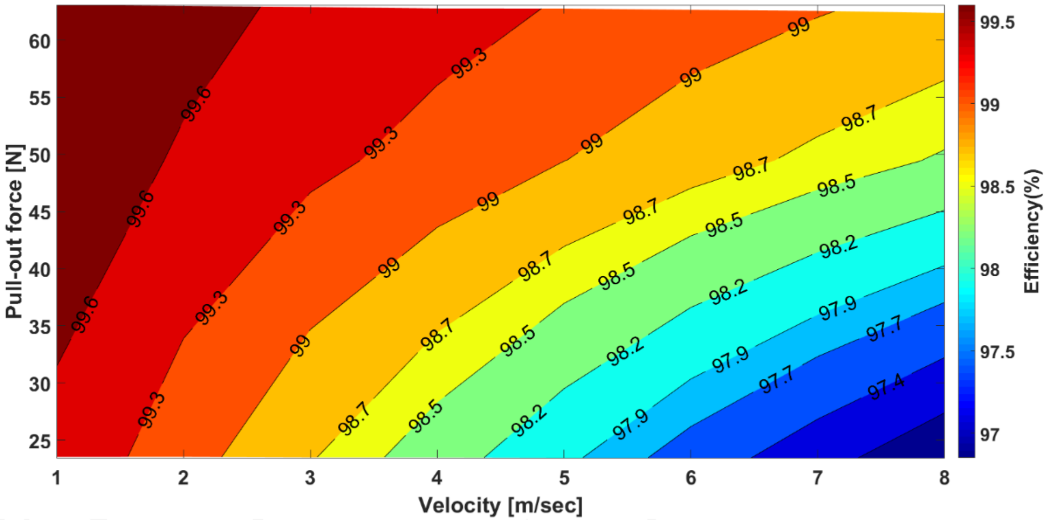

Fig. 4.33: Efficiency map for magnet-to-reluctance type MLS.

4.7 Conclusion

Following an investigation on the losses of magnet-to-magnet and magnet-to-reluctance type MLS; the magnet-to-reluctance type MLS has lower losses than the magnet-to-magnet type MLS as the magnets are mounted only on the nut. However, as mentioned previously, the magnet-to-reluctance type MLS can achieve lower shear stress. Effect of initial position and insertion of glue insulation gap on losses for both types of MLS is investigated. The losses values for both types of MLS are load dependent and affected by the insulation gap between magnets and mild steel. In terms of efficiency both types of MLS can provide an efficiency more than 97 % due to consideration of magnetic losses only. Based on the overall evaluation including the total average steady state losses, material cost, efficiency, and simplicity in construction, the magnet-to-reluctance type MLS is chosen rather than the magnet-to-magnet MLS for hardware implementation.

5 Experimental investigation

5.1 Introduction

The contribution in this chapter is the magnetization of a magnet, to produce helically shaped flux density, between 3-4 Tesla using helically shape coils. A double sided single coil fixture is chosen to validate the impulse magnetization of helical shape magnet. As shown previously in chapter 3, the double sided fixture can provide better magnetising field on the outer surface of the magnet compared to a single sided fixture. This means more magnet saturation and more domain aligmnets and as a result enhancing the remanence of the magnet after magnetisation. The manufacturing procedures of the prototype is carried out in steps including the manufacturing of the inner and the outer fixture, sticking of magnet rings to perform the desired cylindrical magnet and the assembling of the prototype as one unit. Magnetisation process is disscussed using the magnetiser and the produced helically shaped magnetic field is shown using a green magnetic field viewing film. A test rig is designed as a combination of linear and linear-to-rotary bearings for force measurments. The test rig is designed to record the transmitted force between the permanent magnet nut and the double start steel screw with a HBM Z6 10 kg force transducer.

5.2 Manufacturing procedures

The coil used in the double sided single coil fixture employs a 2 mm diameter wire as mentioned before, the inner part of the fixture is double start mild steel screw with a length of 80 mm without extensions on both sides of the screw, inner diameter 9.5 mm, outer diameter 14.5 mm and 10 mm lead. The helical grooves were designed to accommodate the coil and the insulation. The iron thread has dimensions of a 2.3 mm width and a 2.5 mm depth. The gap between the threads was left to be 2.7 mm enough for the insulation inserted around the coil. The inner mild steel screw of the fixture is machined with two centered extensions on both ends to facilitate handling on a lathe as shown in Fig. 5.1. The 2 mm diameter coil is wound around the screw, as shown in Fig. 5.2, after covering the wire with high temperature insulating Kapton tape which exhibits excellent dielectric insulation properties, high heat resistance (290^{o}C for short term) and is both flame and chemical resistant. Furthermore, to provide mechanical support and prevent movement, the coil and screw are covered with fiberglass tape with a total thickness of 0.75 mm. A Durapot 862 resin and hardener are employed with 100 to 80 % mix ratio is used as a composite. The resin has excellent electrical, moisture and chemical resistance. It can withstand temperatures up to 315^{o}C in normal conditions and 230 ^{o}C in severe environments. After brushing the fiberglass tape with the resin, it is cured for four hours at 120^{o}C in an oven. Fig. 5.3 (a) shows the inner screw after curing the fiberglass tape in the oven for four hours. Fig. 5.3 (b) shows the inner screw after machining to fit the inner diameter of the magnets.

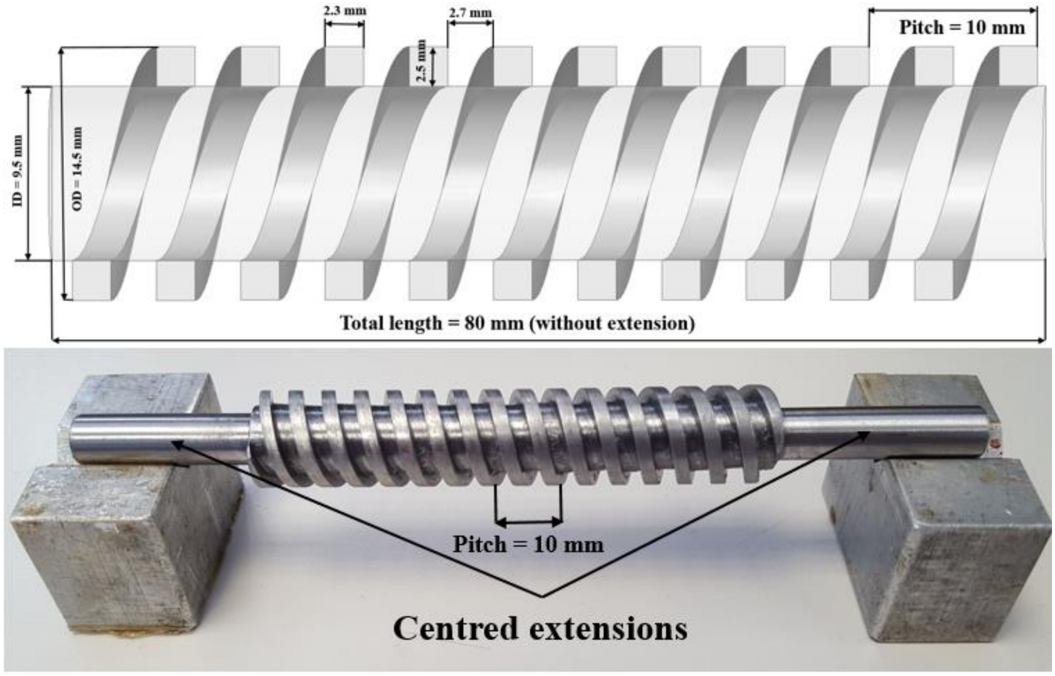

Fig. 5.1: Inner mild steel screw with two-centred extensions.

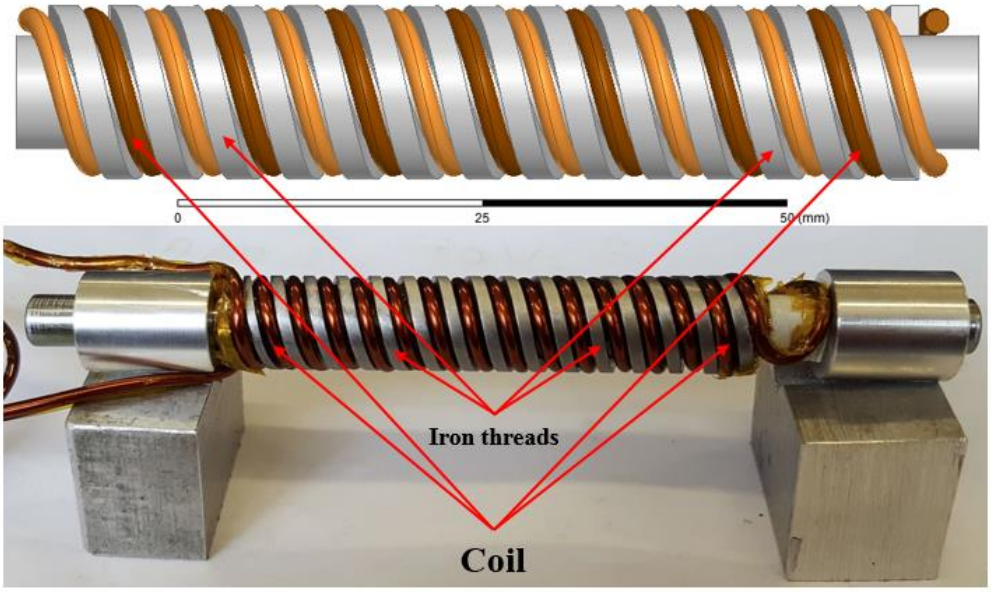

Fig. 5.2: The 2 mm diameter coil covered by high-temperature Kapton tape.

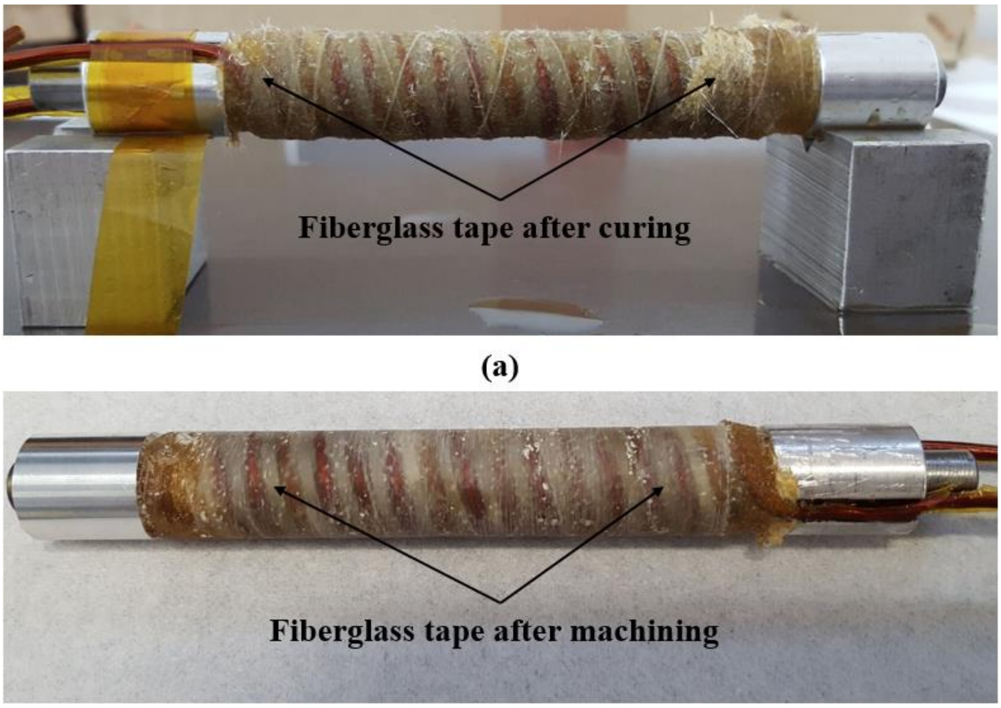

(a)

(b)

Fig. 5.3: (a) Fiberglass tape after curing, (b) Fiberglass tape after machining.

The prototype is finalised by soldering ring connectors on the terminals of the coil, as shown in Fig. 5.4. The insulation test between the coil and the mild steel screw was carried out to ensure correct insulation between the screw and the coil. A BM 206 Megger is used for this test. It supports the continuity test up to 1000 volt. The 40 mm magnets are produced by stacking five magnet rings each of 8 mm width as shown in Fig. 5.5. Duralco NM 25 resin, the bonding magnet resin, is used to stick the five magnet rings together. It can resist high temperature up to 260^{o}C.

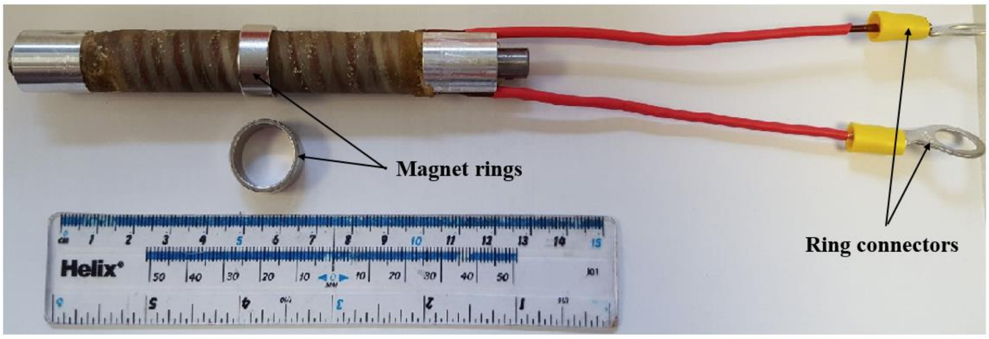

Fig. 5.4: A magnet ring on inner screw.

Fig. 5.5: Five 8 mm magnet rings stacked together to form 40 mm magnet.

The 40 mm magnet is placed at the mid-distance of the screw to prevent the non-uniform magnetic field, produced at the ends of the coil, from affecting the distribution of the magnetic field on the magnet. So, a hollow plastic ring was placed at the start of the screw, and the magnet ring is then fixed with another hollow cylinder from the other side and tightened with a small bolt. The magnet, hollow cylinder, and the hollow plastic ring are aligned together with a red line to ensure the correct position of the magnet during discharging phase as shown in Fig. 5.6. This step will keep the magnet placed in a fixed position during magnetisation process.

The design of the outer fixture part is more complicated. The coil on the outer fixture part needed to be wound helically on the inner part of the outer fixture. As shown in Fig. 5.7, the dimensions of the Tufnol cylinder has to be the same in length, thread depth and width, lead, and spacing between threads as the mild steel screw. The outer coil is wound around a former, with the same diameter as the inner diameter of the outer fixture part, then inserted in Tufnol cylinder. Choosing Tufnol as it is a non-metallic non-conductive material with good mechanical properties.

The insertion of the coil inside the Tufnol cylinder is more difficult, and the Tufnol had to be cut to two halves to insert the coil in the Tufnol grooves. The two parts of Tufnol cylinder are then put together with Araldite. After that, the fiberglass tape wrapped around the Tufnol cylinder and impregnated with the same resin used for the screw as shown in Fig. 5.8.

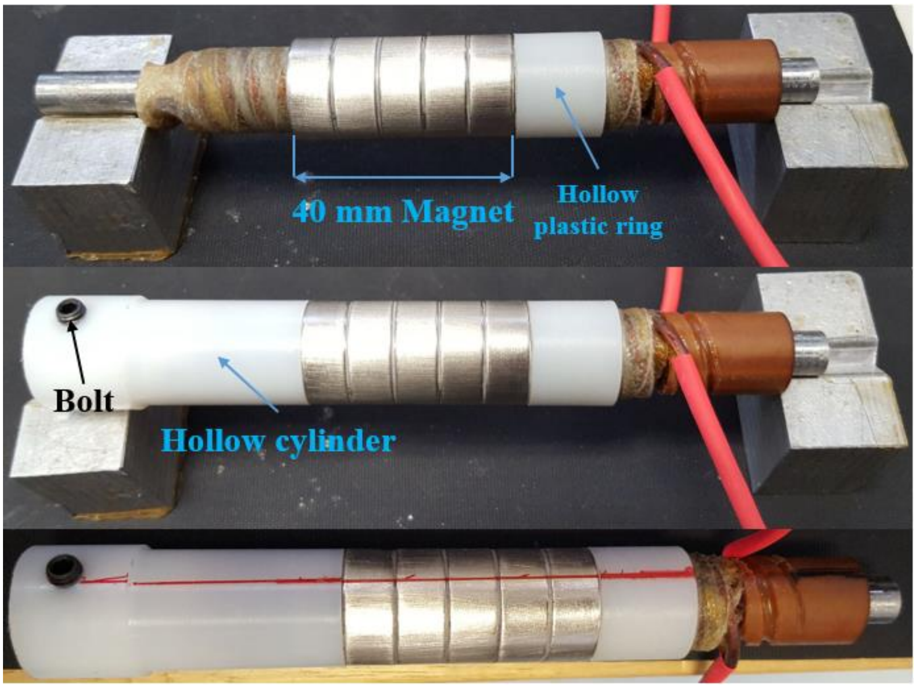

Fig. 5.6: Placing the 40 mm magnet in the mid-distance of the screw.

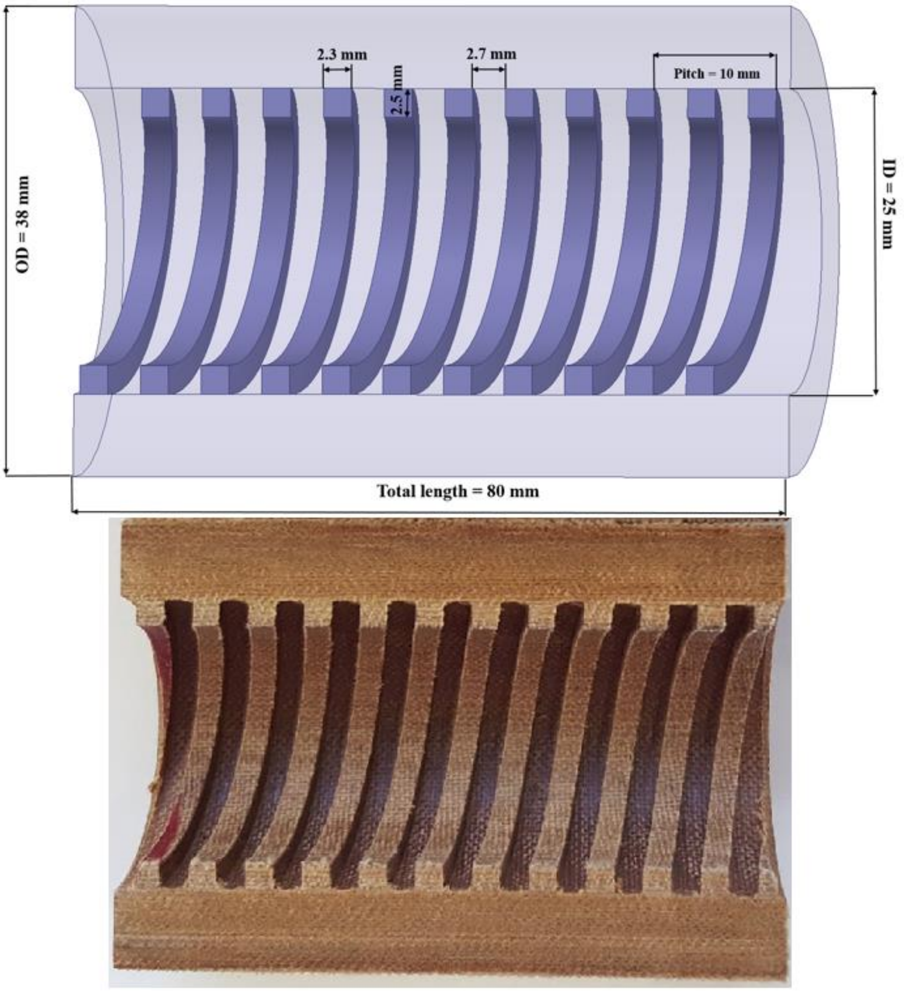

Fig. 5.7: The outer fixture part which made of Tufnol.

Fig. 5.8: Tufnol outer fixture with fiberglass tape after machining.

Now, the outer and inner fixture parts are ready to be integrated together to form the double-sided single conductor fixture. The two coil terminals of the Tufnol cylinder are connected to ring connectors as done before for the mild steel screw. The inner screw is inserted inside the Tufnol cylinder, and the magnet is placed and fixed in position by adjusting the bolt on the hollow cylinder making the fixture ready for firing as shown in Fig. 5.9.

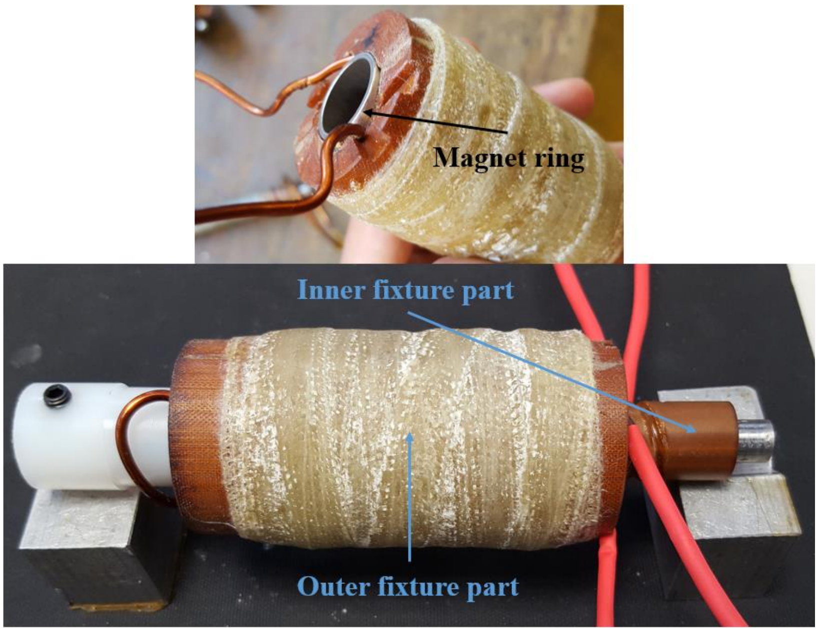

Fig. 5.9: Single conductor double-sided fixture.

5.3 Magnetisation process

The actual resistance and inductance of the fixture were measured by HIOKI 3522 LCR meter. The resistance of the fixture is found to be 16.04 mΩ, and the inductance is 1.47 uH, these values are higher than the values indicated in chapter 3 as the prototype has longer coil terminals to be connected to the magnetiser and has end winding, also, the inductance is calculated at the frequency of the current pulse of the used magnetiser. The double-sided fixture with its four terminals is then connected across the two terminals of the magnetizer shown in Fig. 5.10. One terminal, from outer fixture part, with the positive rail, other, from the inner screw, with the negative rail and the remaining two terminals are then connected in series to complete the circuit as shown in Fig. 5.11.

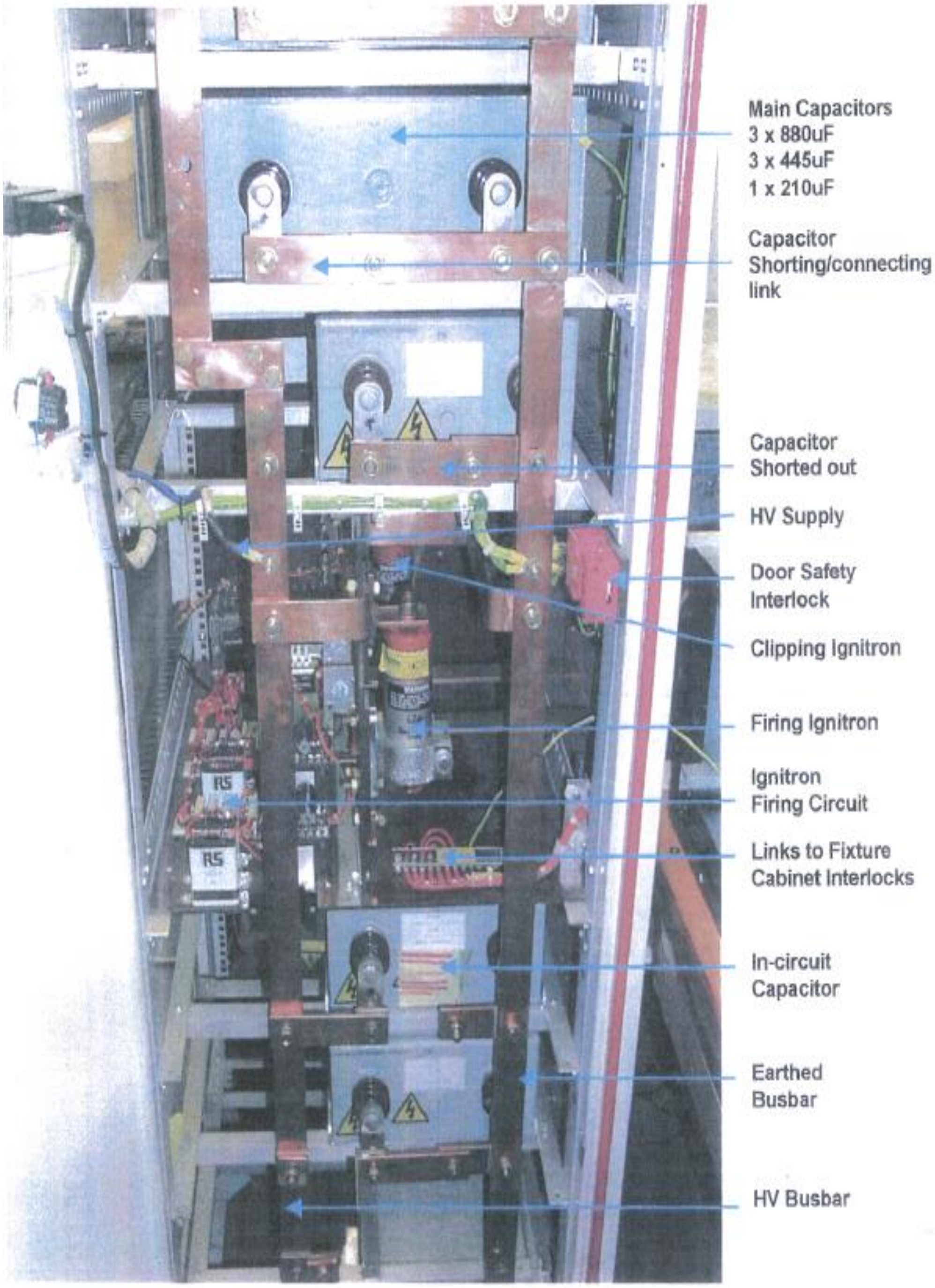

Fig. 5.10: Front view showing main capacitors and busbars of the magnetizer.

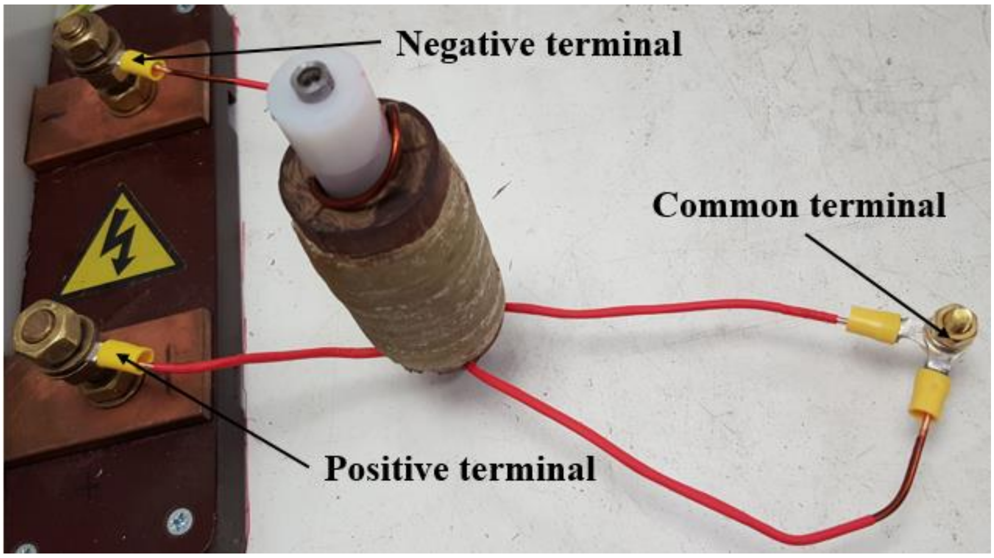

Fig. 5.11: Connection of double-sided fixture with the magnetizer.

The magnetizer is fired at different voltages. It is fired at 500, 1000, 1500, 1750 and 2000 volt. The highest current pulsed is given at 2000 volt which was 29.6 kA. The highest current pulse that can be given by the magnetizer is 30 kA. So, the fixture was not tested above 2000 volt.

A 3D MAXWELL model and MATLAB/SIMULINK model are developed employing the exact dimensions of the prototype. The 3D MAXWELL model with coupled circuit is shown in Fig. 5.12. MATLAB/SIMULINK model is shown in Fig. 5.13. In both models, the internal resistance and inductance of the magnetizer are added in the simulation. The internal resistance of the magnetizer is measured and found to be 2.37 mΩ with a equivalent series inductance of 1.883 uH. The capacitor bank is 1.252 mF and charged at 2000 volt.

During discharge phase, the current pulse is recorded by digital storage oscilloscope DSO-X 2002A with a maximum peak current of 29.64 kA, while simulated results by MAXWELL 3D and the maximum peak current is found to be 27.86 kA, 6% lower. On the other hand, the maximum current predicted using MATLAB/SIMULINK is 30.84 kA 3.9% larger than the experimental value, as shown in Fig. 5.14. Temperature rise is an important factor which must be taken into consideration as mentioned earlier in chapter 3. The 1.252 mF capacitor charged at 2000 volt can raise the temperature in the fixture during discharge phase to 113°C as shown in Fig. 5.15. Accordingly, this increases the resistance of the fixture from 16.04 mΩ to 21.7 mΩ as shown in Fig. 5.16. The resulting magnetic flux density at the maximum peak current on the outer, inner and centre of magnet surface is shown in Fig. 5.17. The peak value of the magnetic flux density at the half distance of the pole-pitch exceeds 3T at the peak of the current pulse.

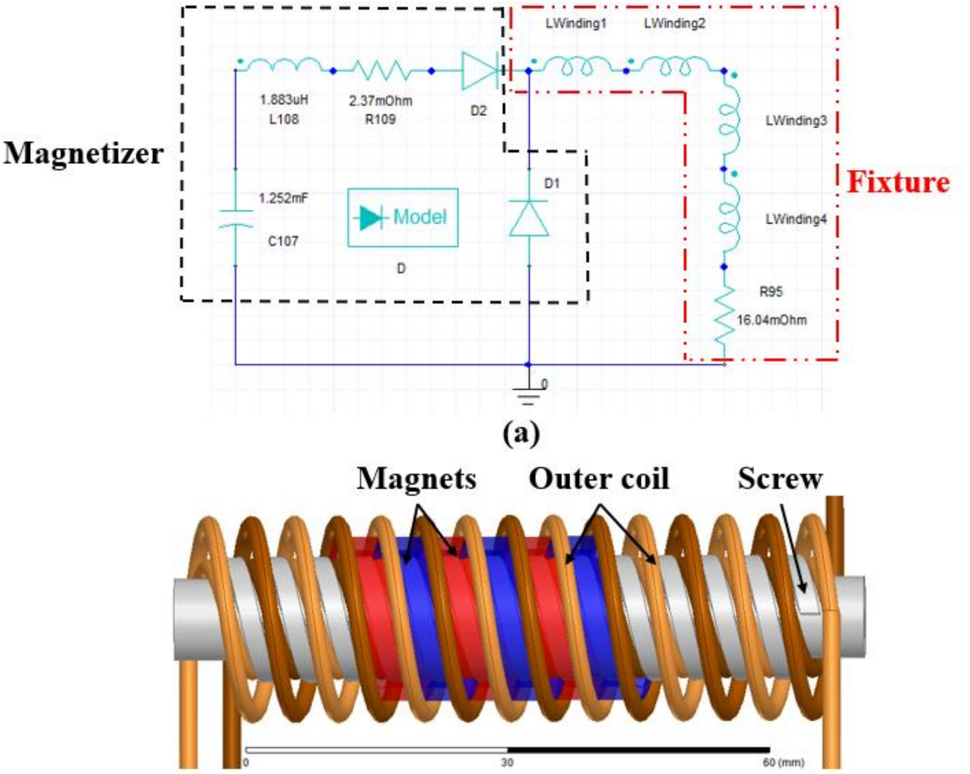

(a)

(b)

Fig. 5.12: (a) Excitation circuit, (b) 3D MAXWELL model.

As a result of the coil configuration in the fixture, a helically shaped magnetic field can be detected on the surface of the magnet as shown in Fig. 5.18.

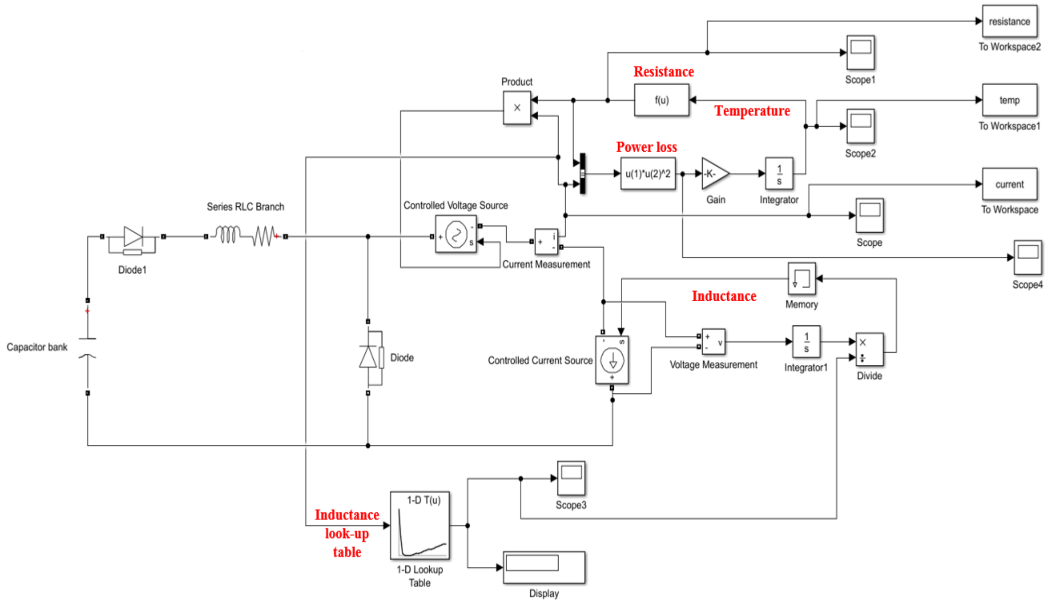

Fig. 5.13: Block diagram of discharging phase for the magnetizer.

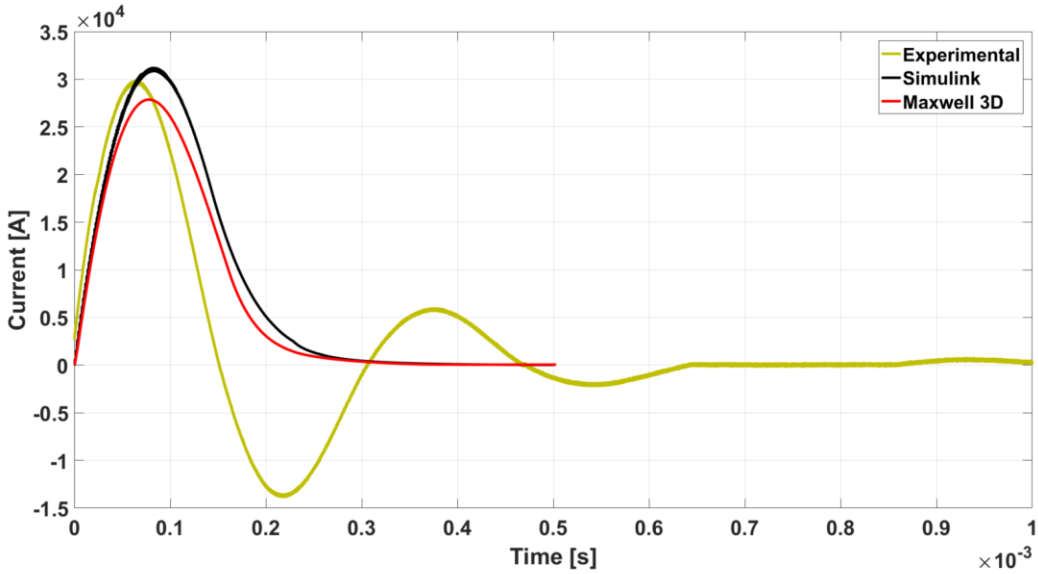

Fig. 5.14: Experimental current pulse during discharging phase compared with MAXWELL and MATLAB/SIMULINK.

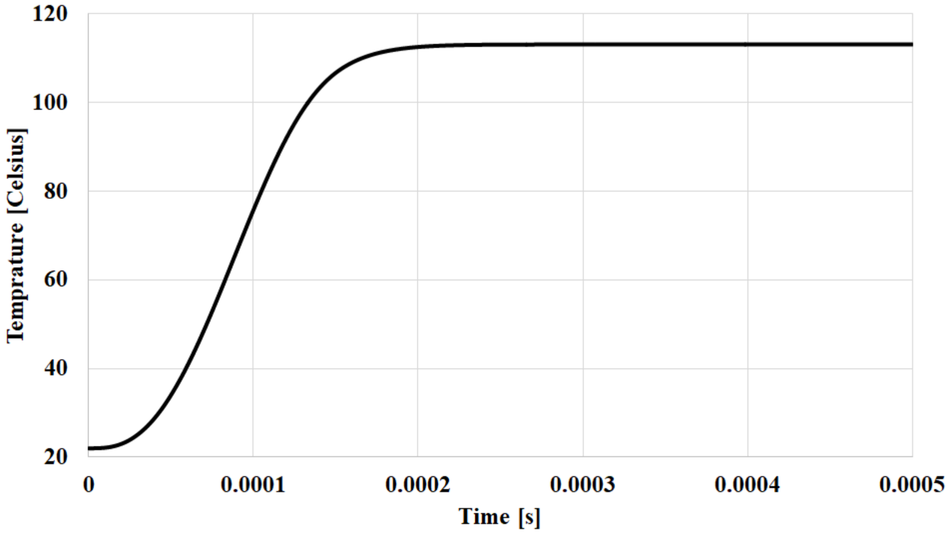

Fig. 5.15: Temperature rise in single conductor double-sided fixture during magnetisation process.

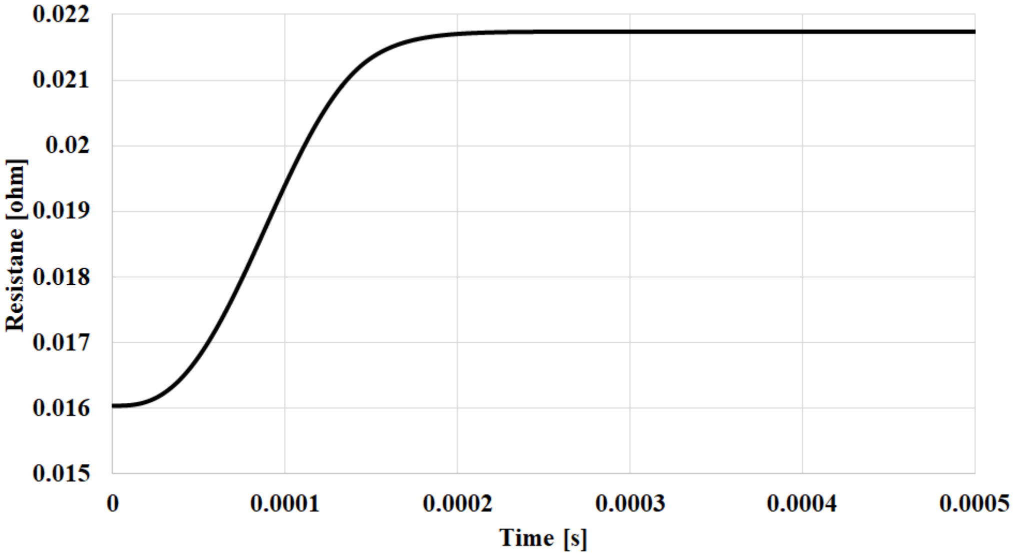

Fig. 5.16: Resistance change in single conductor double-sided fixture during magnetisation process.

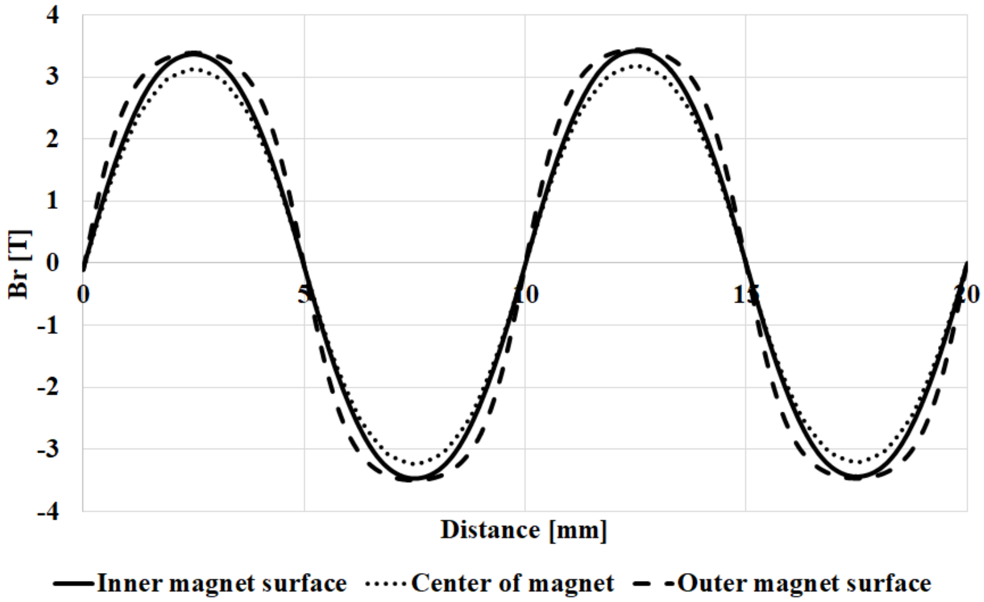

Fig. 5.17: Magnetic flux density waveform along the length of the magnet at the peak current.

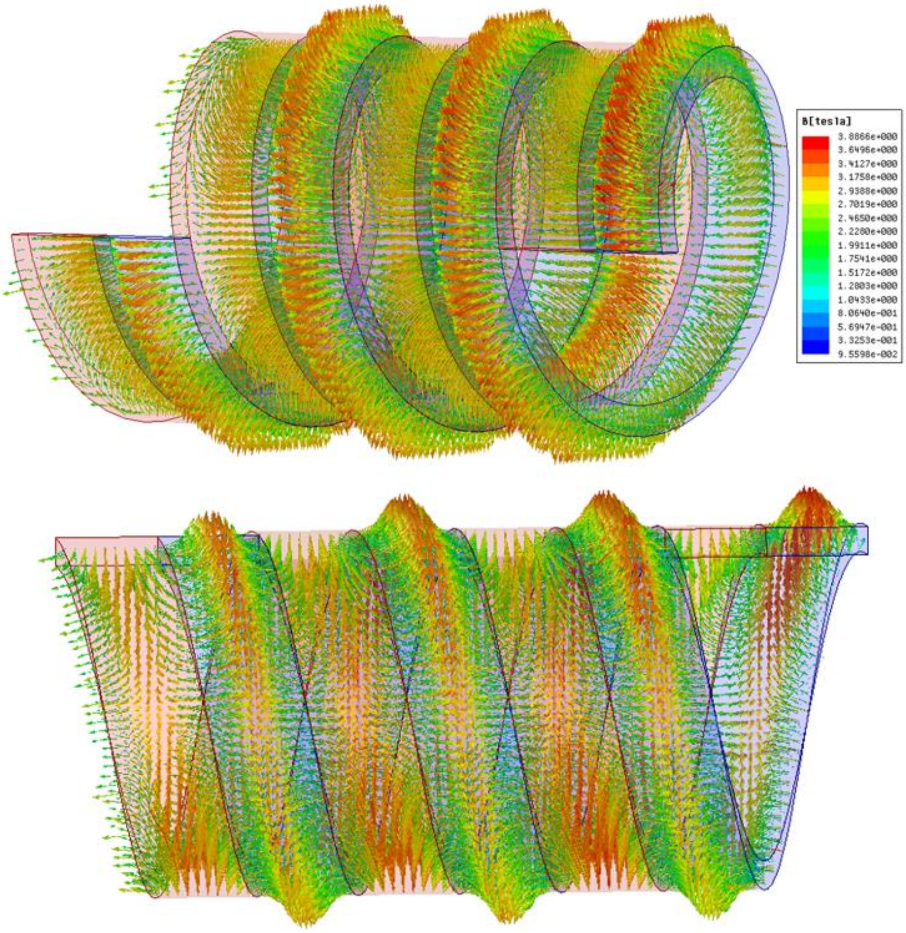

Fig. 5.18: Helically shaped magnetic flux density distribution produced by inner and outer coils at the peak value of current pulse (simulated by Maxwell 3D).

After the firing process, the signal caught on the scope in Fig. 5.14 indicates a failure in the clipping ignitron of the magnetiser that prevents the discharging current from oscillating in the negative direction. So, the magnets are not fully magnetised and the negative current demagnetise the magnets by the end of the magnetisation process. For a successful magnetisation process, the experiment was carried out in ARNOLD MAGNETICS COMPANY using their 3000 kV 15 kJ magnetiser. The fixture is fired at only 30 % of the magnetiser's energy for safety considerations. The output current pulse recorded on the scope has a maximum value of 28.75 kA as shown in Fig. 5.19. The produced magnetic field after magnetisation is a helically shaped magnetic field shown by a green magnetic field viewing film as shown in Fig. 5.20. It can be easily shown in Fig. 5.21 the generated 4 pole-pairs as a result of the designed magnetising fixture.

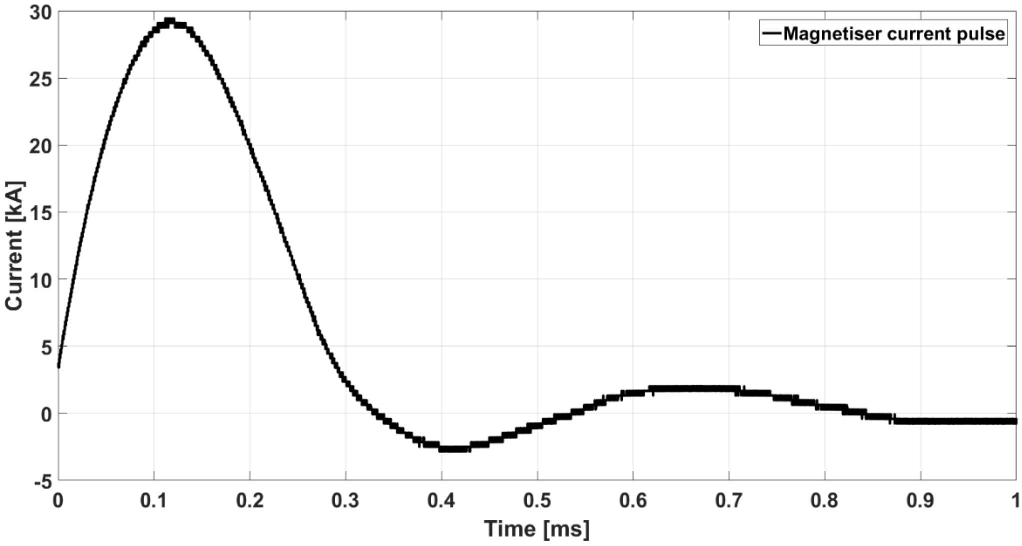

Fig. 5.19: Current pulse of ARNOLD MAGNETICS' magnetiser at 30 % of its maximum energy.

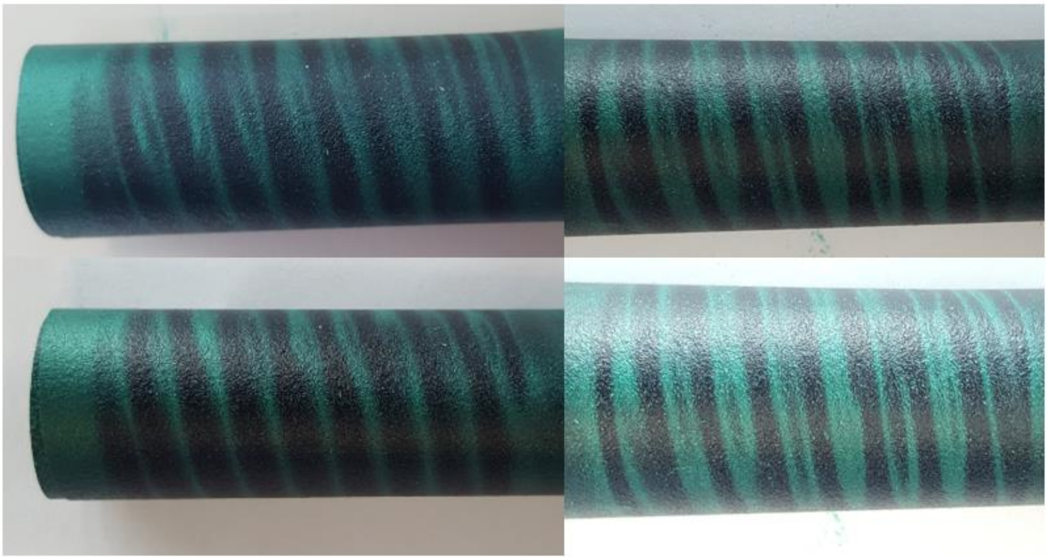

Fig. 5.20: A green magnetic field viewing film showing the helical shape magnetic field generated form the cylindrical magnetised magnet.

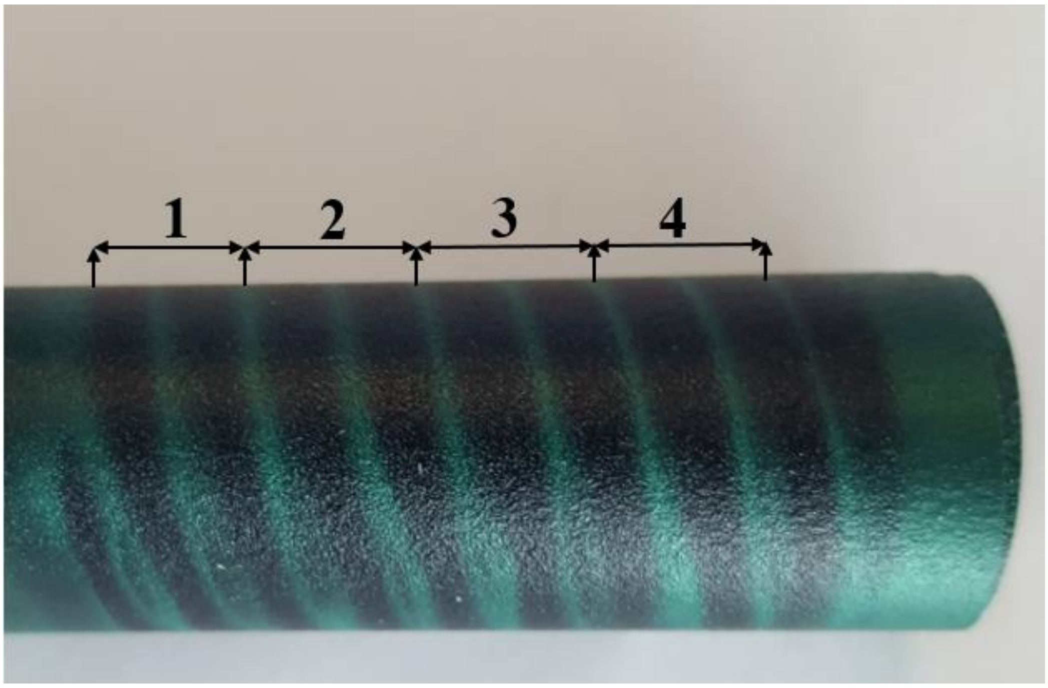

Fig. 5.21: The 40 mm helically magnetised cylindrical magnet with its 4 pole-pairs.

5.4 Test rig

5.4.1 Design

For force measurements, a test rig is designed to measure the transmitted force between the nut and the screw as shown in Fig. 5.22. Detailed dimensions for magnet-to-reluctance MLS prototype are shown in Fig. 5.23.The test rig is built as a combination of linear and linear-to-rotary bearings as shown in Fig. 5.24. The transmitted force between the nut and the screw is recorded by a 10 kg force transducer as shown in Fig. 5.25. The magnetised magnet is assembeled with a back-iron nut and is integrated with a two start helical iron screw as shown in Fig. 5.22. As shown in the figure, the screw has two extensions where two linear bearings can support the screw in a horizontal position. The nut is connected to linear-to-rotary bearings that provide linear motion for the screw when the nut rotates. The direction of linear motion of the screw is towards the force transducer that measures the transmitted force between the nut and the screw. The force transducer is calibrated such that for each 1 kg applied load is equivalent to 1.67 mV as shown in Fig. 5.26. The rotation of the nut is controlled by an arm connected to a rectangular plate which is divided into 90 slots each slot is 2^o apart from the next slot to form 180^o angle slots plate as shown in Fig. 5.27. For each 2^o of rotation, the screw begin to move forward pushing the force transducer which in turns indicates the pushing force in mV.

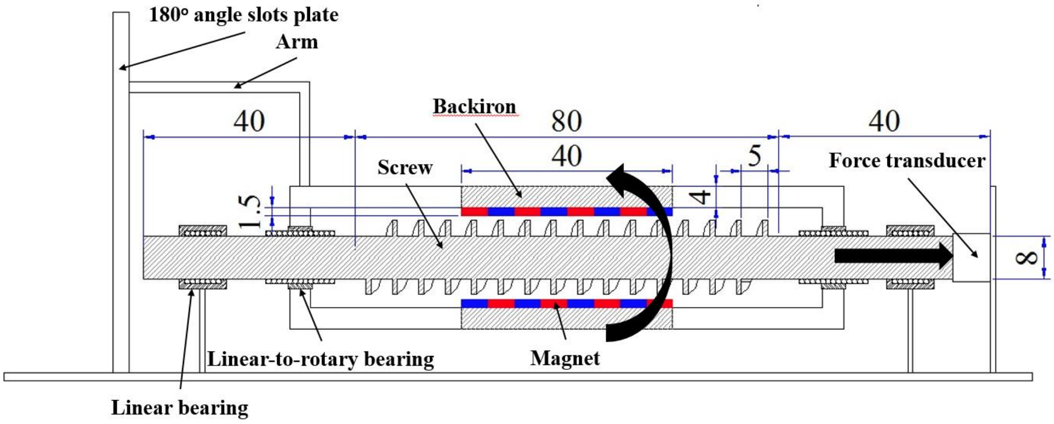

Fig. 5.22: Schematic diagram for the proposed test rig.

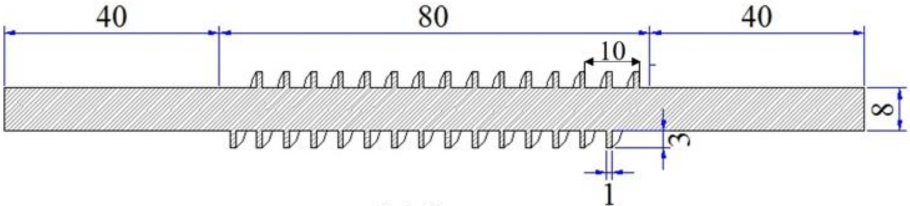

(a) Screw

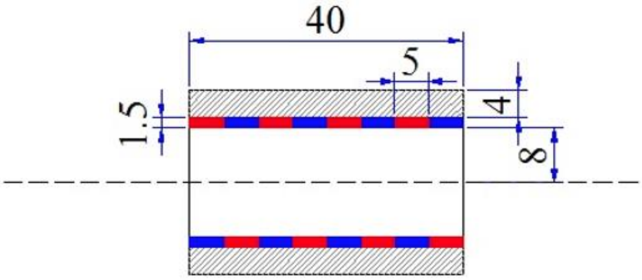

(b) Nut

Fig. 5.23: Detailed dimensions for magnet-to-reluctance MLS prototype.

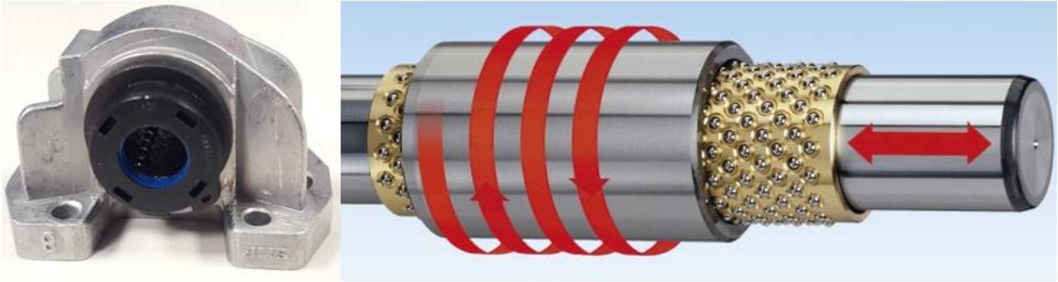

(a) (b)

Fig. 5.24: (a) SKF linear bearing, (b) NORDEX linear-to-rotary bearing.

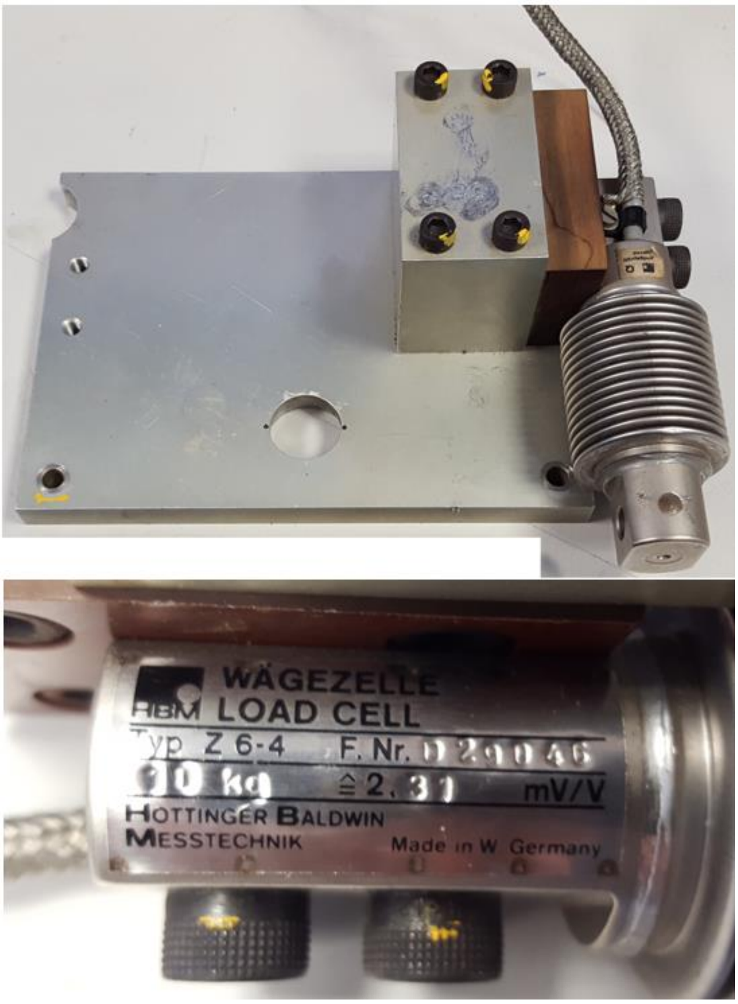

Fig. 5.25: HBM Z6 10 kg force transducer (Note: the measured calibration coefficient is 1.67mV/kg) .

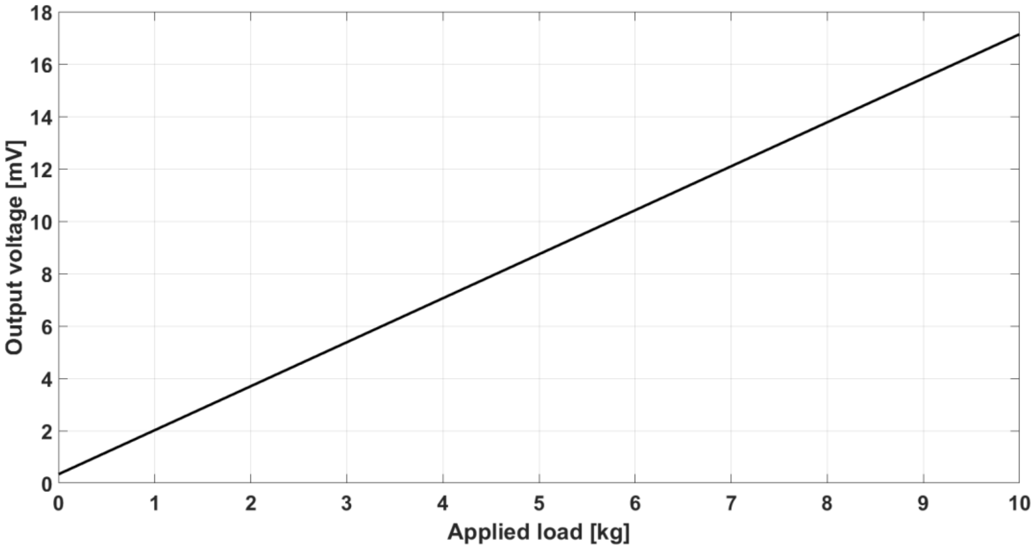

Fig. 5.26: Force transducer calibration.

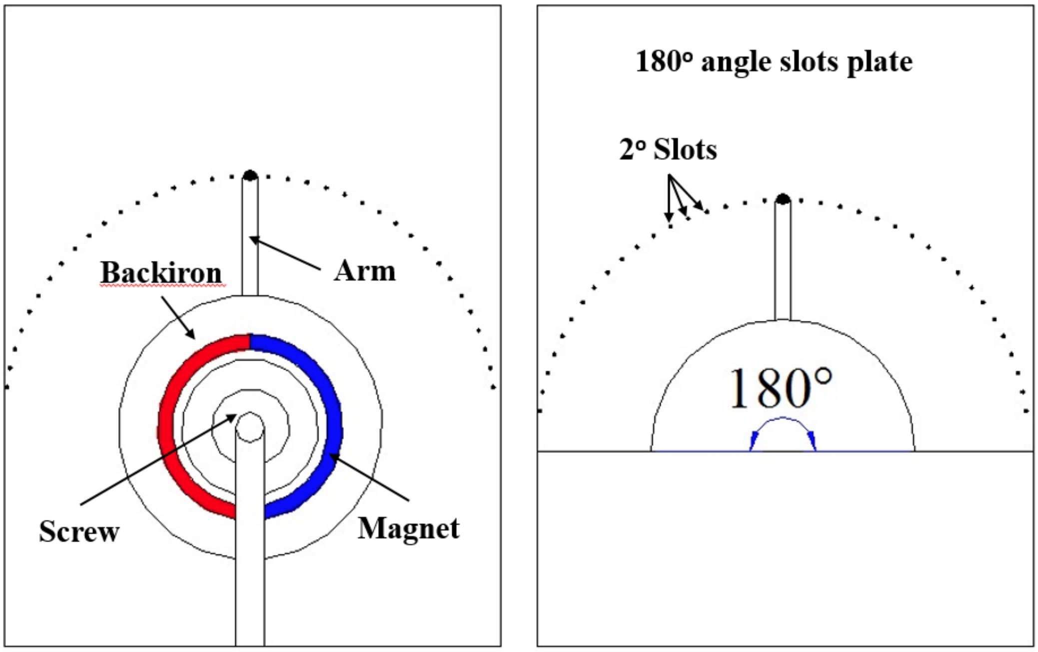

Fig. 5.27: Side view for the test rig showing the 180° angle slots plate.

5.4.2 Measurements

The test rig is manufactured and assembled in the workshop of the UNIVERSITY OF SHEFFIELD. The prototype is shown in Fig. 5.28. The test rig is assembled with the HBM Z6 10 kg force transducer at one end of the screw where the force is transmitted by the rotation of the external casing that covers the nut assembly.

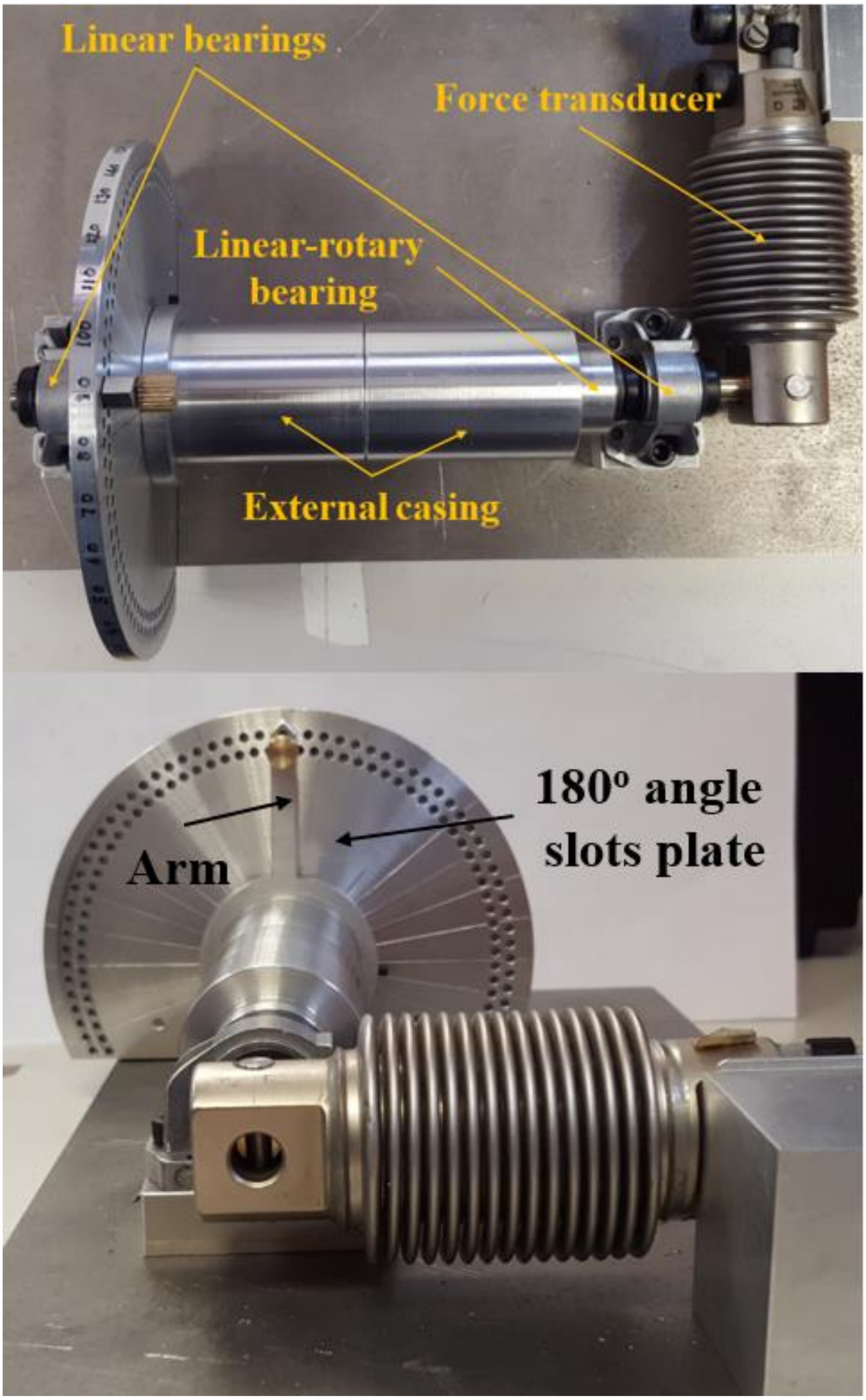

Fig. 5.28: Test rig prototype assembled with the HBM Z6 10 kg force transducer.

The screw is prevented from the rotation by using the sealed linear bearings at both ends of the screw. This allows the screw to move in linear direction and pushing the linear force transducer. The external casing is rotated by 90 steps, each step is equal to 2°, which is corresponding to 180° as shown in Fig. 5.29.

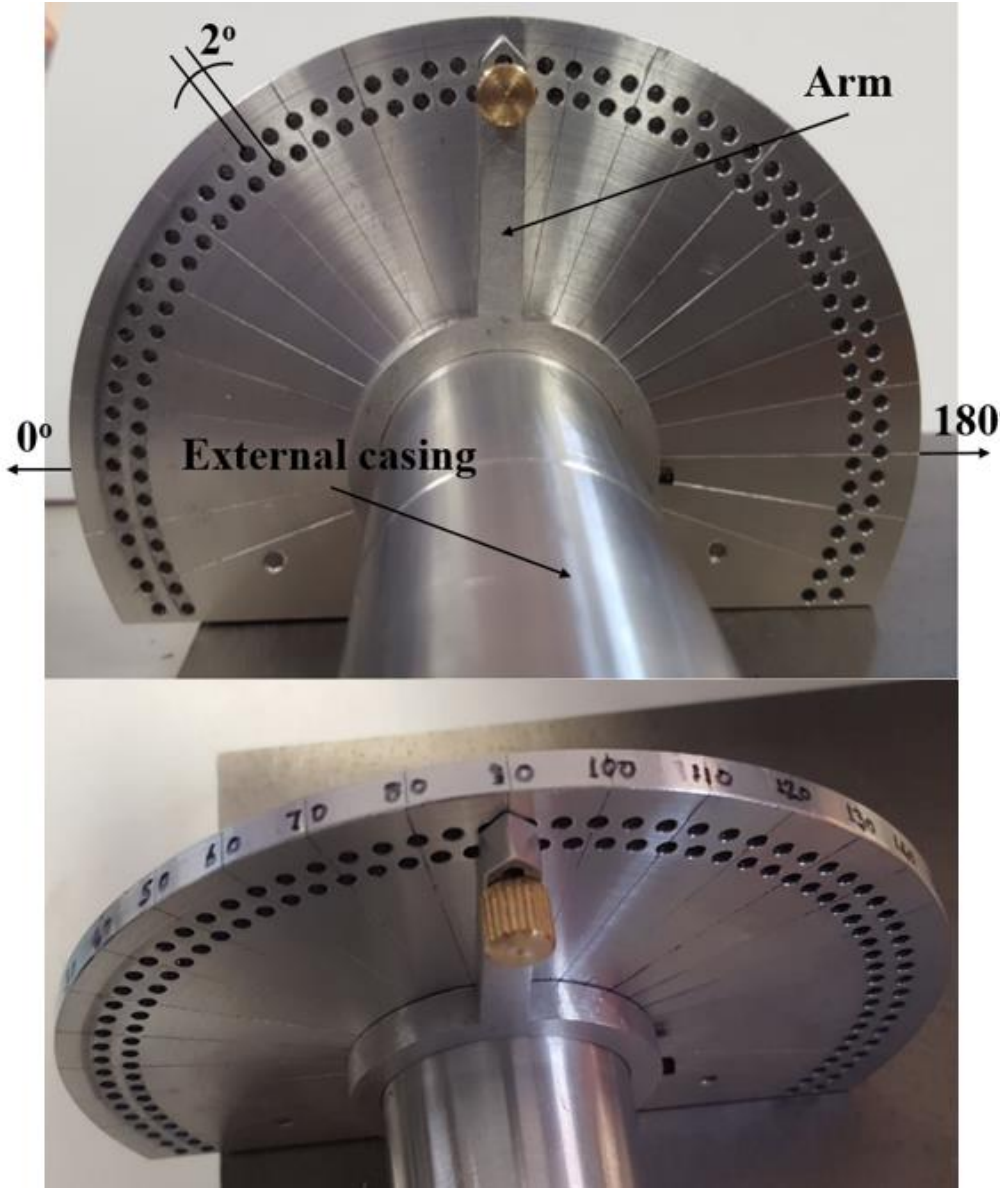

Fig. 5.29: The 180° angle slots plate.

First, the force transducer is removed and the nut is rotated in steps up to 180° and the corresponding linear distance travelled is recorded. Fig. 5.30 shows the variation of the linear displacement of the screw with the angular rotation of the nut, which confirms that the linear displacement of the screw is ${}^{\lambda}/_{2\pi} \times$ the angular displacement of the nut.

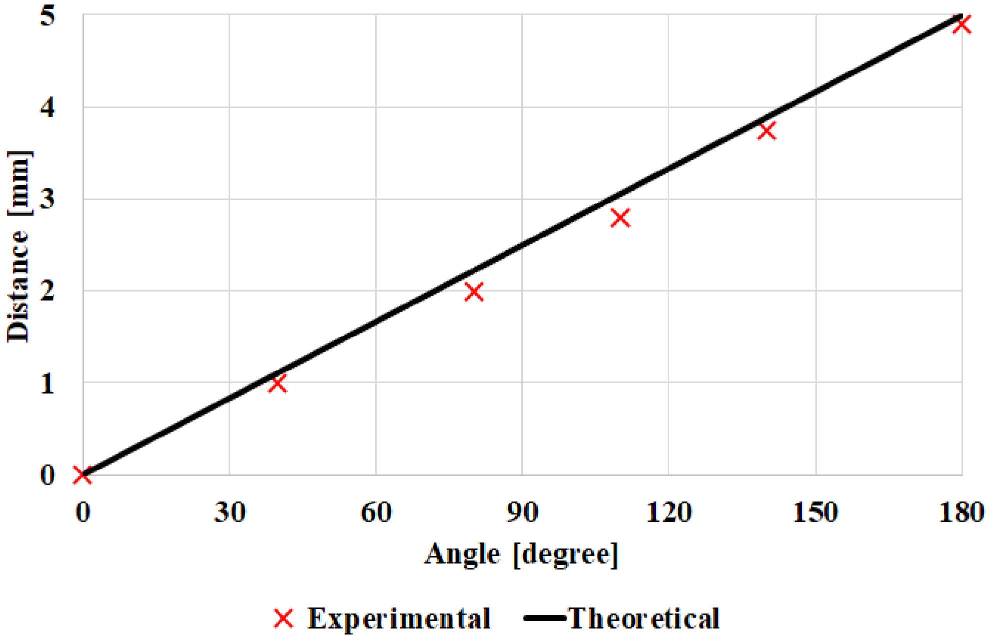

Fig. 5.30: The rotation of external case by 180° and its equivalent translation motion.

The transmitted force is recorded using two different methods. In method 1, the external case is rotated until the maximum transmitted force is realised. The maximum recorded transmitted force is 25 N, this force is the resultant of the magnetic force transmitted from the magnets and the stiction force resulting from the friction between the bearings and the screw. This stiction force works against the magnetic force and can be represented as:

$$F_m - F_s = 25\ N \tag{5.1}$$

where, F_m is the transmitted magnetic force, and F_s is the stiction force.

In method 2, another way to detect the transmitted force is carried out. The force transducer is removed from the test rig and the test rig is placed in a vertical position and a platform is placed on the top of the screw. Weights are added on the platform, as shown in Fig. 5.31, and the corresponding travelled distance for the screw is recorded until slipping occurs. The maximum recorded transmitted force before slipping is 32 N. In this case, the stiction force works with the magnetic force and can be represented as:

$$F_m + F_s = 32\ N \tag{5.2}$$

The maximum transmitted force of the test rig predicted from MAXWELL is 60 N as shown in Fig. 5.32. The simulated model has the parameters stated in Table 5.1. The model assumes ideal magnetisation distributions, and ideally cut double start screw. However, closer look at the iron threads on the screw reveals they are on average about 0.75mm instead of the 1mm width assumed in the modelling, with large variations between 0.55mm to 0.88mm as shown in Fig. 5.33. This was caused by difficulties during the cutting of the relatively small screw. Fig. 5.34 shows the variation of the pull-out force with the iron thread width. It can be seen that a significant drop in the pull-out force results if the iron thread width is less than 1mm, and at 0.75mm, the force would be reduced by around 10N.

Furthermore, the magnets used in the test rig are experimental radially isotropic rings, and quality control may not be perfect. The density of the magnet given by the manufacturer is 7500 kg/m^3 but the measured density is 7192 kg/m^3. This could be a result of inefficient compression of the grains of the magnet powder leading to lower remanence than the grade might have and as a result affecting the saturation of the magnet.

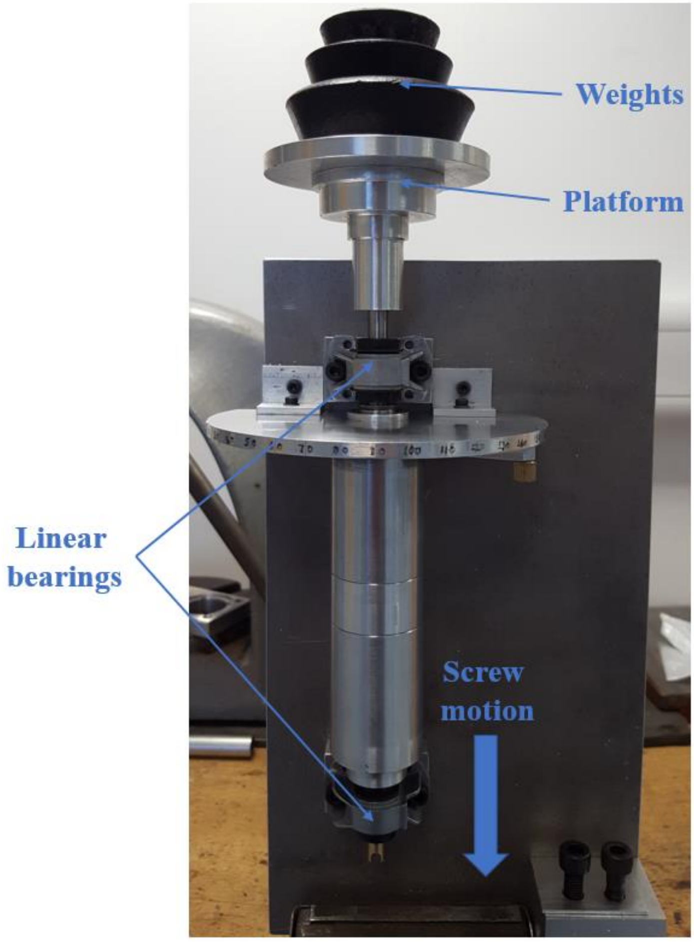

Fig. 5.31: Test rig placed in vertical position for measuring maximum thrust force.

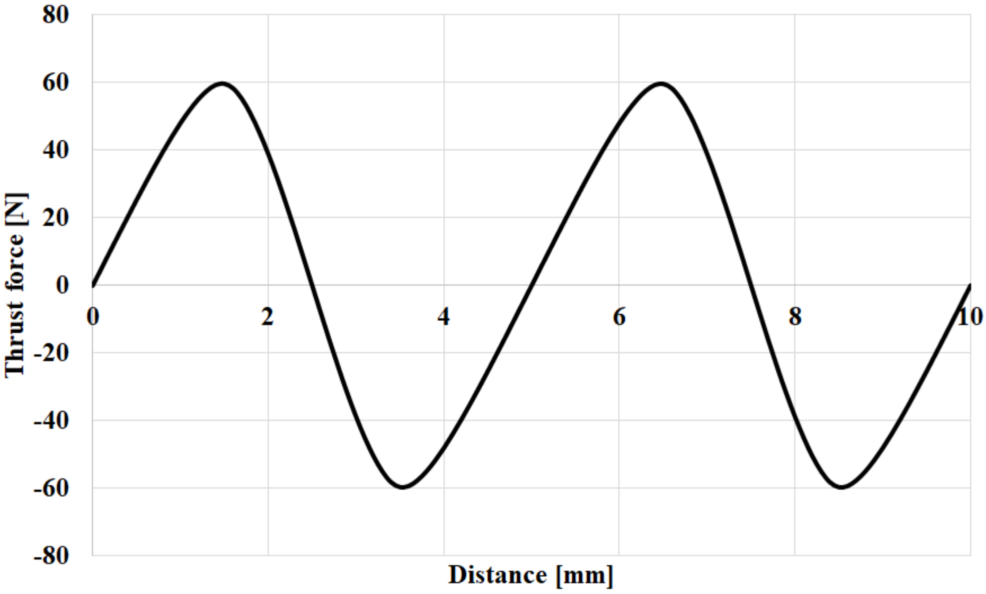

Fig. 5.32: Thrust force from Maxwell's model for magnet-to-reluctance type MLS assuming that the test rig parameters are ideal.

Table 5.1: Dimensions and parameters for magnet-to-reluctance type MLS model.

Back-iron thickness	4 mm
Air-gap	1 mm
Magnet thickness	1.5 mm
Pole-pitch	5 mm
Magnet pole-pairs	4
Iron thread depth	3 mm
Iron thread width	1 mm
Magnet type	N45SH
Remanence	1.32 T
Coercivity	979 kA/m
Magnet density	7500 kg/m^3
Magnet resistivity	180 μΩ.cm
Mild steel density	7860 kg/m^3
Mild steel conductivity	6289308 S/m

Fig. 5.33: Measuring the width of screw threads.

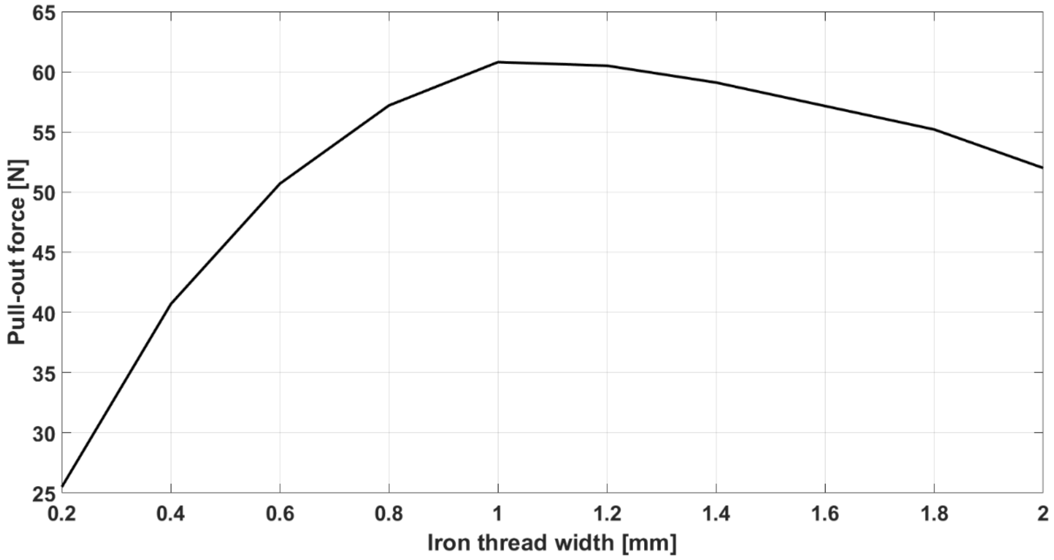

Fig. 5.34: Variation of the pull-out force with the iron thread width.

The measured dimensions of the magnets and screw are now included in the model, and the remanence is now reduced to 1.25T to reflect the measured density. Furthermore, the magnets are divided into three regions inner, outer, and middle regions. Each region is divided into five parts assuming fully saturated part in the middle and the lowest saturated part is on the edge as shown in Fig. 5.35. The chosen dimensions of the saturated parts are as per Fig. 5.17. Fig. 5.36 shows the distribution of magnetisation assumed in the updated model. Fig. 5.37 shows that, the predicted output pull-out force is reduced from 60N to 42N. Also, an average value of the transmitted force generated by the test rig from method 1 and 2 is generated. The assumptions taken in the simulation have a significant effect on the thrust force, however, further reduction in thrust force would occur if the experimental magnets are not fully anisotropic.

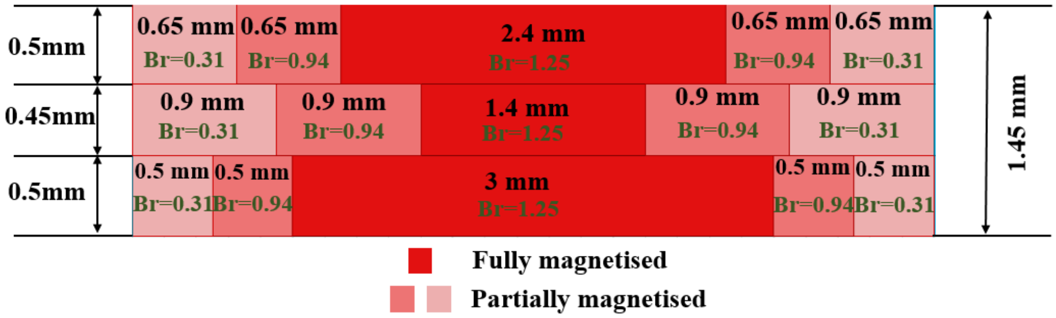

Fig. 5.35: North pole magnet assuming fully magnetised parts in the middle and lower magnetised parts on the edge.

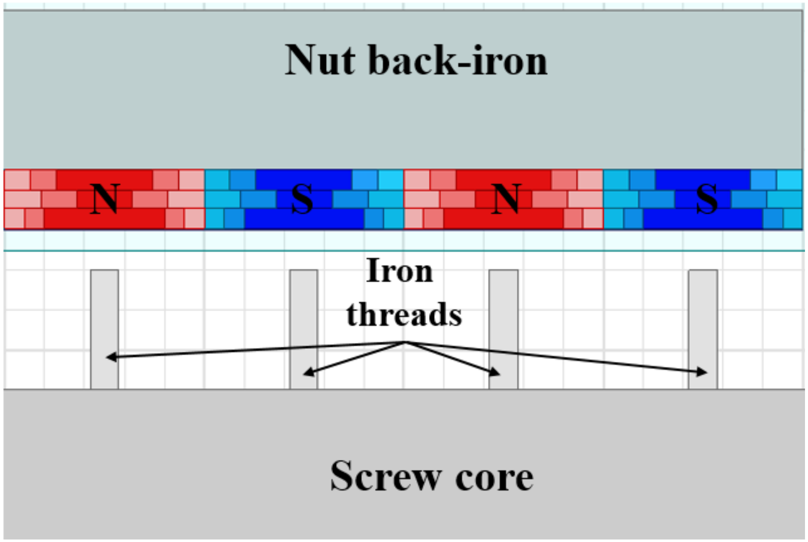

Fig. 5.36: The updated MAXWELL model.

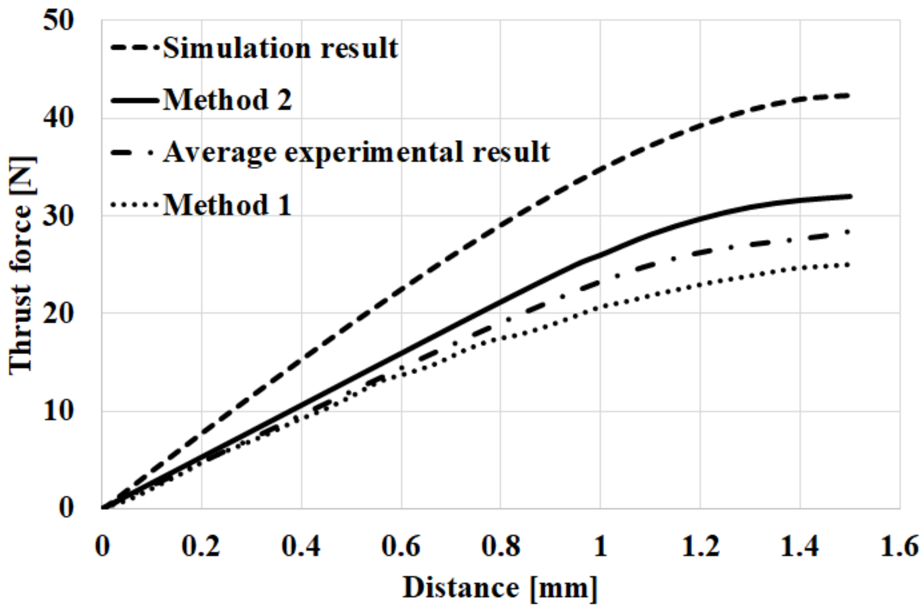

Fig. 5.37: Thrust force generated from test rig and the updated MAXWELL model.

5.5 Conclusion

This chapter presented the design and manufacturing of single conductor double sided fixture employed for magnetising cylindrical magnet to produce helically shaped magnetisation distribution. Fabrication procedures are discussed in details including the magnetisation process that is carried out at the UNIVERSITY OF SHEFFIELD and ARNOLD MAGNETICS COMPANY. A MATLAB/SIMULINK model is developed to predict the magnetising current waveform and taking into consideration the effect of temperature on resistance.

In addition, the magnetised magnet is assembled with a reluctance type MLS and integrated with a test rig manufactured in the work shop of the UNIVERSITY OF SHEFFIELD. The aim of using the test rig is to measure the maximum transmitted force generated from the MLS. In order to eliminate the effects of stiction, two methods are carried out for determination of the maximum transmitted force. The prototype is checked and the parameters of the simulation model are updated, which resulted in a significant drop in the simulated transmitted force. The updated parameters are related to iron thread width, magnet material, magnet dimension, and the assumed saturated volume of the magnet after the magnetisation process. The prototype was very sensitive to any variation occurs in the hardware model. The tolerances in manufacturing and magnet’s magnetic pattern needs more control as this will recover much of gap in performance prediction.

6 Case study – application for UAV launch

6.1 Introduction

A potential application using a MLS is the launch of a UAV. The launch process using a MLS hasn't been reported and systems used for launching UAVs are mini-launchers, manual launchers, universal UAV launchers and heavy launchers for large UAVs [20] as shown in Fig. 6.1. The proposed UAV launched by the MLS is used for crop inspection in agricultural fields, which includes taking video and still pictures that can be stored on board or transmitted wirelessly. A selected UAV of typical mass of 3.2 kg and required launch velocity of about 8 m/s is selected as a case study for launching a UAV using a MLS. The UAV model is EMT Aladin with 1.46 m wingspan and 1.53 m length as shown in Fig. 6.2 [104]. The selected UAV is attached to a platform mounted on the translator of the proposed MLS which is rotated by an external motor as shown in Fig. 6.3. The force required to launch the UAV at a speed of 8 m/s as previously mentioned in [104], within a specified value of force must be determined.

First, the aerodynamic drag force is calculated by:

$$F_d = 0.5 \times C_d \times A_f \times \rho_a \times V^2 \tag{6.1}$$

where, C_d is the non-dimensional drag coefficient, A_f is the frontal area facing the air flow in m^2, ρ_a is the air density in kg/m^3 and V is the velocity of the model in m/s.

Fig. 6.1: Types of UAV launchers: (a) mini-launcher, (b) hand launching, (c) heavy launcher and (d) universal launcher [20].

Fig. 6.2: EMT Aladin UAV model [104].

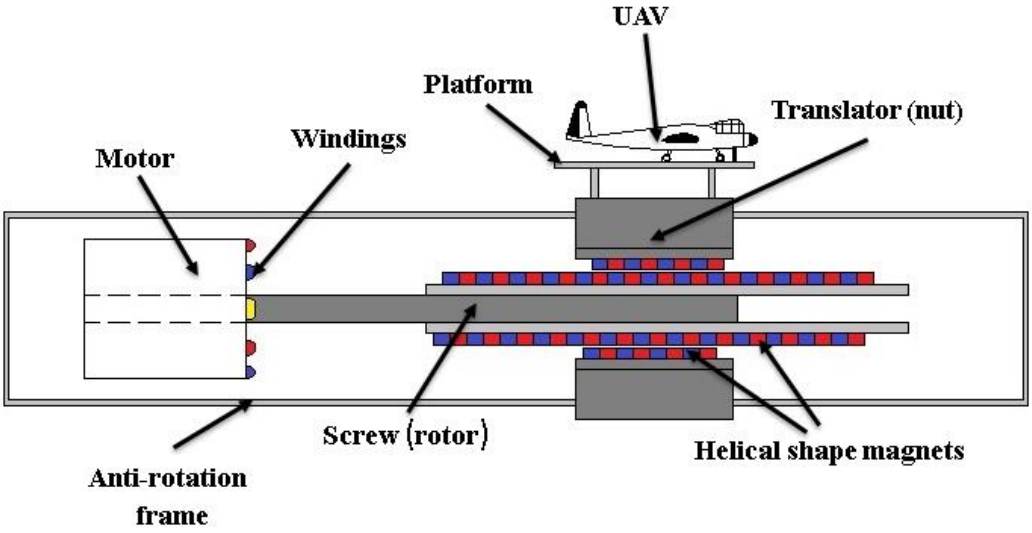

Fig. 6.3: Proposed MLS model.

Assuming that the model is divided into three parts [105, 106]:

a) The streamlined body (wings) of the UAV with drag coefficient of 0.04.

b) Elliptical fuselage of the UAV with drag coefficient of 0.6.

c) Rectangular shape platform on which the UAV will be mounted over it during launching with drag coefficient of 1.5.

By using (6.1) the aerodynamic drag force at 8 m/s is estimated to be 2.5 N. In addition to the drag force, the force required to accelerate the combined mass of the nut, the UAV and the platform is given by:

$$F = m_t \times a \tag{6.2}$$

$$m_t = m_{UAV} + m_{nut} + m_{platform} \tag{6.3}$$

where, m_{UAV} is the mass of the UAV, m_{nut} is the mass of the nut and $m_{platform}$ is the mass of the platform.

According to the equation of motion, under constant acceleration, velocity and acceleration are related by:

$$V^2 = V_o + 2as \tag{6.4}$$

where V_o is the initial velocity (equals to zero), s is the travelled distance before take-off, and the acceleration is then given by:

$$a = {}^{V^2}\!/_{2s} \tag{6.5}$$

The total required force can be calculated as the sum of the drag force and the force required to accelerate the total mass:

$$F_t = F + F_d \tag{6.6}$$

However, the motor is required to produce a torque in order to overcome the total force F_t, as well as the inertial load due of the inertia of the rotating screw. Total inertia referred to the shaft of the motor, which includes the inertia of the screw and the motor, as well as the equivalent inertia of sliding masses, i.e. nut, platform, and UAV, is given by:

$$J_{total} = J_{screw} + J_{nut} + J_{motor} + J_{load} \tag{6.7}$$

$$J_{nut} = m_{nut} \times (\frac{\lambda}{2\pi})^2 \tag{6.8}$$

$$J_{load} = m_{load} \times (\frac{\lambda}{2\pi})^2 \tag{6.9}$$

J_{screw} and J_{motor} are the inertias of the screw and motor, respectively, J_{nut} is the equivalent inertia of the nut and J_{load} is the equivalent inertia of the load including mass of UAV and the platform.

Therefore, the torque produced by the motor is given by:

$$T_{motor} = \left(J_{total} \times \left(\frac{2\pi}{\lambda}\right) \times a\right) + (F_d \times \left(\frac{\lambda}{2\pi}\right)) \tag{6.10}$$

As discussed in chapter 2, the MLS can be built in different ways:

1) Magnet-to-magnet type MLS.
2) Reluctance type MLS.

For each type, optimization in design needs to take place to achieve the optimum dimensions for a successful launch of the selected UAV. However, before optimization, the relationship between screw parameters and its effect on the torque, force, and inertia (that needed to be overcome) must be discussed to provide a general framework on the performance of the launch system.

6.2 Magnet-to-magnet MLS

In the analysis, for magnet-to-magnet type MLS, achievable shear stress is assumed to be between 100 to 250 kN/m^2 corresponding to leads varying from 5 to 20 mm as previously mentioned in chapter 2. For a chosen shear stress, e.g 150 kN/m^2, and lead of 15 mm, the effect of variation of screw diameter and screw length on the required force, inertia of screw, required torque and lead length can be shown in Fig. 6.4 to Fig. 6.7.

As shown in Fig. 6.4, the higher value of required force is associated with lower length of screw and higher screw diameter. The stepping in the values of the required force is related to the integer number of the leads chosen for the nut length (i.e. one lead is equal one pole-pair). Also, in Fig. 6.5, the inertia of screw is affected by large dimensions of screw. As diameter and length of screw get higher, inertia of screw is increased and higher torque is required for successful launch.

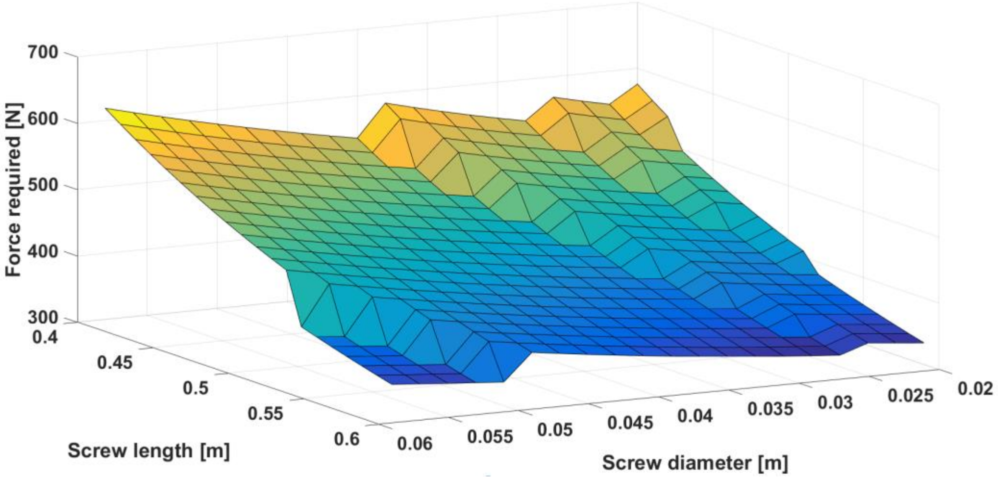

Fig. 6.4: Variation of required force with screw diameter and length for magnet-to-magnet MLS.

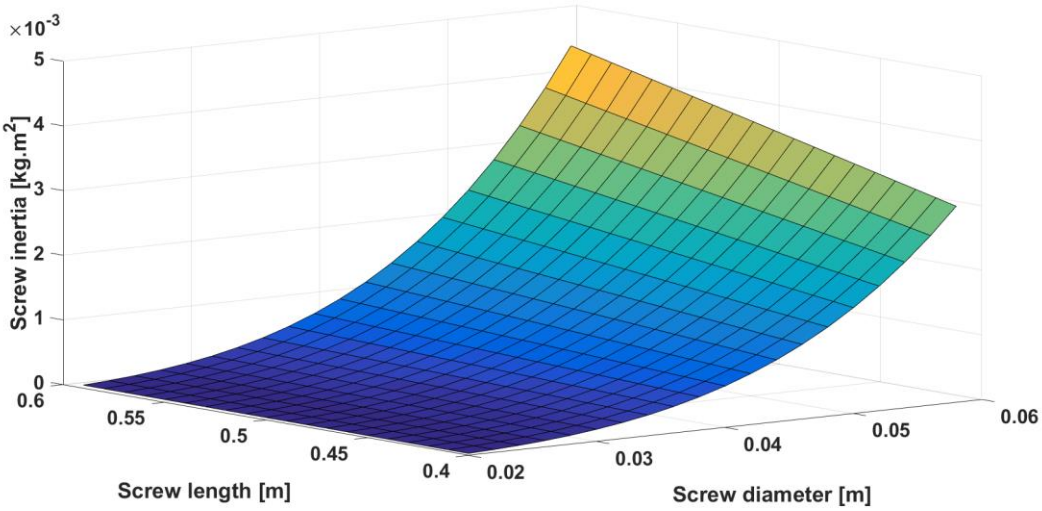

Fig. 6.5: Variation of screw inertia with screw diameter and length for magnet-to-magnet MLS.

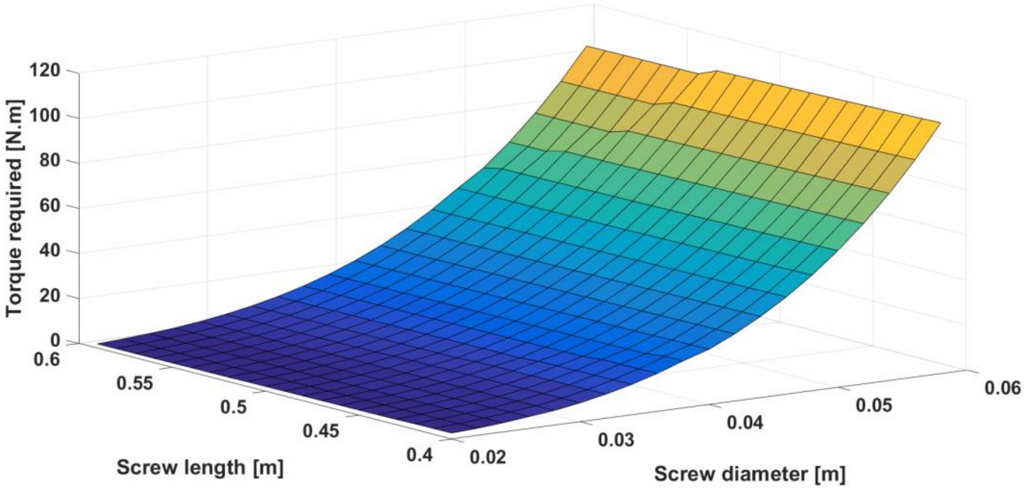

Fig. 6.6: Variation of required torque with screw diameter and length for magnet-to-magnet MLS.

In Fig. 6.6, the torque required for successful launch increases with the screw diameter. Predictions for nut length is also included as seen in Fig. 6.7, where at given diameter and length of the screw a specific nut length is recommended for a successful launch.

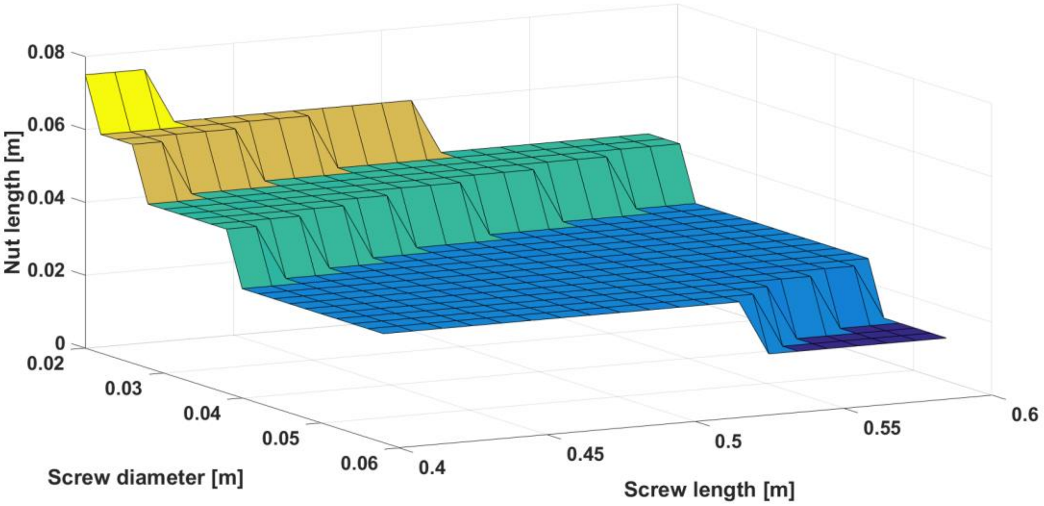

Fig. 6.7: Variation of nut length with screw diameter and length for magnet-to-magnet MLS.

6.3 Magnet-to-reluctance

For magnet-to-reluctance type MLS, achievable shear stress is assumed to be between 40 to 60 kN/m^2 for leads varying from 10 to 20 mm as previously mentioned in chapter 2. For a shear stress, e.g 60 kN/m^2, and lead of 15 mm, the effects of varying screw diameter and screw length on the required force, inertia of screw, required torque, and lead length are investigated.

In Fig. 6.8, the length of the screw is starting to vary from 500 mm as a minimum limit for a successful launch. The transmitted force gained from a magnet-to-reluctance MLS might fail to meet the required force at the initial screw length. At this point, magnet thickness and pole-pitch are the corresponding parameters in which their variation may generate the required force for a successful launch. In Fig. 6.9, it can be seen that the inertia of screw for magnet-to-reluctance MLS is lower than that of magnet-to-magnet MLS.

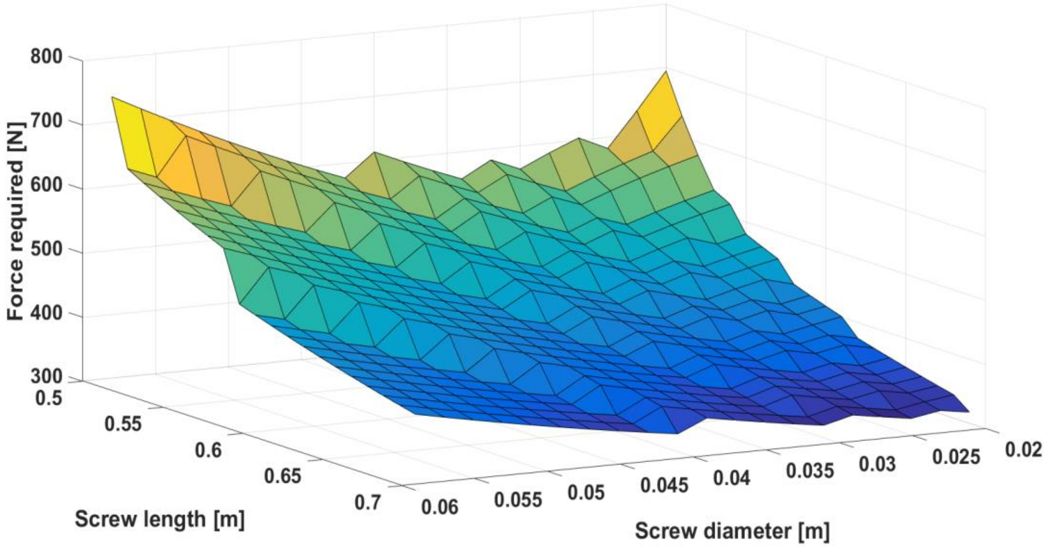

Fig. 6.8: Variation of force required with screw diameter and length for magnet-to-reluctance MLS.

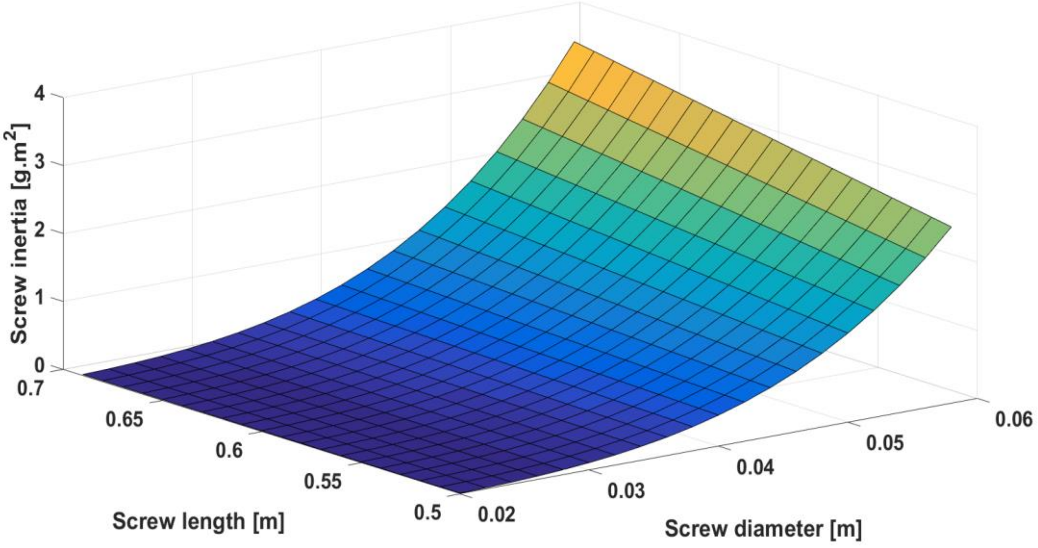

Fig. 6.9: Variation of screw inertia with screw diameter and length for magnet-to-reluctance MLS.

In Fig. 6.10, the torque required for successful launch also increases with increased screw diameter. As screw diameter increases, higher torque is required to overcome mass and inertia. A magnet-to-reluctance MLS requires lower torque than a magnet-to-magnet MLS to ensure a successful launch.

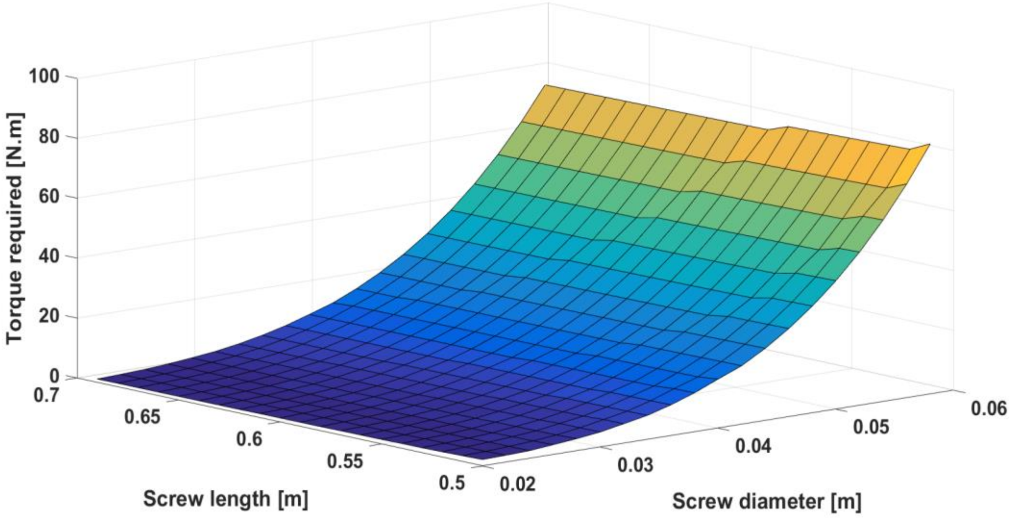

Fig. 6.10: Variation of torque required with screw diameter and length for magnet-to-reluctance MLS.

In terms of nut length, a magnet-to-reluctance MLS requires longer nut length than a magnet-to-magnet MLS to achieve successful launch. In comparison to magnet-to-magnet MLS, a magnet-to-reluctance MLS may require 13 pole-pairs, as shown in Fig. 6.11, at the same time that a magnet-to-magnet MLS requires 4 pole-pairs for successful launch, as shown in Fig. 6.7, if 15 mm lead, 20 mm diameter and 500 mm screw length are selected.

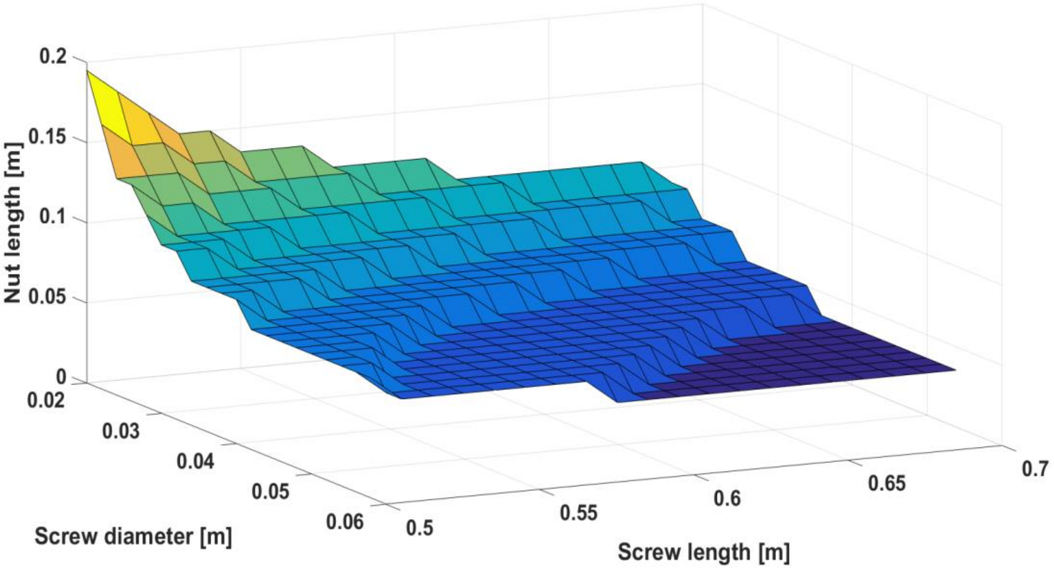

Fig. 6.11: Variation of nut length with screw diameter and length for magnet-to-reluctance MLS.

6.4 Effect of screw deflection

The deflection of the screw beam from its centre axis is also an important parameter in the design of the MLS which must be taken in consideration. The deflection is affecting the air-gap length between the screw core and the nut. The deflection is maximum at the centre of the screw beam if it is supported from both ends. As shown in Fig. 6.12, the screw is assumed to be supported at both ends and under a uniformly distributed load over its length.

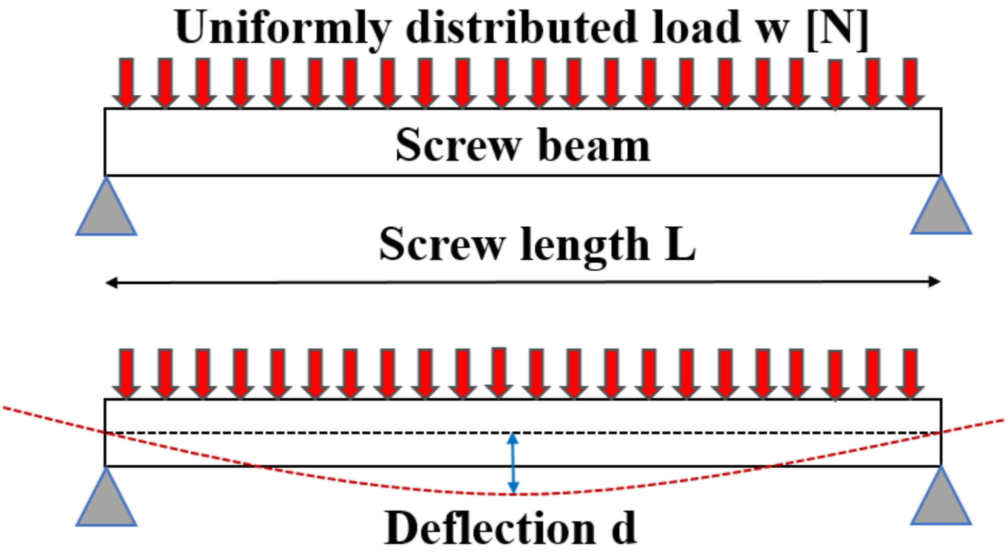

Fig. 6.12: Uniformly distributed load on the screw beam.

The maximum deflection caused by the uniformly distributed load w [N] can be calculated as follows [107]:

$$d = \frac{5wL_b^3}{384EI_m} \tag{6.11}$$

The formula in (6.11) is calculated using the double integration method of the moment [108] as follows:

$$d = \iint \frac{M(x)d^2x}{EI_m} \tag{6.12}$$

where, d is the maximum deflection from the centre axis caused by the load applied on the screw beam, M(x) is the moment at distance x along the screw length, E is Young's modulus of elasticity of the beam's material, I_m is the area moment of inertia of the beam, L_b is the length of the beam, and w is the weight of the beam in Newtons.

The deflection is mainly affected by the cube of length "L_b", as shown in (6.11), of the screw. Fig. 6.13, shows the variation of deflection with screw diameter and length under the effect of the weight of the screw beam only (uniformly distributed load). As shown in the figure, the deflection can reach to 12 mm at screw length of 2 m and diameter of only 10 mm.

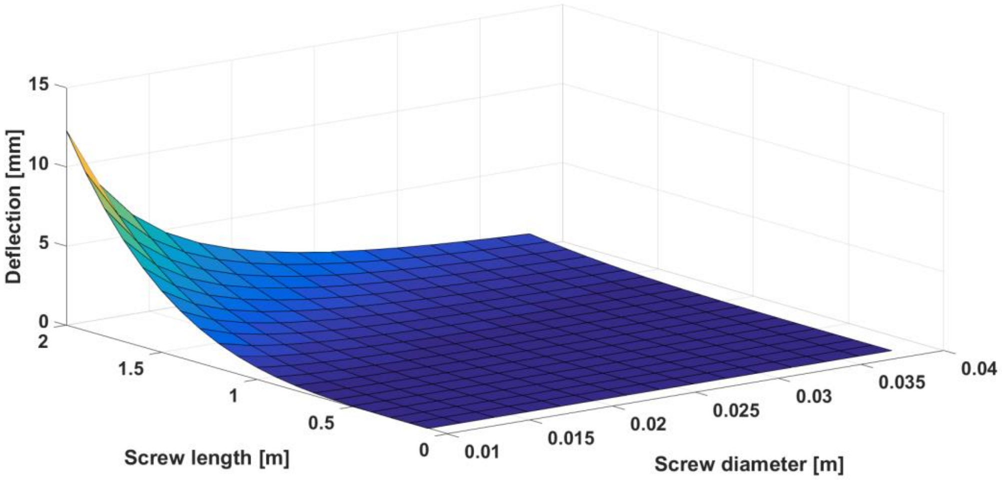

Fig. 6.13: Variation of deflection with screw diameter and length under the effect of the distributed load along the screw beam.

In addition to the uniformly distributed load on the screw beam, the beam is also affected by the magnetic force of unbalanced magnetic pull when the nut reaches the position of maximum deflection d. In this case the air-gap between the screw and the nut is not the same around the circumference. The magnetic force can be considered as concentrated point load to be added to the uniformly distributed load during deflection calculation as shown in Fig. 6.14.

In this case the maximum deflection caused by both uniformly distributed load and concentrated point load at the centre can be calculated as follows [109]:

$$d = \frac{5wL_b^3}{384EI_m} + \frac{F_cL_b^3}{48EI_m} \tag{6.13}$$

where, F_c is the concentrated point load at the centre of the beam screw.

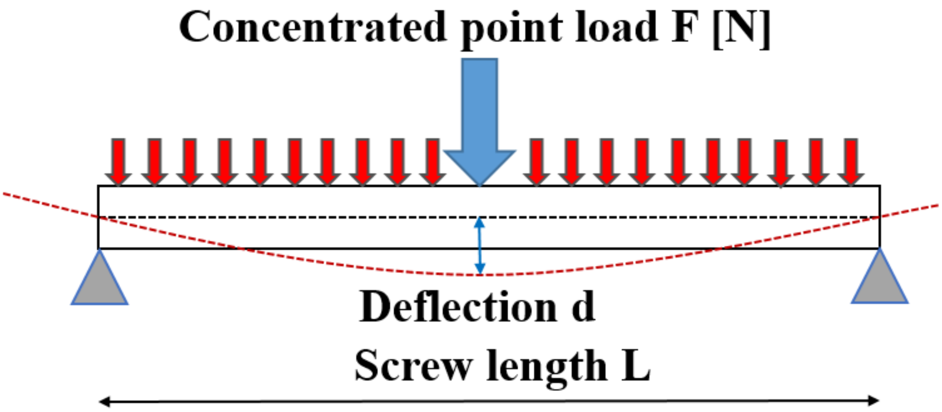

Fig. 6.14: Uniformly distributed load on the screw beam with concentrated point load at the centre.

To show the effect of the magnetic force in Y direction, the screw is assumed to move in +ve Y direction with offset distance as shown in Fig. 6.15.

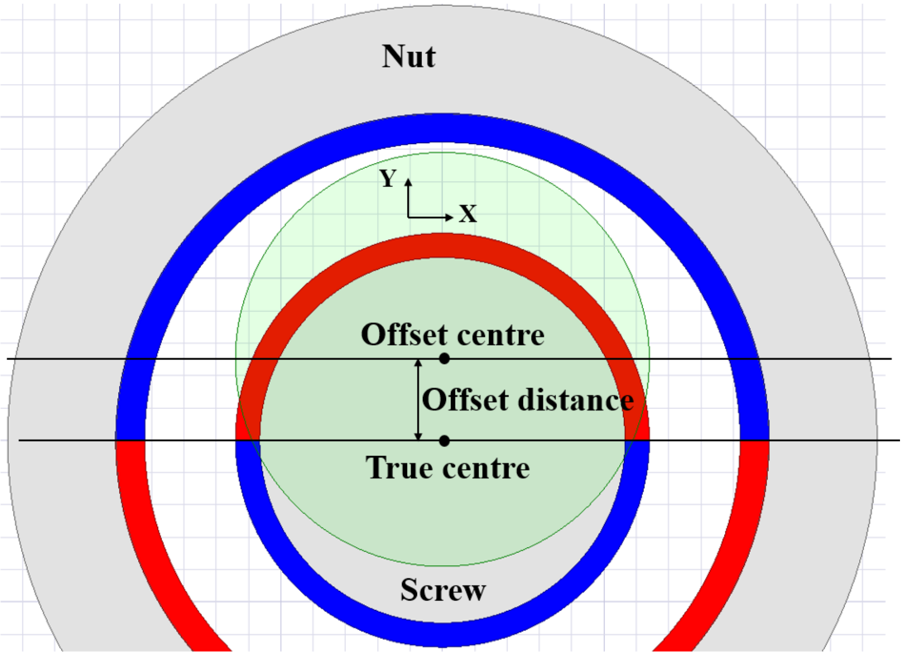

Fig. 6.15: Offset distance in Y direction.

For an air-gap of 1 mm between the nut and the screw and the magnets used in the experimental work, the offset distance is varied between zero and 0.7 mm so that the gap between the screw and the nut is 0.3 mm in the +ve Y direction and 1.7 mm in the –ve Y direction for maximum offset of 0.7 mm as shown in Fig. 6.16.

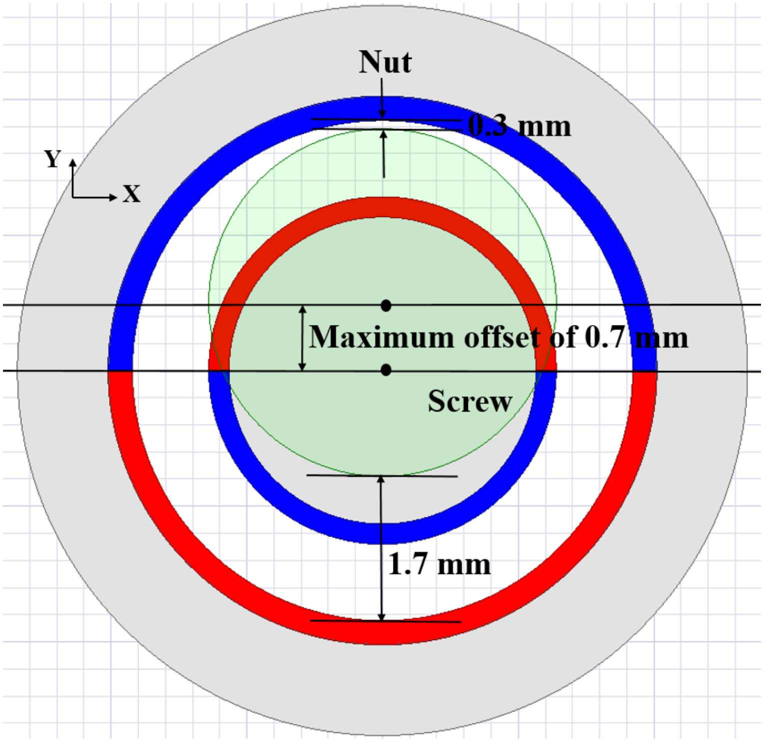

Fig. 6.16: Maximum offset distance in Y direction.

Fig. 6.17 and Fig. 6.18 show the force in Y direction which adds on the weight of the screw beam. Results are generated for magnet-to-magnet and magnet-to-reluctance MLS at zero and maximum transmitted force positions. As the offset increases, the generated force in Y direction also increases which changes the air-gap over the circumference. In this case equation (6.13) can be rewritten as follows:

$$d = \frac{5wL_b^3}{384EI_m} + \frac{kdL_b^3}{48EI_m} \qquad (6.14)$$

$$d = \frac{5wL_b^3}{384EI_m} / [1 - \frac{kL_b^3}{48EI_m}] \qquad (6.15)$$

where, k is the slope of the curve drawn in Fig. 6.17 and Fig. 6.18, which shows the variations of the unbalanced magnetic force for the magnet-to-magnet and the magnet-to-reluctance MLS, respectively. For the 500 mm magnet-to-reluctance MLS with 20 mm diameter, as an example, the maximum deflection that might occur as a result of the uniformly distributed load on the screw beam with the concentrated point load at the centre of the beam is 12 µm, as calculated by (6.15), which has no significant effect on electromagnetic performance.

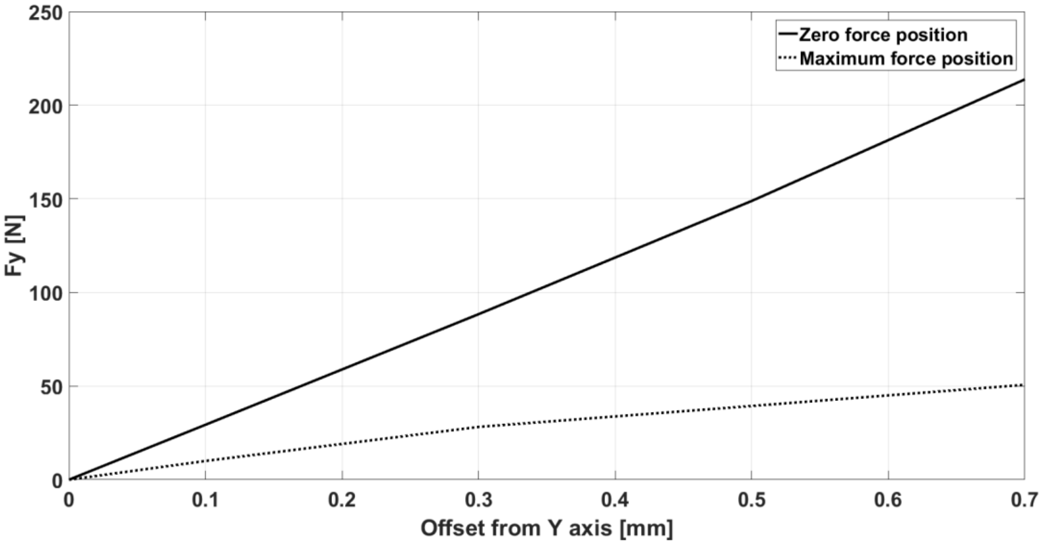

Fig. 6.17: Variation of magnetic force in Y direction with offset for magnet-to-magnet type MLS.

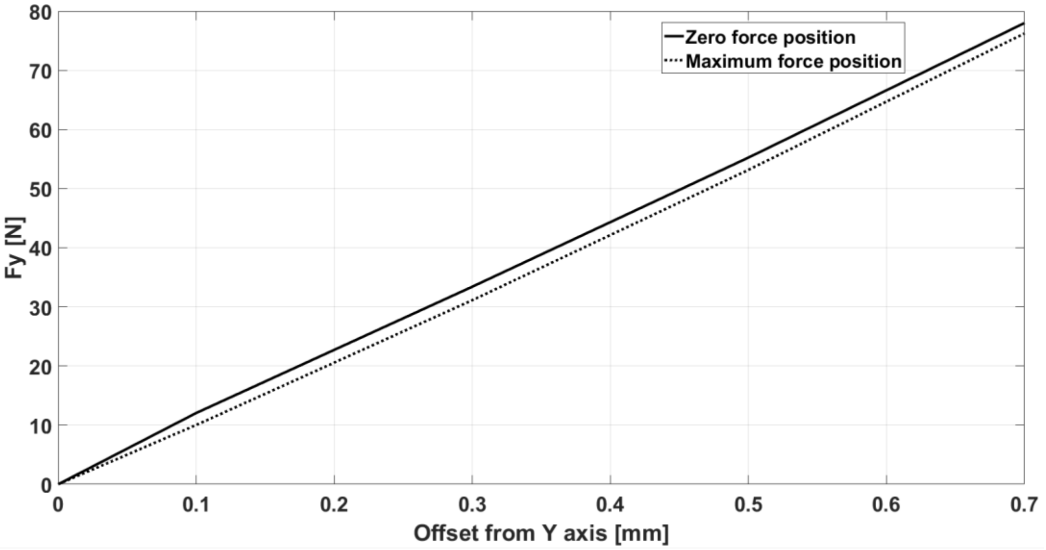

Fig. 6.18: Variation of magnetic force in Y direction with offset for magnet-to-reluctance type MLS.

6.5 Detailed case study

At this stage, an example is chosen to show the relationship between the variation of the screw diameter and its effect on the torque, force, and inertia (that needed to be overcome) for a successful launch. The length of the screw is assumed to be fixed at 500 mm where the deflection of the screw can be neglected as shown in Fig. 6.13. By choosing a constant lead of 15 mm and magnet thickness of 1 mm, for example, the variation of the required force and the pull-out force with the change in diameter of screw for different pole-pairs on the nut for a magnet-to-magnet MLS are investigated. It can be seen that, for one pole-pair, as shown in Fig. 6.19 to Fig. 6.22, the pull-out force is much lower than the force required for successful launch. However, for two pole-pairs, the gap between the required and pull-out forces is declining but still the pull-out force is unable to achieve successful launching. For three pole-pairs, a successful launching could be achieved if the diameter of screw is larger than 37 mm, at that moment, the pull-out force is higher than the required force. Also, a successful launching process could be achieved when the diameter of the screw is larger than 26 mm for four pole-pairs. The larger number of pole-pairs applied, the lower diameter of screw could be utilised and therefore, lower inertia is achieved and lower motor torque is required.

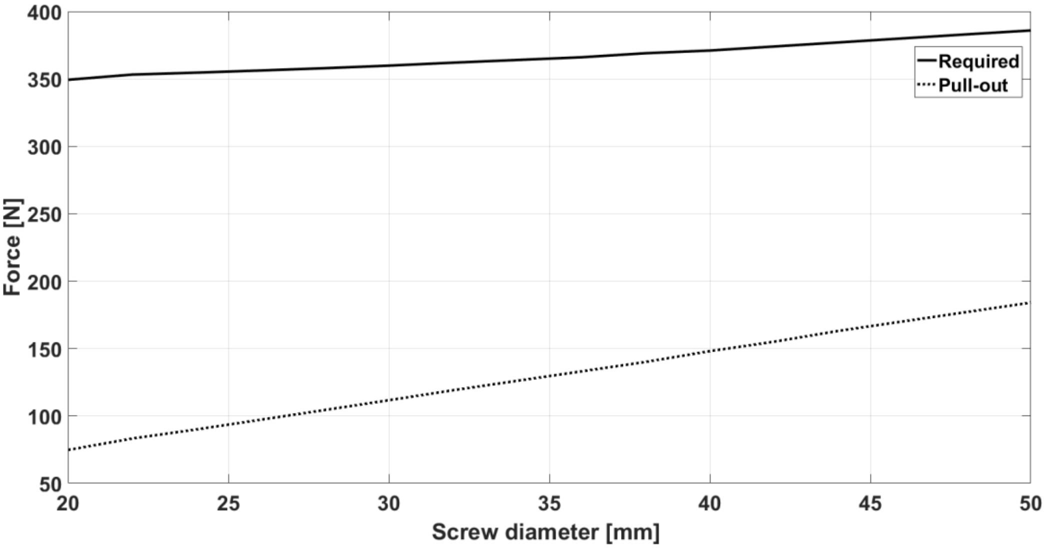

Fig. 6.19: Variation of required and pull-out forces with diameter of screw for one pole-pair and lead = 15 mm.

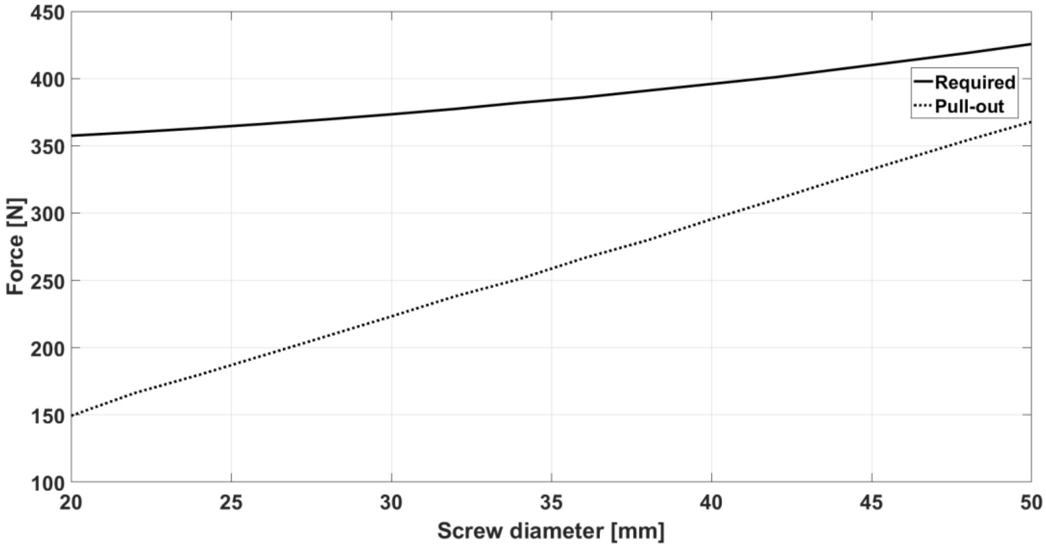

Fig. 6.20: Variation of required and pull-out forces with diameter of screw for two pole-pairs and lead = 15 mm.

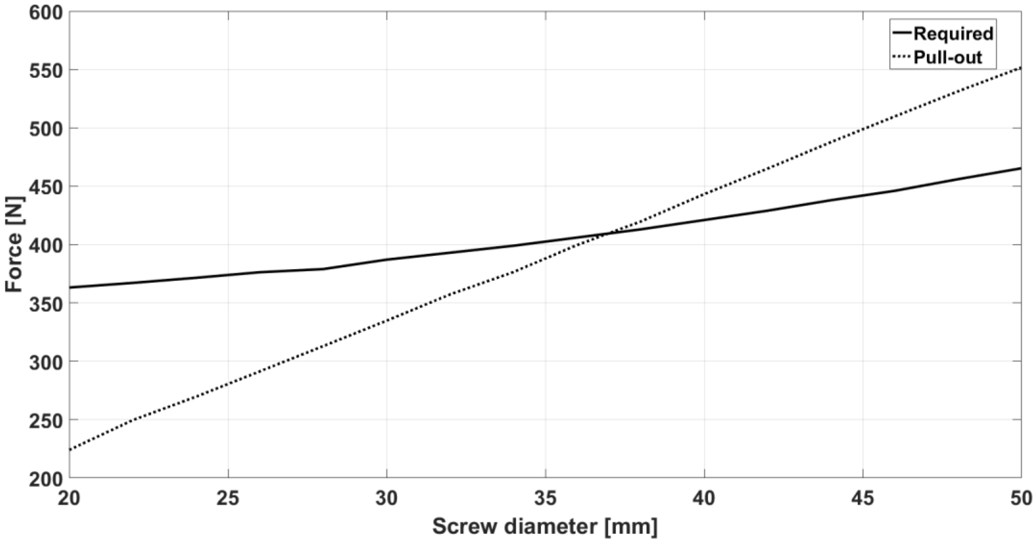

Fig. 6.21: Variation of required and pull-out forces with diameter of screw for three pole-pairs and lead = 15 mm.

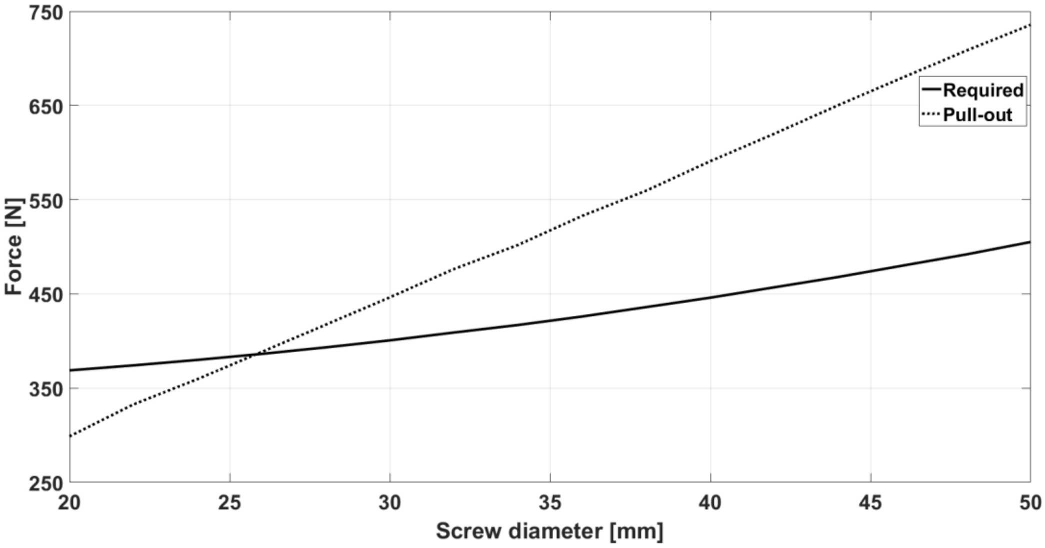

Fig. 6.22: Variation of required and pull-out forces with diameter of screw for four pole-pairs and lead = 15 mm.

Fig. 6.23, shows the variation of the motor torque with the diameter of the screw, where it can be seen that the effect of the number of poles on the nut, the mass of the nut, platform and UAV on the torque are negligible, and the required torque is dominated by the inertia of the 500 mm screw, as could be seen in Fig. 6.24, which show the variation of the screw inertia with the diameter of the screw.

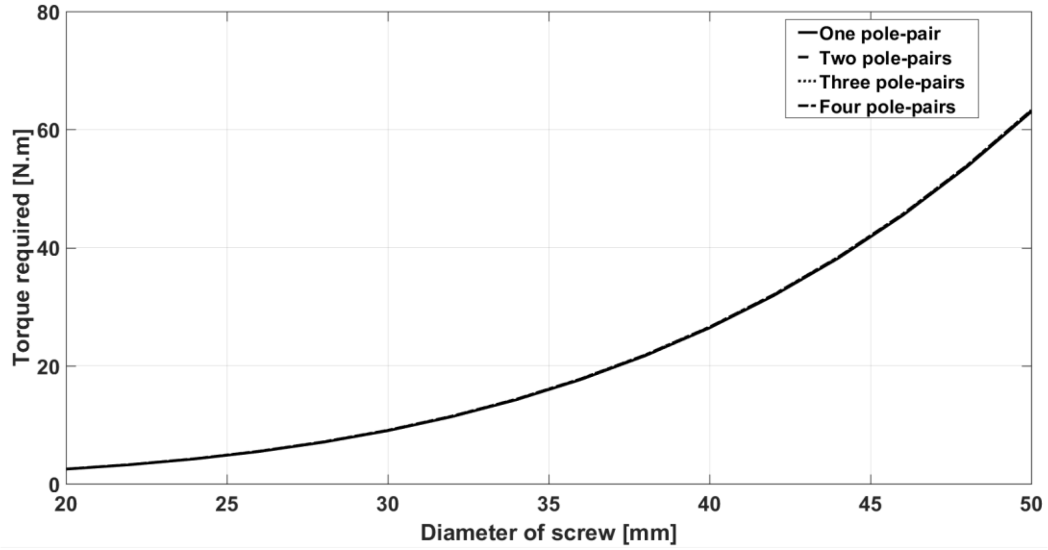

Fig. 6.23: Variation of required torque with diameter of screw for lead = 15 mm.

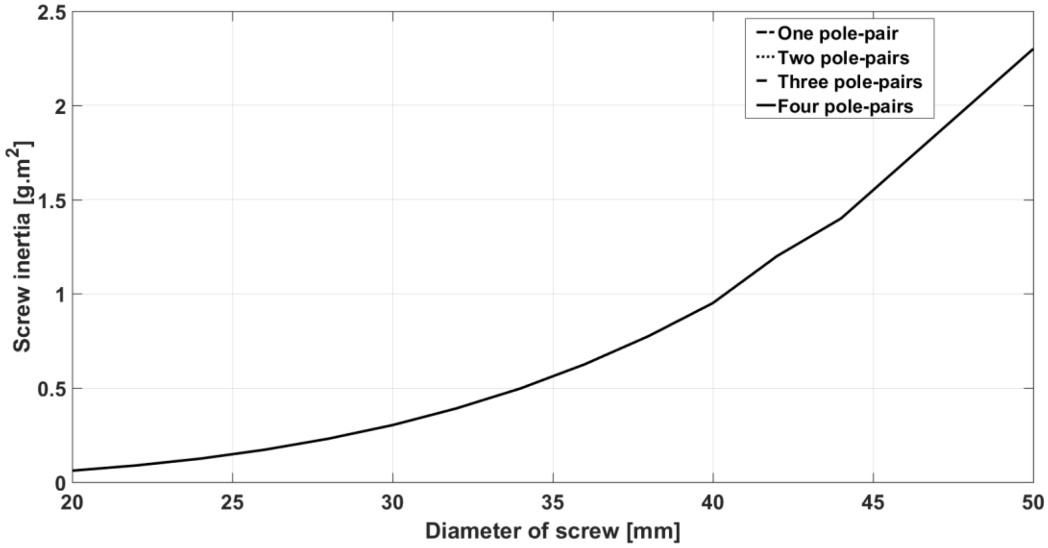

Fig. 6.24: Variation of screw inertia with diameter of screw for lead = 15 mm.

In order to investigate the effect of the lead, a 20 mm lead is chosen for example, and the length of the screw is fixed at 500 mm. The behaviour obtained from the variation of screw diameter at different pole-pairs with the required force is similar to that as in lead = 15 mm as shown in Fig. 6.25 to Fig. 6.28, however, the values of required force are higher than lead = 15 mm as the force is dependent on the mass and volume of screw. It can be seen that, for higher pole-pairs, the required force can be achieved easily for smaller screw diameter which can be translated into lower volume, mass, inertia, magnets, cost, and motor torque requirements. Although the lead is changed, similar torque characteristics can be obtained, as shown in Fig. 6.29. It can be seen that, as diameter increases, a higher motor torque is required to overcome the additional inertia and volume added as a load.

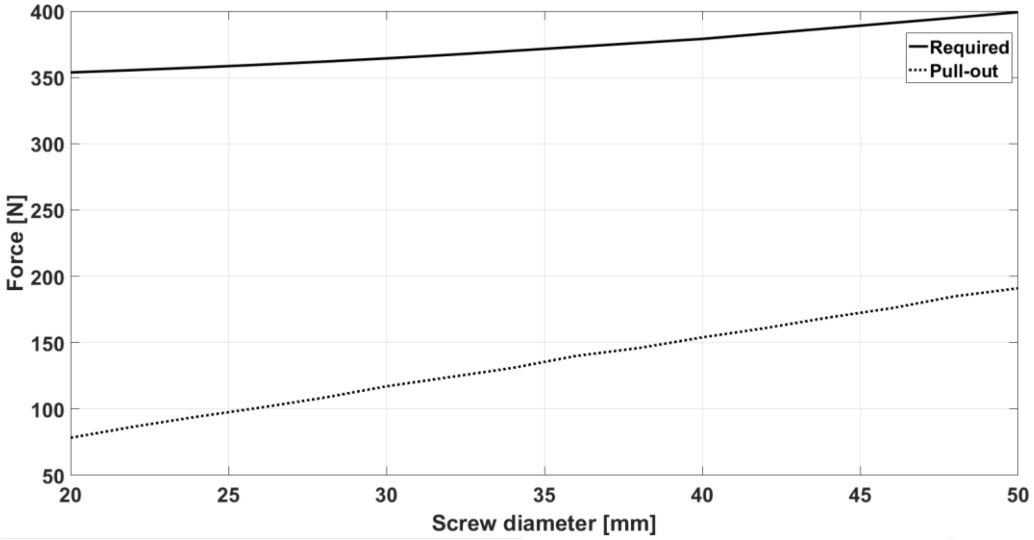

Fig. 6.25: Variation of required and pull-out forces with diameter of screw for one pole-pair and lead = 20 mm.

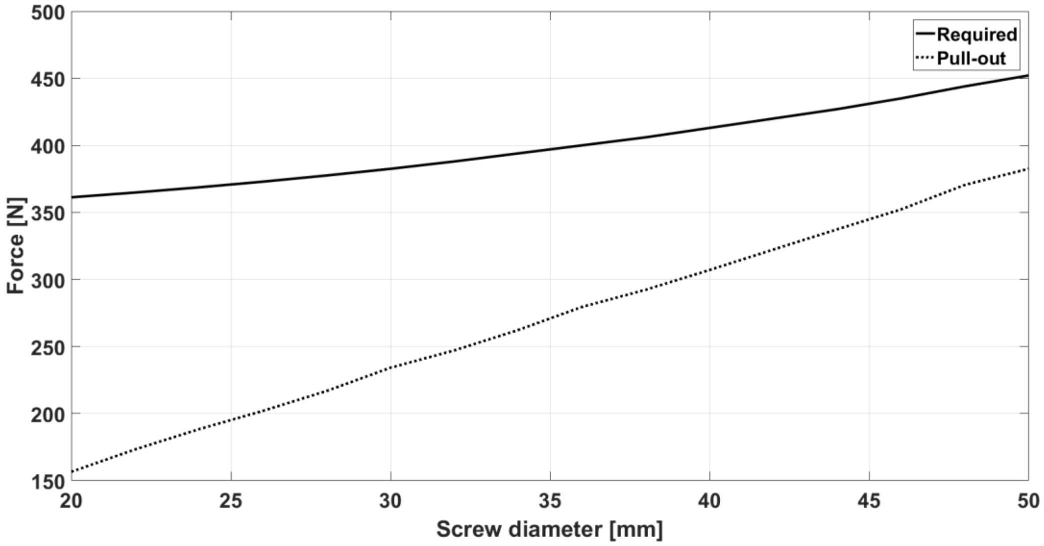

Fig. 6.26: Variation of required and pull-out forces with diameter of screw for two pole-pairs and lead = 20 mm.

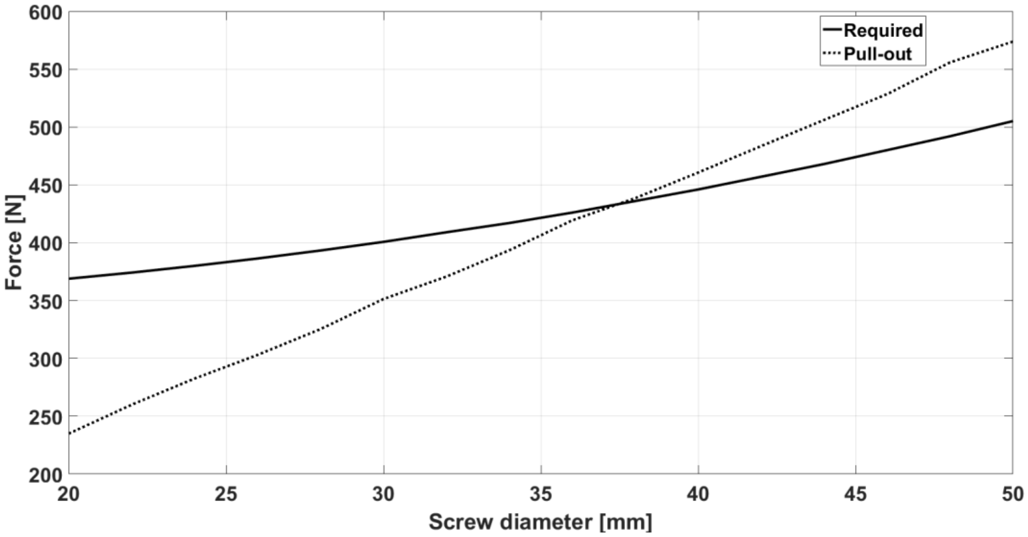

Fig. 6.27: Variation of required and pull-out forces with diameter of screw for three pole-pairs and lead = 20 mm.

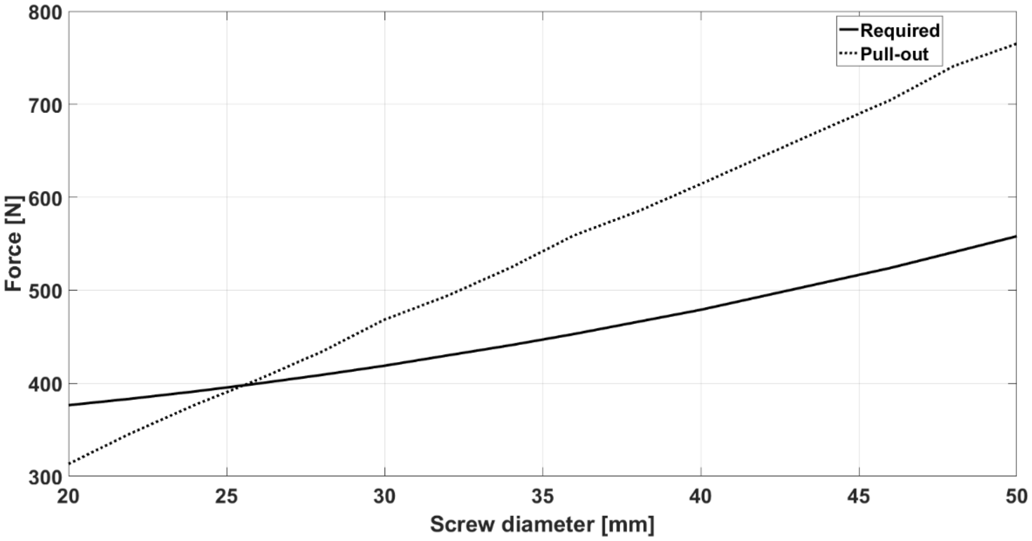

Fig. 6.28: Variation of required and pull-out forces with diameter of screw for four pole-pairs and lead = 20 mm.

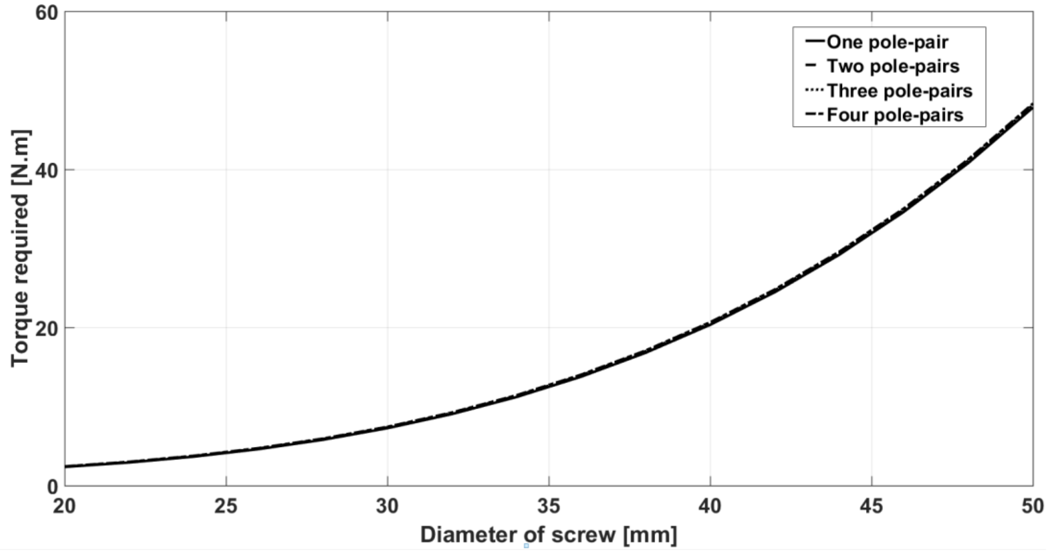

Fig. 6.29: Variation of required torque with diameter of screw for lead = 20 mm.

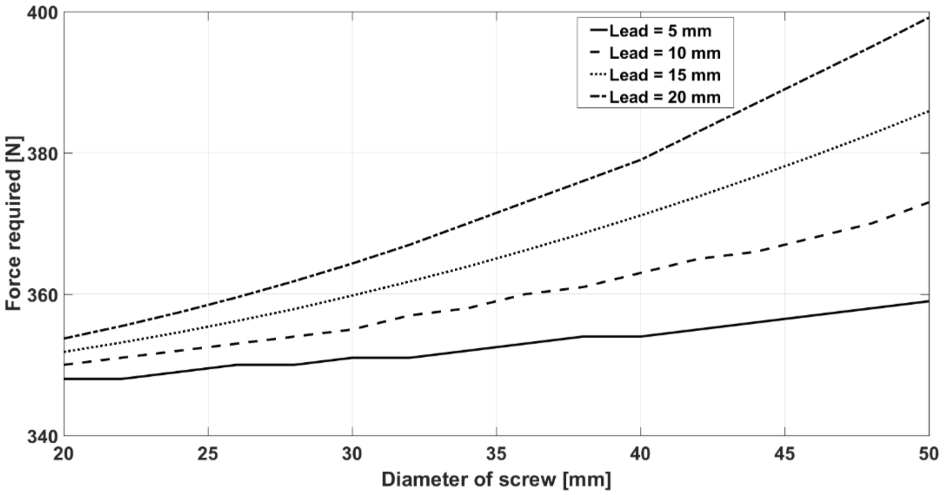

Fig. 6.30: Variation of required force with diameter of screw for one pole-pair at different leads.

To get a complete picture of the effect of changing the screw diameter on the required force, torque, and inertia (that needed to be overcome), the number of pole-pairs is fixed at one pole-pair and the lead is varied from 5 to 20 mm by step 5 mm. The variation of the required force against the change in diameter of screw for different lead can be shown in Fig. 6.30. It can be seen that, as the lead increases the value of the force that is needed to accelerate the UAV is increasing as the force required is affected by the length of the nut.

Finally, the behaviour of the torque against the change in the diameter of the screw for one pole-pair can be seen in Fig. 6.31. The rate of increase in torque for lower lead is much higher than the rate of increase of torque with higher lead, that’s because the inertia increases proportionally with lower lead values.

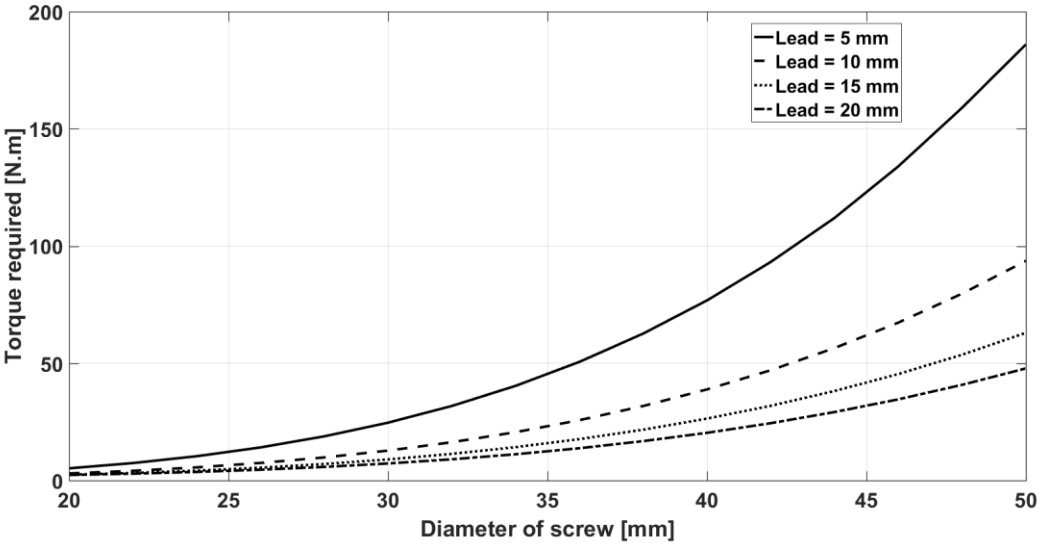

Fig. 6.31: Variation of required torque with diameter of screw for one pole-pair at different leads.

6.6 Conclusion

A case study concerned with the application of MLS to the launch of a UAV is presented. It is shown that, similar behaviour of variation of torque, force, and inertia with diameter of screw is observed for reluctance and magnet-to-magnet type MLS. Although in reluctance type MLS the shear stress is lower than that of magnet-to-magnet MLS, the inertia of screw and torque required are lower than that of magnet-to-magnet MLS.

In summary, for successful launch, reluctance type MLS provides lower inertia and as a result lower motor torque required in addition to the lower cost associated with the reduced usage of magnet material.

7 Conclusions and future work

In this thesis, the MLS is introduced in its three main types, magnet-to-magnet, magnet-to-reluctance and magnet-to-conductor MLS. Investigation on pull-out force and shear stress is carried out on each type of MLS. Variations of the shear stress and the thrust force with air-gap, magnet thickness, and lead are investigated. Accordingly, the recommended types of MLS are chosen based on the results.

In addition, a novel impulse magnetisation technique is proposed and utilised for magnetising a cylindrical shape magnet to generate a helical shape magnetic field instead of using small curved magnets for generating the same helical magnetisation distribution. Different fixture configurations are considered and the design parameters for the magnetising fixture are investigated. In addition, a MATLAB/SIMULINK model is developed to predict the magnetising current waveform and estimate the change in coil resistance. Moreover, comparison between different types of fixtures is carried out regarding the temperature rise, resistance change, and the value of magnetic field density achieved on the surface of the magnet, and a fixture topology is selected.

Furthermore, losses and efficiency of MLS are predicted at different velocities. Losses for magnet-to-magnet and magnet-to reluctance type MLS are investigated using 3D JMAG simulation package as rotation and translation motions can be modeled at the same time. The effect of load condition on the losses is investigated for both types of MLS. As a conclusion, results show that the average steady state total loss of magnet-to-reluctance type MLS is lower than that of magnet-to-magnet type MLS, and efficiencies in excess of 99% are achieved.

A double sided impulse magnetisation fixture is designed and manufactured, and detailed descriptions of the manufacturing procedures for the fixture is included. Furthermore, a test rig for the measurements of the transmitted force between the nut and the screw is developed. Results confirm that for linear motion of 5 mm corresponds to nut rotation of 180°. However although the measured pull-out force resulted from the test rig is lower than expected in simulation and that's was explained by supporting reasons.

Last but not least, a case study investigating the employing a magnetic screw for launching a UAV is presented. The idea is novel and hasn't been used before. General relationships between screw parameters and their effects on screw inertia, the torque produced by the drive motor, and transmitted force are discussed to provide a general framework on the working principle of the screw for both selected types of MLS.

For future research, some points could be proposed as follows:

- Investigate the feasibility of impulse magnetisation for different magnet sizes and lead lengths.

- Investigate methods of integrating a magnet screw system with a drive motor.

- Similar to other magnetic transmission systems, magnetic screw is also a compliant transmission, and special attention should be given to control, in particular position control where the screw is more likely to be employed. Thus, its performance under fine position control should be investigated, and appropriate control schemes should be developed.

REFERENCES

[1] H. Fair, "Electromagnetic propulsion: a new initiative," *IEEE Transactions on Magnetics*, vol. 18, pp. 4-6, 1982.

[2] M. R. Doyle, D. J. Samuel, T. Conway, and R. R. Klimowski, "Electromagnetic aircraft launch system-EMALS," *IEEE Transactions on Magnetics,* vol. 31, pp. 528-533, 1995.

[3] S. Rashleigh and R. Marshall, "Electromagnetic acceleration of macroparticles to high velocities," *Journal of Applied Physics,* vol. 49, pp. 2540-2542, 1978.

[4] M. Doyle, G. Sulich, and L. Lebron, "The benefits of electromagnetically launching aircraft," *Naval engineers journal,* vol. 112, pp. 77-82, 2000.

[5] B. Reck, "First design study of an electrical catapult for unmanned air vehicles in the several hundred kilogram range," *IEEE transactions on magnetics,* vol. 39, pp. 310-313, 2003.

[6] C. Li and B. Kou, "Research on electromagnetic force of a large thrust force permanent magnet synchronous linear motor," in *Electromagnetic Launch Technology (EML), 2012 16th International Symposium on*, 2012, pp. 1-4.

[7] J. Lu, X. Zhang, S. Tan, X. Guan, W. Ma, and S. Song, "Research on a linear permanent magnet brushless DC motor for electromagnetic catapult," *IEEE Transactions on Plasma Science,* vol. 43, pp. 2088-2094, 2015.

[8] E. R. Laithwaite, "Linear electric machines—A personal view," *Proceedings of the IEEE,* vol. 63, pp. 250-290, 1975.

[9] H. Robertson, L. C. M. Bolton, and L. M. Thomson, "An advanced linear motor system for electromagnetic launch: development and opportunities," in *Pulsed Power symposium, 2005. The IEE (Reg. No. 2005/11070),* 2005, pp. 29/1-29/6.

[10] Krepelka. *Boeing F/A-18 Hornet Flight Notes*. Available: http://krepelka.com/fsweb/learningcenter/aircraft/flightnotesboeingfa18hornet.htm

[11] Wikipedia. (2018, 15 August). *Railgun*. Available: https://en.wikipedia.org/wiki/Railgun

[12] S. Shope, J. Alexander, W. Gutierrez, R. Kaye, M. Kniskern, and F. Long, "Results of a study for a long range coilgun naval bombardment system," SANDIA NATIONAL LABS ALBUQUERQUE NM2001.

[13] Z. automation. (2018, 15 August). *Critical speed*. Available: https://www.zappautomation.co.uk/ecalculators.html

[14] Drylin. (15 August). *Drylin linear guide systems*. Available: https://www.igus.co.uk/contentData/Product_Files/Download/pdf/05_01_GL6_UK_drylin_einl_NEU.pdf

[15] H. Gurol, "General atomics linear motor applications: moving towards deployment," *Proceedings of the IEEE,* vol. 97, pp. 1864-1871, 2009.

[16] H.-W. Lee, K.-C. Kim, and J. Lee, "Review of maglev train technologies," *IEEE transactions on magnetics,* vol. 42, pp. 1917-1925, 2006.

[17] B. Rochard and F. Schmid, "Benefits of lower-mass trains for high speed rail operations," in *Proceedings of the Institution of Civil Engineers-Transport*, 2004, pp. 51-64.

[18] M. Palmer and R. Lenard, "A revolution in access to space through spinoffs of SDI technology," *IEEE Transactions on magnetics,* vol. 27, pp. 11-20, 1991.

[19] D. Bauer, J. Barber, and H. Swift, "Application of electromagnetic accelerators to space propulsion," *IEEE Transactions on Magnetics,* vol. 18, pp. 170-175, 1982.

[20] D. R. G. Cristina Gómez "Small-Scale Airborne Platforms for Oil and Gas Pipeline Monitoring and Mapping," REDWING/AICSM –UCEMM, UNIVERSITY OF ABERDEEN 2015.

[21] A. Benjamin, "Magnetic screw," US Patent 1,562,730, Nov. 24, 1925.

[22] H. T. Faus, "Magnetic transmission," US Patent 2,371,511, March 13, 1945.

[23] J. Gerrard and R. Paul, "Rectilinear screw-thread reluctance motor," *Electrical Engineers, Proceedings of the Institution of,* vol. 118, pp. 1575-1584, 1971.

[24] R. Paul, "Magnetic rotary-linear or linear-rotary converter," *Electric Power Applications, IEE Journal on,* vol. 2, pp. 135-138, 1979.

[25] G. Dawkins and D. Rhodes, "An Electromagnetic Rotary-to-Linear Coupler," in *Proceedings of the Int. Conf. on Electrical Machines, Brussels, Belgium*, 1978.

[26] J. Hashimoto and Y. Kubo, "Magnetic screw device," US Patent 5,687,614, Nov. 18, 1997.

[27] S. Pakdelian and H. A. Toliyat, "Trans-rotary magnetic gear for wave energy applicaion," in *Power and Energy Society General Meeting, 2012 IEEE*, 2012, pp. 1-4.

[28] R. K. Holm, N. I. Berg, M. Walkusch, P. O. Rasmussen, and R. H. Hansen, "Design of a magnetic lead screw for wave energy conversion," *Industry Applications, IEEE Transactions on,* vol. 49, pp. 2699-2708, 2013.

[29] N. Berg, M. Walkusch, and R. Holm, "Design of a Magnetic Lead Screw for Wave Energy Conversion," in *annual energy seminar, Aalborg University*, 2012.

[30] J. Ji, Z. Ling, J. Wang, W. Zhao, G. Liu, and T. Zeng, "Design and Analysis of a Halbach Magnetized Magnetic Screw for Artificial Heart," *Magnetics, IEEE Transactions on,* vol. 51, pp. 1-4, 2015.

[31] N. I. Berg, R. K. Holm, and P. O. Rasmussen, "Design and test of a novel magnetic lead screw for active suspension system in a vehicle," in *Electrical Machines (ICEM), 2014 International Conference on*, 2014, pp. 470-477.

[32] N. I. Berg, R. K. Holm, and P. O. Rasmussen, "A novel magnetic lead screw active suspension system for vehicles," in *Energy Conversion Congress and Exposition (ECCE), 2014 IEEE*, 2014, pp. 3139-3146.

[33] T. Finocchiaro, T. Butschen, P. Kwant, U. Steinseifer, T. Schmitz-Rode, K. Hameyer, *et al.*, "New linear motor concepts for artificial hearts," *Magnetics, IEEE Transactions on,* vol. 44, pp. 678-681, 2008.

[34] J. Wang, K. Atallah, and W. Wang, "Analysis of a magnetic screw for high force density linear electromagnetic actuators," *Magnetics, IEEE Transactions on,* vol. 47, pp. 4477-4480, 2011.

[35] S. Pakdelian, N. W. Frank, and H. A. Toliyat, "Principles of the trans-rotary magnetic gear," *Magnetics, IEEE Transactions on,* vol. 49, pp. 883-889, 2013.

[36] V. Bhandari, *Design of machine elements*: Tata McGraw-Hill Education, 2010.

[37] K. Lu, Y. Xia, W. Wu, and L. Zhang, "New helical-shape magnetic pole design for Magnetic Lead Screw enabling structure simplification," *Magnetics, IEEE Transactions on,* vol. 51, pp. 1-4, 2015.

[38] S. Pakdelian and H. A. Toliyat, "Design aspects of the trans-rotary magnetic gear," in *IECON 2012-38th Annual Conference on IEEE Industrial Electronics Society*, 2012, pp. 1720-1725.

[39] M. Mita, N. Hirao, and F. Kimura, "Magnetic screw rod using dual state 0.6 C–13Cr–Fe bulk magnetic material," *Journal of applied physics,* vol. 91, pp. 6997-6999, 2002.

[40] N. G. Vitale, "Rotary torque to axial force energy conversion apparatus," US Patent 6,190,409 B1, Feb. 20, 2001.

[41] K. Lu and W. Wu, "Electromagnetic Lead Screw for Potential Wave Energy Application," *Magnetics, IEEE Transactions on,* vol. 50, pp. 1-4, 2014.

[42] Z. Ling, W. Zhao, J. Ji, and G. Liu, "Design of a New Magnetic Screw With Discretized PMs," *Applied Superconductivity, IEEE Transactions on,* vol. 26, 2016.

[43] B. L. Gysen, J. L. Janssen, J. J. Paulides, and E. A. Lomonova, "Design aspects of an active electromagnetic suspension system for automotive applications," *Industry Applications, IEEE transactions on,* vol. 45, pp. 1589-1597, 2009.

[44] N. Amati, A. Festini, and A. Tonoli, "Design of electromagnetic shock absorbers for automotive suspensions," *Vehicle System Dynamics,* vol. 49, pp. 1913-1928, 2011.

[45] B. Ebrahimi, H. Bolandhemmat, M. B. Khamesee, and F. Golnaraghi, "A hybrid electromagnetic shock absorber for active vehicle suspension systems," *Vehicle System Dynamics,* vol. 49, pp. 311-332, 2011.

[46] B. L. Gysen, T. P. Van der Sande, J. J. Paulides, and E. A. Lomonova, "Efficiency of a regenerative direct-drive electromagnetic active suspension," *Vehicular Technology, IEEE Transactions on,* vol. 60, pp. 1384-1393, 2011.

[47] I. Martins, J. Esteves, G. D. Marques, and F. P. d. Silva, "Permanent-magnets linear actuators applicability in automobile active suspensions," *Vehicular Technology, IEEE Transactions on,* vol. 55, pp. 86-94, 2006.

[48] N. I. Berg, R. K. Holm, and P. O. Rasmussen, "Theoretical and experimental loss and efficiency studies of a magnetic lead screw," in *Energy Conversion Congress and Exposition (ECCE), 2013 IEEE*, 2013, pp. 2185-2192.

[49] R. K. Holm, N. I. Berg, M. Walkusch, P. O. Rasmussen, and R. H. Hansen, "Design of a magnetic lead screw for wave energy conversion," in *Electrical Machines (ICEM), 2012 20th International Conference on*, 2012, pp. 618-626.

[50] H. Polinder, M. E. C. Damen, and F. Gardner, "Linear PM Generator system for wave energy conversion in the AWS," *IEEE Transactions on Energy Conversion,* vol. 19, pp. 583-589, 2004.

[51] N. Bianchi, S. Bolognani, D. D. Corte, and F. Tonel, "Tubular linear permanent magnet motors: an overall comparison," in *Industry Applications Conference, 2002. 37th IAS Annual Meeting. Conference Record of the*, 2002, pp. 1266-1273 vol.2.

[52] K. J. Strnat, "Modern permanent magnets for applications in electro-technology," *Proceedings of the IEEE,* vol. 78, pp. 923-946, 1990.

[53] W. H. Hayt and J. A. Buck, *Engineering electromagnetics* vol. 7: McGraw-Hill New York, 2001.

[54] J. Ormerod and S. Constantinides, "Bonded permanent magnets: Current status and future opportunities," *Journal of applied physics,* vol. 81, pp. 4816-4820, 1997.

[55] G. Jewell, D. Howe, and C. Riley, "The design of radial-field multipole impulse magnetizing fixtures for isotropic NdFeB magnets," *IEEE transactions on magnetics,* vol. 33, pp. 708-722, 1997.

[56] K.-S. Kim, M.-R. Park, H.-J. Kim, S.-H. Chai, and J.-P. Hong, "Estimation of Rotor Type Using Ferrite Magnet Considering the Magnetization Process," *IEEE Transactions on Magnetics,* vol. 52, pp. 1-4, 2016.

[57] J. Bae, S.-J. Kim, S.-C. Go, H.-W. Lee, Y.-D. Chun, C.-J. Ree*, et al.*, "Novel configuration of the magnetizing fixture for a brushless permanent-magnet motor," *IEEE Transactions on Magnetics,* vol. 45, pp. 2807-2810, 2009.

[58] G. W. Jewell, "The computer-aided design and analysis of impulse magnetizing fixtures," University of Sheffield, 1992.

[59] G. Jewell and D. Howe, "Post-assembly impulse magnetization of brushless DC motors equipped with rare-earth magnets," in *Electrical Machines and Drives, 1991. Fifth International Conference on,* 1991, pp. 16-20.

[60] Z. Ping, L. Yong, W. Yan, and C. Shukang, "Post-assembly magnetization of brushless DC motor," in *Power Electronics and Motion Control Conference, 2004. IPEMC 2004. The 4th International*, 2004, pp. 560-562.

[61] S. Ho, H. Li, and W. Fu, "A post-assembly magnetization method of direct-start interior permanent magnet synchronous motors and its finite-element analysis of transient magnetic field," *IEEE Transactions on Magnetics,* vol. 48, pp. 3238-3241, 2012.

[62] S. Sriveni, V. K. Chinnaiyan, and J. Jerome, "A simple low cost energy efficient magnetizer for industrial applications," in *Power Electronics, 2006. IICPE 2006. India International Conference on*, 2006, pp. 94-97.

[63] G. Jewell and D. Howe, "Impulse magnetization strategies for an external rotor brushless DC motor equipped with a multipole NdFeB magnet," in *Permanent Magnet Machines and Drives, IEE Colloquium on,* 1993, pp. 6/1-6/4.

[64] G. Jewell and D. Howe, "Computer-aided design of magnetizing fixtures for the post-assembly magnetization of rare-earth permanent magnet brushless DC motors," *IEEE Transactions on magnetics,* vol. 28, pp. 3036-3038, 1992.

[65] D. McDonald, "Magnetizing and measuring B & H in high energy product rare earth permanent magnets," *IEEE Transactions on magnetics,* vol. 22, pp. 1075-1077, 1986.

[66] C. K. Lee and B. I. Kwon, "Design of post-assembly magnetization system of line start permanent-magnet motors using FEM," *IEEE transactions on magnetics,* vol. 41, pp. 1928-1931, 2005.

[67] M.-F. Hsieh, Y.-M. Lien, and D. G. Dorrell, "Post-assembly magnetization of rare-earth fractional-slot surface permanent-magnet machines using a two-shot method," *IEEE Transactions on Industry Applications,* vol. 47, pp. 2478-2486, 2011.

[68] J. J. Stupak Jr, "Methods of magnetizing permanent magnets," *EMCW Coil Winding Show,* vol. 1, 2000.

[69] S.-y. Chen, K. Huang, and F. Juang, "Improvement of a capacitor discharge impulse magnetizer circuit," in *Power Electronics and Drive Systems, 2003. PEDS 2003. The Fifth International Conference on*, 2003, pp. 1162-1163.

[70] P.-s. Kim and Y. Kim, "A future cost trends of magnetizer systems in Korea," in *Industrial Electronics, Control, and Instrumentation, 1996., Proceedings of the 1996 IEEE IECON 22nd International Conference on*, 1996, pp. 991-996.

[71] J. K. Lee, "The analysis of a magnetizing fixture for a multipole Nd-Fe-B magnet," *IEEE Transactions on Magnetics,* vol. 24, pp. 2166-2171, 1988.

[72] R. VanderHeiden, A. Arkadan, and J. Brauer, "Nonlinear transient finite element modeling of a capacitor-discharge magnetizing fixture," *IEEE transactions on magnetics,* vol. 29, pp. 2051-2054, 1993.

[73] G. H. Ravell, "An overview of magnet processing," in *Electrical Electronics Insulation Conference, 1995, and Electrical Manufacturing & Coil Winding Conference. Proceedings*, 1995, pp. 69-71.

[74] G. Jewell, D. Howe, and T. Birch, "Simulation of capacitor discharge magnetisation," *IEEE Transactions on Magnetics,* vol. 26, pp. 1638-1640, 1990.

[75] P.-S. Kim, Y. Kim, and S.-H. Baek, "EFFICIENT DESIGN OF CAPACITOR DISCHARGE IMPULSE MAGNETIZER SYSTEM FOR 8-POLE MAGNET," *한국자기학회지,* vol. 5, pp. 828-832, 1995.

[76] P.-S. Kim and Y. Kim, "Part I-circuit, thermal and cost modeling of impulse magnetizer," in *Power Electronics and Drive Systems, 1999. PEDS'99. Proceedings of the IEEE 1999 International Conference on*, 1999, pp. 371-376.

[77] P.-S. Kim, Y. Kim, and B.-Y. Hong, "An investigation to general characteristics of impulse magnetizer. I. Circuit, thermal and cost modeling of impulse magnetizer," in *Industry Applications Conference, 1999. Thirty-Fourth IAS Annual Meeting. Conference Record of the 1999 IEEE,* 1999, pp. 1707-1714.

[78] P.-S. Kim, Y. Kim, and N.-H. Yim, "Exact parameter estimation of impulse magnetizer and, thermal analysis under this parameter," in *Power Electronics and Motion Control Conference, 2000. Proceedings. IPEMC 2000. The Third International*, 2000, pp. 1050-1055.

[79] M. Hsieh and Y. Hsiu, "Characteristic analysis for IPM motors with post-assembly magnetization," in *Electrical Machines and Systems, 2005. ICEMS 2005. Proceedings of the Eighth International Conference on*, 2005, pp. 240-242.

[80] J. K. Lee and E. Furlani, "The optimization of multipole magnetizing fixtures for high-energy magnets," *Journal of Applied Physics,* vol. 67, pp. 1570-1575, 1990.

[81] M.-F. Hsieh, Y.-C. Hsu, and D. G. Dorrell, "Design of large-power surface-mounted permanent-magnet motors using postassembly magnetization," *IEEE Transactions on Industrial Electronics*, vol. 57, pp. 3376-3384, 2010.

[82] M. Przybylski, D. Kapelski, B. Ślusarek, and S. Wiak, "Impulse Magnetization of Nd-Fe-B Sintered Magnets for Sensors," *Sensors*, vol. 16, p. 569, 2016.

[83] C. Riley, G. Jewell, and D. Howe, "Design of impulse magnetizing fixtures for the radial homopolar magnetization of isotropic NdFeB ring magnets," *IEEE transactions on magnetics*, vol. 36, pp. 3846-3857, 2000.

[84] P.-S. Kim, "On the modeling of impulse magnetizing fixture considering field and thermal characteristics," in *Power Electronics and Drive Systems, 2001. Proceedings., 2001 4th IEEE International Conference on*, 2001, pp. 705-710.

[85] C. Lee and G. Jang, "Development of a new magnetizing fixture for the permanent magnet brushless DC motors to reduce the cogging torque," *IEEE Transactions on Magnetics*, vol. 47, pp. 2410-2413, 2011.

[86] A. M. TECHNOLOGIES. (18 April 2018). *Sintered Neodymium-Iron-Boron Magnets N45SH*. Available: http://www.arnoldmagnetics.com/wp-content/uploads/2017/11/N45SH-151021.pdf

[87] S. Xue, J. Feng, S. Guo, Z. Chen, J. Peng, W. Chu, *et al.*, "Iron Loss Model under DC Bias Flux Density Considering Temperature Influence," *IEEE Transactions on Magnetics*, 2017.

[88] J.-H. Ahn, S.-M. Jangr, K.-H. Kim, and J.-H. Choi, "Analysis on driving characteristic of high speed permanent magnet synchronous motor for compressor of electric vehicle with driving method," in *Vehicle Power and Propulsion Conference (VPPC), 2012 IEEE*, 2012, pp. 223-226.

[89] C. Kim, K. Shin, J. Kim, J. Ahn, and J. Choi, "Iron loss analysis and reduction techniques of magnetic geared permanent magnet motors," in *Magnetics Conference (INTERMAG), 2017 IEEE International*, 2017, pp. 1-1.

[90] M. Popescu, T. Miller, D. Ionel, S. Dellinger, and R. Heidemann, "On the physical basis of power losses in laminated steel and minimum-effort modeling in an industrial design environment," in *Industry Applications Conference, 2007. 42nd IAS Annual Meeting. Conference Record of the 2007 IEEE*, 2007, pp. 60-66.

[91] J. Li, T. Abdallah, and C. R. Sullivan, "Improved calculation of core loss with nonsinusoidal waveforms," in *Industry Applications Conference, 2001. Thirty-Sixth IAS Annual Meeting. Conference Record of the 2001 IEEE*, 2001, pp. 2203-2210.

[92] H. Phyu and J. Quan, "Analysis of rotor eddy current loss with different magnetization directions in PM BLDC motor," in *Electrical Machines and Systems (ICEMS), 2015 18th International Conference on*, 2015, pp. 1170-1175.

[93] M. Mueller, S. Williamson, T. Flack, K. Atallah, B. Baholo, D. Howe, *et al.*, "Calculation of iron losses from time-stepped finite-element models of cage induction machines," in *IEE Conference Publication*, 1995, pp. 88-92.

[94] B. Baholo, K. Atallah, P. Mellor, D. Howe, M. Mueller, T. Flack*, et al.*, "Effect of high frequency flux ripple on iron loss in induction machines," *Journal of magnetism and magnetic materials,* vol. 157, pp. 444-446, 1996.

[95] K. Ali, K. Atallah, and D. Howe, "Prediction of mechanical stress effects on the iron loss in electrical machines," *Journal of applied physics,* vol. 81, pp. 4119-4121, 1997.

[96] T. Gonen, *Electrical Machines with MATLAB®*: CRC Press, 2011.

[97] D. Maga, M. Zagirnyak, and D. Miljavec, "Additional losses in permanent magnet brushless machines," in *Power Electronics and Motion Control Conference (EPE/PEMC), 2010 14th International*, 2010, pp. S4-12-S4-13.

[98] S.-J. Kim, E.-J. Park, S.-H. Lee, and Y.-J. Kim, "A gear efficiency improvement in magnetic gear by eddy-current loss reduction," in *Electromagnetic Field Computation (CEFC), 2016 IEEE Conference on*, 2016, pp. 1-1.

[99] G. Jang, M. Koo, J. Kim, K. Kim, and J. Choi, "Characteristic analysis of eddy current loss in permanent magnet linear synchronous generator considering tapped holes in movers using 3D analytical method," in *Magnetics Conference (INTERMAG), 2017 IEEE International*, 2017, pp. 1-1.

[100] J. D. Ede, K. Atallah, G. W. Jewell, J. B. Wang, and D. Howe, "Effect of axial segmentation of permanent magnets on rotor loss in modular permanent-magnet brushless machines," *IEEE Transactions on industry applications*, vol. 43, pp. 1207-1213, 2007.

[101] Y. Hu, S. Zhu, and C. Liu, "Permanent magnet eddy current loss analysis of interior PM machines for electric vehicle application," in *Magnetics Conference (INTERMAG), 2017 IEEE International*, 2017, pp. 1-1.

[102] Z. Zhu, Y. Chen, D. Howe, and J. Gliemann, "Rotor eddy current loss in single-phase permanent magnet brushless dc motor," in *Industry Applications Conference, 2007. 42nd IAS Annual Meeting. Conference Record of the 2007 IEEE*, 2007, pp. 537-543.

[103] K. Atallah, D. Howe, P. H. Mellor, and D. A. Stone, "Rotor loss in permanent-magnet brushless AC machines," *IEEE Transactions on Industry Applications*, vol. 36, pp. 1612-1618, 2000.

[104] W. contributors. (18 April 2018). *EMT Aladin*. Available: https://en.wikipedia.org/w/index.php?title=Special:CiteThisPage&page=EMT_Aladin&id=806367595

[105] W. contributors. (1 April 2018). *Drag coefficient*. Available: https://en.wikipedia.org/w/index.php?title=Special:CiteThisPage&page=Drag_coefficient&id=833668610

[106] M. Sadraey, *Aircraft Performance: Analysis*: VDM Publishing, 2009.

[107] A. F. a. P. Association, "BEAM DESIGN FORMULAS WITH SHEAR AND MOMENT DIAGRAMS," ed: American Forest and Paper Association Washington, DC, 2005.

[108] B. C. Punmia, *Mechanics of Materials*. New Delhi: LAXMI PUPLICATIONS (P) LTD, 2002.

[109] L. O'Rourke. (18 April 2018). *The Mathematics of Simple Beam Deflection*. Available: https://www.raeng.org.uk/publications/other/15-beam-deflection